

Advanced Vehicle Power Technology Alliance Fiscal Year 2018 (FY18) Annual Report (1 Oct 2017 – 30 Sep 2018)

Department of the Army
(RDTA-COS-EBO)
Department of Energy



30 January 2019

Mr. David Howell

Acting Director, Vehicle Technologies Office, Department of Energy-Energy Efficiency and Renewable Energy (VTO, DOE-EERE).

Mr. Jeffrey Langhout

Director, United States Army Tank Automotive Research, Development and Engineering Center (TARDEC), United States Army Research Development and Engineering Command (RDECOM), United States Army Materiel Command (AMC).

Disclaimer: Reference herein to any specific commercial company, product, process or service by trade name, trademark, manufacturer, or otherwise; does not necessarily constitute or imply its endorsement, recommendation, or favoring by the United States Government, the Department of Energy (DOE) or the Department of the Army (DA). The opinions of the authors expressed herein do not necessarily state or reflect those of the United States Government, the DOE or DA, and shall not be used for advertising or product endorsement purposes.

This Page Intentionally Blank

ACKNOWLEDGEMENTS

The Advanced Vehicle Power Technology Alliance (AVPTA) between the Department of Energy (DOE) and the Department of the Army (DA) was publicly announced in July 2011. The Alliance underscores the urgency for energy security; in particular, an emphasis on developing advanced technologies that enable commercial and military ground vehicles to become significantly more energy efficient. Individually and collaboratively, the DOE and DA have a long history of successfully developing innovative vehicle technologies. The Alliance is chartered to accelerate the conceptualization and transition into deployment of inventive and creative energy-saving concepts that the Nation needs to achieve energy security.

This report summarizes the seventh year of technical effort and output of the Alliance's Technology Focus Area (TFA) working groups. The TFAs are respectively led by DOE and DA Subject Matter Experts (SMEs) that jointly recommend and oversee project portfolios in areas of interagency mutual technical interest.

We acknowledge the significant contributions of the DOE and DA administrative and technical personnel who in seven years have grown the Alliance from a notional concept into a self-sustaining and highly-productive entity. Work product generated by the Alliance has migrated into commercial and military applications through industry partners.

We specifically acknowledge Dr. Paul D. Rogers, TARDEC Director from 2013 to 2018, for providing invaluable leadership, insight and inter-agency communication, coordination and collaboration to the Alliance.

Mr. David Howell
Acting Director, Vehicle Technologies Office, Department of Energy-Energy Efficiency and Renewable Energy (VTO, DOE-EERE).

Mr. Jeffrey Langhout
Director, United States Army Tank Automotive Research, Development and Engineering Center (TARDEC), United States Army Research Development and Engineering Command (RDECOM), United States Army Materiel Command (AMC).

This Page Intentionally Blank

CONTENTS

Topic	Page(s)
Cover Page	1 - 2
Acknowledgements	3 - 4
Contents	5 - 6
Executive Summary	7 - 8
Introduction	9 - 10
Technology Focus Area Descriptions	11 - 14
Project Technical Reports	15 - 234
TFA1: Advanced Combustion Engines & Transmissions	15 - 18
TFA2: Lightweight Structures & Materials	19 - 78
TFA3: Energy Recovery & Thermal Energy	79 - 80
TFA4: Alternative Fuels & Lubricants	81 - 114
TFA5: Electrified Propulsion Systems	115 - 126
TFA6: Energy Storage & Batteries	127 - 170
TFA7: Analytical Tools (Modeling & Simulation)	171 - 188
TFA9: Autonomy-enabled Technologies	189 - 190
TFAE: "Extended Enterprise" Activities	191 - 234
Appendix	
A: DOD / DOE Memorandum of Understanding (MOU)	235 - 240
B: AVPTA Renewed/Extended Charter	241 - 244

This Page Intentionally Blank

EXECUTIVE SUMMARY

The AVPTA Mission is to leverage “resources to improve transition of technologies into both the commercial and military marketplace,” and “industrial research and development (IRAD) involving commercial automotive and defense ground vehicle manufacturers to transition technologies and increase precompetitive research and development.”

The following summaries document the work product of twenty-three (23) projects contained within the AVPTA portfolio. Project performers include Automotive Industry Original Equipment Manufacturers (OEMs) and Tier 1 / 2 Suppliers, Defense Industry OEMs and Suppliers, DOE national laboratories, DOD Research Laboratories, Contract Research Organizations, Universities and Colleges, Small and Other Category Businesses.

Some of the projects reported upon herein were among the seven (7) original projects that formed the Alliance’s foundation and enabled its rapid start-up. In many instances, DOE and DA mutually leveraged respective ongoing projects by infusing personnel, contributing resources, and providing mutual experience/expertise. This quickly expanded the Alliance technical network and reach, and provided access to activities beyond those directly funded by the Alliance. An example is TARDEC SME engagement in the VTO Annual Merit Review (AMR) during which TARDEC personnel are exposed to the complete VTO project portfolio including participating/contributing as review panel members. Joint participation in the AMR helps to formulate areas of mutual technical interest (AOIs) that contain the description, scope and deliverables for future new-start projects.

Also reported upon herein are projects that were jointly selected for start-up in preceding Fiscal Years. The Alliance has developed and instituted a sustainable, new-start project review and selection process based upon VTOs annual Funding Opportunities Announcements process and timeline. The process leverages DOE’s National Energy Technology Laboratory Contract Office to rapidly obligate and efficiently track project funding by individual performer.

Since its inception in 2011, DOE and DA have contributed a total of \$132.5M towards jointly-funded Alliance projects. The result has been a level of effort/output that neither agency would have realized without the interagency collaboration.

Report Prepared by:

Scott Schramm, Technical Advisor, External Business Office, TARDEC/RDECOM/AMC

Gurpreet Singh, Program Manager, VTO, DOE-EERE

This Page Intentionally Blank

INTRODUCTION

There are two high level drivers that led to the development of the AVPTA. The first is the elevation of energy efficiency and security as points of emphasis throughout the Army and the Department of Defense (DOD) as a whole. For the Army, a major milestone in this was the development of the Army Energy Security Implementation Plan (AESIP) in 2009. Within the AESIP goal to Increase Energy Efficiency across Platforms and Facilities, there was an objective to increase the efficiency of tactical equipment. At the DOD level, the Operational Energy Strategy is a principle-guidance document for the Department's approach to ensure energy security for operational forces.

The second was a call by the DOD for strengthened interagency partnering. This was set forth in its 2010 Quadrennial Defense Review. Energy security was identified as an excellent opportunity area for such a partnership. To this end, the Department of Energy (DOE) and DOD worked to craft a Memorandum of Understanding (MOU) to establish a partnering framework to enhance national energy security. This MOU is included as Appendix A. The MOU calls for the Departments to work together in a wide range of technical areas; including efficient transportation and overall energy efficiency.

DA and DOE worked together under the auspices of this MOU to develop a charter for working together in a wide range of vehicle technologies. This charter describing the Alliance was originally signed by the Honorable Daniel B. Poneman, Deputy Secretary of Energy and the Honorable Joseph W. Westphal, Under Secretary of the Army; and in 2016 was renewed/extended for five (5) additional years under the signatures of the Honorable Elizabeth Sherwood-Randall, Deputy Secretary of Energy and Honorable Patrick J. Murphy, Under Secretary of the Army (see Appendix B).

DOE's Office of Energy Efficiency and Renewable Energy (EERE) supports early-stage research of energy efficiency, renewable energy, and transportation technologies that enhance energy affordability, reliability, and resilience and strengthen U.S. energy security, economic growth, and environmental quality. A critical step in any new technology development is having it accepted and deployed in the marketplace. Teaming with DOD provides an attractive pathway for early utilization of the novel energy-saving ideas coming from the DOE research portfolio. These agencies priorities are summarized in the following table:

Remainder of Page Intentionally Blank

DOD & DOE Priorities

DOD Operational Energy Strategy	DOE Vehicle Technologies Office
Reduce Energy Demand: <ul style="list-style-type: none"> - Reduce: <ul style="list-style-type: none"> • Overall Operational Energy Demand • Mission Risks & Costs - Improve Energy Usage Efficiency 	Improve Energy Efficiency of the Transportation Sector
Expand & Secure Energy Supply: <ul style="list-style-type: none"> - Diversify Energy Sources - Protect Energy Supply Access 	Increase Domestic Energy Security Support American Energy Dominance Reduce Operating Cost for Consumers and Business
Integrate Operational Energy Considerations Into: <ul style="list-style-type: none"> - Planning Activities and Force Development 	Improve Global Competitiveness of U.S. Industry Improve Domestic Manufacturing

With strong support from senior leadership, the agencies collaborated at the Executive and SME Levels to identify AOs that are the founding principles for describing each of the Alliance’s Technology Focus Areas (TFAs). The respective TFA descriptions follow.

Remainder of Page Intentionally Blank

TECHNOLOGY FOCUS AREA (TFA) DESCRIPTIONS

TFA1: Advanced Combustion Engines & Transmissions

Advanced air-fuel management systems and novel combustion regimes have the potential to dramatically increase efficiency and power density, while at the same time reducing emissions. Meeting the challenge of developing and optimizing the combustion of common petroleum fuels, including Jet Propellant-8 (JP8), or biofuels in advanced engines requires a new level of the understanding of the physical and chemical phenomena of the Direct Injection (DI) diesel engine, which will be strongly affected by the different fuel properties which in turn affect fuel/air mixture preparation, combustion and emissions.

Advanced transmissions can allow the engine to operate more frequently in regions of high efficiency and transmit more torque while maintaining drivability. Of particular interest for further Research & Development (R&D) are approaches and devices to increase launch-assist device efficiency, and to increase the number of gear ratios. Among possible options for investigation are higher gear count automatic transmissions, Dual Clutch Transmissions (DCT), wet and dry clutch launch devices, multi damper torque converters, Continuously Variable Transmissions (CVTs), and binary transmissions.

TFA2: Lightweight Structures & Materials

Reduction of vehicle gross weight is an effective approach to reduce energy consumption during the vehicle usage, regardless of their energy sources (e.g., liquid fuels or electric batteries). Lightweight materials such as aluminum (Al) alloys, magnesium (Mg) alloys, high-strength steel, and carbon-polymer composites have been considered to replace low carbon steels conventionally used in automotive components. Challenges exist, however, to integrate components made of these lightweight materials into vehicle structures to achieve maximum weight reduction, while maintaining structural rigidity, crash safety, production quality and cost parity.

TFA3: Energy Recovery & Thermal Management

In current vehicles, approximately 60% of the chemical energy of fuel is lost in the form of waste heat, dissipated by the exhaust and cooling systems. The former offers high-grade heat that approaches temperatures of 800°C while the latter is a considerably more modest heat source at approximately 120°C. Of significant interest are exhaust heat recovery systems, including Organic Rankine cycles, as well as mechanical and electrical turbo-compounding. In addition, through the development of cost-competitive advanced second generation thermoelectric (TE) devices for vehicle applications vehicle fuel efficiency, performance, and emissions can be improved. Thermo-electric devices can convert engine waste heat to useful electrical power, to be used either assisting propulsion or for powering hotel loads. By integrating high Figure of Merit TE devices in

the vehicle architecture, thermal management of vehicles can become significantly more efficient.

TFA4: Alternative Fuels & Lubricants

Alternative fuels and lubricants can facilitate or enhance conventional engine technology, as well as advanced combustion regime engine operation such as Homogeneous Charge Compression Ignition (HCCI) or Low Temperature Combustion. For alternative fuels, the focus should be on drop-in fuels or blend stocks that displace petroleum-derived fuels in vehicle applications without significant infrastructure changes or requirements. New developments in base oil and additive packages can reduce viscosity while maintaining temperature requirements, thereby improving engine and transmission efficiency.

TFA5: Electrified Propulsion Systems

Electric drive options range from mild battery-alternator systems to full parallel and series systems or all electric drive, and require engineering trade-offs between fuel consumption benefit and system complexity, reliability and cost. However, to achieve efficient solutions, electrical materials and devices will require higher conversion efficiencies and power/energy densities than are currently possible. The next generation electric drive vehicles will benefit from improved and lower cost batteries, novel electric motors, thermoelectric waste heat recovery, and power electronic devices and electrical topologies that are capable of handling increased loads and multiple combinations of sources and accessories. Activities focus on hybrid system power electronics and electric machines.

TFA6: Energy Storage & Batteries

Stakeholders desire to improve existing battery chemistries, develop advanced battery technologies (high power and high energy systems), and conduct ultra-capacitor research. Military goals are to improve the availability of onboard power, reduce energy demand/consumption, expand the energy supply to military operations and build energy security into future forces in the specific areas of: silent watch capability, electromagnetic armor and starting/lighting/igniting (SLI). Civilian/commercial goals are to reduce the petroleum demand and promote US economic competitiveness in advanced hybrid electric vehicles and electric vehicles. Advanced lead-acid batteries, ultra-capacitors, lithium-ion batteries, lithium sulfur and lithium-air batteries are joint areas of interest. Both agencies are also interested in improving on-board safety, developing battery test protocols and promoting codes and standards.

TFA7: Analytical Tools (Modeling & Simulation)

Diverse fuel sources, advanced combustion modes, hybrid/electrified powertrains, energy harvest/waste heat recovery technologies, and using lightweight materials substantially elevate the complexities of efficient vehicle powertrain systems and impose critical challenges for system integration and control. These efficient vehicle powertrain sub-

systems, with new characteristics and strongly interactive dynamics, necessitate research on system integration and advanced control strategies. An integrated and analytical systems approach ensure that the various sub-systems of the vehicle work seamlessly, reliably and synergistically to optimize coordination so as to maximize vehicle energy efficiency, power density and emission reduction potential in real-world applications. Through state-of-the-art modeling and analysis, concepts and strategies can be screened during the vehicle design stage, and most promising candidates and key pathways to bring them to realization in an effective time frame can be identified. Critical components and/or systems needing specific development can also be identified and analyzed with simulation tools.

TFA9: Autonomy-enabled Technologies

Autonomy-enabled technologies have the promise to significantly decrease fuel consumption through a variety of mechanisms. For example, platooning, where vehicles travel close to each other in order to reduce aerodynamic drag at high speeds, can only be achieved through connectivity and automation. A significant source of excess fuel consumption comes from vehicle operators driving in a sub-optimal manner, such as exceeding optimal speeds and accelerating and decelerating too quickly. Intelligent systems can help increase fuel efficiency by providing information to the driver to improve operational behavior, by determining more efficient routes based on topography or traffic conditions, or by taking control of certain vehicle functions. An automated traffic management system, implemented through a system of autonomous vehicles connected with intelligent roadway infrastructure, could greatly reduce vehicle start/stops and slowdowns, optimizing traffic flow, and improving mobility in urban driving. Preliminary research by the National Renewable Energy Laboratory (NREL) indicates that platooning could increase fuel efficiency by 10%, eliminating driver inefficiencies another 15%, and completely automating the vehicle transportation system could yield a 40% improvement. However, these estimates are based on a limited number of experiments, which may not include the full range of variability that a real world system would experience, nor potential second-order effects, such as an increase in vehicle miles traveled. Accordingly, additional analysis and targeted experimentation are needed to more fully explore the limitations that these autonomy-enabled technologies may have in regards to increasing fuel efficiency across the transportation system.

TFAE: “Extended Enterprise” Activities

“Extended Enterprise” Activities projects are technically ‘endorsed’ by the DOE Vehicle Technologies and/or Fuel Cell Technologies Office(s) (DOE-VTO, FCTO), but because the project scope of work does not directly align with a VTO or FCTO Funding Opportunities Announcement Area of Interest (FAO-AOI), DOE does not contribute project funds. TARDEC funds the projects to which VTO and FCTO representatives have meeting access and about which receive technical reports.

PROJECT TECHNICAL REPORTS

(Start on Page 15)

AVPTA Technology Focus Area 1: Advanced Combustion, Engines & Transmissions

Temperature-Following Thermal Barrier Coatings for High-Efficiency Engines

DOE-VTO TFA Lead: Mr. Ken Howden
TARDEC TFA Lead: Dr. Peter Schihl

Principal Investigator(s):
Mr. Toby Schaedler

Affiliation:
HRL Laboratories
Malibu, CA

Project Start: Q2FY17
Estimated Completion: Q3FY20

Objective:

The objective of this project is to increase the efficiency of internal combustion engines by 4% to 8% with thermal barrier coatings within the cylinder and exhaust ports that add less than ~\$250 in cost to a 4-cylinder engine. Benefits will be derived from:

- In-Cylinder Efficiency improvements through lower heat losses
- Increased effectiveness of exhaust energy recovery and after-treatment with higher exhaust temperatures under highly dilute conditions
- Lower parasitic losses due to reduced cooling demands

Strategic Context:

This project topic supports TARDEC's 30-Year Strategy VS.LOE.KO 1.3.3, which states: "enable ground vehicles to operate at increased speeds and extended ranges while requiring reduced frequency of resupply." Engines are expected to be the dominant form of propulsion in military vehicles for the next 30 years, subsequently reducing heat transfer and increasing efficiency fits this objective.

Accomplishments:

- Progress was made in developing microsphere structure through the variation of sintering pressure. Greater compaction pressure will result in higher density and smoother surface to enhance surface sealing.
- Two generations of aluminum pistons coated were tested in the first year.
- Intake and exhaust valves were coated and tested. Results showed that the key to a successful porous insulation coating is a robust, impenetrable surface sealing layer.

OPSEC1890

- Modeling effort was able to capture all heat transfer effects of interest. Modeling was able to show that performance of the coating with the sealing layer is highly dependent on the mass and heat capacity of the sealing layer.

Introduction:

In current passenger cars, only ~22% of the fuel energy is used to move the vehicle, while ~29% is lost to the cooling systems. By limiting heat losses from the combustion chamber with insulating coatings, fuel energy can be redirected into additional piston work and into the exhaust stream, where it can be partially recovered. Previous efforts with conventional ceramic thermal barrier coatings applied to surfaces in the combustion chamber have achieved only minor improvements in efficiency because the coating surface stabilized at high temperatures. The high in-cylinder surface temperature heats the incoming gases, which lowers volumetric efficiency and increases propensity for knock, resulting in degraded engine performance. In this project, HRL will develop advanced thermal barrier coatings that combine low thermal conductivity with low heat capacity. These unique properties allow the surface temperature of the coating to follow rapid changes in gas temperature during each combustion cycle, while reducing heat losses to the cooling system. Together with General Motors, HRL will optimize these coatings for application on piston crowns and other surfaces in the combustion chamber guided by simulations.

Approach:

Temperature-Following insulation allows surfaces to stay cool during the intake and compression stroke, which will help volumetric efficiency and compression work. During combustion, the Temperature-Following coating surface can increase rapidly to provide insulation benefits. Over the entire cycle, Conventional insulation's expansion benefits are negated by the increased compression work, while Temperature-Following shows improvements over Metal in compression & expansion. This allows in-cylinder insulation to provide all the benefits of lower heat rejection, but with none of the volumetric efficiency or knock drawbacks.

Thermal conductivity and volumetric heat capacity were independently varied to determine the material properties necessary for maximizing the temperature swing. High levels of porosity were determined to be necessary to decrease both the volumetric heat capacity (density) and the thermal conductivity. HRL has developed hollow nickel-alloy microsphere TBCs with an average diameter of 30 -50 μ m and 1 -2 μ m shell thickness. These microspheres can be sintered together to form high-temp metal matrices with over 90% porosity. Microsphere TBCs can be applied using dry molds, slurries, or air spraying. The surface must be sealed to avoid ingress of hot combustion gasses and unburned fuel vapor. A process was created for applying the microsphere-based insulation to aluminum components, such as the pistons.

Remainder of Page Intentionally Blank

Results and Discussion:

Intake and exhaust valves were coated with the microspheres and a 2.5 μ m Ni foil as the sealing layer. All of these components showed that the sealing layer was prone to puncture in many spots, some of which coincided with pre-test visible irregularities. Cross-sections revealed the microsphere structure survived the pressure and temperature intact, but the foil layer was poorly supported by it in the breached spots. The cause was an uneven packing density throughout the microsphere layer.

Two generations of aluminum pistons were tested in the first year. The learnings from the first were applied to creating the second. Generation 1A piston microsphere layers were created in a similar manner to the valves, and thus had many of the same permeability issues. Additionally, they had poor bonding between the copper disk and aluminum pistons, which lead to the separation of the part along this seam. Generation 1B incorporated improvements in microsphere packing shown previously, as well as a copper pocket design to seal the sides of microsphere layer. Better brazing techniques used for adhesion, but a bubble still formed between Cu & Al.

Conclusions:

The microsphere-based insulating material is meeting the target material properties of 0.2 W/m-K Conductivity and 0.2 MJ/m³-K for temperature-swing insulation. The microsphere insulation layer successfully survived the in-cylinder environment with no observed degradation to the microsphere structure. Drastic improvements in the impermeability of the sealing layer have been made and alternative processes are being pursued to eliminate interstitial gas penetration. Bonding to current aluminum pistons has been problematic, but work continues to solve the issues in parallel to thermal barrier materials development on steel components.

References:

- [1] T. Schaedler, P. Andruskiewicz, "Temperature-Following Thermal Barrier Coatings for High-Efficiency Engines", June 21, 2018, DOE Vehicle Technologies Annual Merit Review
- [2] Project Summary/Abstract for Public Release, HRL Laboratories, Control Number 1384-1672

Figure is on the Next Page:

Figure:

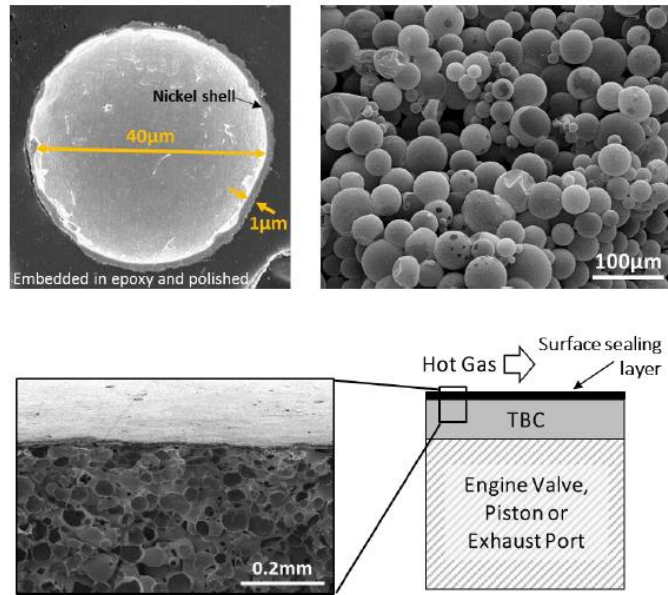


Figure 1: Hollow nickel-alloy microsphere TBC

Remainder of Page Intentionally Blank

AVPTA Technology Focus Area 2: Lightweight Structures & Materials

**Multi-Material Joining (MMJ) – Weld Wire Characterization in Welding
Advanced High-Strength Steels (AHSS)**

**DOE-VTO TFA Lead: Sarah Kleinbaum
TARDEC TFA Lead: Ravi Thyagarajan**

**Principal Investigator(s):
Matthew Rogers**

**Affiliation:
TARDEC-SIE-SES-PLE-Material-
Integration & Application Team**

**Project Start: Q1FY14
Estimated Completion: Q2FY19**

Objectives:

- Understand the joint quality and welding process efficiency of welded armor steels
- Establish weld wire selection criteria for the new MIL-Standard on the welding of armored steel
- Provide practitioners a point of comparison between current joining practices and future welding practices.
- Create validation data for ballistic and blast models of welded armor plates.

Strategic Context:

- The project data will transition and be used by both TARDEC engineers and vehicle manufacturers to further optimize vehicle designs. The data will identify optimal weld wire / material combinations to maximize weld filler material properties. The information will be transitioned to Original Equipment Manufacturers (OEMs) and suppliers through the military weld standard.
- The project supports TARDEC's Value Stream 2 by providing PMs with data and standards for improving weld quality for all steel vehicles. The same data and standards can be transitioned to the automotive industry.
- The project continues to build on the AVPTA MMJ investments in making TARDEC a joining center of excellence. The level of detail and fidelity of study speaks to TARDEC's in-depth expertise in welding.
- Future plans are to expand the study to include aluminum materials (2xxx, 5xxx, 6xxx, and 7xxx).

OPSEC1890

Accomplishments:

- **Phase 1:** Funding has been allotted as of mid Q2FY18. Bending dies and software have arrived as of July 6th 2018. Training took place on July 17th 2018 on equipment. Bend samples and Charpy impact samples are 25% completed. Instron equipment was down for 2 weeks as of the end of Oct 2018 to be relocated. Once equipment is recertified, testing will continue.
- **Phase 2:** Data conversion and analysis results from samples @ 100% complete as of Q4FY18, Final report is scheduled for Q1FY19. Currently waiting on updates from Phase 1 to complete report.
- **Phase 3:** Completed testing in May of 2016. Data conversion and analysis results from samples @ 100% complete. Final report 25% completed in Q1Y19. Currently waiting on updates from Phase 1 to complete report.

Introduction:

The chemical and mechanical properties of armor steel used by the US Army are similar to advanced high strength steels used in the automotive industry. The ultimate tensile strength ranges from 150 ksi to 300 ksi depending on the armor grade selected. The last MIL standard for welding armor was canceled in 1998 and replaced with the Ground Combat Vehicle Welding Code (GCVWC)-Steel, which has never been updated and has no engineering guidance for the selection of weld wire. Additionally, neither the old MIL standard nor the GCVWC-Steel include any recommendations based on newer armor grades and new welding techniques. There are also no published industry guidelines for welding of advanced high strength steels, which the government could use to weld armor. This has led to a proliferation of welding techniques by the defense contractors, which in turn has led to a general decrease in weld quality and the proliferation of defects, such as cracks induced by hydrogen embrittlement.

Performance of welded joints is critical to the performance and reliability of ground vehicles. The performance depends on many factors associated with the welding. One key factor is the type of weld wire, of which there are many. A weld wire is classified by weld process and tensile strength. The preferred process for welding plate armor in ground vehicles is Gas Metal Arc Welding (GMAW) pulse. Weld wire tensile strength ranges from 70 ksi to 120 ksi; some ground vehicle manufacturers have even used austenitic stainless steel filler metals. Unfortunately, the weldments made from these wires in combination with modern armor materials have not been characterized. There is also a general lack of knowledge of the mechanical and ballistic performance, in terms of joint efficiency, of these wires. Joint efficiency is defined as the ratio of the properties of the welded armor to the properties of the base metal armor. If the joint efficiency of each weld wire is known, then proper filler metal selection criteria can be established and implemented through a the new weld standard.

In addition to establishing selection criteria for the welding of armor steel, the data obtained in this study will be used to validate material models for ballistic and blast modeling and simulation. This data can be used by both TARDEC engineers and vehicle manufacturers to further optimize vehicle designs.

OPSEC1890

Approach:

The project is divided into three phases:

Phase 1: Investigate the mechanical and metallurgical properties of welded armor using various weld wires.

This phase involves robotically welding MIL-DTL-12560 class1, MIL-DTL-46100 class1, and ASTM A514 Grade A to themselves in 14" x 21" x 1/2" single V-groove sample. Filler materials are solid wire, stainless steel, and metal core filler. Various tensile strengths ranging from approximately 70ksi-140ksi will be used. All samples will be welded internally at TARDEC/Center for System Integration (CSI). The samples will then undergo tensile, hardness, fatigue, charpy impact, hydrogen embrittlement (see Table 1). Once this is complete, the samples will be ranked for performance. The highest performers will move to Phase 2.

Phase 2: Perform high strain rate events using a ballistic shock test with a welded H-plate.

This phase involves taking the highest filler performers from Phase 1 and robotically welding them into a 3'x 3' x 1/2" H-plate configuration. The same single V-Groove configuration will be used throughout this test as well. Once the plates are welded and radiographically tested they will be sent over to the TARDEC SABL lab for Ballistic Shock testing (see Table 2). If the samples pass, they will be used for Phase 3

Phase 3: Perform penetration testing to determine magnitude of vulnerability.

This phase involves taking the performers from Phase 2 and robotically welding 2' x 2' x 1/2" single V-groove plates. Penetration testing will determine the joint efficiency as defined by the magnitude vulnerability (see Table 3). These tests are performed with a high speed camera and flash x-ray to record the dynamic deformation during the ballistic shock test. Understanding the dynamic deformation response is crucial to improving our understanding of weld responses to high strain rate events

Results and Discussion:

In the first year, the overall study plan was completed and the welding material and weld wires procured. In addition, it was necessary to develop an automated manner to weld standard I-plates and H-plates for testing. Figures 1 & 2 show the hardware fixture that was developed to robotically weld the large sample of I- and H-plates. Figure 1 shows a completed I-plate weld, and Figure 2 shows how an H-plate looks by comparison.

One issue that was not anticipated was that the MIL-DTL-46100 (high hard) material became highly magnetic from the shoot penning cleaning process. This required the additional step of demagnetizing the material before welding to prevent arc blow (see Figure 4).

Phase 1: Welding of the I-plates has been completed. Figure 5 shows a sample hardness scan of a completed weld zone. Figure 6 shows how all the weld characterization samples are cut from a single plate. Three samples will be cut from different plates for

OPSEC1890

each weld wire / parent material combination to obtain statistical validity of the results. Phase 1 is currently about 25% complete. For the tensile samples, one of the four sets of tensile bars for every combination has been complete. We currently have data to understand what the trends look like. As tensile strength goes below 80ksi or above 120ksi ultimate tensile strength yield strength properties begin to change. It is too early to tell but it is believed that they will be a level that will be acceptable ranging from 80ksi to 100ksi

Phase 2: Currently is at 100% complete with testing. The range has shot the remaining 25 H-Plates as of Q4FY18. Digital Imaging Correlation (DIC) software/ analysis was added to the testing in order to better understand the deflection on the steel at high strain rate. Final report is scheduled for Q2FY19. Currently waiting on updates from Phase 1 to complete report.

Phase 3: is 100% complete and the final report is being completed Final report 25% completed in Q1Y19. Currently waiting on updates from Phase 1 to complete report.

Conclusions:

The Phase 1 plates will be tested and analyzed. The remaining Phase 2 plates will take approximately 9 months to weld. The data that was collected, has been provided for input to the new MIL-STD-3040 for welding. MIL-STD-3040 has utilized the data and testing criteria to develop mechanical acceptance criteria.

This data will transition and be used by both TARDEC engineers and vehicle manufacturers to further optimize vehicle designs. This data will transition to Industry, PMs, Depots, and Arsenalns through the new welding MIL standard, by creating filler metal selection charts. The data from this project will also be easily transitioned to help industry, such as the automotive and heavy equipment companies, in the selection of weld filler materials for their types of AHSS due to the similarities in properties. The data obtained in this study will also be used to refine material models for modeling and simulation (M&S).

References:

- [1] MIL-STD-3040
- [2] AWS D1.1
- [3] AWS A2.4
- [4] ASTM A514
- [5] MIL-DTL-46100
- [6] MIL-DTL-12560
- [7] Quantifying Hydrogen Induced Cracking (HIC) Susceptibility of Welding Filler Wires Used in the Welding of Armor Steel
- [8] Matthew Rogers, "Quantifying Hydrogen Induced Cracking (HIC) Susceptibility of Welding Filler Wires Used in the Welding of Armor Steel", Nov 2016, <https://www.dtic.mil/dodtechspace/docs/DOC-25241>

Tables and Figures:

Table 1: Phase 1 Test, Test Location and Timeframe

Test	Locations	Time Frame
Robotically welded samples	TARDEC CSI weld area	FY14
Tensile Testing	TARDEC Materials Lab	FY14/FY15/FY17/FY18/FY19
Hardness Testing	TARDEC Materials Lab	FY14/FY15
Charpy Impact	TARDEC Materials Lab	FY14/FY15/FY17/FY18/FY19
Bend Samples	TARDEC Materials Lab	FY18/FY17

Table 2: Phase 2 Test, Test Location and Timeframe

Test	Locations	Time Frame
Robotically welded samples	TARDEC CSI weld area	FY14/FY15
Radiographic Test	ANAD	FY15
Ballistic Shock Test	TARDEC GVSP SABL	FY15/FY16/FY18

Table 3: Phase 3 Test, Test Location and Timeframe

Test	Locations	Time Frame
Robotically welded samples	TARDEC CSI weld area	FY15
Radiographic Test	Outside Contractor	FY16
Penetration Test	TARDEC GVSP SABL	FY16



Figure 1: Fixture for Robotic Welding of Phase 1 plate

Remainder of Page Intentionally Blank



Figure 4: Demagnetizing Process

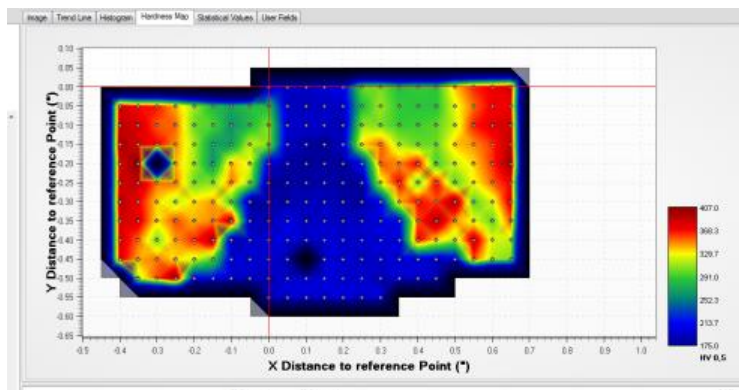


Figure 5: Sample of Micro hardness profile



Figure 6: Phase 1 I-plate Marked Samples for Standardized Weld Characterization Tests

Remainder of Page Intentionally Blank

This Page is Intentionally Blank

AVPTA Technology Focus Area 2: Lightweight Structures & Materials

Multi-Material Joining (MMJ) – High Strength Weld Wire Development Suitable for High Strength 5XXX and 6XXX Aluminum Alloys

**DOE-VTO TFA Lead: Sarah Kleinbaum
TARDEC TFA Lead: Ravi Thyagarajan**

**Principal Investigator(s):
Mr. Matthew Watson
Arconic Defense Inc.
100 Technical Drive
New Kensington, PA 15069**

**Mr. Martin M. McDonnell
Mr. Mike Foley
U.S. Army TARDEC
Product Lifecycle Engineering - Materials**

**Project Start: Q1FY13
Completed: Q4FY18**

Objectives:

- Develop a weld wire for welding high strength aluminum plate, particularly 6055; such that the weld joints exhibit improved mechanical properties and corrosion resistance over the incumbent weld wire material.
- Fusion weld 5083 and 6055 with the newly developed high strength filler wire.

Strategic Context:

- Permits the light weighting and improved performance of new vehicles, as well as increased protection for the Warfighter, due to a 20% strength increase in 6xxx alloys
- Improves the maintainability and repairability of legacy vehicles.
- Attractive for commercial transportation applications to cost effectively save weight.

Remainder of Page Intentionally Blank

Accomplishments:

Results are summarized for each filler developed during the project.

- Filler Alloy C56U
 - C56U filler can produce crack free welds when joining 6013 to itself or 5083.
 - C56U has similar tensile properties to filler 4043 when welding 6013 to 6013 and when welding 6013 to 5083, but higher shear strength and ductility, as seen in Figure
- Filler Alloys C138H and C139H
 - Restrained tee Gas Tungsten Arc (GTA) welding trials of C138H and C139H indicate that they produce crack free weldments when joining 6055 to 6055, 6055 to 5083, and 5083 to 5083.
 - Tensile testing of GTA butt welds indicate that C138H and C139H provide a ~19% and 26% improvement in tensile strength vs. the current MIL-DTL-32262A minimum (6055 welded with 4943 filler), respectively.
 - Gas Metal Arc (GMA) weldments using C139H to join 6055-6055, achieved an as-welded transverse average tensile strength of 36.8 ksi (254 MPa), exceeding the MIL-DTL-32262A minimum of 24 ksi (165 MPa) for 6XXX by 53%.
 - The static as-welded joint efficiency (welded condition / base metal strength) was 60% for the transverse Ultimate Tensile Strength (UTS). The GMA welded C139H bend specimens achieved 5.7% elongation.

Introduction:

Military vehicles have been subjected to steadily increasing levels of blast threats. In response, the armor community has developed applique solutions, allowing upgrades to the vehicle survivability. However, the solutions are not optimized for weight or performance and result in parasitic weight that significantly reduces fuel efficiency. Rarely is the armor integrated with the vehicle structure, which would result in a lighter armor solution, as well as eliminate the weight associated with applique attachment systems. In vehicle structures that do integrate the armor with the structure, such as blast hulls and underbody structures, armor options are limited to those materials, alloys and product forms that can be readily Gas Metal Arc (GMA) welded.

The development of high strength aluminum alloys, multi-alloy aluminum monolithic plate, and the ability to produce large forgings has led to the ability to provide technically advanced armor systems that provide enhanced survivability while minimizing weight. These materials must be joined together to create a “system” or be integrated into the vehicle structure. There are several joining technologies that may be employed, including mechanical fasteners, adhesive bonding, friction welding, and fusion welding. Joining techniques can result in joints and associated regions that are lower strength and constitute the “weak link” of the system. These regions may be thickened to compensate for the strength reduction associated with the joining technique, resulting in increased material and weight. Weight increases result in an increase in fuel use, an increase in drive train and suspension requirements, and a performance loss. Advanced joining

technologies need to be developed to enable these higher performance materials to be joined in a manner that optimizes the vehicle weight, as well as structural and survivability performance.

High strength 6XXX aluminum alloys, such as 6055, have ~20% higher strength than aluminum alloys currently used in combat vehicles and armor systems. They offer the potential to significantly improve performance and reduce weight and cost. However, when welding 6XXX high strength alloys, the only commercially available filler wires that can be used to fusion weld these alloys without cracking (4043, 4943, 4047 and 4145), produce welds with limited shear strength and ductility. This, in turn, limits their capability to withstand blast and shock loads. Because the joints produced with these filler wires are significantly weaker than the parent material, the full benefits of the high strength 6xxx alloys cannot be realized. As such, the components must be designed to compensate for the weakness of the joining method used, usually resulting in increased weight.

In addition, when welding high strength 6XXX alloys to 5XXX (e.g. 5083), the use of 4XXX fillers leads to the formation of brittle $MgSi_2$ at the fusion zones of the welds with the 5XXX parent metal. Alternately, when welding high strength 6XXX/5XXX alloy combinations with Mg based 5XXX filler alloys (e.g. 5556, 5356, 5183), the formation of Mg/Cu low melting eutectics at the fusion zones of the welds leads to cracking. To address the shortcomings associated with using commercially available 4XXX or 5XXX filler wires to GMA weld high strength 6XXX alloys to themselves or 5XXX alloys, the Arconic Technology Center (ATC) is developed and evaluated weld filler alloys that would result in higher welded joint strength. Specifically, ATC is developing new high Mg weld filler alloys with the following benefits:

- Enables joining high strength 6xxx alloys to each other and 5xxx alloys
- Enables fusion welds with high shear strength, ductility and blast/shock resistance
- Features chemistries that balance property requirements with corrosion susceptibility
- Eliminates the formation of brittle $MgSi_2$ that occurs when using 4XXX filler to fusion weld high strength 6XXX to 5XXX alloys

Phase I focused on evaluating a bench scale high strength filler wire alloy. In 2009, Arconic developed alloy C56U, a 5XXX filler targeted specifically for welding alloy 6013 to itself and other high Mg 5XXX series alloys used in the defense and commercial transportation markets. The focus of Phase I was to cast and fabricate alloy C56U as a welding electrode/filler for Gas Metal Arc (GMA) welding to enable crack free weldability, static strength and corrosion testing.

Phase II of the program initially focused on refinement and optimization of the chemistry of C56U to optimize the corrosion and mechanical properties. However, upon review with TARDEC, the emphasis was shifted to new filler alloy chemistries for welding alloy 6055.

Phase III focused on casting and drawing new filler alloys, C138H and C139H, into GMA welding electrode and evaluating the weldability and static tensile testing of welded 6055 plate.

Approach:

Milward Alloys cast four 100-pound ingots of C56U alloy. Whereas the chemistries met target levels, the hydrogen content was elevated (0.17-0.57 cc/100g) for all four ingots, compared to the cast hydrogen target level of <0.12 cc/100g, shown in Table 1. The cast ingot lots were to be tracked through the filler wire fabrication process, to identify materials with lower levels of hydrogen. Milward Alloys also extruded the ingots into 1" (25.4 mm) diameter bars, which were then transferred to Beneke and drawn down to 0.43" (11 mm) diameter rod. The 0.43" rod was transferred to AlcoTec Wire Co. for final drawing and processing into 0.047" (1.2 mm) and 0.063" (1.6 mm) diameter welding electrode. Unfortunately, all traceability of the four ingots was lost, making it impossible to preferentially select ingot cast lots with the lowest hydrogen content.

GMA weldability trials were conducted using 0.5" (12.7 mm) thick base metal 6013-T651 and 6061-T651, using the newly produced C56U filler, as well as alloy 4043 and 5183 fillers for baseline comparison. Restrained Tee testing was used for weldability screening; the results of these weldability trials are shown in Figure and Table .

Representative butt welds were produced using each spool of C56U electrode received from AlcoTec, followed by radiographic inspection and tensile property testing. These butt welds were made using 0.5" (12.7 mm) thick alloy 6013. Unfortunately, all weldments exhibited excessive porosity within the weld due to the high hydrogen content of the cast ingot. It was decided to discontinue all welding trials using this batch of electrodes.

To insure control of casting quality and hydrogen content, all future casting was done using internal Arconic capabilities and casting quality control processes. Arconic's Massena facility continuously cast 3/8" diameter rod for this project. However, a minimum order of 10,000 lbs. of 3/8" (9.4 mm) rod was required. Two coils containing 5000 lbs. each were delivered to the Arconic Technology Center. One coil was placed in storage while the second was shipped to Hobart for finishing: drawing and surface cleaning of 150 pounds of the rod into 0.047" (1.2 mm) and 0.063" (1.6 mm) diameter welding electrode.

Additional GMA butt welds made using 0.5" (12.7 mm) thick alloy 6013-T651 with the C56U electrode produced by Massena and Hobart exhibited acceptable radiographic weld porosity levels. Static tensile and corrosion testing was performed on these weldments. Test results for weldments of 6013, 5083, and a combination of the two base metals, using the C56U, and 4043 and 5183 weld filler alloys are detailed in Figure 3. Results indicate that C56U has similar properties to filler 4043 when welding 6013 to 6013, and when welding 6013 to 5083, with C56U or 5183 fillers. The tensile properties are similar as all specimens failed in the 6013 Heat Affected Zone (HAZ). When welding 5083 to 5083, C56U filler and 5183 filler exhibit similar tensile properties.

Corrosion testing indicated that C56U alloy has a propensity for intergranular corrosion (IG), as well as stress corrosion cracking (SCC), after exposure to elevated temperatures. The weld nugget in the as-welded condition showed low mass loss (<15 mg/cm²) in the ASTM G67, Nitric Acid Mass Loss Tests (NAMLT) test, which indicates resistance to IG and SCC. However, after exposure to 100°C for 1 week, the weld nugget exhibited a mass loss greater than 25 mg/cm², indicating susceptibility to IG and SCC. This suggests that the weld can become susceptible to

OPSEC1890

IG and SCC after exposure to elevated temperatures and/or after long-term ambient exposure, a condition referred to as sensitization.

Additionally, ASTM G69 results indicate that the weld nugget is anodic to the HAZ and base metal in the 6013-6013 weld with C56U-1 filler. In welded joints, the optimal condition is that the weld has the same or similar corrosion potential as the base metal. If that is not possible, the preferred configuration is that the weld is less susceptible than the base metal. In the 6013-6013 welds with C56U-1 filler, the optimal or preferred condition was not achieved. The galvanic corrosion potential between the weld and the base metal required further evaluation.

At the end of Phase I, it was determined that the C56U chemistry needed further refinement to reduce the propensity for corrosion of the weld joint. The Phase II project focused on optimizing the weld wire chemistry, formulated through careful alteration of the welding filler alloy's primary elements: Mg, Ti, and B, and the ratios between them. These alterations were informed by metallurgical principles and results from past welding trials. Arconic had proposed to cast and draw three variants of the C56U filler wire alloy. Each variant of the filler wire would then be drawn to 0.063" (1.2 mm). The variants would be used to join 6013, 6055 and 5083 to themselves, as well as each other, to test the weld properties. The variant chemistries would be evaluated based on the results of weldability trials and static tensile property testing.

However, during the August 2014 technical review, TARDEC requested that the project focus shift to the development of a high strength filler wire for 6055, rather than 6013. The Army Research Laboratory (ARL) was already in the process of classifying 6055 as "weldable" based on their recent ballistic shock test results. Since 6055 was already one of the alloys of choice in Arconic's proposed test matrix, this request was easy to implement. This shift in project focus was also supported by the need to refine the filler wire chemistry to address corrosion concerns. Therefore, subsequent efforts focused on developing a filler wire alloy for 6055.

Several candidate chemistries were developed for GMA weld filler alloys to join 6055 to 6055. The method for fabricating screening quantities of these chemistries in-house was as follows:

- Rectangular book mold castings were produced within each alloy composition
- Book molds were homogenized, machined, and rolled to approximately 0.160" (4 mm) thick
- Strips of welding filler were saw cut from the rolled sheet, chemically cleaned and dried
- The cut rod was used to Gas Tungsten Arc (GTA) weld restrained Tee test specimens, which were visually, and penetrant inspected and cross sectioned to inspect for cracking
- Those filler alloys with minimal cracking were selected, and used to produce GTA Butt welds for tensile property evaluations

GTA weld trials were conducted on several chemistries, as well as commercially available fillers 4943, 4043 and 4145. All fillers, except for 4145, had unacceptable results in the Restrained Tee test, including 4943, even though 4943 weldments joining 6055 plate had successfully passed ballistic shock tests performed by ARL in 2014. The welds exhibited extensive cracking in the HAZ of the 6055 weld cross sections. The cracking was not open to the surface and was not detectable by visual or dye penetrant inspection as indicated in Figure 4.

Due to these unfavorable results, four (4) new chemistries (W07-W10) were developed for welding 6055. Book molds of the four new alloy chemistries were cast and processed into GTA welding filler rods. GTA weldability trials, using the restrained Tee specimens, indicated that chemistries W09 and W10 performed very well, based on weld quality and dye penetrant tests, as shown in Figure These chemistries were selected for continued development and given new designations, C138H and C139H.

Next, crack-free GTA butt welds were produced in 0.5" thick 6055, using both C138H and C139H. The tests were repeated 4 times for each chemistry, with no cracking detected. Each weld was evaluated via metallography (Figure 6.) and dye penetrant inspection, with favorable results. Slightly more porosity was noted in the C138H GTA welds as compared to C139H, but neither exhibited unacceptable levels of porosity. Tensile tests also indicated that both alloys achieved strengths meeting the required minimums. C138H provided an approximately 19% increase in tensile strength, as compared to the current MIL-DTL-32262A minimum (6055 Welded with 4943), and C139H provided an approximately 26% increase.

In addition, crack-free restrained Tee welds were produced by GTA welding 6055 to 5083 with both C138H and C139H fillers. Die penetrant inspection showed no visible cracking (Figure 7.).

The ability of these fillers to weld 5083 to 5083 was also evaluated, using a crack prediction model, developed by Arconic using IRAD funding. The model suggested that there is a slight risk of cracking. Based on these results, 5083-5083 Restrained Tee weldments were fabricated using C139H filler wire. No cracking was observed visually, or with die penetrant.

ASTM G67, NAMLT of 6055-6055 butt welds, using both C138H and C139H, yielded slightly higher mass loss than seen for a traditional 5xxx alloy. This was expected as C138H/C139H alloys have more copper than 5XXX alloys.

Phase III focused on fabricating commercial quality GMA weld filler wire to further evaluate C138H and C139H. Four billet casting trials were conducted to produce material for GMA welding evaluations. Relatively small amounts are needed at the initial evaluation stage, so approximately 100 lb. billets were cast at Milward Alloys, Inc. A total of seven 100 lb. billets were cast, with four of the billets being useable for further evaluation. Of the remaining three, one was an unsuccessful cast, and two others tested outside of composition limits. Hydrogen results were generally high (0.2-0.26 cc/100gram) for all billets, but not so much as to be unusable for trials. As a result, approximately 200 lbs. each of C138H and C139H was usable for further processing and weld trials.

Milward Alloys conducted the initial trials to extrude the C139H billet to 0.75" (19mm) diameter rod. After several attempts and modifications to the extrusion process, C139H was extruded, but at an extremely slow speed and with unacceptable surface condition. It was determined that the Milward Alloys press did not have the capacity for the die design being used. Additional trials at Milward Alloys would require a die redesign to reduce the total extrusion ratio.

In an attempt to reduce delivery time for the final diameter GMAW filler wire, two Arconic extrusion facilities were then used, Building and Construction Systems (BCS) Cranberry, PA and Pimalco Chandler, AZ. C138H and C139H alloys exhibit characteristics of 5XXX, 7XXX and

OPSEC1890

2XXX alloys, indicating that they may exhibit high flow stresses and work hardening when undergoing deformation processes. These strength characteristics require the use of high load capacity equipment and facilities, and potentially increased processing time due to the need for additional trials and processing steps. In fact, BCS Cranberry was unable to successfully extrude the alloy billets, as their press load capacity was not high enough to overcome the flow strength of the billets, typically referred to as die “breakout”.

Arconic Pimalco was chosen for the next extrusion trials, due to higher load capacity presses. In June of 2016, Pimalco was able to successfully extrude the C138H and C139H alloy ingots to 0.75” (19mm) diameter rod. The C138H and C139H extruded rods were sent to Beneke for drawing down to 0.118” (3mm) diameter. Beneke had been successful in drawing earlier filler alloys but encountered problems with breaking the cold welds between coil lengths when drawing C138H and C139H. This is because these compositions are significantly higher in Mg and Zn than typical aluminum 5XXX filler wire alloys. Therefore, the flow stress (yield strength) of the material is higher than that of traditional filler alloys. These compositions also work harden more than traditional 5XXX alloys, leading to high tensile stresses during the drawing process. Therefore, the cold welds between coils experience high tensile loads and fracture, requiring additional time to re-weld between drawing passes. Additional drawing passes are also needed, as smaller reductions in diameter must be employed for each drawing pass.

In September 2016, despite significant material losses, Beneke completed drawing of the remaining C138 and C139 material to 0.118” (3mm) diameter, and Hobart Aluminum of Traverse City, MI began drawing and processing of the wire to welding electrode of 0.062” (1.6mm) diameter. Despite a conservative approach to drawing down to 0.062” diameter, two drawing dies were damaged, further delaying the schedule. In February 2017, Hobart was able to successfully complete processing of approximately 50lbs of C139H wire. Due to schedule and funding issues, further processing of the C138H alloy was stopped.

Because of the anticipated processing difficulties and costs associated with producing a commercial grade filler wire of these alloys, C138H and C139H are not considered viable options for joining 6055. In addition, TARDEC had already qualified 6055 as a “weldable” armor when fusion welded with filler alloy 4943. After discussion and approval from TARDEC, the contract was modified to focus funding and efforts on the development of filler alloys enabling the fusion welding of 7085 armor. The remaining 6055 Phase III task was to complete GMA weld evaluation of the C139H filler via restrained Tee and butt weld specimens, subjected to dye penetrant metallographic inspection. Tensile testing of transverse welds and all weld metal specimens, as well as transverse guided bend tests were used for weld procedure qualification.

Three replicates of Restrained Tee specimens 12” (300mm) long were welded without visual or dye penetrant indications. Butt weld panels 24” x 24” (600mm x 600mm) were welded parallel to the rolling direction of the 6055-T651. The single vee butt joints utilized a 60° included angle with a 0.438” (11.1mm) depth of groove prep. Other than minimal scattered porosity within the weld radiographs, no weld discontinuities were noted.

Results and Discussion:

Phase I: the C56U filler alloy could successfully produce crack free weldments when joining 6013 to 6013 and 6013 to 5083 alloys. C56U has similar tensile properties to filler 4043 when welding 6013-6013 and when welding 6013-5083 with C56U or 5183 filler. The weldments exhibit similar tensile properties because all tensile failures occurred in the HAZ of the 6013. C56U weldments joining 6013-T6 to 6013-T6 attained an average Ultimate Tensile Strength (UTS) of 34.4 ksi (127 MPa), a Tensile Yield Strength of 19.8 ksi (136 MPa), and 7.7% elongation. This represents a 58% joint efficiency (UTS of welded joint/UTS of parent metal X 100%), or a 42% joint strength knock-down factor. Higher shear strengths and improved ductility can be achieved with C56U filler alloy compared to 4043. Corrosion testing indicated, however, that after exposure to elevated temperatures and/or long-term ambient exposure, C56U has a propensity for IG, as well as SCC. The weld nugget in the as-welded condition showed low mass loss (<15 mg/cm²) in ASTM G67 test, which indicates acceptable resistance to IG and SCC. After exposure to 100°C/ 1 week, the weld nugget had mass loss of above 25 mg/cm², which indicates susceptibility to IG and SCC, a condition referred to as “sensitization”.

Phase II: the project shifted to the development of filler alloys for crack free GMA welding of alloy 6055, and the need for these filler alloys to exhibit improved corrosion performance over C56U. Restrained tee GTA welding trials of C138H and C139H indicated that they produced crack free weldments when joining 6055-6055, 6055-5083, and 5083-5083. Tensile testing of GTA butt welds indicated that C138H attained a UTS of 28.6 ksi (197 MPa), a TYS of 20.5 ksi (141 MPa) and 3% elongation. C139H GTA weldments attained a UTS of 32.5 ksi (224 MPa), a TYS of 21.6 ksi (149 MPa) and 4.5% elongation. These GTA weldment properties show that C138H and C139H provide a ~19% and 26% improvement in tensile strength vs. the current MIL-DTL-32262A minimum (6055 Welded with 4943), respectively. In addition, ASTM G67 NAMLT corrosion testing of C138H and C139H GTA weldments indicated that they demonstrate acceptable resistance to IG and SCC, and are not prone to sensitization.

Phase III: C138H and C139H filler compositions proved to be extremely difficult to extrude and draw, critical processes in filler wire fabrication. C138H and C139H alloys exhibit characteristics of 5XXX, 7XXX and 2XXX alloys, indicating that they may exhibit high flow stresses and work hardening when undergoing deformation processes. These strength characteristics required the use of high load capacity equipment and facilities, and increased processing time due to the need for additional trials and processing steps. The initial extrusion trial was unsuccessful, as the press load capacity was not high enough to overcome the flow strength of the C138H or C139H billets, a process step typically referred to as die “breakout”. A second extrusion trial, using a high load capacity press was utilized, and the C138H and C139H alloy billets were successfully extruded into 0.75” (19mm) diameter rod. Drawing of the rod to the needed filler wire diameter of 0.62” (1.62mm) was also problematic and time consuming. Wire drawing requires that coils be joined to create continuous lengths, prior to the drawing operation. This joining is achieved via cold welding of the coil end, which repeatedly fractured during many of the required drawing passes. This is because C138H and C139H compositions are

OPSEC1890

significantly higher in Mg and Zn than traditional aluminum 5XXX filler wire alloys, which results in higher flow stress (yield strength) of these materials. These compositions also work harden more than traditional 5XXX alloys, leading to high tensile stresses during the drawing process. Therefore, the cold welds between coils experience high tensile loads and fracture, requiring additional time to re-weld between drawing passes. Additional drawing passes are also needed, as smaller reductions in diameter must be employed for each drawing pass.

Due to the issues with extruding and drawing, no C138H filler wire of GMA quality was produced, and only a limited amount of C139H GMA filler wire was available for evaluation. GMA weldments using C139H to join 6055-6055, achieved an as-welded transverse UTS of 36.8 ksi (254 MPa), a TYS of 24.5 ksi (169 MPa), and elongation of 5.5%. This exceeds the MIL-DTL-32262A minimum of 24 ksi (165 MPa) for 6XXX by 53%. The static as-welded Joint Efficiency (welded condition / base metal strength) was 60% for the transverse UTS. The GMA welded C139H bend specimens also exhibited acceptable performance with no discontinuities and achieved 5.7% elongation.

Even though C138H and C139H achieved good properties and produced sound crack free weldments, these filler alloys are not considered viable candidate compositions for commercial grade GMA filler wire. Traditional processes for drawing these alloys down to filler wire diameter resulted in scrap rates greater than 90%.

Conclusions:

The major difficulties encountered in this project impacted the timing and schedule significantly. Many of sources of delays were associated with:

- 1) Alloy prototyping (both technical challenges and the time involved),
- 2) The time and effort involved in alloy evaluation/characterization and
- 3) Problems were experienced with ingot casting, extruding, drawing, and finishing.

To address each of these issues it is recommended that:

- 1) Metallurgical models be refined and employed in the compositional prototyping process as well as in the prediction of mechanical properties; 2)
- 2) A networked and streamlined supply chain able to handle the prototype volumes involved in the effort should be developed and include academia, small businesses, and consortia.

The final detailed report for this project is available from the PIs or the TFA Leads listed for the project.

Figures and Tables Begin on the Next Page

Figures and Tables:

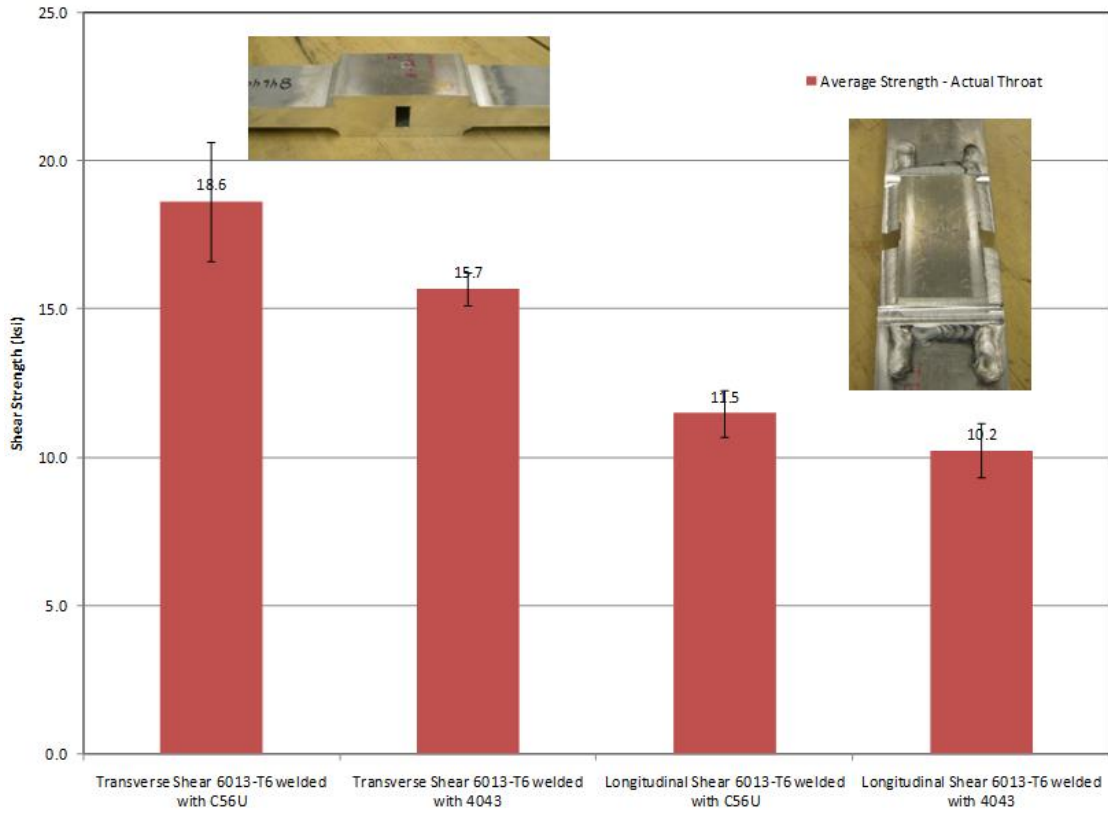


Figure 1: Improved Shear Strength of C56U Over 4043 Filler Alloy

Table 1: Hydrogen Content of First Four Ingots Cast at Milward Alloys

ID	Ingot Hydrogen (cc/100g)	Extrusion Hydrogen (cc/100g)		
		Leading	Middle	Trailing
90127	0.17	0.25	0.43	0.31
90128	0.54	0.46	0.53	0.52
90129	0.57	0.48	0.55	0.58
90130	0.46	0.53	0.49	0.39

Target Hydrogen Level: < 0.12 cc/100g

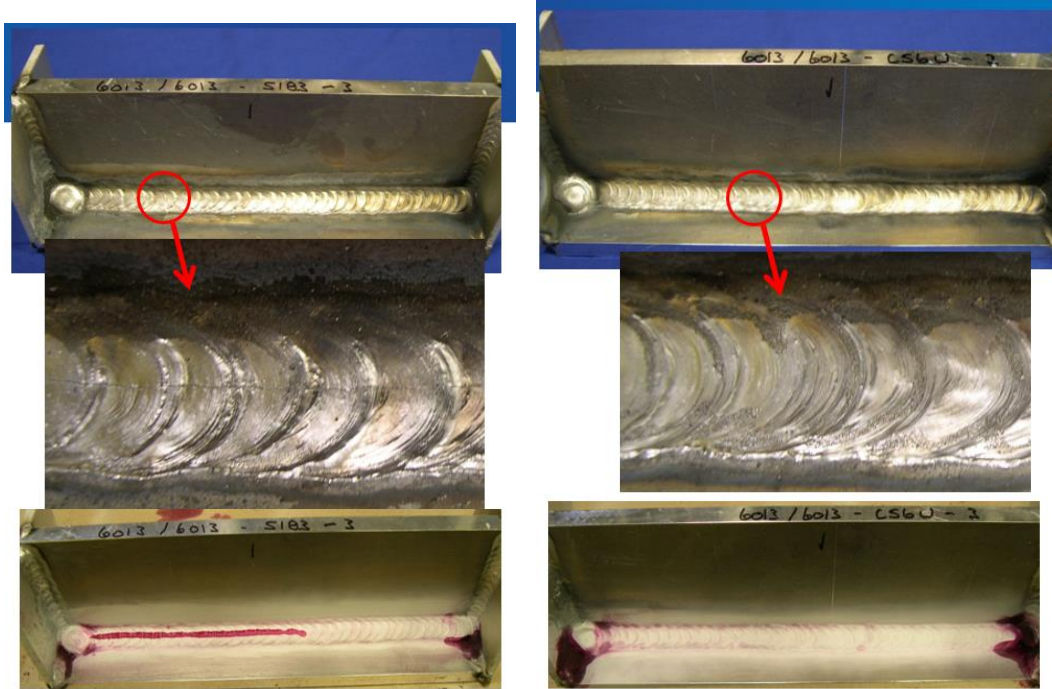


Figure 2: Alloy 6013-T6 to 6013-T6 Restrained Tee Test Specimens
Left: Welded with 5183 filler (As-welded and Dye Penetrant Inspected)
Right: Welded with C56U filler (As-welded and Dye Penetrant Inspected)

Remainder of Page Intentionally Blank

Table 2. Assessment of Restrained Tee Test Specimens Welded with the 4043, 5183 and C56U fillers

Sample #	Test Condition	Alloy Combinations		Filler Alloy	Visual	Dye Penetrant
		Material Combination				
899210-1	1	6061-T651	6061-T651	4043	No discontinuities noted	No discontinuities noted
899210-2	1	6061-T651	6061-T651	4043	No discontinuities noted	No discontinuities noted
899210-3	1	6061-T651	6061-T651	4043	No discontinuities noted	No discontinuities noted
899210-4	1	6061-T651	6061-T651	4043	No discontinuities noted	No discontinuities noted
899207-1	2	6013-T651	6013-T651	4043	No discontinuities noted	No discontinuities noted
899207-2	2	6013-T651	6013-T651	4043	No discontinuities noted	No discontinuities noted
899207-3	2	6013-T651	6013-T651	4043	No discontinuities noted	No discontinuities noted
899207-4	2	6013-T651	6013-T651	4043	No discontinuities noted	No discontinuities noted
899208-1	3	6061-T651	6061-T651	5183	No discontinuities noted	No discontinuities noted
899208-2	3	6061-T651	6061-T651	5183	No discontinuities noted	No discontinuities noted
899208-3	3	6061-T651	6061-T651	5183	No discontinuities noted	No discontinuities noted
899208-4	3	6061-T651	6061-T651	5183	No discontinuities noted	No discontinuities noted
899206-1	4	6013-T651	6013-T651	5183	157 mm crack side 1 / 70 mm crack side 2	Confirmed visual
899206-2	4	6013-T651	6013-T651	5183	115 mm and 15 mm cracks side 1 / 50 mm crack side 2	Confirmed visual
899206-3	4	6013-T651	6013-T651	5183	158 mm crack side 1 / 37 mm and 68 mm cracks side 2	Confirmed visual
899206-4	4	6013-T651	6013-T651	5183	no crack side 1 / 20 mm and 15 mm cracks side 2	Confirmed visual
899206-1	5	6061-T651	6061-T651	C56U	No discontinuities noted	No discontinuities noted
899206-2	5	6061-T651	6061-T651	C56U	No discontinuities noted	No discontinuities noted
899206-3	5	6061-T651	6061-T651	C56U	No discontinuities noted	No discontinuities noted
899206-4	5	6061-T651	6061-T651	C56U	No discontinuities noted	No discontinuities noted
899206-1	6	6013-T651	6013-T651	C56U	No discontinuities noted	No discontinuities noted
899206-2	6	6013-T651	6013-T651	C56U	No discontinuities noted	No discontinuities noted
899206-3	6	6013-T651	6013-T651	C56U	No discontinuities noted	No discontinuities noted
899206-4	6	6013-T651	6013-T651	C56U	No discontinuities noted	No discontinuities noted
899211-1	31	6013-T651	5083-H131	5183	No discontinuities noted	No discontinuities noted
899211-2	31	6013-T651	5083-H131	5183	No discontinuities noted	No discontinuities noted
899211-3	31	6013-T651	5083-H131	5183	No discontinuities noted	No discontinuities noted
899211-4	31	6013-T651	5083-H131	5183	No discontinuities noted	No discontinuities noted
899212-1	30	6013-T651	5083-H131	C56U	No discontinuities noted	No discontinuities noted
899212-2	30	6013-T651	5083-H131	C56U	No discontinuities noted	No discontinuities noted
899212-3	30	6013-T651	5083-H131	C56U	No discontinuities noted	No discontinuities noted
899212-4	30	6013-T651	5083-H131	C56U	No discontinuities noted	No discontinuities noted

Figures Continue on the Next Page

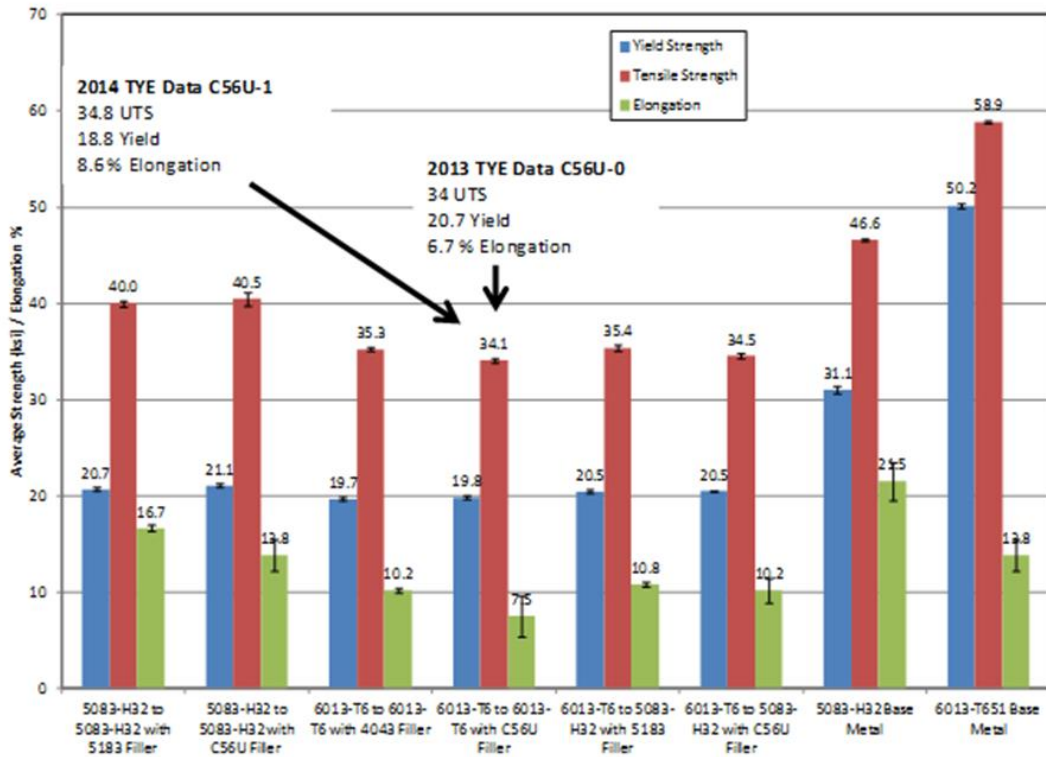


Figure 3. As-welded static tensile data for 6013, 5083 and combinations of both, welded with C56U, 5183 and 4043 fillers. Includes some Arconic pre-project data

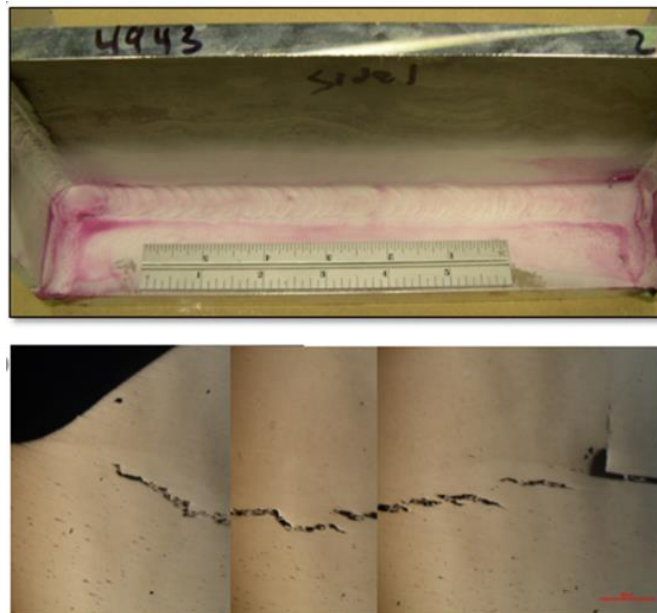


Figure 4. Penetrant and cross section of 6055-T6 to 6055-T6 0.5" (12.7mm) thick GTA Restrained Tee weld with 4943 filler (approved filler for welding 6055)

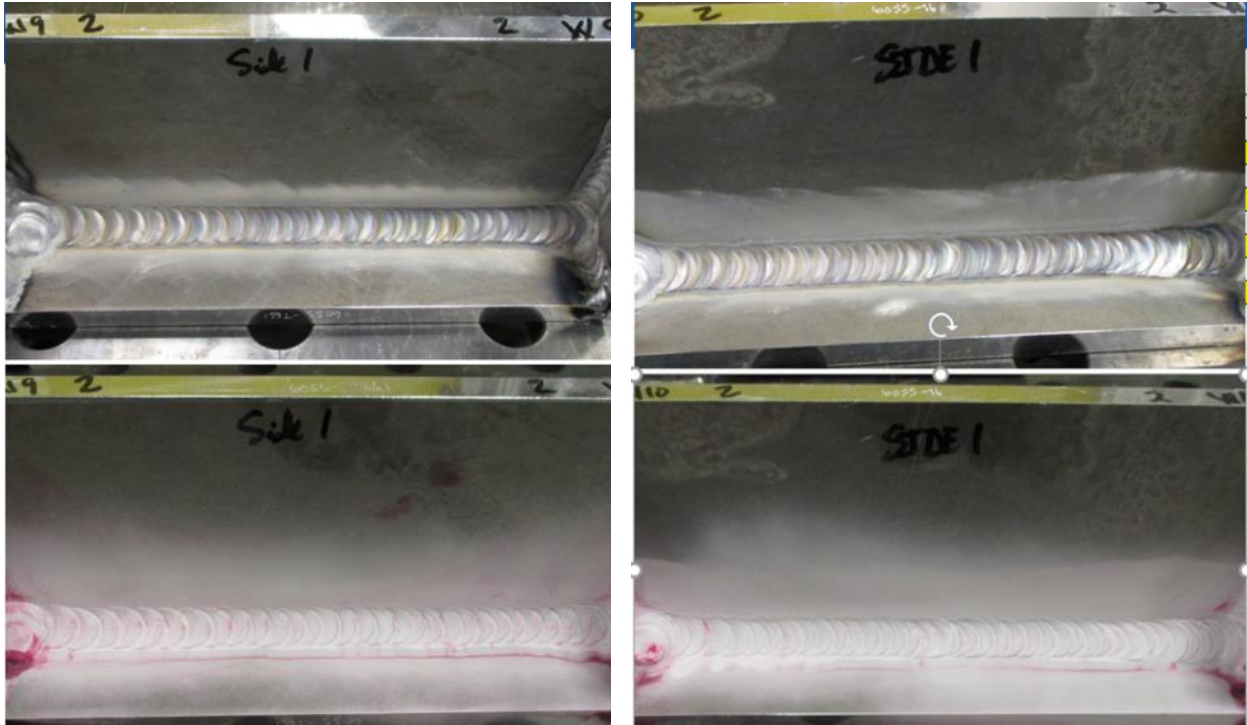


Figure 5. As-welded and penetrant inspected 6055-T6 to 6055-T6 0.5" (12.7mm) thick GTA Restrained Tee weld with W9 (C138H) filler [left] and W10 [right].

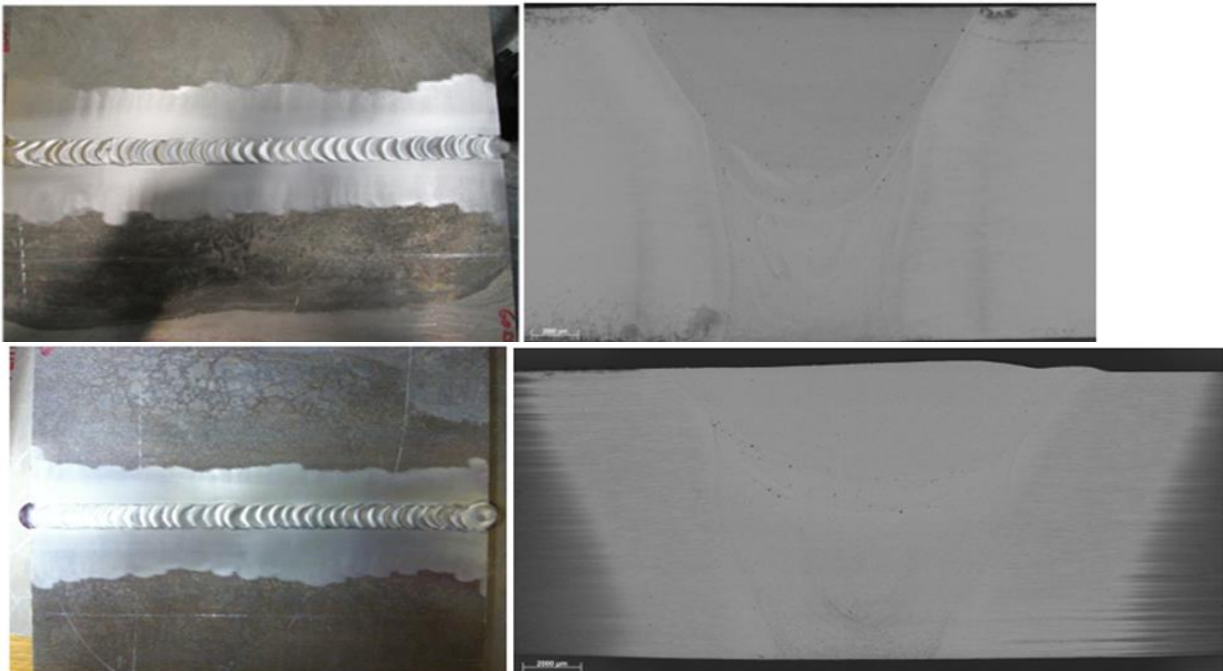


Figure 6. GTA butt-welded 6055-T6 to 6055-T6 0.5" (12.7mm) with W9 (C138H) filler [top] and W10 (C139H) filler [bottom]; with cross sections.

OPSEC1890

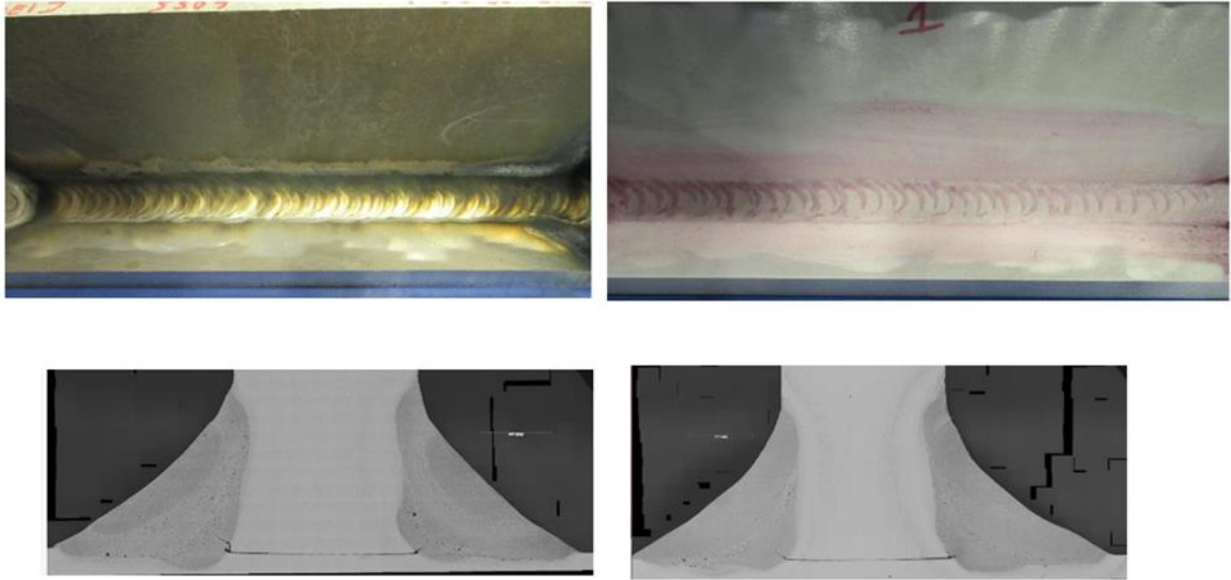


Figure 7. Representative GMA welded 6055-T651 Restrained Tee specimens with C139 filler in the as-welded and penetrant inspected conditions along with cross sections

Remainder of Page Intentionally Blank

This Page is Intentionally Blank

AVPTA Technology Focus Area #2: Lightweight Structures and Materials

**Breakthrough Techniques for Dissimilar Material Joining - Thick Section
Scribe for Dissimilar Aluminum-Steel Joints**

**DOE-VTO TFA Lead: Sarah Kleinbaum
TARDEC TFA Lead: Ravi Thyagarajan**

**Principal Investigator:
Dr. Scott Whalen
Pacific Northwest National Laboratory
902 Battelle Blvd.
P.O. Box 999, MSIN K2-03
Richland, WA 99352**

**Project Start: Q1FY16
Estimated Completion: Q1FY19**

Objectives:

- Develop solid-phase technologies that enable joining of Rolled Homogeneous Armor (RHA) to Blast Grade Aluminum for combat system light-weighting applications.
- Improve joint strength compared to conventional fusion and state-of-the-art friction stir approaches that rely exclusively on intermetallic bonding as the only joining mechanism.
- Utilize novel temperature control algorithms and spray-cooled thermal boundary conditions to tailor material properties of the joint.
- Reduce tool cost by orders of magnitude compared to current friction stir approaches.
- Characterize process window and repeatability.
- Develop friction stir butt joints in thick section AA2139.

Strategic Context:

- This strategic input area addresses directly addresses the Army Modernization Priority #2 Next Generation Combat Vehicles (NGCV).
- This is an enabling technology that will allow lightweight advance materials and armor to be utilized for the manufacturing of military systems.
- This enabler can be directly applied to advanced armor solutions and vehicle protection suites.
- This input area could also be applied to Expeditionary Mission Command, Future Vertical Lift and Robotics and Autonomous Systems (RAS) capabilities.

OPSEC1890

- The Army's modernization priority of mobility, lethality and protection of brigade combat teams is another strategic input area to which this technology can be applied.

Accomplishments:

AA6061

- Completed localized corrosion testing at Oregon State University using Scanning Vibrating Electrode Technique (SVET). Testing shows that a thin (Iron Aluminum) FeAl Intermetallic (IMC) layer within the dovetail reduces corrosion rate compared to when no IMC is present. AA6061-RHA system.
- Completed Finite Element Analysis (FEA) simulations comparing lap shear strength of 1, 2 and 3 groove dovetail joints (trapezoidal and rectangular) for AA6061. The maximum thickness of Al where failure occurs in the base metal rather than within the dovetail was also determined.
- Achieved 12 linear feet of joining with a single Friction Stir Dovetailing (FSD) tool in AA6061.

AA7099

- Preliminary success joining AA7099 to RHA using new hybrid FSD/Buttering approach.
- Developed tooling and dovetail geometry that reduced asymmetry of AA7099 penetration into dovetail groove during hybrid FSD/Buttering joints between AA7099 and RHA.
- Performed initial FSD joining trials for AA7099 to RHA using a cold spray Al-12Si interlayer to reduce migration of Zinc (Zn) into the IMC formed at the RHA surface.
- Compared effect of different spray cooling levels on hardness for FSD joints in 1.0" thick AA7099 at University of South Carolina. Benefit of spray cooling peaks at 0.2 gallons per min (gpm).

AA2139

- Joined 1.0" thick AA2139 in a butt-weld configuration having 86% joint efficiency.
- New MP-159 tool design reduced torque by 50% in 1.0" thick AA2139 butt-welds.

Conference Presentations

- FSD research of AA6061/RHA at the 12th International Symposium on Friction Stir Welding (12ISFSW) in Chicoutimi, Quebec, Canada, June 26-18, 2018.
- Modeling and Simulation of FSD lap-shear AA6061/RHA at WCX 18: SAE World Congress Experience, April 10-12, 2018.
- FSD overview at Defense Manufacturing Conference, Dec 4-7, 2017.

Publications and Patents

- Scripta Materialia: “Joining thick section aluminum to steel with suppressed FeAl intermetallic formation via friction stir dovetailing”
- The Minerals, Metals and Materials Society (TMS), Friction Stir Welding and Processing X Symposium, San Antonio TX, Mar. 10-14. 2019: “Joining AA7099 to Ni-Cr Steel using Friction Stir Dovetailing”
- “Friction Stir Interlocking” US Patent Application 15/794,687. Oct. 2018.
- “Joining AA7XXX Series Aluminum to Steel using AA6XXX Friction Stir Dovetailing” Provisional Patent Application. Sept. 2018.

News Media

- Press release resulting in 50+ secondary internet news articles, Apr. 2018.
- News story “Joining Aluminum to Steel” written by Tech Beat, Tribology and Lubrication Technology, Aug. 2018.
- News story “Researchers Can Now Join Aluminum and Steel for Lighter Vehicles” written by Design News, July 2018.
- News story on FSD, KNDU-Television, Kennewick, WA, July 2018.

Introduction:

Reducing the weight of military vehicles to increase energy efficiency, agility, and mobility [1] can be accomplished by replacing steel components with aluminum (Al). This requires the ability to join metals with vastly different material properties and has led to the investigation of numerous alternative joining techniques [2]. Joining Al to steel is particularly difficult due to large differences in material properties such as melting temperature, density, coefficient of thermal expansion, and flow stress that govern fusion and friction-based welding. In addition, a high chemical affinity with limited solubility also encourages the formation of intermetallic compounds (IMCs), which typically result in brittle failure of the joined parts [3]. Although a large body of work exists for metallurgical friction-based joining of Al to steel, only a few studies report data for Al or steel thicknesses exceeding 6 mm [4-6]. This is primarily because 1) friction techniques for joining thin sheets do not generally scale well for thick plates and 2) these approaches suffer from uncontrolled growth of FeAl intermetallics which result in brittle failure modes [7-9]. Cost is also an issue with exotic tool materials having complex features being required for friction stir approaches. The challenges for joining Al to steel are magnified when thick structures are required, such as those utilized in military combat vehicles and mobile structures. In light of these challenges, Friction Stir Dovetailing (FSD) has been developed as a new technique for low cost joining thick section aluminum to steel.

Work performed in FY18 culminated with the publication of a journal article in *Scripta Materialia* [10], in April of 2018, detailing the process development and mechanical properties for RHA-AA6061 joints made by FSD. The accomplishments outlined in this paper served as the bulk of

the 2017 final report and will not be repeated here. Modeling and simulation of these joints was performed in 2018 with a paper being drafted for the *Journal of Materials Processing Technology*. Based on these successes, the project moved toward joining of RHA to blast grade AA7099-T7451 in FY18. In addition, a small task was added to perform temperature controlled friction stir welds on AA2139 in an effort to increase joint efficiency in one inch thick sections. Work on RHA-AA7099 and AA2139 will be summarized herein.

Approach:

Modeling and Simulation of RHA-AA6061 Joints Made by FSD

A finite element analysis (FEA) was carried out in order to predict the load carrying capacity and failure location for Al thicknesses between 12.7 mm and 50.8 mm with different numbers of dovetails. It is well established that three distinct regions result from the thermal cycle during FSW processing of precipitation hardened Al alloys. These regions are commonly known as the nugget zone, thermo-mechanically affected zone (TMAZ) and heat affected zone (HAZ) The numerical results and corresponding experimental investigation are in agreement and suggest that the developed methods can be used effectively for design and analysis of FSD joints using standard FEA tools. Figure 1. presents hardness mapping of Al in a typical Al-RHA FSD joint. Demarcation between different regions is indicated by the black dashed lines. Vickers micro-hardness mapping was generated for the Al side using a CLARK CM-700AT indenter with 500 gm-force of indentation loading for 12 sec dwell time at the spacing of 1 mm and 1.25 mm in the weld transverse and thickness directions respectively.

The five distinct regions identified during hardness mapping are: (a) Region I: Al base materials with average hardness of 110 HV, (b) Region II: HAZ with average hardness of 75 HV, (c) Region III: combined area of HAZ minimum and TMAZ with average hardness of 49 HV, (d) Region IV: upper weld nugget zone with average hardness of 68 HV and (e) Region V: combined area of lower weld nugget zone and TMAZ with average hardness of 45 HV. Identification of the TMAZ is challenging because of the ultra-narrow region of high grain deformation within the weld zone. Therefore, the TMAZ was partially divided within Region III and V based on the nature of material flow in the FSD process.

Miniature tensile testing was conducted at the middle of dovetail in order to experimentally determine the mechanical properties of weld Region III and V since similar hardness was measured in these two regions. Figure 2 presents a typical transverse section of an Al-RHA FSD weld with an overlaid miniature tensile specimen at the location where specimens were extracted (Figure 2a). Individual specimens before and after testing illustrate the failure location (Figure 2b). Engineering and true stress-strain curve of the mini-tensile specimens are shown in (Figure 2c) and represents the engineering and true strain as averaged from eight tests for each curve. Figure 2b shows that failure of the mini-tensile specimens occurred near Region V and that the metallurgical bond at the Al-RHA interface remaining completely intact.

A key feature of FSD joints is the IMC layer which bonds the Al and RHA along the root of the dovetail. Because mini-tensile tests fail in the nugget material rather than at the

OPSEC1890

IMC interface, a surface-to-surface tie constraint at the site of metallurgical bonding is justified (8 mm centered along Al-RHA interface) and was applied using the ABAQUS analysis default discretization method. Frictional contact (coefficient of friction = 0.3) was defined at all other Al-RHA interfaces outside the IMC region. Figure 3 describes all applied mechanical boundary conditions.

Results and Discussion:

Three different FSD joint conditions from previously published results in [10] were compared with the FEA simulations in order to validate the modeling approach. Figure 4a compares the published force vs. displacement data (dashed lines) and FEA simulation (solid lines) for a single trapezoidal dovetail without IMCs (black) and with IMCs (green) along with a single rectangular dovetail with IMCs (red). The FEA simulations capture the general trend for the descending region of the curve, however, some deviation exists due to complexities associated with necking failure. Nevertheless, the simulations accurately capture the failure location and morphology when compared to the experimentally tested specimens Figure 4b. From this comparison of tensile data and imagery, we conclude that the numerical simulations are accurately reflecting the experimental testing.

Figure 5a compares FEA simulations of double FSD joints (solid lines) with experimental data (dashed lines) to further validate the modeling approach. Load vs. displacement curves for trapezoidal dovetails with IMCs (green) and without IMCs (black) are shown along with rectangular dovetails without IMCs (red). It is observed that the simulated curves are slightly lower than the experimental results. This under prediction can be attributed in part to the inhomogeneity of material properties in Region III (HAZ and TMAZ) compared to that of Region V, which are assumed in the model to be similar due to the nearly equivalent hardness values. Nevertheless, the overall trends in simulated load vs. displacement are in good agreement with experimental data in Figures 5a and 5b.

In order to support even thicker Al sections, a triple pass FSD joint was simulated with Al thicknesses above 20.32 mm. Figure 6 illustrates the spatial contour predicted from equivalent plastic strain (PEEQ) for triple FSD joints with Al thicknesses ranging from 20.32 mm to 50 mm. The initial localization of strain and failure location were predicted in Region III for Al thicknesses up to 25.4 mm. For 31.75 mm and 38.1 mm Al, strain localization was observed in Region III and Region V of the dovetail located farthest from the loading side of Al. Failure was predicted simultaneously in these regions. Competition of strain localization continued simultaneously in Region III and Region V for 44.45 mm thick Al with failure occurring in Region III. However, for 50.8 mm thick Al, the predicted failure was observed in Region V as shear failure of all three dovetail necks despite strain localization being observed in Region III. As such, the maximum supportable Al thickness lies somewhere between 44.55 mm and 50.80 mm.

The load vs. displacement curve for the triple pass FSD joints with varying Al thickness is shown in Figure 7. As the Al thickness increases, the load carrying capacity of the lap joint also increases. The load carrying capacity of FSD joints in lap shear is a direct result of the mechanical interlocking and metallurgical bonding within the dovetail. In this study, the FEA simulations predict that two and three pass FSD joints were able to support Al

thicknesses of at least 17.78 mm and 44.45 mm respectively without failure in the dovetail joints.

RHA-AA7099 Joints Made by FSD

The same process developed for joining RHA-AA6061 [10] was employed for joining RHA-AA7099. Slightly different gains were required for the temperature control algorithm due to differences in thermophysical properties between AA6061 and AA7099. Welds were performed with temperature controlled to 440C, 420C, and 400C at the shoulder in order to avoid incipient melting within the AA7099 precipitates. As shown in Figure 8, the FSD process was successful in fully extruding AA7099 down into the RHA dovetail groove.

SEM analysis (shown at right of Figure 8) shows the formation of a 4 micron thick intermetallic layer. Composition of the IMC was determined to be a Zn-rich phase as seen in Figure 9. It is known from literature [12] that the Zn-rich phase of Fe-Al, especially as such a thick layer, would likely result to brittle failure during lap shear tensile testing.

Lap shear test results for the RHA-AA7099 joints made by FSD (dashed lines) are shown in Figure 10 compared against the RHA-AA6061 FSD joints previously reported [10]. Despite AA7099 being substantially stronger than AA6061, the peak load at failure was similar and the extension at failure was much less. Analysis showed that brittle failure of the thick Zn-rich intermetallic layer was responsible for low load and poor elongation. The inset of Figure 10 shows fracture at the interface and shearing of the triangular aluminum ligament within the dovetail. Similar results were observed for shoulder temperatures at 440C, 420C, and 420. As a result, it was determined that alternative approaches should be pursued to reduce the percentage of Zn at the RHA interface or eliminate it all together. The follow sections provide an overview of these efforts where two new techniques are being pursued.

FSD RHA-AA7099 Joints with Al-12Si Cold Spray Interlay

In this approach, an interlayer is used between the aluminum and steel to prevent interaction of the Zn-rich AA7099 with RHA during processing. To accomplish this, a 2-3 mil thick Al-12Si layer is deposited by cold spray along the root of the dovetail prior to FSD. This is indicated by the yellow line in Figure 11. While acting as a barrier to Zn interaction with RHA, the Si is anticipated to form a less brittle, and thinner, Si-rich IMC similar to that formed during AA6061 FSD.

Preliminary experiments have shown that AA7099 is fully intermixed and bonded with the Al-12Si layer as shown in Figure 12. These welds occurred with a tool tip temperature of 435C and Z-force of 16,000 lbf. The void space, and lack of disruption of the RHA surface, indicate that the tool tip was not engaged with the RHA as is needed for effective FSD. As such, tensile test results were similar to those obtained without the Al-12Si interlayer. Experiments will be repeated in FY19 were the tool tip is fully engaged with the RHA.

RHA-AA7099 Joints with AA6061 FSD Buttering Layer

This multi-step approach is shown in Figure 13. Step 1, the baseline FSD process is used to join AA6061 to RHA with a robust Si-rich IMC layer having a thickness of 75-150 nanometers. Step 2, the AA6061 plate is machined off including a rectangular trench down into the dovetail groove. This leaves a roughly 0.05" layer of AA6061 metallurgically bonded to the RHA. Step 3, a plate of AA7099 is then joined to the AA6061 "buttering" layer via traditional friction stir welding. A cross section of a completed hybrid joint is shown in Figure 14. Multiple combinations of tool geometry and machined trench configuration were explored to ensure that AA7099 was pushed below the top of the dovetail groove as shown in Table 2.

Figure 15 shows the results of lap shear testing for hybrid AA7099, AA6061, RHA joints for various geometries and compared to the baseline AA6061 FSD process [10] shown in purple. These results show that it is possible to use an AA6061 buttering layer and still achieved higher failure load with AA7099 (green), which outperforms purely AA6061 joints.

AA2139 Thick Section Friction Stir Butt-Welds

Temperature control butt welds were performed on 1.0" thick AA2139 in an effort to achieve 90% joint efficiency. Numerous tool geometries and process parameters were investigated to achieve full penetration and raise the minimum the HAZ hardness as high as possible. Fig. 16 shows an example of a full penetration weld. Welds were performed at 2 inches per minute (ipm) and 3 inches per minute since a faster weld speed reduces heat input thereby resulting in less coarsening of the precipitates in the HAZ. Fig. 17 shows hardness mapping for 2 ipm and 3ipm welds with the 3 ipm case having higher hardness in the nugget and HAZ.

Tensile test results for welds performed at 2 ipm and 3 ipm are shown in Fig. 18. A maximum of 400 MPa was achieved with an elongation of 11.5%. Table 3 shows the joint efficiency for 2 ipm and 3ipm with a maximum of approximately 86% being realized. In FY19, weld speeds of 4 ipm and 6 ipm will be investigated since a torque upgrade has recently been completed on the machine to enable higher speed. Spray cooling of liquid nitrogen mist behind the tool will also be attempted to minimize growth of precipitates in the HAZ.

Conference Presentations

The following project briefings were presented:

- 12th International Symposium on Friction Stir Welding, June 26-28, 2018.
- SAE WCX World Congress Experience, Apr. 10-12, 2018.
- Defense Manufacturing Conference (DMC) 2017, 2018
- *Friction Stir Welding and Processing IX* TMS 2017,
- 7th Annual Global Automotive Lightweight Materials Summit, Aug. 22-24, 2017

OPSEC1890

- TARDEC Ground Vehicle Survivability Symposium (GVSS), Nov. 16-17, 2016,
- Global Automotive Lightweight Materials Series: Lightweight Vehicle Manufacturing, Feb 24-25, 2016
- PNNL Graduate Research Symposium, 2016, 2017

Publications

The following articles were published:

- Md. Reza-E-Rabby, K. Ross, N. Overman, M. Olszta, M. McDonnell, S. Whalen, “*Joining Thick Section Aluminum to Steel with Suppressed FeAl Intermetallic Formation via Friction Stir Dovetailing*,” *Scripta Materialia*, 148, 63-67, 2018.
- N. Canter, “*Joining Aluminum to Steel*,” *Tribology and Lubrication Tech Beat*, pp. 14-15, Aug. 2018.
- Reza-E-Rabby, K. Ross, S. Whalen, Y. Hovanski, M. McDonnell, “*Solid-State Joining of Thick-Section Dissimilar Materials Using a New Friction Stir Dovetailing (FSD) Process*,” *Friction Stir Welding and Processing IX*, 67-77, 2017.

Patent Applications

The following patent applications were submitted:

- S. Whalen, Md. Reza-E-Rabby, K. Ross, M. McDonnell, “*Joining AA7XXX Series Aluminum to Steel using AA6XXX Friction Stir Dovetail Interlayer*,” *Provisional Patent Application*, Sept. 2018.
- K. Ross, S. Whalen, Md. Reza-E-Rabby, “*Friction Stir Interlocking*,” *US Patent Application 15/794,687* filed on 10/26/2017.
- S. Whalen, K. Ross, Md. Reza-E-Rabby, Y. Hovanski, “*System and Process for Joining Dissimilar Materials and Solid-State Interlocking Joint with Intermetallic Interface Formed Thereby*,” *US Patent Application 15/694,565* filed on 9/1/2017.

Conclusions:

Significant progress was made toward modeling and simulation of aluminum-steel joints made by Friction Stir Dovetailing. The new modeling approach can be used as a tool to calculate the maximum section thickness that can be sustained for a given dovetail configuration. Development of two novel methods for joining AA7099 to RHA began in FY18. These methods include 1) the use of an Al-12Si cold spray interlayer as a barrier to Zn-rich IMC formation and 2) a hybrid approach where an FSD buttering layer is used as the interlayer to which AA7099 is joined by conventional friction stir welding. For 1.0” thick AA2139, butt joints were welded with a joint efficiency of 86%. Presentations were made at three conferences, one journal article was published, two patents were filed, and a press release was issued which resulting in numerous internet and printed news stories, and even spot on local television.

References:

- [1] E. Polsen, L. Krogsrud, R. Carter, W. Oberle, C. Haines, A. Littlefield, Lightweight Combat Vehicle S and T Campaign, US Army TARDEC/Ground System Survivability Warren United States, 2014.
- [2] K. Martinsen, S. Hu, B. Carlson, CIRP Annals-Manufacturing Technology 64(2) (2015) 679-699.
- [3] T. Tanaka, T. Morishige, T. Hirata, Scripta Materialia 61(7) (2009) 756-759.
- [4] T. Nishida, T. Ogura, H. Nishida, M. Fujimoto, M. Takahashi, A. Hirose, Science and Technology of Welding and Joining 19(7) (2014) 609-616.
- [5] T. Ogura, Y. Saito, T. Nishida, H. Nishida, T. Yoshida, N. Omichi, M. Fujimoto, A. Hirose, Scripta Materialia 66(8) (2012) 531-534.
- [6] E.E. Patterson, Y. Hovanski, D.P. Field, Metallurgical and Materials Transactions A 47(6) (2016) 2815-2829.
- [7] K. Kimapong, T. Watanabe, Materials transactions 46(4) (2005) 835-841.
- [8] R.P. Mahto, R. Bhoje, S.K. Pal, H.S. Joshi, S. Das, Materials Science and Engineering: A 652 (2016) 136-144.
- [9] Y. Wei, J. Li, J. Xiong, F. Zhang, Journal of materials engineering and performance 22(10) (2013) 3005-3013.
- [10] Md. Reza-E-Rabby, K. Ross, N. Overman, M. Olszta, M. McDonnell, S. Whalen, Scripta Materialia, (148), 63-67, 2018.
- [11] Abood, A.N., Saleh, A.H., Abdullah, Z.W., 2013. Effect of heat treatment on strain life of aluminum alloy AA 6061. Journal of Materials Science Research 2, 51.
- [12] Mathieu, A. Shabadi, R. Dissimilar Material Joining Using Laser (Aluminum to Steel Using Zinc-Based Filler), Optics and Laser Technology, 39 (3), 652-661, 2007.

Figures and Tables

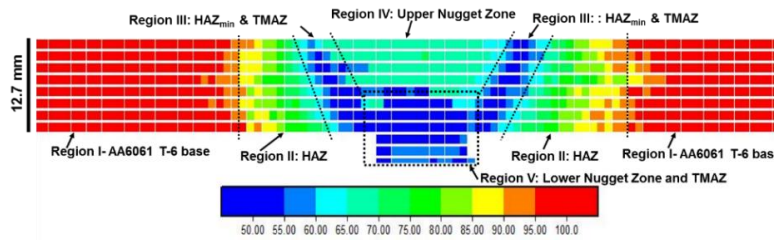


Figure 1. Contour plot of micro-hardness distribution over the Al side of a single FSD joint with distinct regions indicated by black dashed lines.

Figures Continue on the Next Page

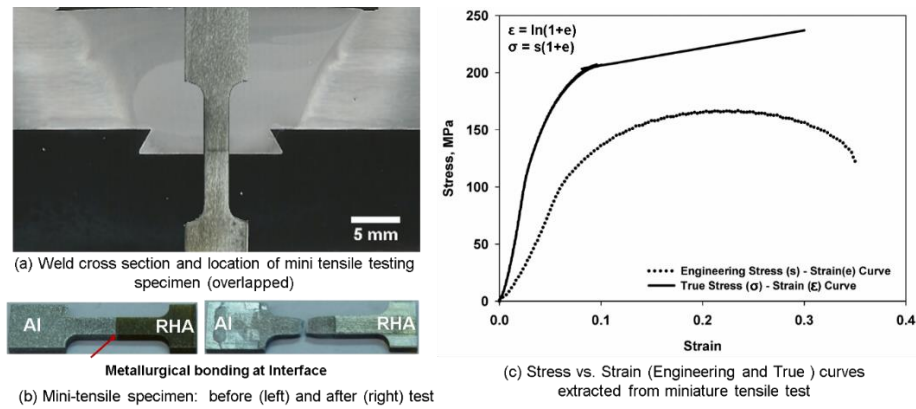


Figure 2. Miniature tensile testing of specimens extracted from the FSD dovetail: (a) Weld cross section and location of mini-tensile testing specimen (overlaid), (b) Mini-tensile specimen before (left) and after (right) testing, and (c) Stress vs. strain (engineering and true) curves measured during mini-tensile testing.

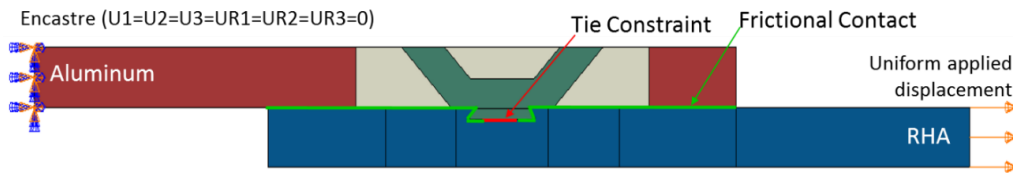


Figure 3. Boundary conditions for FSD lap shear simulation.

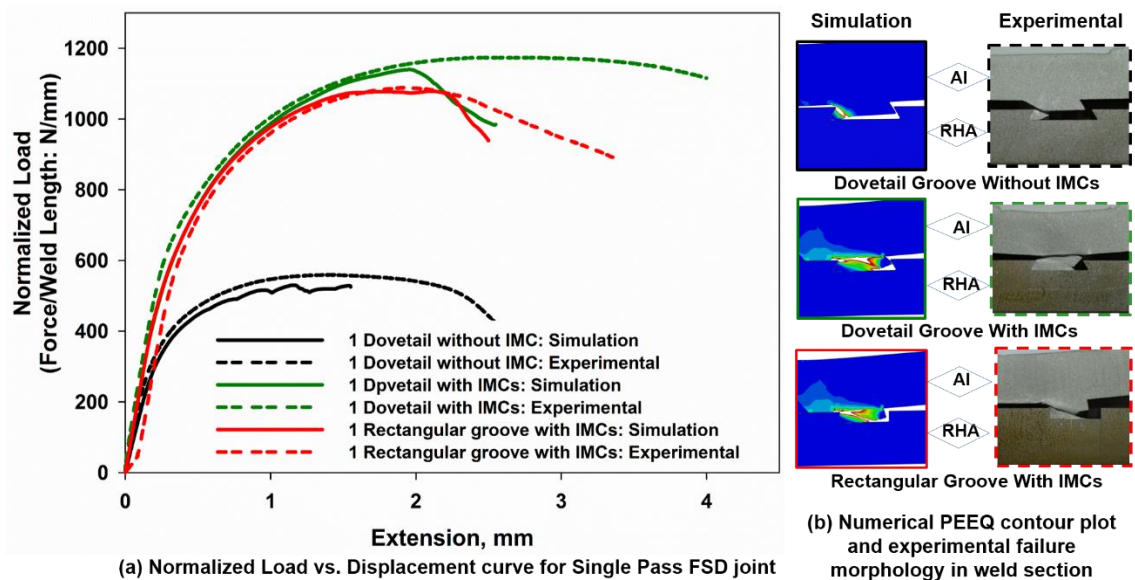


Figure 4. (a) Load per unit joint length vs. extension for single pass FSD joints; (b) failure location and morphology from simulations and experiments

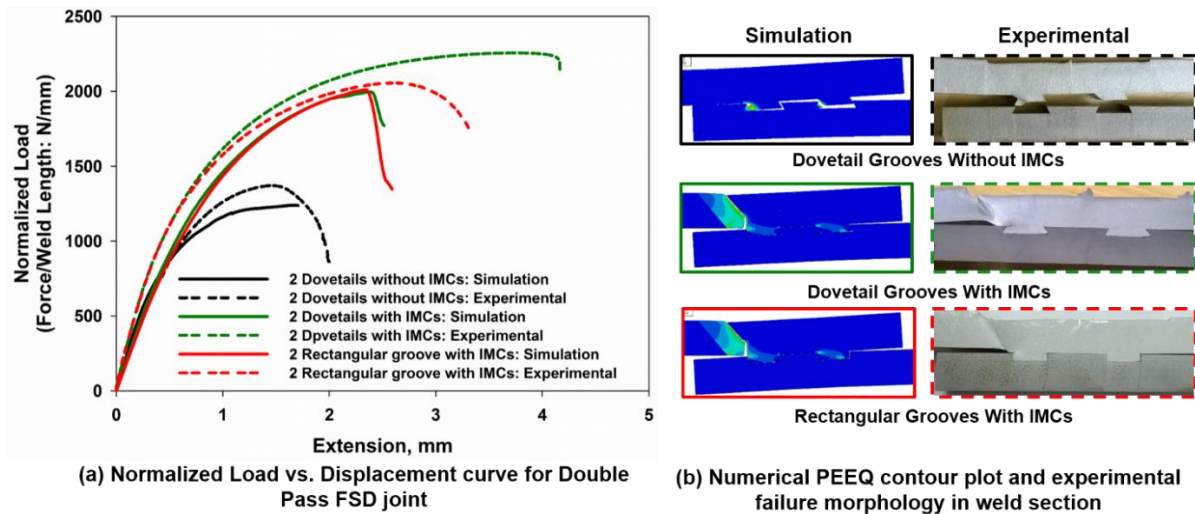


Figure 5. (a) Load per unit joint length vs. extension for double pass FSD joints along with (b) failure location and morphology from simulations and experiments.

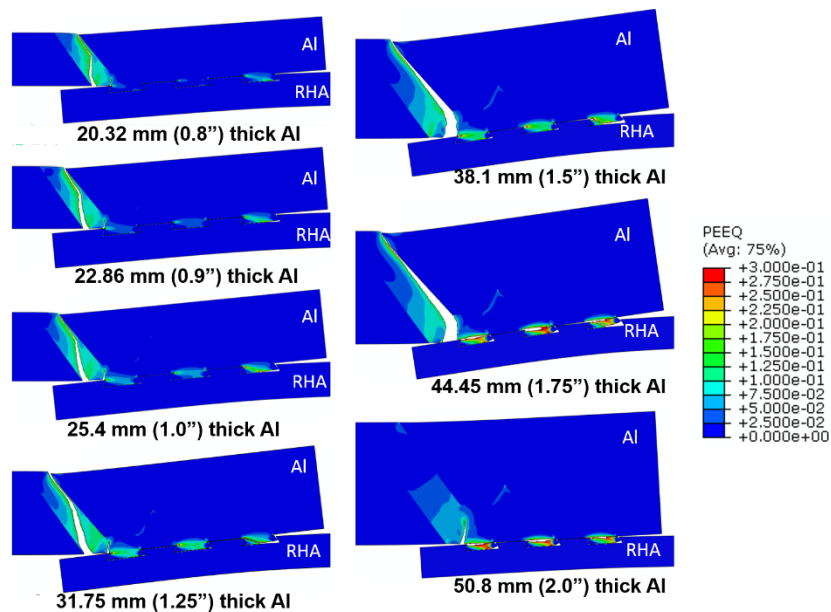


Figure 6. PEEQ spatial contour plot of triple pass FSD joints with different Al thickness.

Figures Continue on the Next Page

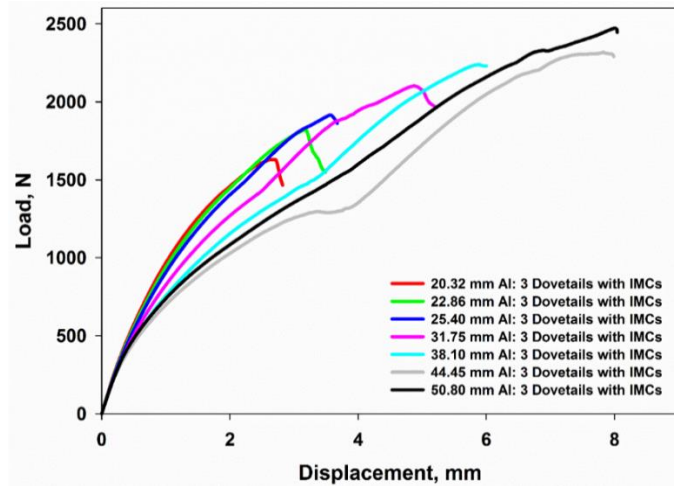


Figure 7. Load vs. displacement for triple pass FSD joints having different Al thickness.

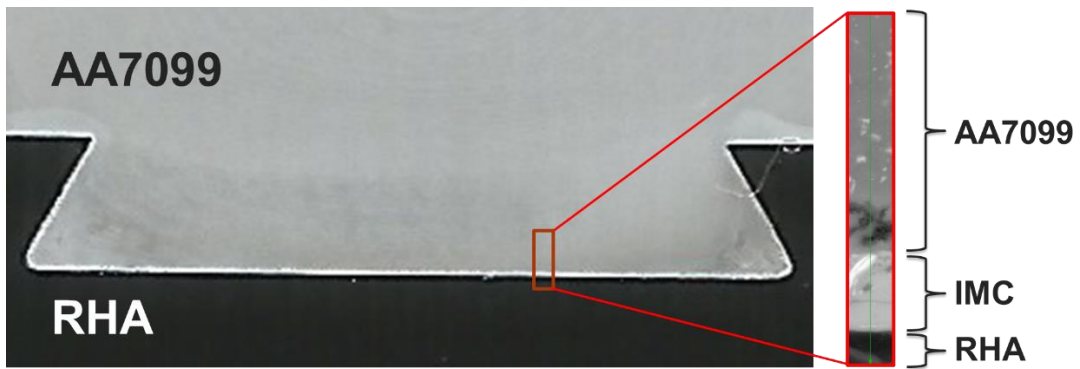


Figure 8. FSD of AA7099 to RHA with formation of thick intermetallic layer shown.

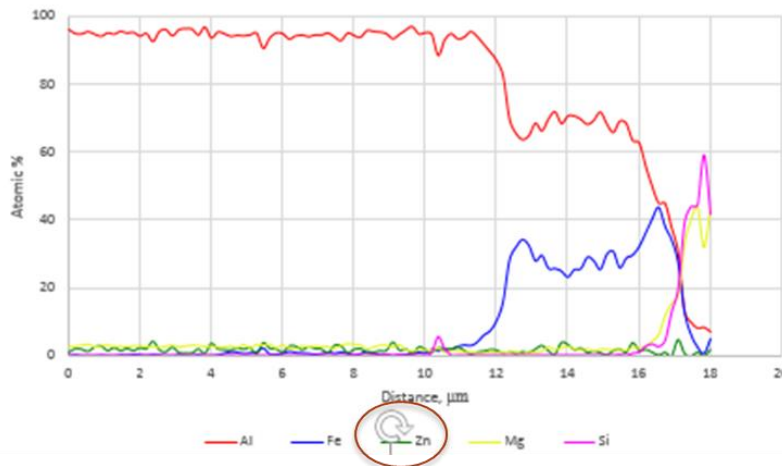


Figure 9. Composition of IMC showing presence of Zn.

OPSEC1890

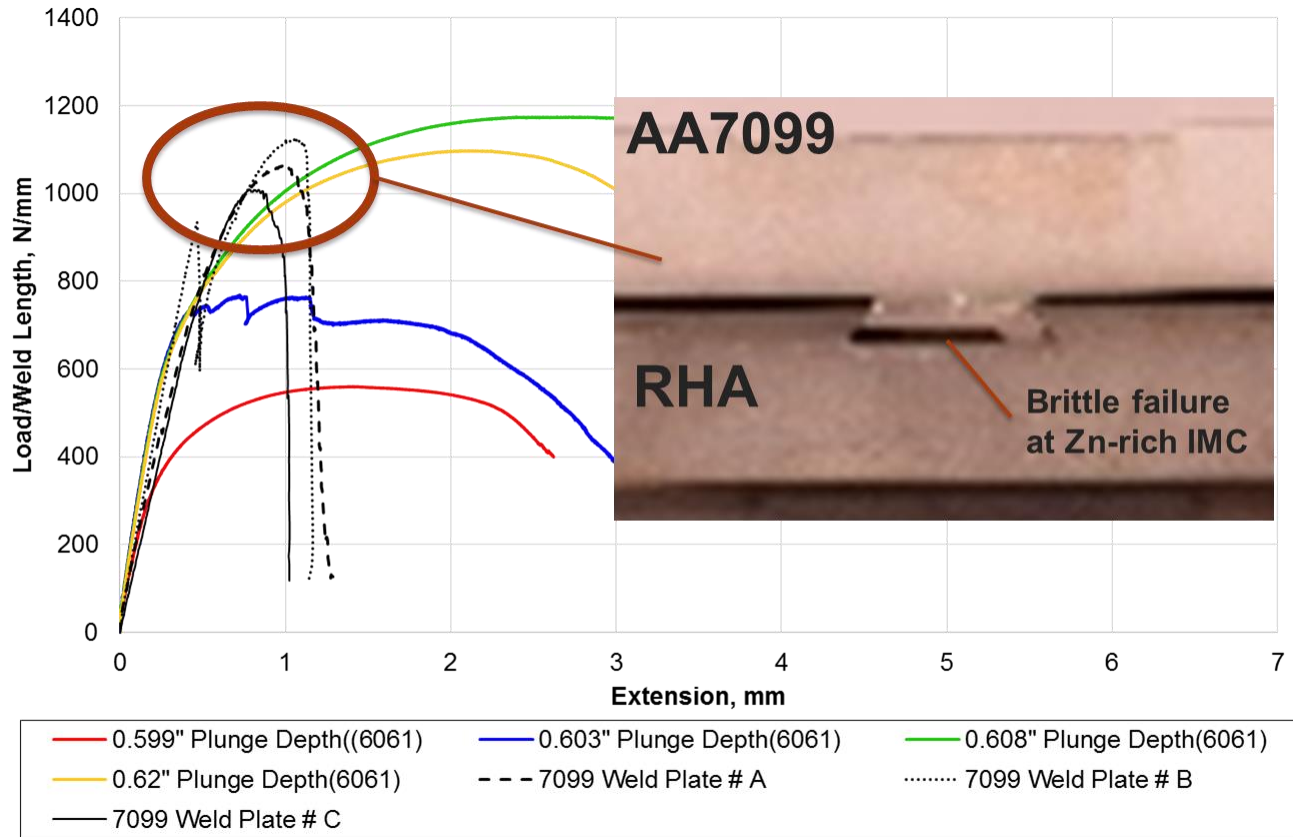


Figure 10. Comparison of lap shear testing for RHA-AA6061 FSD and RHA-AA7099 FSD.

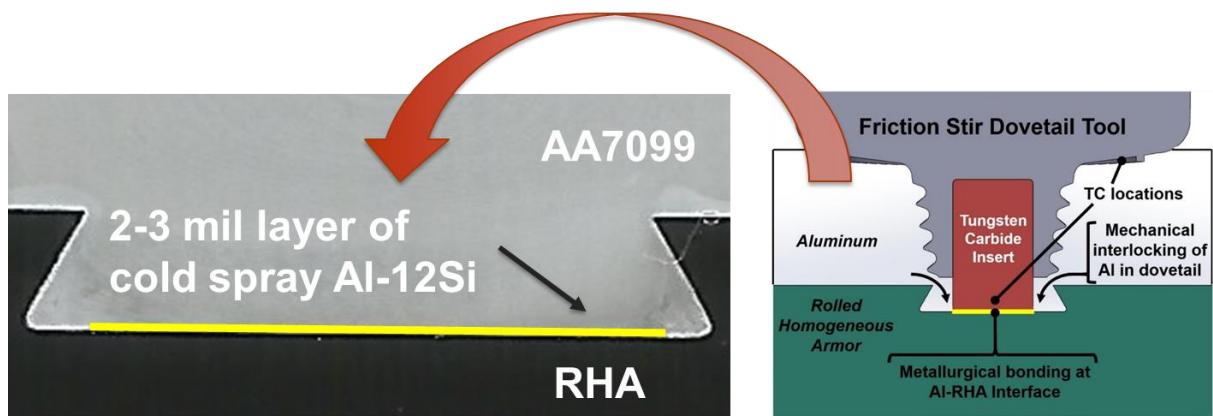


Figure 11. FSD of RHA-AA7099 after first cold spraying a 2-3 mil thick layer of Al-12Si into the root of the RHA dovetail.

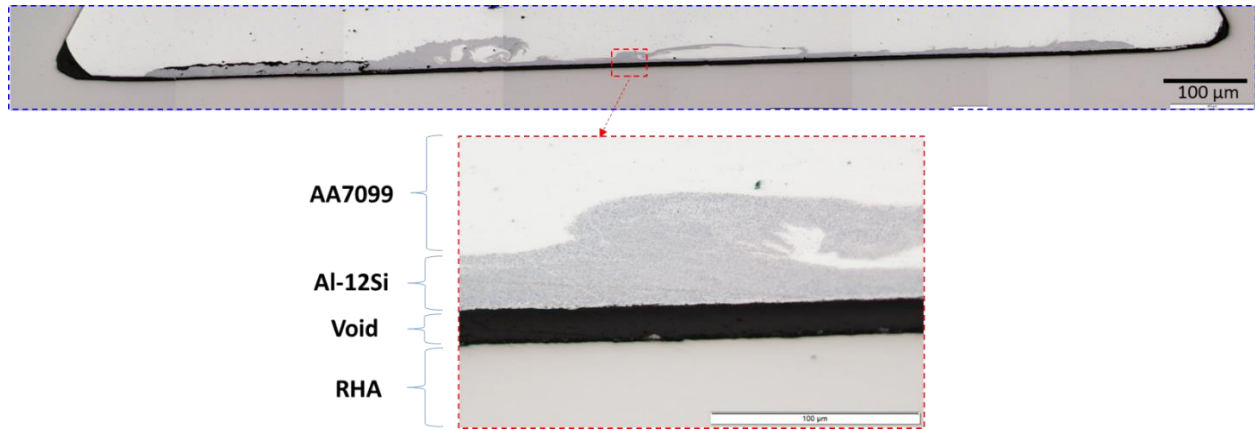


Figure 12. FSD of AA7099 to RHA with Al-12Si cold spray interlayer.

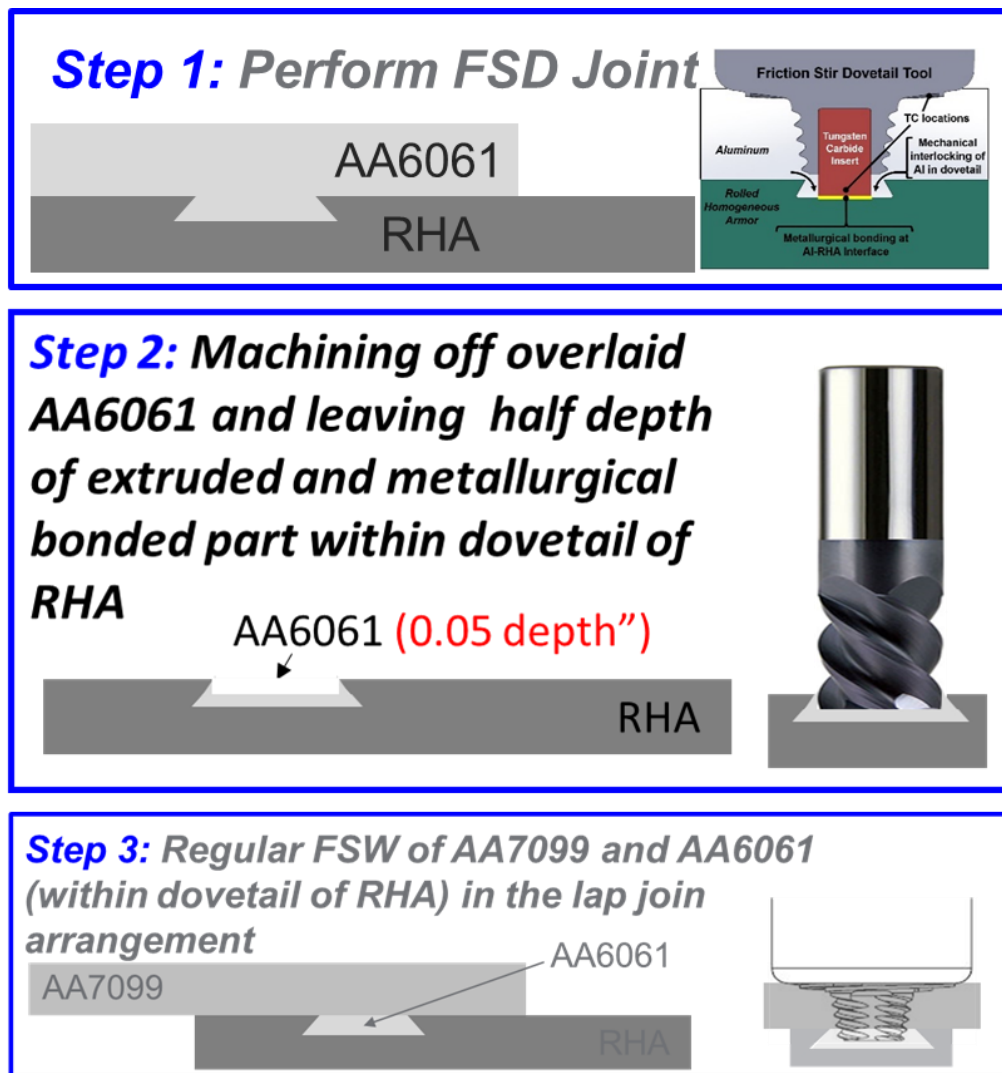


Figure 13. Process for AA7099-RHA joints containing an AA6061 FSD buttering layer.

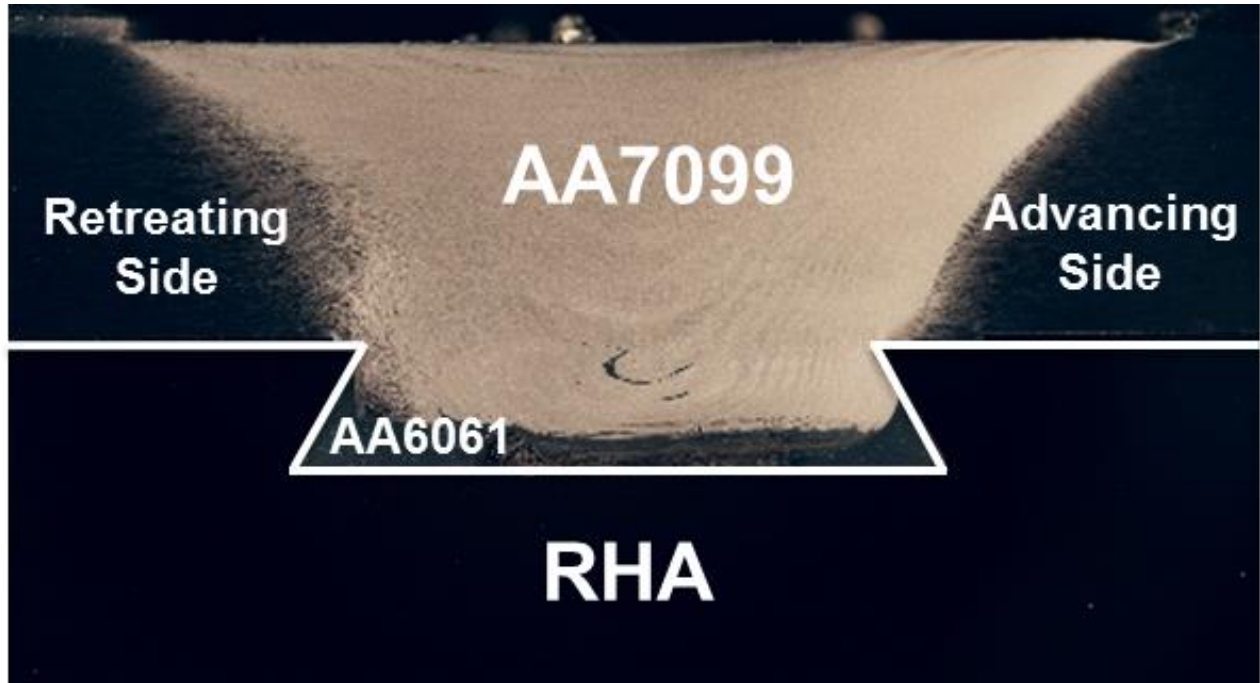


Figure 14. Cross section of hybrid AA7099, AA6061, RHA dovetail joint

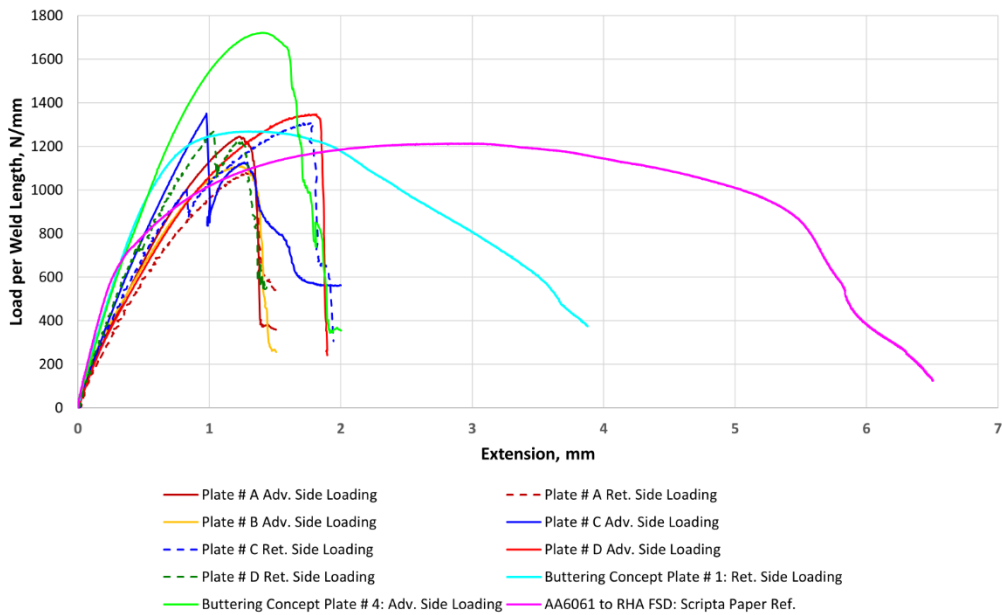


Figure 15. Lap shear test results comparing hybrid AA7099, AA6061, RHA joints with typical FSD of AA6061.

OPSEC1890

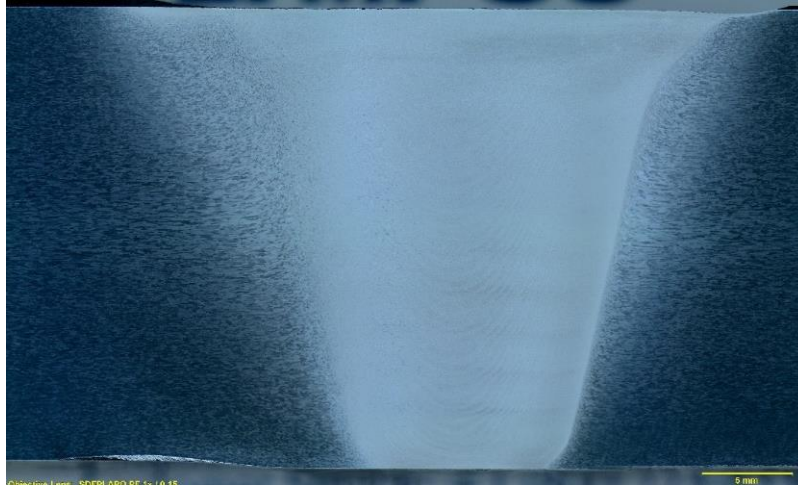


Figure 16. Full penetration friction stir weld in 1.0" thick AA2139.

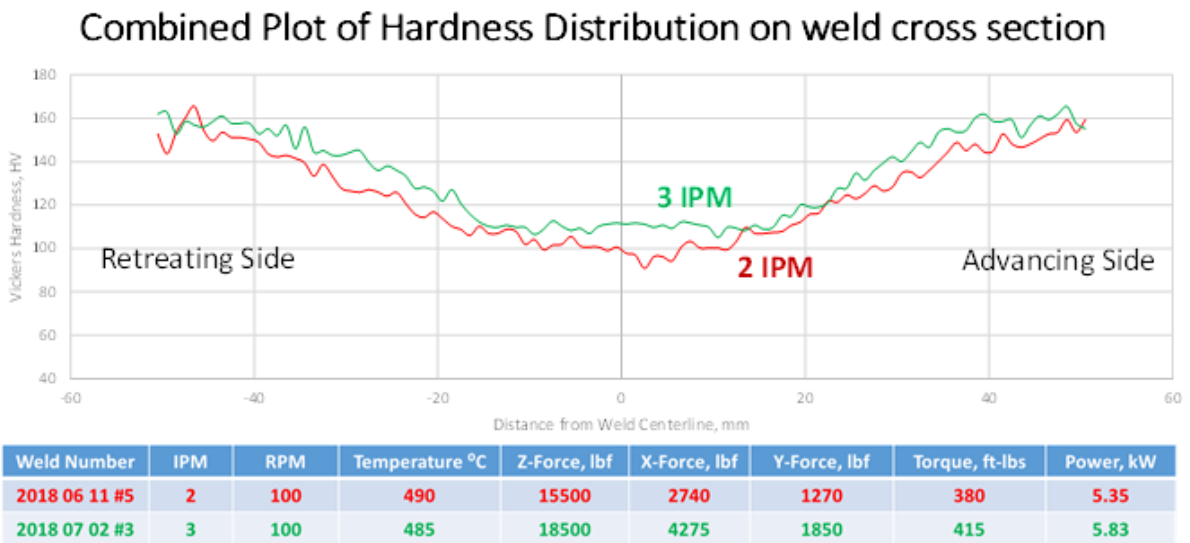


Fig. 17. Hardness mapping showing improvement for welds performed at 3 ipm.

Figures Continue on the Next Page

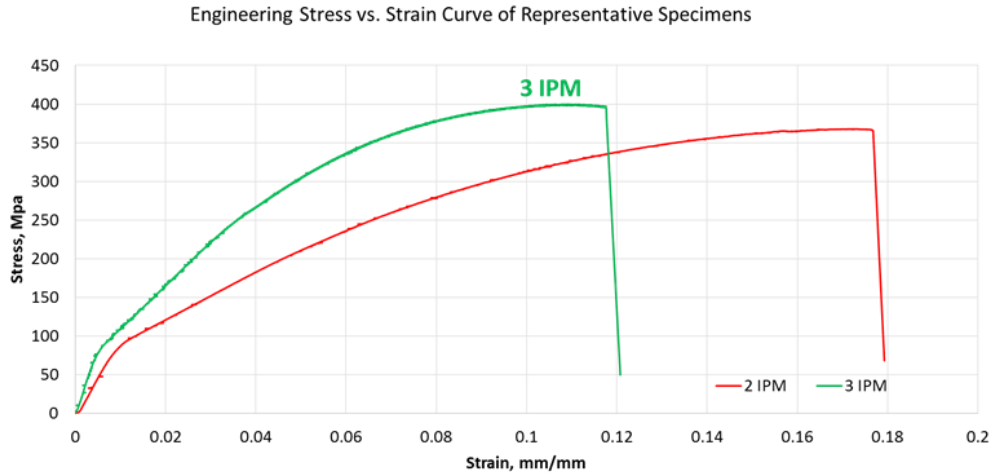


Figure 18. Tensile test results for 1.0” thick butt welds in AA2139.

Table 1. Summary of the mechanical properties assigned to the five regions identified within the processed Al and adjoining RHA.

Materials	Weld Region	Young’s Modulus, GPa	Poisson’s Ratio	Density gm/cc	Yield MPa	Plastic Properties
AA6061 T6	I	68.9	0.33	2.7	276	[11]
AA6061 T4	II & IV	68.9	0.33	2.7	145	[11]
AA6061-FSD	III & V	68.9	0.33	2.7	79	Fig. 3
RHA	-	210	0.28	7.8	820	N/A

Tables Continue on the Next Page

Table 2. Combinations of FSW tool and dovetail machining configurations investigated to maximize penetration of AA7099 into the dovetail and minimize push up of AA6061 above the RHA plate surface.

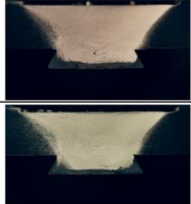
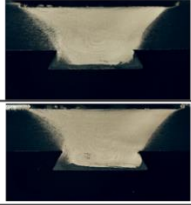
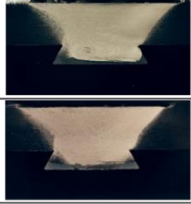
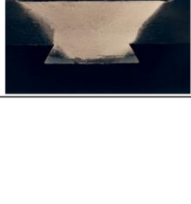
Plate #	Machined AA6061	FSW Tool in Second Pass	Weld Cross Section	Applied Load on	Max. Load, N/mm	Extension at Max. Load, mm
A				Advancing Side	1259 ± 32	1.27
				Retreating Side	1087 ± 8	1.30
B				Advancing Side	1115 ± 37	1.24
				Retreating Side	-	-
C				Advancing Side	1308 ± 75	2.12
				Retreating Side	1317 ± 47	1.78
D				Advancing Side	1356 ± 35	1.77
				Retreating Side	1391 ± 258	1.23

Table 3. Joint efficiency for 1.0" thick butt welds in AA2139.

2 IPM

Specimen label	Tensile stress at Maximum Load (MPa)	Joint Efficiency compared to BM Strength of 460 MPa
A1	376.00	81.7%
A3	374.46	81.4%
A5	374.63	81.4%

3 IPM

Specimen label	Tensile stress at Maximum Load (MPa)	Joint Efficiency compared to BM Strength of 460 MPa
1	396	86.1%
2	400	87.0%
3	395	85.9%

AVPTA Technology Focus Area 2: Lightweight Structures and Materials

Breakthrough Techniques for Dissimilar Material Joining – Brazing Dissimilar Metals with a Novel Composite Foil

**DOE-VTO TFA Lead: Sarah Kleinbaum
TARDEC TFA Lead: Ravi Thyagarajan**

**Principal Investigator(s):
Dr. Timothy Weihs**

**Affiliation: Johns Hopkins University
3400 N Charles St.
Baltimore, MD 21218**

**Project Start: Q1FY15
Completed: Q2FY18**

Objectives:

- To develop, characterize, and assess novel reactive foils that are based on reduction-oxidation (redox) chemical reactions for use in dissimilar alloy bonding applications.

Strategic Context:

- This technology will be applied to future Programs of record (PORs) requiring dissimilar material lap joints.
- The technology supports the TARDEC Strategy enabling new capability in the design and application of dissimilar material lap joints.
- A patent application has been submitted with the intent of licensing the technology to a materials manufacturer, who will then sell to the automobile industry.
- Follow-on activities may include further AVPTA interest to investigate increasing joint strength, reducing cost and / or developing foils for other material combinations. TARDEC-specific follow-on may include lap joint ballistic shock evaluations.

Remainder of Page Intentionally Blank

Accomplishments:

- Determined baseline strengths for bonding aluminum (Al) 6061, magnesium (Mg) AZ31 (aluminum 3% and zinc 1%), aluminum coated boron steel (ACBS), and hot stamped boron steel (HSBS) with Al:CuO-based, Al:Cu₂O-based and Al:NiO-based Redox Foils using initial Redox Foil fabrication techniques. (Al: Aluminum, Cu: Copper, CuO: Cupric Oxide, Cu₂O: Cuprous Oxide, NiO: Nickel Oxide)
- Processed ball-milled, composite powders into diluted Redox Foil with higher reactivity using conventional swaging and rolling techniques. Achieved dissimilar bond strengths as high as 10 MPa (MegaPascal).
- Identified Cu vapor as the gaseous species during the propagation of reactions within ball-milled, mechanically processed Redox Foils with a Al:Cu₂O:Cu chemistry.
- Produced vapor deposited Al:Cu₂O:Cu foils as a model system with five different levels of Cu dilution and identified an optimized level of dilution.
- Increased homogenization of the diluent in Redox Foils by incorporating the diluent into the ball-milling process, resulting in suppression of Cu vapor during propagation and successfully compared result microstructure length scales of Redox Foils with finite element method (FEM) heat dissipation models.
- Reduced the solidification temperature on cooling by over 100 °C by replacing the Cu diluent with Ag (Silver), thereby producing a braze alloy and stronger bonds.
- Investigated the use of Ti:2B (Titanium diboride) reaction system to produce hot, molten scaffold to minimize porosity and enable braze to flow.
- Investigated use of Ti-C-Cu system as alternative to Al:Cu₂O:Diluent thermite system.

Introduction:

Reactive materials have been used to join metals for over 100 years ever since Hans Goldschmidt discovered that reactive aluminum and iron oxide could produce molten iron capable of joining railroads.^{1,2} This was called the thermite process, where aluminum reduces a metal oxide creating molten metal, alumina, heat, and often gaseous products. Initial joining use of these chemistries involved powdered mixtures and a mold so that the molten braze created by the reduction-oxidation reaction can flow into joints. More recently, reactive multilayer foils using intermetallic formation reactions have been used as a heat source.³⁻⁵ These joints do not produce their own braze, and therefore require pre-wetting of solder or braze layers to enable joining. Reactive joining provides a fast, efficient bonding approach, allowing one to use high temperature brazes that cannot be used on certain alloys.

This project aimed to combine the concepts of the two types of reactive joining described above. By utilizing a thermite composition, the exothermic reaction can create its own braze without requiring any pre-coated solder or braze layers on the components. Further, by creating a fully dense foil, the joint can be formed without any mold or complicated fixture. The braze is created at the location of the joint as shown in Figure 1 and does not need to flow into the joint area, as is the case with typical thermite joining. To reduce the amount of gas produced by thermite reactions, the mixture is diluted with excess metal. Adding diluent decreases the reaction

velocity, decreases the total amount of heat, and decreases the reaction temperature. Adding diluent also has the benefit of increasing the quantity of molten metal braze in the products as compared to undiluted thermites.⁶

The chemistry and microstructure of the Redox Foil determines how rapidly a given exothermic reaction will propagate within the foil. The chemistry also determines the characteristics of the braze that is formed. By engineering the reaction properties of the foil, we can tailor the reaction for joining many dissimilar metal combinations. Because the reactions propagate quickly (on the order of 1 m/s), the heat is produced for a short period of time, and very locally. This allows for brazing of dissimilar combinations that cannot be joined with traditional furnace brazing (such as joining steel to magnesium alloys).

Approach:

To develop a Redox Foil capable of joining dissimilar metals, we produced two different types of foils. The first foil is made by mechanically processing constituent powders (Redox Foil),^{6,7} and the other is fabricated by vapor phase processing (PVD).^{5,8} The Redox Foil, is the economical solution that can be easily scaled for automotive applications. PVD foils, on the other hand, have well-defined geometries for scientific inquiry. These ideal microstructures are critical for understanding the processes that occur during propagation, and aid in engineering the necessary microstructure which we emulate in the Redox Foils. In the early stages of the effort, we determined that the Al:Cu₂O system is the most promising system for joining, with the diluent typically Cu, but some foils with Ag dilutions were also prepared, as will be described.

The Redox Foil fabrication process involves three steps. First constituent powders are ball-milled to produce nanocomposite powders. This step was added in FY 2015 to reduce the reactant spacing between the aluminum fuel and the oxide. Initially, only the Al and metal oxide were milled together prior to consolidating into a dense Redox Foil. These foils are labeled BM. However, due to analysis from the PVD foils in FY 2016, it was determined that the Cu diluent needs to be more uniformly incorporated into the final Redox Foil. Therefore, the diluent was added to the ball milling (BM) process, prior to the consolidation step. These foils are labeled BM+D, D denoting Diluent. After milling, the powders are packed into a tube and then compacted by swaging, a radial reduction technique. Finally, the swaged tubes are rolled flat and the tube encasing the powders is removed leaving the fully dense Redox Foil.

The PVD foils are made using magnetron sputtering. The sputtering chamber contains three targets, Al, Cu₂O-Cu, and Cu. Inside the chamber, substrates are rotated past each target producing layered foils of a planar geometry.

We employed a variety of experimental techniques to analyze the microstructure and reaction of the foils. Characterize microstructure we used cross-sectional optical microscopy (OM) and scanning electron microscopy (SEM). To characterize the propagating reactions in the foils we used high speed videography coupled with emission spectroscopy. High speed videos allowed us to determine propagation velocities, a key metric for how fast the reaction is producing heat. The emission spectroscopy was used to identify if vapor species are produced by the reactions,

as well as to approximate reaction temperatures. Slow heating experiments, including differential scanning calorimetry (DSC) and thermogravimetric analysis (TGA), were also used to characterize the thermal properties of reactive materials and resulting braze. Finally, the Redox Foils were used to join Al 3003, Mg AZ31, and hot stamped boron steel (HSBS), and the shear strengths of resulting bonds were tested.

Results and Discussion:

The initial Redox Foils were made using single phase Al, Cu, Ni, NiO, CuO, and Cu₂O powders, and during bonding these foils generated significant gas and ejected particles.⁵ Given both gas production and particulate ejection are detrimental to the strength of the bonds being formed with these foils, we attempted to reduce both phenomena by diluting the foils with excess Ni or Cu. Figure 2 displays the normalized mass ejection fraction as a function of dilution for the three oxide chemistries examined. Normalized mass ejection is defined as the mass of the ejected material collected divided by the mass of the original Redox Foil for the experiment. For all three systems, as dilution increases, the average particulate ejection decreases. For the Al:NiO:Ni system, the particle ejection becomes negligible once dilution increases above 10% by mass, whereas for both CuO systems there is still considerable mass ejection even as dilution is increased to 40 weight (wt) %. The Al:Cu₂O system ejects less mass than Al:CuO system and drops to essentially no mass ejection at 40 wt% dilution.

While excess Ni or Cu lowers the reaction temperature of the foils and minimizes gas production and particle ejection, it also slows reaction propagation, increasing the chance the reactions will quench during bonding. To assess this impact of dilution, we performed velocity measurements on samples from the Al:NiO, Al:CuO, and Al:Cu₂O systems. The results are plotted in Figure 3. Trends are similar to those seen for mass ejection. Al:CuO foils appear relatively insensitive to dilution, with average velocity values between 1-2 meters per second (m/s) until 40 wt% Cu, while velocity in Al:NiO foils drops off considerably after only 10 wt% Ni dilution. Differences in velocity between the Al:NiO and Al:CuO systems increase by nearly an order of magnitude as the respective diluents are added, while the Al:NiO and Al:Cu₂O system approach similar values at high dilutions. In addition, we determined the amount of dilution that could be added to the Al/NiO/Ni, Al/Cu₂O/Cu, and Al/CuO/Cu foils and still have the foils self-propagate across a bonding configuration. We found that the Al/NiO/Ni and Al/Cu₂O/Cu systems could only be diluted 10% before quenching in a bond, while the very reactive Al/CuO/Cu system could be diluted 40wt% before quenching.

In addition to assessing the properties of the initial Redox Foils, preliminary bonds were made using these foils. The Al:CuO foils created porous braze interfaces due to the mass ejection caused by the gas generated by the thermite reaction. Even the heavily diluted case of Al:CuO:40%Cu resulted in substantial particulate ejection from the bond interface. Despite these limitations, the Al:CuO:40%Cu foil was still able to bond all substrates, including Al 6061, Mg AZ31, HSBS, and ACBS. The Al:NiO foils did not produce any noticeable particulate ejection, but the strength of the resulting bonds was less than that of the Al:CuO system as depicted in Figure 4(a). There are two reasons that the NiO-based foils did not perform as well as the CuO-

based foils. First, the Al:NiO systems produced more alumina, by volume than the Al:CuO system, due to their lower reactivity and smaller degrees of dilution that still allow propagation within a bond. Second, the molten nickel from the thermite reaction does not wet the bonding substrates as well as the molten copper. This is shown in Figure 4(b) where a high speed camera captures the molten nickel balling up on the surface of the aluminum substrate.

To make the diluted Redox Foils more reactive and to reduce the risk of quenching, we focused on producing more reactive powders by forming composite powders via ball-milling of the initial, single phase powders as shown schematically in Figure 5. Initial experiments were performed using Al and NiO powders and a clear reduction in reactant spacing can be seen in Figure 6. This led to increased reaction propagation velocities compared to Redox Foils prepared from single-phase powders as shown in Figure 7. For the Al:Cu₂O system, we found that ball milling increases the average propagation velocity by a factor of 3 in 20 wt% diluted foils and a factor of nearly 7 in 40 wt% diluted foils. All ball-milled powder Redox Foils propagated faster than their single-phase counterparts. We also tested ball-milled Redox Foils in a joining configuration to determine whether the reactions would quench in the bonding interface. Quenching tests were performed in bonds where the same component alloys were joined together (Mg AZ31 to Mg AZ31 and Al 6061 to Al 6061) using conventional and ball-milled Redox Foils. The results are shown in Figure 8. In all cases, the highest dilution that could be fully propagated through a bond interface was increased by at least 20 wt% when bonding with ball-milled Redox Foils.

While the Redox Foils that were made utilizing BM powders propagated faster than the initial Redox Foils made with single phase powders (Figures 8 and 9(a)), we observed that many of the BM-based foils disintegrated during propagation, resulting in lots of mass ejection from the reaction front. To investigate the cause of the mass ejection, we obtained emission spectra during the reactions to identify gaseous species. The emission spectra for Al:Cu₂O:Cu BM-based foils are presented in Figure 9(b) (red traces). For the 20wt% and 30wt% foils, there are multiple peaks including broad peaks at 490 and 500 nanometers (nm). These correspond to CuO and possibly AlO emission. The sharper peak at 510 nm corresponds to Cu emission. The 40wt% Ball milled (BM)-based foil does not show any peaks and has a smooth emission curve. These results indicate that the lower dilution BM-based foils produce Cu vapor during the propagation process. This vapor can create pressure that causes much of the material to be ejected. The ejection of material is detrimental to the joining process as it creates pores in the resulting braze. An example of a dissimilar bond made with a Al:Cu₂O:20Cu BM foil is given in Figure 10. While the strength of the resulting bond reach as high as 10 MPa in shear strength, these bonds include substantial porosity. These pores are weak points that can significantly limit the strength of the resulting bonds.

To understand the gas production, we fabricated PVD foils of Al:Cu₂O chemistry and added different amounts of Cu diluent into the foils.⁸ Five different foils were fabricated, with Cu layer thicknesses of 0 nm (Bilayer), 25 nm, 50 nm, 75 nm, and 100 nm. The Al and Cu₂O layer thickness remained constant throughout, so dilution increases with Cu thickness. Note that as the Cu layer thickness (dilution) increases, the peaks in the emission spectra decreased, as shown in Figure 11. The bilayer had very prominent emission peaks, and the high speed video displayed lots of gas and particulate spray. The 25 nm foil, had some spray and a few peaks.

The other foils showed no sign of emission peaks and no sign of spray or gas vapor. These model PVD foils suggested that Cu vapor production can be suppressed if the diluent is evenly distributed throughout the foil.

To assess the distribution of diluent within the Redox Foils produced using ball-milled powders, we performed an extensive analysis of the distribution of diluent within the BM Redox Foils.⁹ Image analysis was performed on Al:Cu₂O:Cu BM Redox Foils to understand the length scales present in the microstructure. The results are summarized in Figure 12 where the ratio of thermite to diluent is plotted vs the thermite length scale. Larger ratios correspond to smaller levels of dilution. The size of the circle corresponds to the area fraction of length scales within a given ratio. In addition, we performed finite element model (FEM) heat transfer simulations to determine the critical thermite lengths and ratios that are required to suppress Cu gas formation during propagation. The FEM results are summarized in Figure 13. Based on the simulations it was determined that for 20wt%, and 30wt% dilutions, over half of the foil area was capable of producing vapor using the analysis from the simulations. Not surprisingly, both of these foils produced Cu vapor. The 40wt% sample, though, was predicted to have fewer dangerous microstructural length scales, and it did not produce Cu vapor. Therefore, to produce gasless propagation, we concluded that a finer spacing and more homogenous distribution of diluent in the microstructure was needed.

In order to accomplish this in the mechanically processed foils, the Cu diluent was ball-milled with the Al and Cu₂O powders to produce three-phase composite particles.⁹ With this fabrication, the diluent is more intimately mixed with the Al and Cu₂O. We see finer Cu pieces evenly dispersed in the resulting BM+D Redox Foil microstructures (Figure 14). Adding the diluent during milling does suppress the Cu vapor production as desired. The emission spectra of BM+D foils do not exhibit Cu peaks (Figure 9(b)), suggesting that the homogenization of diluent did eliminate gaseous Cu products as was seen with the PVD foils. However, adding Cu during the ball-milling state also reduced the propagation velocities compared to BM foils (Figure 9(a)).

While the BM+D Redox Foils with more uniform distribution of Cu produce less Cu vapor, the strengths of the bonds made with Al:Cu₂O:Cu BM+D foils goes down as dilution increases. At 20wt% dilution, the fracture occurs within the braze, whereas for the 30wt% dilution, the fracture location moves from within the braze to the substrate interface. Strengths and fracture surfaces are shown in Figure 15. This change in fracture location indicates that the molten Cu produced by the reaction did not adequately wet the substrates at higher dilutions. We believe the higher dilution of 30wt% reduces the reaction temperature, and therefore the braze remains molten for a shorter period of time, which is detrimental to wetting of the substrate.

To overcome the wetting issue as you increase the amount of dilution, we substituted Ag for Cu as the diluent. This produced an alloy braze that has a lower solidification temperature. The lower melting temperature should increase the amount of time the braze is molten. The Ag substitution was done with both BM and BM+D fabrication methods. In both cases, the Ag-diluted sample melted at a lower temperature than the Cu diluted sample (Figure 16), suggesting that Ag diluted Redox Foils stays molten for a longer period of time, which we thought would promote wetting of the surfaces.

However, even with these improvements of metal vapor suppression and braze melting temperature reduction, bonds formed with Ag diluted Redox Foils and Cu diluted BM+D Redox Foils still exhibit porosity. Data from the PVD samples suggests that there may be some form of gas generation other than metal vapor formation. Figure 17 shows SEM pre- and post-reaction cross sections of a 100 nm PVD foil that provided no evidence of Cu vapor on reaction. The post reaction image contains large pores, which we suspect are formed by vapor not detected via emission spectroscopy (not metal vapor). We have also performed TGA experiments for both PVD foils and Redox foils which show a 1% mass loss at low temperatures under slow heating conditions. We attributed the mass loss to oxygen release, which may also occur at the faster rates and higher temperatures of propagating foils. This sort of oxygen release has been seen for other thermite systems,¹⁰ and must be overcome in order to produce non-porous brazes with limited mass ejection during propagation.

To minimize the issue of gas generation attributed to oxygen release, we explored the use of high energy formation reactions that could augment the thermite reactions by creating a hot scaffold into which molten braze could flow. We ball milled and compacted Ti:2B powders that have very high adiabatic temperatures and higher melting temperatures, and can form a porous TiB₂ scaffold. We combined the Ti:2B pellets with our traditional thermite powder systems to leverage the best qualities of both reactive systems. The Ti:2B has a high heat output upon reaction, forming TiB₂, which creates a hot, porous, and solid matrix. The thermite acts as an additional heat source while providing molten braze material that solidifies at temperatures approximately 2000°C below the melting point of TiB₂. These metallic products (Cu and Ag) are able to flow into the hot pores of the TiB₂ matrix, decreasing porosity and increasing the degree of connectivity of the metal braze throughout the bond thickness. More molten metal is contributed from the local heating of the substrates (Al 3003), which allows for further pore filling. We fabricated tri-layer pellets with thermite outer layers and a Ti:2B core, as depicted in Figure 18(a), and we demonstrated the ability to produce joints with such tri-layers as shown in Figure 18.

Unfortunately, because B powders are often porous and can be very hygroscopic, the Ti:2B powder compacts produced significant vapor upon reaction and significant mass losses were observed in thermogravimetric analysis (TGA) scans of the elemental starting powders. The bonds formed using these tri-layer structures all showed low strengths as seen in Figure 19.

As an alternative to the Ti:2B system, we synthesized Ti-C-Cu (Titanium-Carbon-Copper) powders using ball milling to leverage the equally exothermic Ti:C (Titanium Carbide) reaction. We investigated a Cu-rich, 0.63CuTiC and a Cu-lean, 0.44CuTiC composition using special WC coated milling vials. Cross-sections of the powders showed limited mixing of Ti, C, and Cu and differential thermal analysis (DTA) scans revealed the formation of TiC, but only at high scan temperatures. We pressed the Cu-rich 0.63CuTiC ball milled powders into pellets, incorporating soft indium powders into the compacts in some cases to minimize porosity. While the pellets could be ignited and did form TiC and Cu or CuIn (copper-indium) brazes, the reactions typically quenched as they propagate between steel samples for bonding. In the few cases where the reactions propagated across the bond interface, the resulting molten braze failed to wet the steel samples and bonding was not accomplished. Thus, reactive foils based on thermite reactions and formation reactions could not produce bonds stronger than 10 MPa in simple shear.

OPSEC1890

Conclusions:

After establishing baseline bonding performance for mechanically fabricated Redox Foils, we identified and undertook multiple strategies for improving the performance of these foils during bonding. We also used sputter-deposited thermite foils as model materials to identify the appropriate extent of dilution to avoid the generation of Cu vapor, as well as other sources of gas generation. We ball-milled Al and NiO powders, Al and CuO powders, and Al and Cu₂O powders to make them more reactive. We also added Cu powders during the ball-milling of the last chemistry to enable a more uniform distribution of diluent within the Al/Cu₂O/Cu foils. All of these steps lead to improvements. Reactivity and reaction velocities were improved and Cu gas generation was minimized. We also lowered the melting temperature of the resulting braze by adding Ag powders to the Redox Foils. However, gas generation via oxygen release was identified as a final, remaining source of vapor and could not be eliminated. This gas generation led to voiding in the bond interfaces and weak bonds. We then utilized mixtures of Ti/B and Ti/C/Cu powders to produce Reactive Foils without the generation of oxygen vapor. However, these foils could not be made reactive enough to propagate through and fully wet components during bonding. In the end, we could not meet our goals for bond strength in dissimilar metal bonds.

References:

- [1] Goldschmidt, H. Process of Joining Metal Pieces. Google Patents January 6, 1903.
- [2] Wang, L. L.; Munir, Z. A.; Maximov, Y. M. Review Thermite Reactions: Their Utilization in the Synthesis and Processing of Materials. *J. Mater. Sci.* 1993, 28, 3693–3708.
- [3] Wang, J.; Besnoin, E.; Duckham, A.; Spey, S. J.; Reiss, M. E.; Knio, O. M.; Weihs, T. P. Joining of Stainless-Steel Specimens with Nanostructured Al/Ni Foils. *J. Appl. Phys.* 2004, 95 (1), 248–256.
- [4] Duckham, A.; Spey, S. J.; Wang, J.; Reiss, M. E.; Weihs, T. P.; Besnoin, E.; Knio, O. M. Reactive Nanostructured Foil Used as a Heat Source for Joining Titanium. *J. Appl. Phys.* 2004, 96 (4), 2336.
- [5] Weihs, T. P. *Fabrication and Characterization of Multilayer Films and Foils*; 2014.
- [6] Kinsey, A. H.; Slusarski, K.; Woll, K.; Gibbins, D.; Weihs, T. P. Effect of Dilution on Reaction Properties and Bonds Formed Using Mechanically Processed Dilute Thermite Foils. *J. Mater. Sci.* 2016, 51 (12), 5738–5749.
- [7] Woll, K.; Gibbins, J. D.; Slusarski, K.; Kinsey, A. H.; Weihs, T. P. The Utilization of Metal/metal Oxide Core-Shell Powders to Enhance the Reactivity of Diluted Thermite Mixtures. *Combust. Flame* 2016, 167, 259–267.
- [8] Kinsey, A. H.; Slusarski, K.; Krumheuer, E.; Weihs, T.P. *Enhanced reaction velocity and diluent homogenization in Redox Foils using arrested reactive milling thermite powder*, *J. of Mat. Sci.*, 2017, 52, 11077–11090.
- [9] Kinsey, A.H.; Behrou, R., Guest, J. K.; and Weihs, T. P. *Critical heat dissipation length scales in fully dense thermite foils*, *Combustion and Flame*, 2018, 190, 432-440.

- [10] Zhou, L.; Piekiet, N.; Chowdhury, S.; Zachariah, M. R. Time-Resolved Mass Spectrometry of the Exothermic Reaction between Nanoaluminum and Metal Oxides: The Role of Oxygen Release. *J. Phys. Chem. C* 2010, 114 (33), 14269–14275.

Figures:

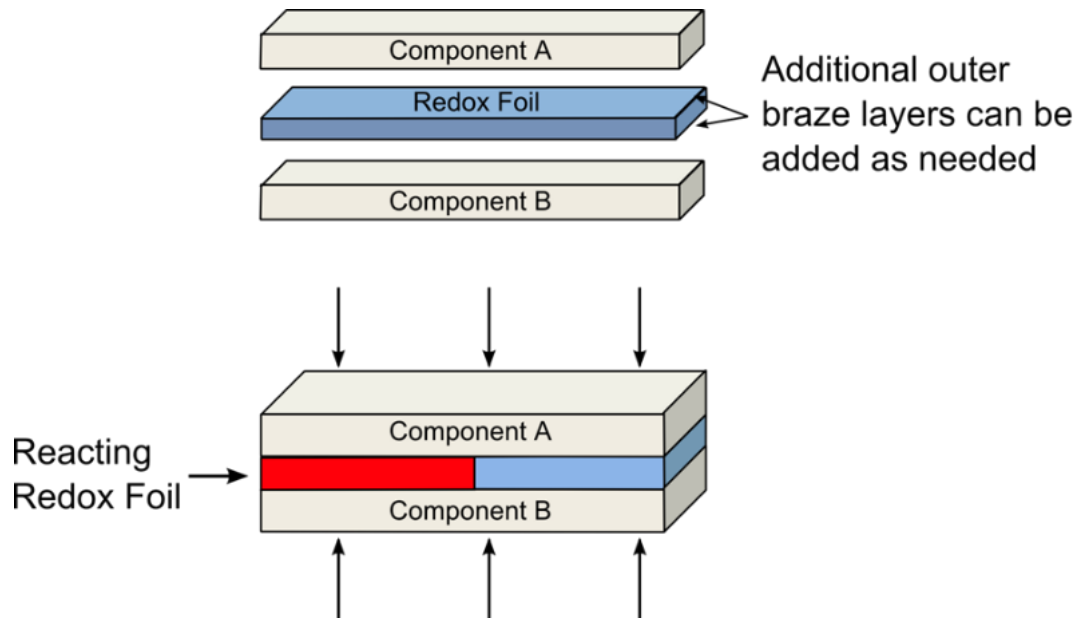


Figure 1: A schematic representation of bonding with a Redox Foil. After ignition, a reaction within the foil self-propagates through the bond interface.

Figures Continue on the Next Page

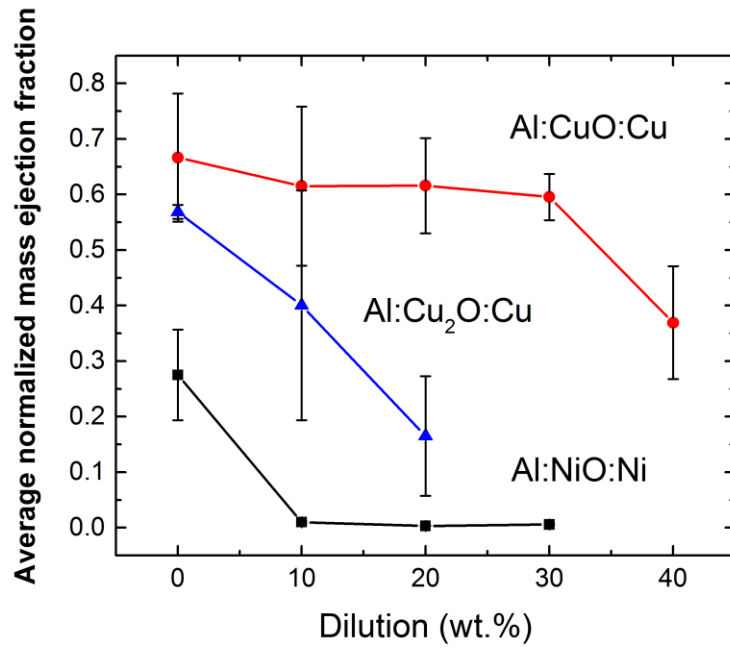


Figure 2: The average normalized mass ejection as a function of dilution for different weight percents of Al:NiO, Al:CuO, and Al:Cu₂O foils, where the diluent is the metal from the starting oxide.

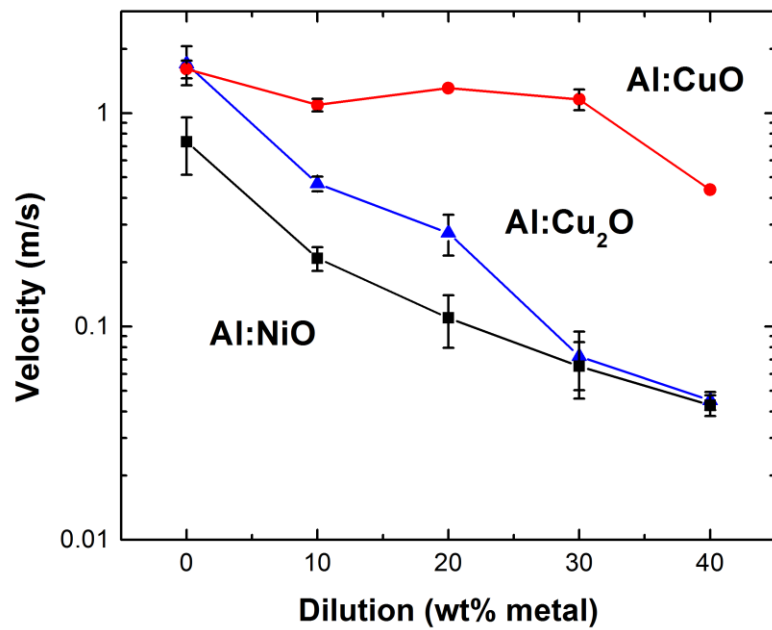
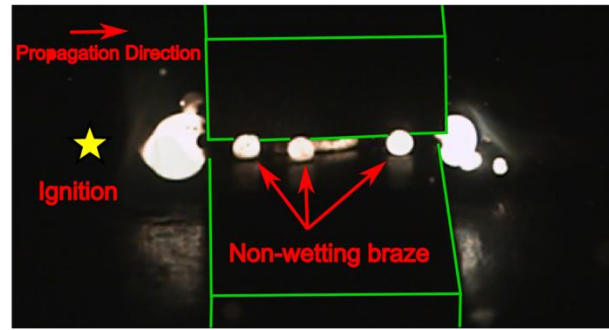
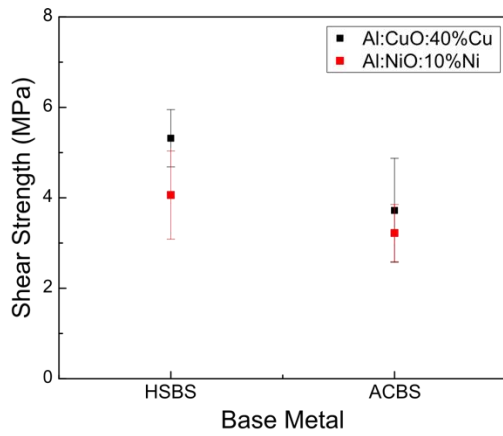


Figure 3: Average propagation velocities of Al:NiO, Al:CuO, and Al:Cu₂O foils as a function of dilution.



a)

b)

Figure 4: a) Shear strengths for bonding HSBS and ACBS with Al:CuO:40%Cu and Al:NiO:10%Ni. b) A frame from high speed video showing molten braze from Al:NiO:10%Ni not wetting the aluminum bonding substrates; bonding substrates have been outlined in green for clarity.

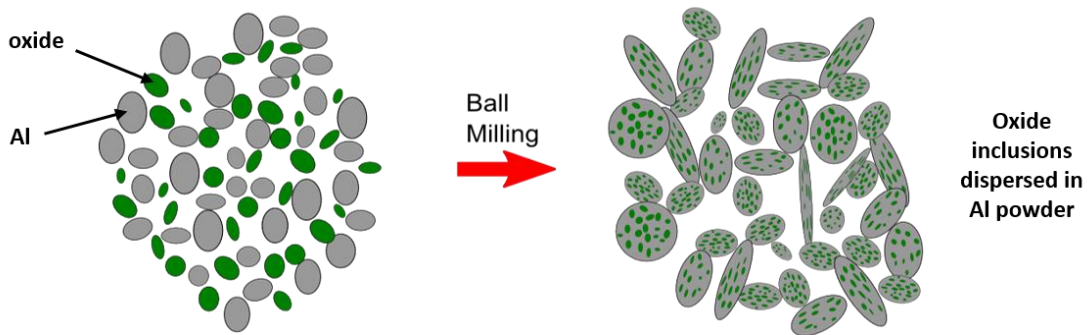


Figure 5: Schematic of powder evolution during ball milling process. Collisions between the milling media and single-phase powders create composite powders containing oxide fragments dispersed in softer aluminum powders.

Figures Continue on the Next Page

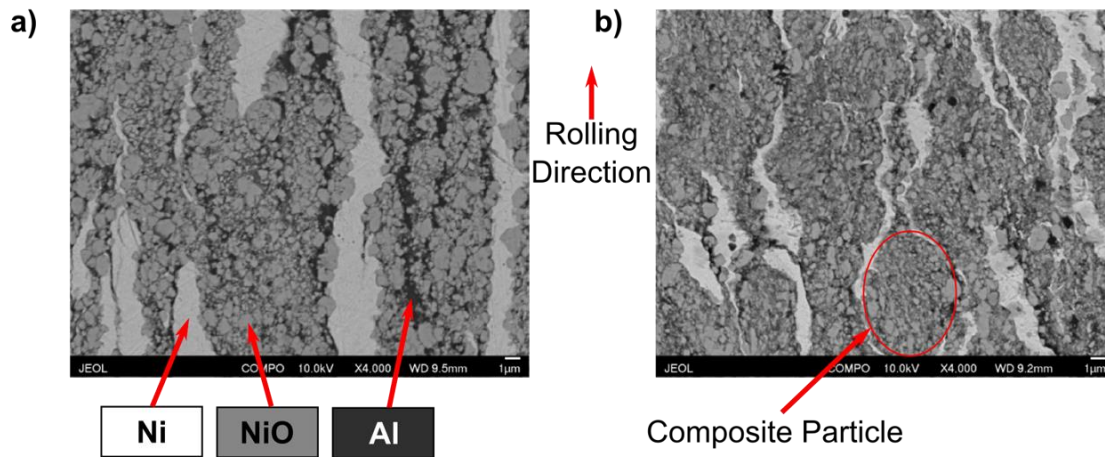


Figure 6: Scanning electron micrographs of Al:NiO:Ni Redox Foil fabricated from (a) single-phase powders, and (b) ball-milled composite powders.

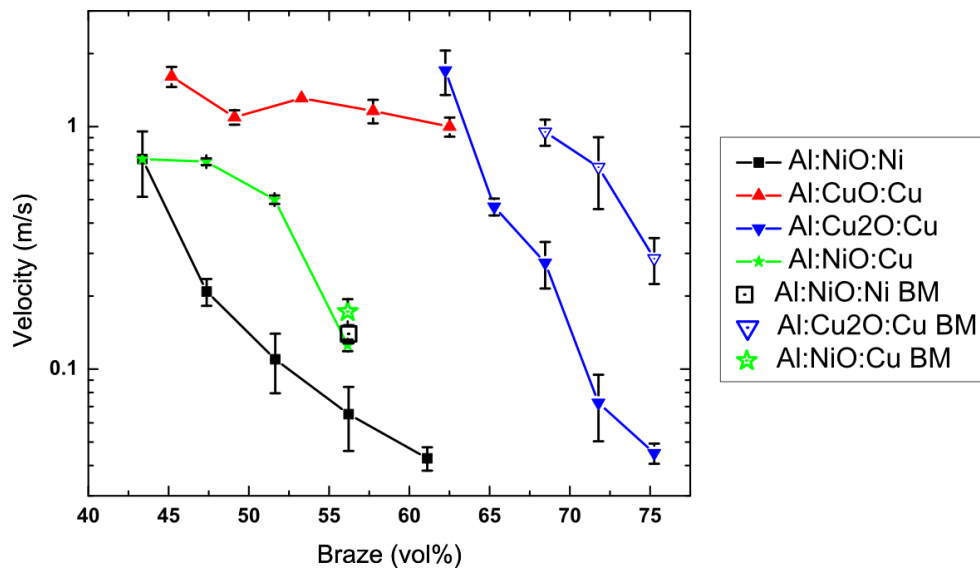


Figure 7: A comparison of propagation velocities for thermite systems produced from single-phase powders and ball-milled (BM) composite powders. Velocities are plotted as a function of expected braze percent by volume, where the balance is the expected alumina content.

Figures Continue on the Next Page

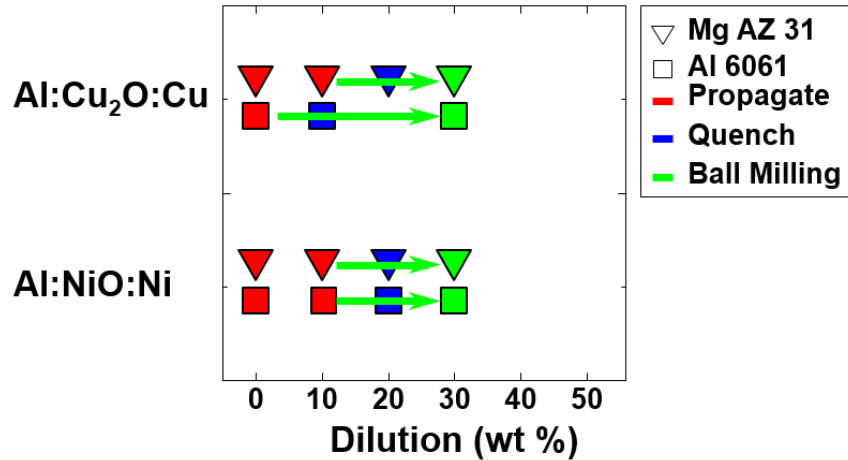


Figure 8: Quenching limits for Al:Cu₂O:Cu and Al:NiO:Ni systems using conventional and ball-milled powders. Foils created from ball-milled powders could be subjected to higher levels of dilution before quenching in the bond interface.

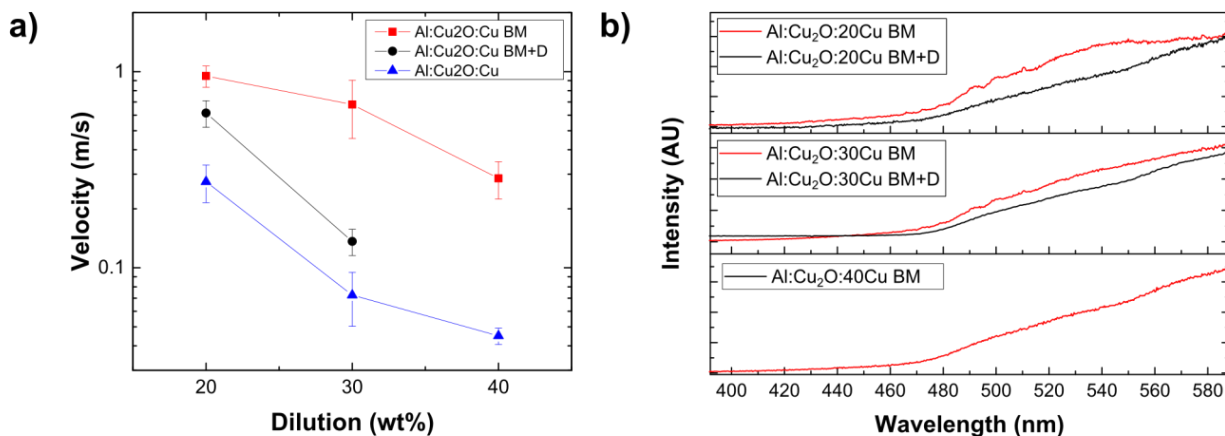


Figure 9: a) Propagation velocity of the Al:Cu₂O:Cu system for three different processing paths, conventional (FY2014), BM (FY2015), and BM+D (FY2016). b) Emission spectroscopy as a function of wavelength for BM (red) and BM+D (black) foils of the Al:Cu₂O:Cu system.

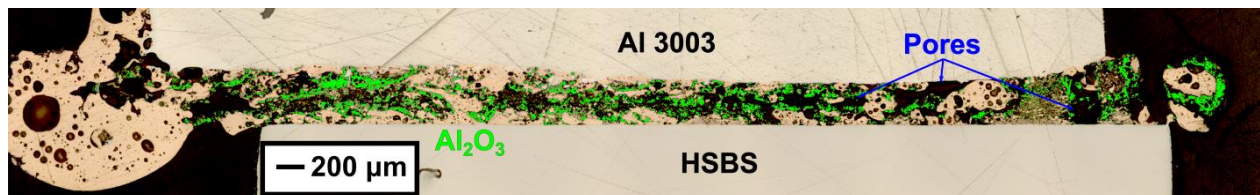


Figure 10: Cross section of dissimilar Al 3003/HSBS bond made with Al:Cu₂O:20Cu BM Foils; the alumina has been false colored green for clarity.

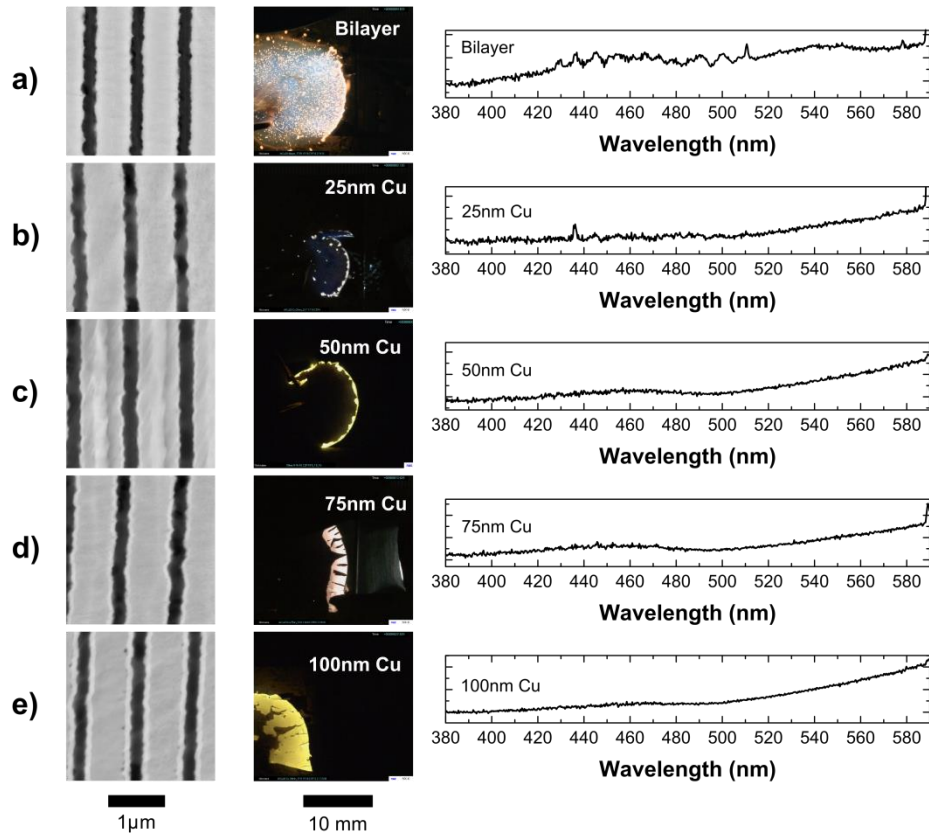


Figure 11: SEM image, high speed video snapshot, and emission spectroscopy of a) bilayer PVD foil and PVD foils with Cu interlayers of thickness b) 25 nm, c) 50 nm, d) 75 nm, and e) 100 nm. In the SEM images, dark is Al, grey is Cu_2O -Cu, and the thin white layer between the two is the Cu layer.

Figures Continue on the Next Page

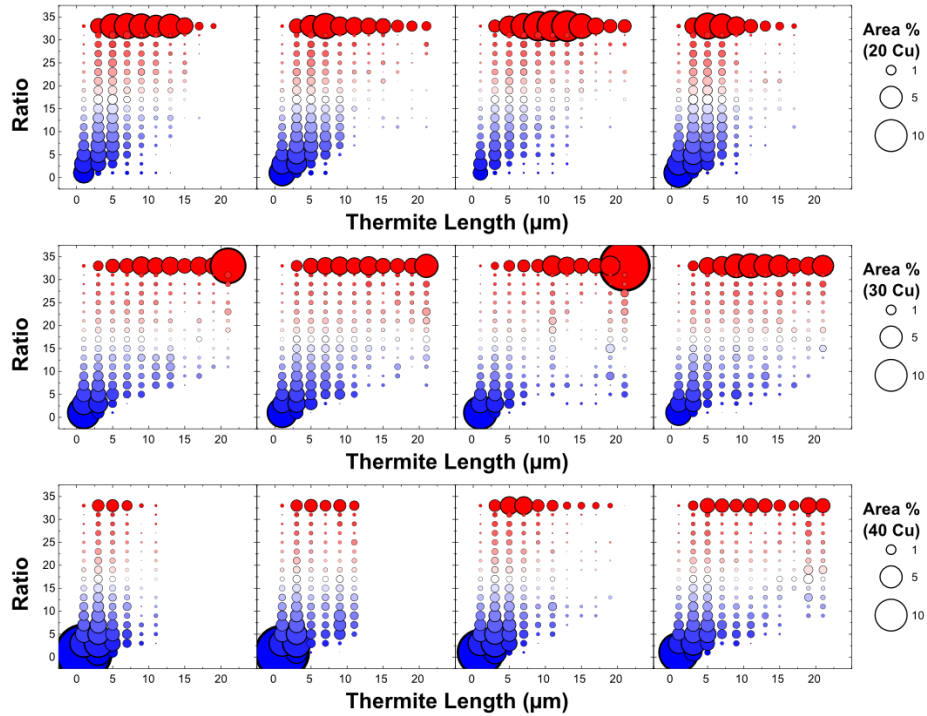


Figure 12: Microstructural analysis of BM Redox Foils.
 Each graph represents analysis on a different region of foil.
 Top row is 20wt% Cu; middle row is 30wt% Cu; and bottom row is 40wt% Cu.

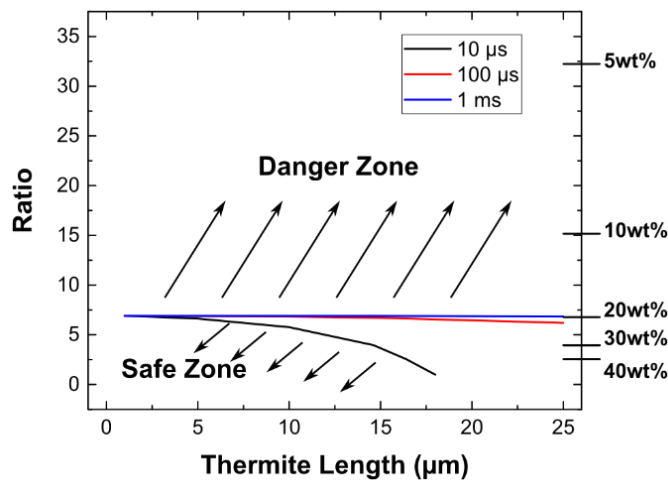


Figure 13: Results from FEM simulations determining what ratio and length scales are required in order to suppress gas formation

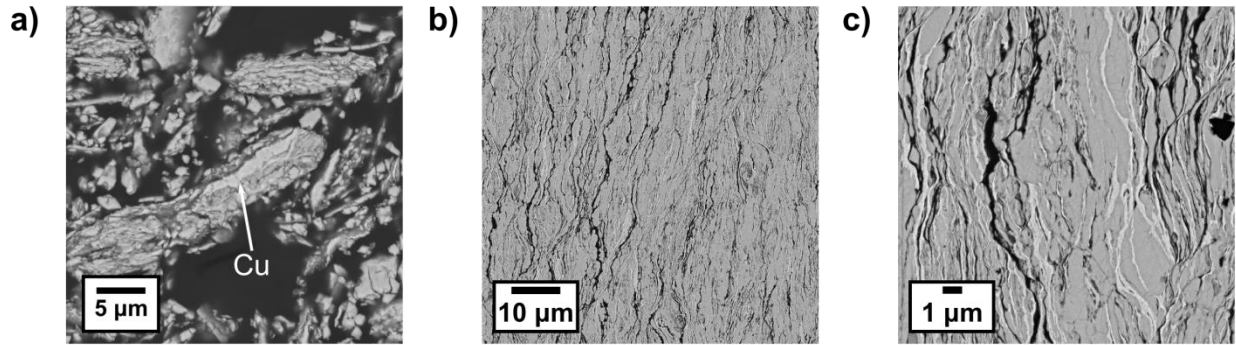


Figure 14: SEM cross sections of a) BM+D powder with Cu inclusion highlighted and images of Al:Cu₂O:30Cu BM+D Redox Foil at low magnification, b), and high magnification, c).

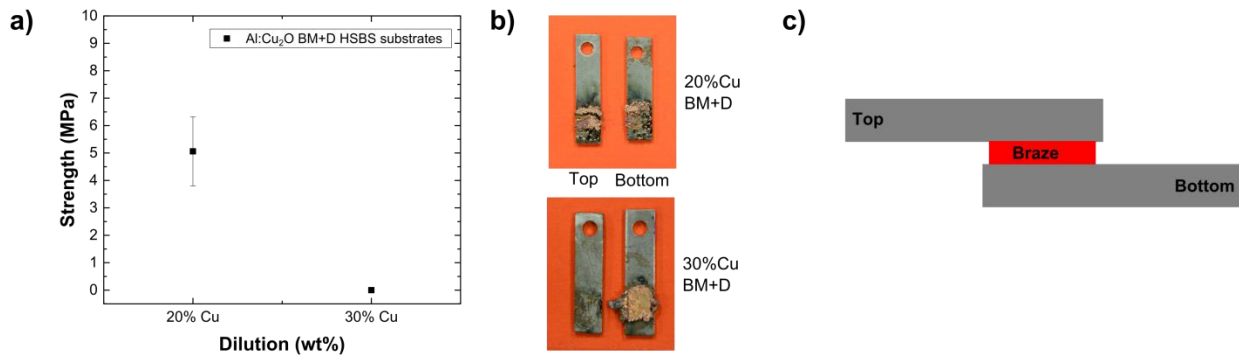


Figure 15: a) Shear strengths of Al:Cu₂O:Cu BM+D foils joining HSBS with representative fracture surfaces in b) and a schematic of the lap shear joint for fracture location in c).

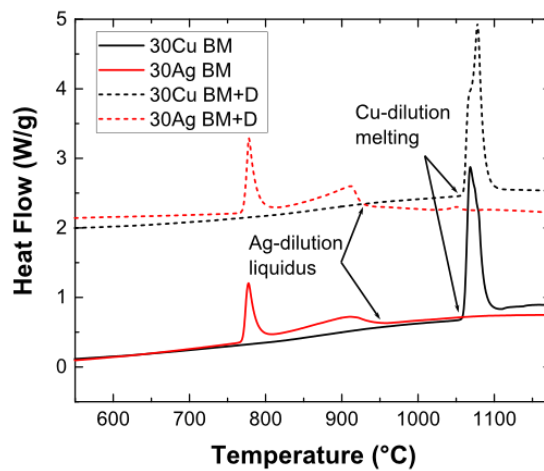


Figure 16: DSC traces of the second heating of Redox Foil indicating that the melting temperatures of the resulting braze is lower when diluted with Ag as opposed to Cu

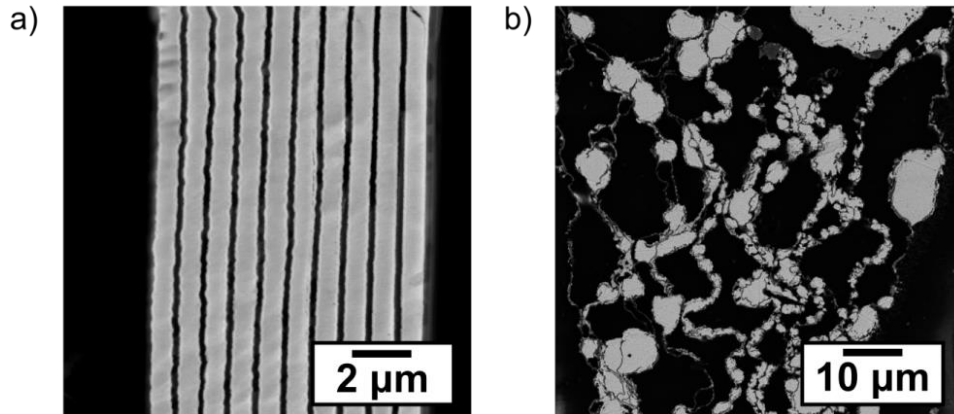


Figure 17: SEM of a) an initial 100 nm PVD foil showing regular layer spacing and a total thickness of approximately 15 μm. b) SEM of a reacted foil with large pores causing an increase in foil thickness.

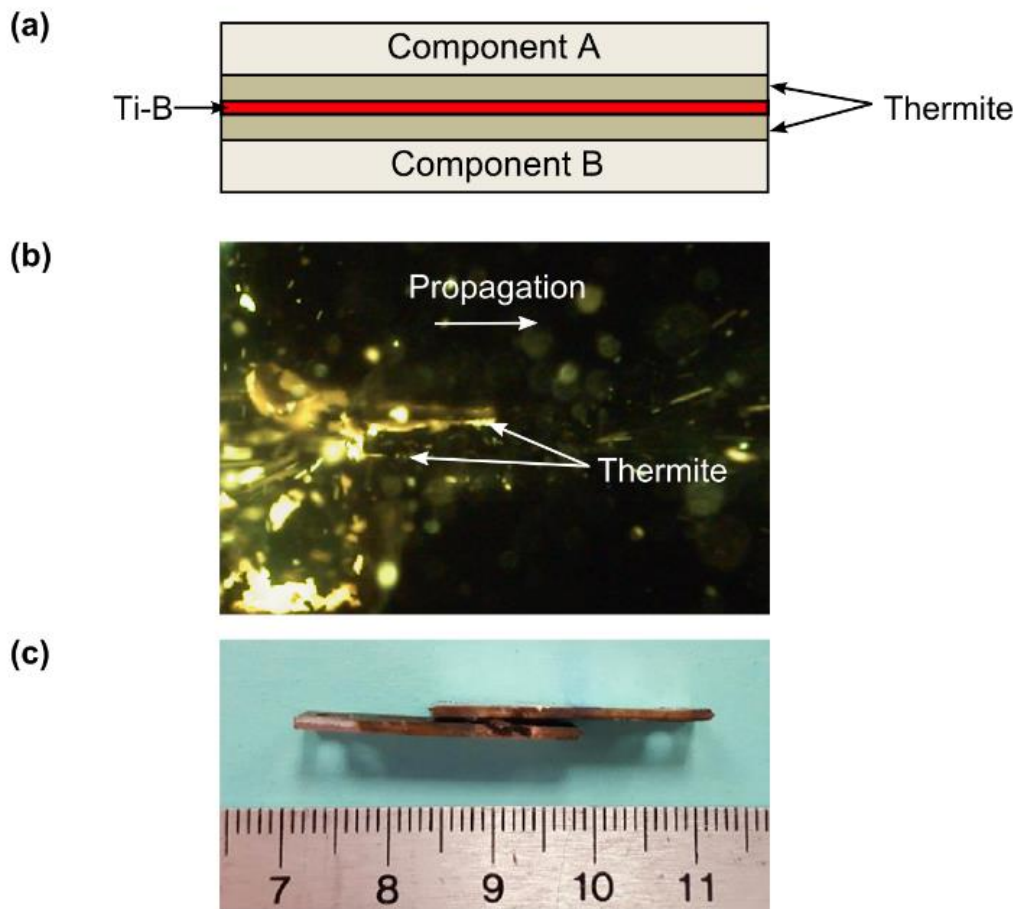


Figure 18: (a) Schematic representation of bonding with a trilayer pellet and (b) video of such a pellet propagating between two Al 3003 substrates producing the joint shown in (c)

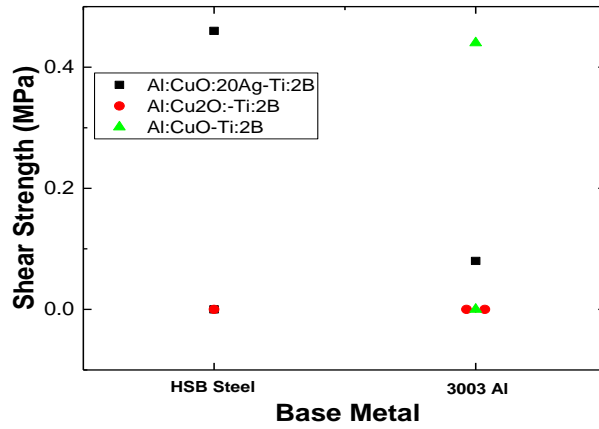


Figure 19: Preliminary bonding results for various combinations of thermite and Ti:2B powders.

Remainder of Page Intentionally Blank

AVPTA Technology Focus Area 3: Energy Recovery & Thermal Management



**DOE-VTO TFA Lead: Steven Boyd
TARDEC TFA Lead: Mary Goryca**

**There was no project activity under this
TFA during FY18.**

Remainder of Page Intentionally Blank

This Page is Intentionally Blank

AVPTA Technology Focus Area 4: Alternative Fuels & Lubricants

Technology Development to Improve Fuel Efficiency through Friction Reduction

**DOE-VTO TFA Lead: Mr. Michael Weismiller
TARDEC TFA Lead: Dr. Jay Dusenbury**

**Principal Investigator:
Dr. Stephen Hsu**

**Affiliation:
George Washington University
GW Energy Initiative
Suite 323, room 323C
Exploration Hall, 20101 Academic Way
Ashburn, VA 20147**

**Project Start: Q2FY15
Estimated Completion: Q2FY19**

Objective:

- To develop friction reduction technology capable of improving fuel efficiency of legacy vehicles by at least 2% over the baseline technology using low viscosity lubricants and material technology options (surface textures, diamond-like carbon films, and bonded lubricant films) without sacrificing durability.

Strategic Context:

- Demonstrate a battlefield fuel reduction and reduce the logistics burden.
- Increase power density and energy efficiency resulting in increased vehicle range, endurance and operational tempo, while reducing the number of logistics convoys on the battlefield.
- Increasing fuel efficiency of ground vehicles to reduce life cycle costs.

Accomplishments:

- Three formulations were tested in engine Chassis dynamometer tests against the baseline 5W-30 GF-5 Premium commercial oil. The new formulations all showed improvement in fuel economy in a modern fuel efficient engine platform.

OPSEC1890

- The 0W-16 formulation was optimized based on the engine chassis dynamometer test results.
- The new V8 engine component parts have extensive surface treatments and coatings. Some coating materials interfere with the surface texturing process. Developed modified fabrication processes and for some parts found alternate parts what are uncoated to fully test the surface technology.
- The 0W-16 formulation was modified and retested in the engine chassis dynamometer test. The revised formulation showed substantial improvement over the previous versions.

Introduction:

In lubricant formulations, base oils of various purities are the solvent and additives are the solute. Additives are added to the solution to impart various performance bench marks. Two types of additives are used, those that control the bulk property such as antioxidants, dispersants, detergents, viscosity modifier (VM), and antifoam; and those that control surface properties, such as anti-wear, friction modifiers, corrosion inhibitors, rust inhibitors, and surface deactivators. The bulk property control agents are either neutrally charged or less polar than the surface active agents; the surface active agents have somewhat hierarchical polarity stacking order to arrange themselves against the sliding surfaces. The anti-wear agent has to be able to adsorb and react with the metal surface to perform its anti-wear function, so the decomposition products of the anti-wear agent; ZDDP (zincdialkyl dithio-phosphate) have to react with the surface active sites (3). The formulation has to be delicately balanced to avoid precipitations and adverse additive-additive interactions rendering some or most of the additives non-functioning.

Over the decades, the basic lubricant chemistries have remained the same but modifications to the molecular structures and finer control have been made. The total amount of additives used, however, has grown steadily to accommodate increasing performance demands. Friction modifiers were introduced in the 1980s and a new engine dynamometer test Seq. VI was developed to measure their effectiveness.

Approach:

Four proposed tasks to reach the goal (multiple lines of defense against friction deterioration and wear):

Task 1: Valvoline will supply a commercial SAE 5W-30 GF-5 lubricant to GWU as the baseline formulation. GWU/Valvoline will work jointly to develop a next generation low viscosity fuel efficient lubricant formulation with at least 2% higher fuel efficiency as measured by Seq. VI engine test. GWU will screen new friction reduction chemistry and tougher anti-wear film chemistry in bench tests to identify potential candidates. Valvoline will incorporate the successful candidates into the formulation for testing. The new formulation will be tested to see whether it achieves the fuel efficiency target (as measured by Seq. VI engine tests).

Task 2: GWU will develop microencapsulation technique (encapsulation, release mechanism, and survivability through engine operation) to create the second line of defense to provide time-release of additives on demand as an option for Task 1.

OPSEC1890

Task 3: GWU will work with GMC on controlling engine component surface topography and fabricate surface textures to increase film thickness and enable more hydrodynamic lubrication mode in the most significant engine components (identified by GMC) to reduce friction throughout a selected engine model. When the specific engine component operation requires additional durability, GWU will deposit DLC film with bonded chemical film on the engine component to provide robust durability.

Task 4: The team will integrate the improved engine component (friction surface technology in Task 3) with the new energy efficient lubricant to evaluate the combined benefits and robustness of the system durability by bench scale simulation tests for a selected engine component. If the results warrant further testing and development, the industrial partners/and or DOE may consider further investment to commercialize the technology.

Results and Discussion:

The friction modifiers optimization investigates the kind of friction modifiers and their combinations, the concentration effect, and the potential interference by and with other additives. The friction tests were conducted using the Plint ring on liner tester using the V8 engine parts cut segments and shown in Figure 1. The tests were conducted using a step-loading test procedure (from 30N to 240N) at 100°C with 24Hz reciprocating sliding speed. A baseline formulation with friction modifier removed was used for comparison. Different friction modifiers both single and combinations of friction modifiers were substituted into the formulation to measure friction levels. The optimized formulation shown in Figure 1B was selected for engine testing.

As one can see from Table 1, we have tested one GF-5 (5W-30) baseline oil, one GF-6A 0W-20 oil, and four 0W-16 prototype formulations. They all show fuel economy improvements under the normal EPA fuel economy testing cycles. The US06 test is outside of the EPA fuel economy testing procedure. It is included in this test sequence to simulate high temperature, high stress, and high acceleration conditions. In this test, 0W-16 oils did not show much improvement over the baseline oil.

The current engine chassis dynamometer test and its vehicle test platform will continue to be refined to measure fuel economy potential of ultralow viscosity oils. The reformulation of our 0W-16 oils will proceed with the addition of microcapsules containing friction modifiers.

Conclusions:

The project is progressing on schedule. The major target of the solicitation has been met with a 2% fuel economy improvement using a newly developed low viscosity lubricant, employing various new technologies. Specifically, from test data gathered in the prior annual report, the newly developed 0W-20 "GF-6A" prototype oil was successfully tested in the Seq. VI E tests and the results showed a 2.39% fuel economy over the baseline oil of 2014 GF-5 commercial 0W-30 oil.

The microcapsules have demonstrated time release properties and now the capsules are ready for trials in real application. The form of trial and how to test their effectiveness are still uncertain since it is a new technology. The microencapsulation process has been scaled up. The original process microencapsulated process was able to produce one gram quantity for each batch. A new process has been developed that can yield 5 to 10 grams of capsules by using larger volume, adjusting the reaction time, and controlling the reaction temperatures.

Figure and Table:

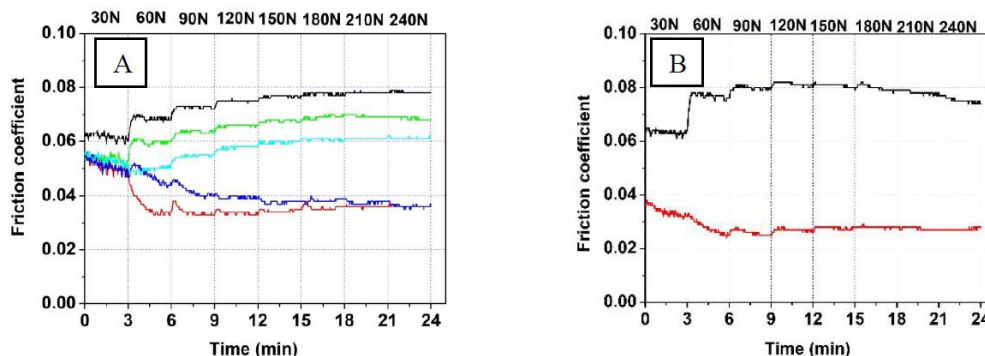


Figure 1. Final friction modifier optimization conducted on the Plint ring and liner test. The ring and liner were taken from the V8 L83 engine. The test was conducted at 100°C, 24Hz speed, step loading from 30N to 240N, with 30N per step. Fig.1A shows un-optimized formulations and Fig. 1B shows the final optimized formulation showing friction level at about 0.025

Table 1. Percent improvement of fuel efficiency of prototype 0W-16 formulations as measured by the vehicle engine chassis dynamometer tests over the baseline 5W-30 GF-5 oil. To improve confidence limit, a total 16 engine tests were run, with the baseline oil ran 8 times to sandwich the candidate oils.

	FTP City cycle mpg	FFE Highway mpg	Combined mpg	US06 mpg
Baseline GF-5 5W-30	23±0.05	36±0.04	27.5±0.04	20±0.14
GW G1 “GF-6A” 0W-20	+1.11%	+0.39%	+0.87%	+1.08%
GW G1 “GF-6B” 0W-16 (A)	+1.33%	+0.47%	+0.99%	+0.33%
GW G2 “GF-6B” 0W-16 (B)	+1.66%	+0.08%	+0.95%	- 0.51%
GW G3 “GF-6B” 0W-16 (C)	+1.05%	+0.92%	+1.16%	-0.15%
Top Tier com. 0W-16 oil	+1.16%	-0.02%	+0.76%	+0.59%

Remainder of Page Intentionally Blank

AVPTA Technology Focus Area 4: Alternative Fuels & Lubricants

Technology Development to Improve Fuel Efficiency through Friction Reduction: Method to Measure, Predict and Relate Friction, Wear and Fuel Economy

**DOE-VTO TFA Lead: Mr. Michael Weismiller
TARDEC TFA Lead: Dr. Jay Dusenbury**

**Principal Investigator:
Dr. Arup Gangopadhyay**

**Affiliation:
Ford Motor Company
2101 Village Road
Dearborn, MI 48121**

**Project Start: Q2FY15
Estimated Completion: Q2FY19**

Objective:

- To develop and demonstrate friction reduction technologies for light, and medium, vehicles that improve fuel efficiency of future vehicles by at least 4% without adverse impacts on engine durability.

Strategic Context:

- Demonstrate a battlefield fuel reduction and reduce the logistics burden.
- Increase power density and energy efficiency resulting in increased vehicle range, endurance and operational tempo, while reducing the number of logistics convoys on the battlefield.
- Increasing fuel efficiency of ground vehicles to reduce life cycle costs.

Accomplishments:

- Completed method development for a single cylinder friction test.
- Completed break-in of five engines; one is a current production engine, four are PTWA coated block engines. Currently the production engine is being set up for performance measurements.

- Completed motored multi-cylinder engine evaluation of production rings against nitride rings. A friction reduction was observed for nitrided rings over production over 1000 to 4000 engine rpm range.
- Completed single cylinder engine testing on one piston skirt coating with cast iron liner.

Introduction:

In lubricant formulations, base oils of various purities are the solvent and additives are the solute. Additives are added to the solution to impart various performance bench marks. Two types of additives are used, those that control the bulk property such as antioxidants, dispersants, detergents, viscosity modifier (VM), and antifoam; and those that control surface properties, such as anti-wear, friction modifiers, corrosion inhibitors, rust inhibitors, and surface deactivators. The bulk property control agents are either neutrally charged or less polar than the surface active agents; the surface active agents have somewhat hierarchical polarity stacking order to arrange themselves against the sliding surfaces. The anti-wear agent has to be able to adsorb and react with the metal surface to perform its anti-wear function, so the decomposition products of the anti-wear agent; ZDDP (zincdialkyl dithio-phosphate) have to react with the surface active sites (3). The formulation has to be delicately balanced to avoid precipitations and adverse additive-additive interactions rendering some or most of the additives non-functioning.

Over the decades, the basic lubricant chemistries have remained the same but modifications to the molecular structures and finer control have been made. The total amount of additives used, however, has grown steadily to accommodate increasing performance demands. Friction modifiers were introduced in the 1980s and a new engine dynamometer test Seq. VI was developed to measure their effectiveness.

Approach:

Ford Motor Company ("Ford") is investigating a novel way to surface texture engine components in Plasma Transferred Wire Arc (PTWA) coating. PTWA utilizes a cathode tube and plasma gas to sputter low carbon steel from a wire feedstock onto a surface. The scope of this effort includes altering the operating voltage and amperage of this apparatus to control the engine component surface porosity level. Highly porous surfaces could better entrain lubricant and hold it locally even under severe conditions.

Ford is also looking into a nanocomposite coating where a hard metal material (metal oxide or metal nitride) is incorporated into an array of a catalyst material. Argonne National Laboratory (ANL) will be involved for this role due to their expertise and knowledge on development and deposition of nanocomposite coatings on pistons and piston rings.

Results and Discussion:

Completed motored friction tests with a production block with cast iron liner with nitrided rings at different temperatures (40°C, 60°C, 100°C, and 120°C) and compared against production rings. Data in Figure 1 demonstrate friction reduction with nitrided rings. However, a slight increase in friction over production rings could be observed at 100°C oil temperature.

Piston ring coatings such as DLC, PVD, and nitrided rings (from Ford supplier) were evaluated against cast iron and high porosity PTWA coating using Plint TE-77 reciprocating machine. Data in Figure 2 shows all ring coatings showed a reduction in coefficient of friction with high porosity PTWA coating compared to production ring and cast iron liner pair. PVD and nitrided rings showed friction reduction primarily in mixed lubrication regime while DLC coating showed friction reduction both under boundary and mixed lubrication regimes. However, more friction reduction was observed under boundary lubrication regime than under mixed regime.

Conclusions:

PTWA coating deposition porosity levels were lower than the target which was believed to be due to different torch characteristics. Porosity analysis of coupons deposited by different torches was completed and found no significant difference. Therefore, the current focus is on identifying suitable honing conditions to reach targeted porosity levels. A design matrix is created to address this in a few phases. In the Phase I, liners have been coated, completed true-up cuts, honed with a particular set of conditions, and liners are being analyzed.

With the development of porous coatings, robust methods are required to assess the quality of the coating's surface. Standard and developed methods can cover a wide range of quality control requirements, such as surface finish, pore size distribution, porosity measurement, etc. Progress has been made to characterize PTWA coatings. A method was developed to use cluster analysis and distribute pores into clusters based on spatial distribution and oil retention.

Friction reductions have been noted through several different coating technologies, including PTWA, nitriding, DLC and plasma vapor deposition. However, the technologies must be tested beyond benchtop tribological testing. Motored engine friction testing is in-progress on the technologies with potential friction benefit as well as vehicle testing to demonstrate the total fuel economy enhancement with the developed technologies.

Figures Start on the Next Page

Figures:

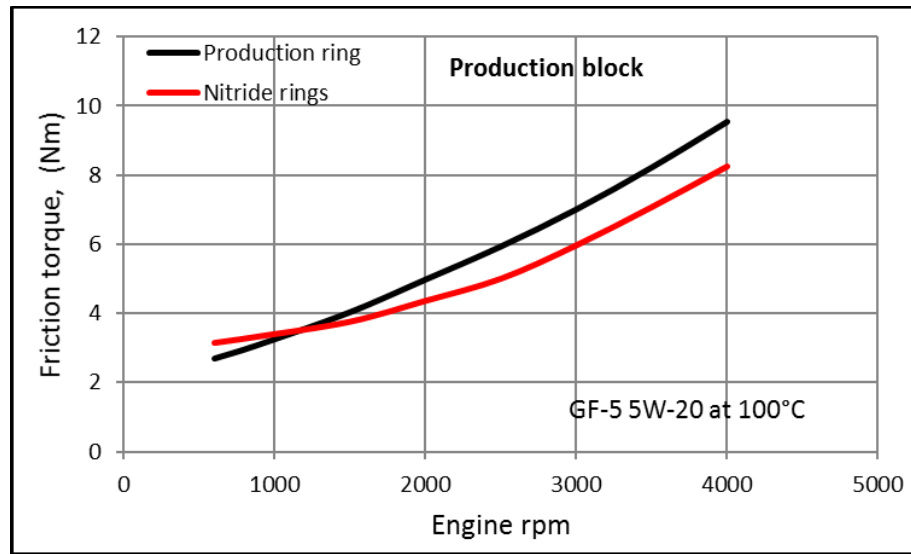


Figure 1. Nitrided piston rings showed reduced friction torque over production rings.

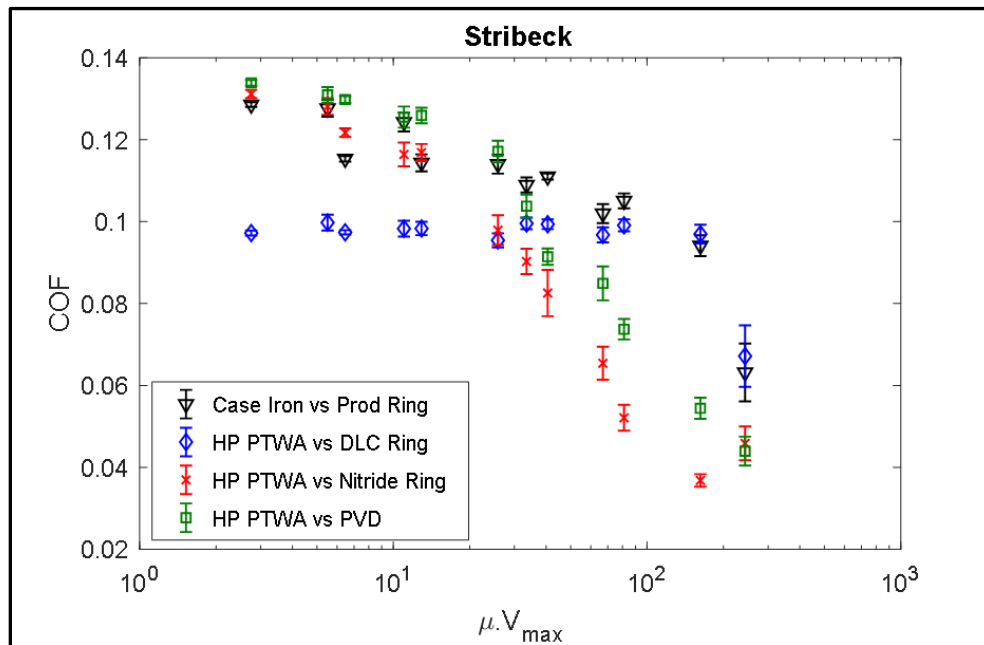


Figure 2. Rings with DLC, PVD coatings, and nitrided rings showed reduction in coefficient of friction in contact with high porosity PTWA coating compared to cast iron and production ring pair.

AVPTA Technology Focus Area 4: Alternative Fuels & Lubricants

Technology Development to Improve Fuel Efficiency through Friction Reduction: Method to Measure, Predict and Relate Friction, Wear and Fuel Economy

**DOE-VTO TFA Lead: Mr. Michael Weismiller
TARDEC TFA Lead: Dr. Jay Dusenbury**

**Principal Investigator:
Dr. Jun Qu**

**Affiliation:
Oak Ridge National Laboratory
1 Bethel Valley Road
Oak Ridge, TN 37831**

**Project Start: Q2FY14
Estimated Completion: Q4FY19**

Objectives:

- To provide the lab-scale fundamental data (open source), model correlations, and full scale verifications to enable more accurate predictions of friction coefficient and wear for a wider range of engines, lubricants, and operating conditions than currently exists.
- To extend the approach to sliding and rolling friction in gears.

Strategic Context:

- Demonstrate a battlefield fuel reduction and reduce the logistics burden.
- Increase power density and energy efficiency resulting in increased vehicle range, endurance and operational tempo, while reducing the number of logistics convoys on the battlefield.
- Increasing fuel efficiency of ground vehicles to reduce life cycle costs.

Accomplishments:

- Ionic liquid additized SAE 0W-12 experimental engine oils were tested in a benchtop tribometer. A lowest friction, highest performance product was identified.
- Both ionic liquid additized formulations outperformed conventional Mobil 1 5W-30 in benchtop tribological testing. However, micro-pitting issues were identified.

OPSEC1890

- Formulation of IL-additized low-viscosity (SAE 0W-16) experimental oils was continued for optimizing the friction and wear performance. A formulation change observed no micropitting when tested.

Introduction:

On 9/28/2013, the ORNL-GM team successfully concluded a 4-year joint project sponsored by DOE Vehicle Technologies Office (VTO) under a Cooperative Research and Development Agreement (CRADA) for developing ionic liquids as next-generation AW additives for engine lubrication. This team made a major breakthrough in developing new groups of oil-miscible ionic liquids (ILs)³⁻⁷, with high thermal stability, ashless, non-corrosiveness, and most importantly effective AW characteristics. Fundamental investigation has correlated the anti-wear and friction reduction mechanisms of IL additives to their physical (absorption) and chemical (tribofilm formation) interactions with the metallic bearing surfaces³⁻⁵. In addition, accelerated catalyst aging tests of the IL suggested potentially less adverse effects on three-way catalysts compared to ZDDP⁶. Working with Lubrizol, the team had developed a prototype IL-additized fully-formulated automotive engine oil (the first ever in the literature). The IL-additized engine oil has low-viscosity (comparable to the pending SAE grade 8) and has demonstrated promising lubricating performance⁶. High-temperature, high-load (HTHL) engine tests showed similar engine wear and oil aging behavior between the IL-additized low-viscosity engine oil and the Mobil 1 5W-30 engine oil⁶. Further, Sequence VID engine efficiency dynamometer tests of this prototype IL-additized engine oil demonstrated an improved fuel economy by 2.01% benchmarked against the Mobil 1 5W-30 engine oil⁶. The initial success of our ionic liquid additive technology has been highlighted at Inside Science⁸ and Green Car Congress⁹, and starts gaining interest from both academia and industry.

Approach:

There are a number of bearing components in an automotive vehicle. The second largest parasitic friction induced energy loss is the 3-5% at the rear axle (next to the 10-12% in the engine) ^{1, 2}, and therefore is identified as the next application for the IL additive technology. GM's modeling predicts a potential recovery of 0.75-1.5% vehicle fuel economy by using a lower viscosity oil. This study proposes to apply ionic liquids to mitigate the challenge of wear protection induced by the reduced oil viscosity. The bearing interface for the rear axle is very different from that in the engine, therefore the IL chemistry will be tailored to better handle the much higher contact stress and longer oil service life required for the rear axle lubricant. This study will also provide us the opportunity to gain deeper fundamental understanding of ILs' anti-wear mechanism such as the roles of the cations and anions, and their advantages in surface absorption and tribofilm formation compared to conventional neutral AW additives. Such understanding will strengthen the scientific basis that we have been building for further material optimization and product development.

ORNL will be leading this joint project with main responsibilities for IL design and synthesis, tribological bench tests, tribofilm characterizations, lubrication modeling, and emission analysis. GM will work with Lubrizol to formulate IL-additized engine and rear axle lubricants. GM will

conduct complementary tribological bench tests, multi-cylinder engine dynamometer tests, and vehicle tests.

Results and Discussion:

After creating, testing, and analyzing more than three dozen formulations, we are getting close to finalizing the engine oil formulation as shown in Figure 1. The final coefficient of friction (COF) and wear volume by the end of the 20 km of ball-on-flat reciprocating sliding tests (on a Plint TE-77 tribometer at 100 N, 10 Hz, and 10 mm stroke) of several top candidates are compared with those of the commercial Mobil 1 SAE 0W-20, as shown in Figure 2.) Note that results at 100 °C is considered as the most important because the engine oil's nominal operation temperature is 80-120 °C. Key observations are:

- Mobil 1 SAE 0W-20 produced moderate micro-pitting at three temperatures. While the friction behavior seemed insensitive to the oil temperature (in a narrow range of 0.07-0.08), the wear volume was increased along with the temperature presumably due to the reduced oil viscosity;
- CPO 312+IL seemed to provide the overall best wear protection considering all three temperatures with no micro-pitting at all (25-80% lower wear than Mobil 1 SAE 0W-20), but had relatively high friction coefficient, particularly 0.112 at 100 °C (30% higher friction than Mobil 1 SAE 0W-20);
- CPO 316+IL was the best performer at 100 °C with low COF (0.043) and low wear (0.05 mm³) and no micro-pitting (45% lower friction and 75% lower wear compared to Mobil 1 SAE 0W-20), however experienced severe pitting at room temperature (RT) causing very high wear (0.67 mm³);
- CPO 320+IL, in contrast, had no pitting issue at RT but suffered the worst pitting at 100 °C with material loss more than 1 mm³ (5X higher than that of Mobil 1 SAE 0W-20). It also lost its low friction feature after 10 km sliding at 150 °C;
- CPO 334+IL shared similarities with CPO 316+IL: excellent performance at 100 °C with low COF (0.05) and low wear (0.04 mm³) and little micro-pitting (35% lower friction and 80% lower wear compared to Mobil 1 SAE 0W-20), but had moderate micro-pitting at RT, not as bad though. The wear volume 0.26 mm³ of CPO 334+IL at RT is in the level as that (0.21-0.24 mm³) of Mobil 1 SAE 0W-20 at elevated temperature, which is acceptable especially considering that an engine oil is only at RT for a very short time during operation.

Thus, CPO 334+IL has been identified to be the top candidate in terms of both producing low boundary friction and low wear.

Conclusions:

Dozens of IL additized lubricants were produced through this project. The project is progressing on schedule with the candidates that have the most promise, showing a significant friction reduction without compromising wear performance. Several other formulations observed micro-pitting wear when tested in high frequency reciprocating lubricant testing, which was alarming.

However, further optimization of various additives in the lubricant formulation produced viable candidates for future engine testing.

Figures:

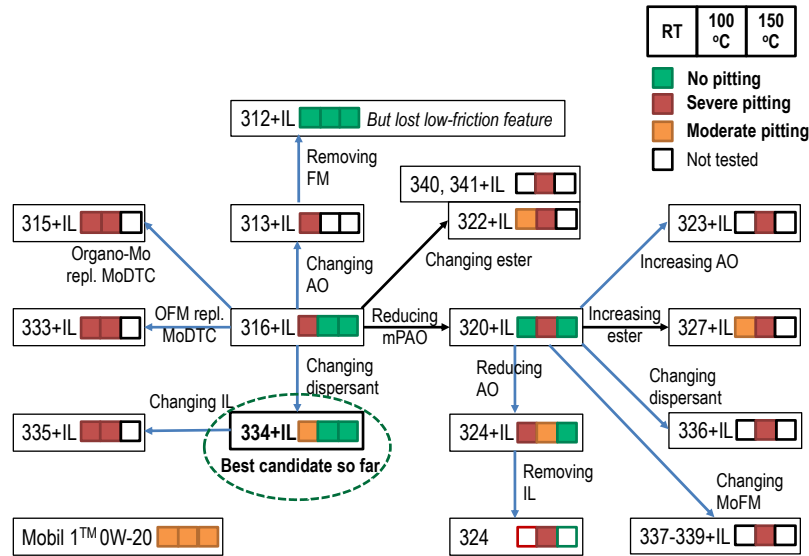


Figure 1. Flow chart showing the process of tailoring the base oil and additive package for low boundary friction, strong wear protection, and minimal micropitting.

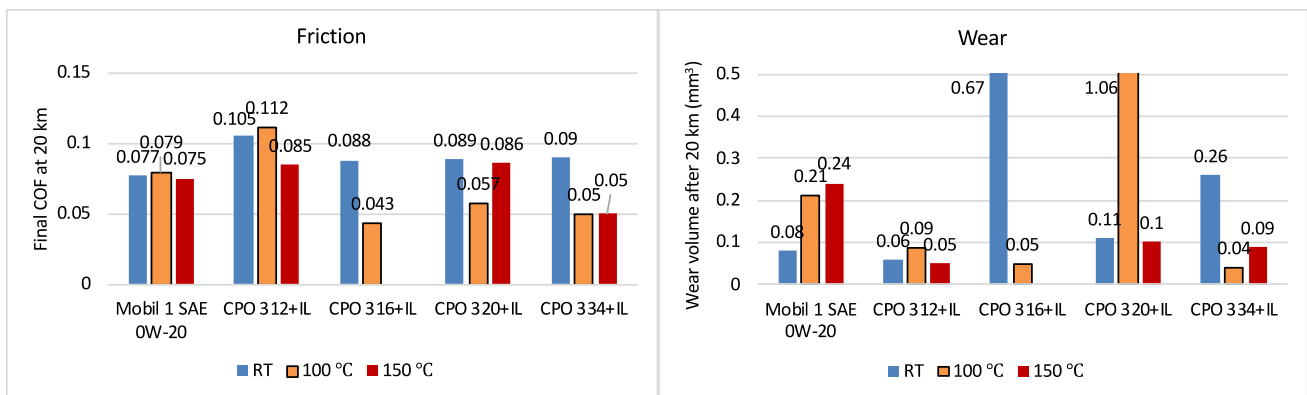


Figure 2. Comparison of boundary friction and wear behavior of top candidate IL-additized low-viscosity (SAE 0W-16) experimental oils and the commercial Mobil 1 SAE 0W-20 engine oil.

AVPTA Technology Focus Area 4: Alternative Fuels & Lubricants

Technology Development to Improve Fuel Efficiency through Friction Reduction: Method to Measure, Predict and Relate Friction, Wear and Fuel Economy

**DOE-VTO TFA Lead: Mr. Michael Weismiller
TARDEC TFA Lead: Dr. Jay Dusenbury**

**Principal Investigator:
Dr. Steve Gravante**

**Affiliation:
Ricardo, Inc.
40000 Ricardo Drive
VanBuren Township, MI 48111**

**Project Start: Q2FY14
Project Terminated**

Objectives:

- To provide the lab-scale fundamental data (open source), model correlations, and full scale verifications to enable more accurate predictions of friction coefficient and wear for a wider range of engines, lubricants, and operating conditions than currently exists.
- To extend the approach to sliding and rolling friction in gears.

Strategic Context:

- Demonstrate a battlefield fuel reduction and reduce the logistics burden.
- Increase power density and energy efficiency resulting in increased vehicle range, endurance and operational tempo, while reducing the number of logistics convoys on the battlefield.
- Increasing fuel efficiency of ground vehicles to reduce life cycle costs.

Accomplishments:

- Ricardo did not produce its cost share for Q4FY17. Project was terminated.

Introduction:

Friction forces and wear performance in engines and other driveline components can be calculated from equations that capture the understanding of the fundamental physics involved. However, accuracy of the results is dependent on measurement or estimation of the friction coefficient used in the calculations. For contacting surfaces in any component system (piston ring or skirt and liner; bearings; gears, etc.) the friction coefficient is a function of lubricant viscosity, relative speed, surface properties and load, which is captured in a Stribeck curve.

For a given set of operating conditions the curve provides a friction coefficient which can be used to calculate FMEP (Friction Mean Effective Pressure). FMEP is a quantification of losses due to friction during engine operation. It combines all types of friction losses from asperity or boundary friction (caused by metal to metal contact) to hydrodynamic friction (caused by viscous losses) and mixed regimes between. Once FMEP is quantified, whether predicted or measured, it can be used to calculate friction impacts on fuel economy.

Approach:

In this program Ricardo will use existing computer models to specify relevant Stribeck conditions (speed and load) for light duty and heavy duty OEM engines (one or more of each). ANL and EMA will make careful measurements of friction and wear using high-precision lab-scale test rigs as a function of surface and lubricant properties over a range of operating temperatures, loads, and speeds typical of engine (or other) components. The data generated will be used, with some processing, as input to Ricardo's codes to improve correlations between model FMEP predictions and measurements of FMEP in engine or driveline tests.

FMEP is equal to the difference between IMEP (Indicated Mean Effective Pressure), which is the theoretical amount of power the engine can produce from the amount of fuel burned, and BMEP (Brake Mean Effective Pressure), which is the amount of power delivered by the crankshaft. Because FMEP is the relatively small difference between two relatively large numbers, accuracy can be poor when determining FMEP by calculating IMEP and subtracting measured BMEP. It can be measured directly in motored tests, but they lack some of the physical realities (temperatures, combustion forces, etc.) of fired engines. Methods to calculate FMEP from well verified models are needed.

The "technology" developed in this project will be FMEP maps as a function of load and speed which, when coupled with IMEP, can be used with suitable weighting factors to predict fuel consumption for any user-specified driving cycle. The lab-scale rig data will be used to predict wear loads (cycle averaged as a function of speed and load) to compare with wear-load-sliding distance calculations. Lubricant effects will be evaluated in terms of both friction losses and wear performance. The models will be used to predict fuel savings and wear, as validated with engine dyno tests by Ricardo and Navistar using an off-the-shelf high viscosity lubricant and a friction-modified low-viscosity synthetic lubricant.

Results and Discussion:

Ricardo did not produce its cost share for Q4FY17. Project was terminated.

Conclusions:

Ricardo did not produce its cost share for Q4FY17. Project was terminated.

Remainder of Page Intentionally Blank

This Page is Intentionally Blank

AVPTA Technology Focus Area 4: Alternate Fuels & Lubricants

Polyalkylene Glycol Based Lubricant for Light and Medium Duty Vehicle Axles

DOE-VTO TFA Lead: Dr. Michael Weismiller
TARDEC TFA Lead: Dr. Jay Dusenbury

Principal Investigator(s):

Dr. Arup Gangopadhyay

Mr. Chintan Ved

Affiliation:

Ford Motor Company

Ford Research and Innovation Center

2101 Village Road, MD 3629, Room 3217

Dearborn, MI 48121

Project Start: Q2FY13

Project Completion: Q4FY18

Objective:

- Develop novel axle lubricant formulation that improves vehicle fuel efficiency by at least 2% without adverse impacts on vehicle performance or durability.

Strategic Context:

- Demonstrate a battlefield fuel reduction and reduce the logistics burden.
- Increase power density and energy efficiency resulting in increased vehicle range, endurance and operational tempo, while reducing the number of logistics convoys on the battlefield.
- Increasing fuel efficiency of ground vehicles to reduce life cycle costs.

Accomplishments:

- Developed a new co-base stock formulation (i.e., mixture of petroleum base oil and oil soluble PAG (OSP)) which uses more environmentally preferable OSP
- New co-base stock formulation passes industry standard performance tests including ASTM D5704 (Oxidation and Thermal Stability), ASTM D6121 (Low Speed/High Torque Load Carrying Capacity), ASTM D7038 (Corrosion Resistance) and ASTM D7452 (High Speed/Shock Loading – Load Carrying Capacity)

OPSEC1890

Introduction:

The axle lubricant (SAE 75W-140) which has been widely used in the market place over the last few years is primarily formulated from polyalphaolefin (PAO) base stock. This investigation focused on polyalkylene glycol (PAG) base stock which is significantly different chemically from PAO. Due to the polar nature of PAG it is hypothesized that it can adsorb relatively easily on contacting surfaces resulting in significant friction reduction and improved fuel economy. Axle efficiency is generally quite high in the high torque range but it can be quite low in the low torque range representative of EPA drive cycles. Therefore, the focus of this project is primarily on improving axle efficiency in the low torque range while maintaining all durability attributes (i.e., no adverse impacts on vehicle performance or durability).

Approach:

Ford Motor Company ("Ford"), in cooperation with Dow Chemical Company and Argonne National Lab developed a polyalkylene glycol (PAG) based axle oil, taking advantage of PAG's natural lubricity, high viscosity index, and excellent oxidation and shear stability. The research project followed a structured approach beginning with lubricant formulations by varying base oil chemistry and additive components followed by physical property characterization. Lubricant performance evaluations started with simple laboratory friction, wear, oxidation, and corrosion tests which guided into identification of performance areas requiring improvements. This required an iterative lubricant reformulation. Once a few acceptable formulations were identified, they were evaluated in more complex component tests including ASTM tests (L-37 - load carrying capacity under low speed and high torque, L42 – load carrying properties under high speed and shock loading, L-60 - thermal and oxidative stability, and L-33-1 moisture corrosion resistance).

Results and Discussion:

Two issues were observed following L-42 tests on candidate formulated with PAG base stock; toxicological and foaming. This required reformulation and repeating all ASTM tests. During repeat tests it was observed that some of the additives precipitated out of solution. Since it was discovered quite late in the program, the team changed direction of the program to focus on an oil soluble PAG as a co-basestock (15-30%) with mineral oil used in a commercial formulation (SAE 75W-85). This formulation strategy helped passing all ASTM tests. This was followed by Ford proprietary gear wear (see Figure 1), axle efficiency, and chassis roll dynamometer tests for fuel economy evaluations (see Figure 2). Axle efficiency was improved up to 7% when a full PAG formulation was used but no such significant improvement was observed with PAG as co-basestock formulation. Chassis roll fuel economy improved by 1.9% with PAG co-basestock formulation (conforming to SAE 75W-85) compared to SAE 75W-140 baseline. However, it was observed that the improvement is mostly due to reduced viscosity of candidate formulation when compared to a full mineral oil based SAE 75W-85 formulation. PAG as co-basestock also exhibited unacceptable wear in proprietary gear wear test.

This investigation highlighted challenges with PAG formulations including identification of additive components that stay in PAG solution for intended duration, and meeting component durability requirement.

Conclusions:

Several bench tests were developed to screen formulations for performance in the L-37 test. Both the pin-on-disk and ball-on-disk methods were able to distinguish between passing and failing L-37 tests. However, due to the limited number of tests run, no firm correlation between the bench tests and performance in the L-37 test could be established. The oxidation test used to screen formulations for performance in the L-60 test appeared to be somewhat predictive for PAG based lubricants, less so for lubricants consisting of blends of oil soluble PAGs and mineral oils.

Development of a PAG-based gear lubricant meeting all requirements of API GL-5 gear lubricants was not successful because of the inability to pass L-42 test. This is primarily due to the limited solubility of available additive component(s) in the PAG.

Formulations with PAG as a co-basestock with mineral oil conforming to SAE 75W-85 (AU6615-F) passed all GL-5 performance tests. There was up to 7% axle efficiency improvement compared to SAE 75W-140 reference oil but no significant improvement compared to SAE 75W-85 reference oil. Chassis roll dynamometer test showed 1.9%, 1.7%, and 1.8% fuel economy improvement compared to SAE 75W-140 oil in city, highway, and combined metro/highway cycles respectively. However, no significant improvement was observed compared to a full mineral oil based SAE 75W-85.

Formulations with PAG as a co-basestock with mineral conforming to SAE 75W-85 exhibited unacceptable gear durability in proprietary Ford tests.

Figures Start on the Next Page

Figures:

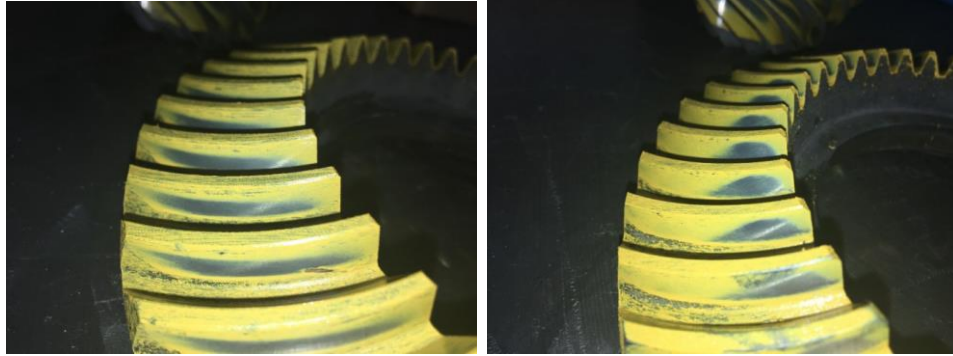


Figure 1. Results from Ford proprietary test. Left: Gear mesh pattern on post test ring gear tested with co-basestock formulation. This post test pattern represents typical gear wear hardware and denoted to be acceptable. Right: Gear mesh pattern on post test ring gear from second axle tested with co-base oil formulation. The post test pattern indicates unacceptable wear, exhibiting a contact that is inconsistent over the full land of the gear teeth and resulting in NVH issues in a vehicle.

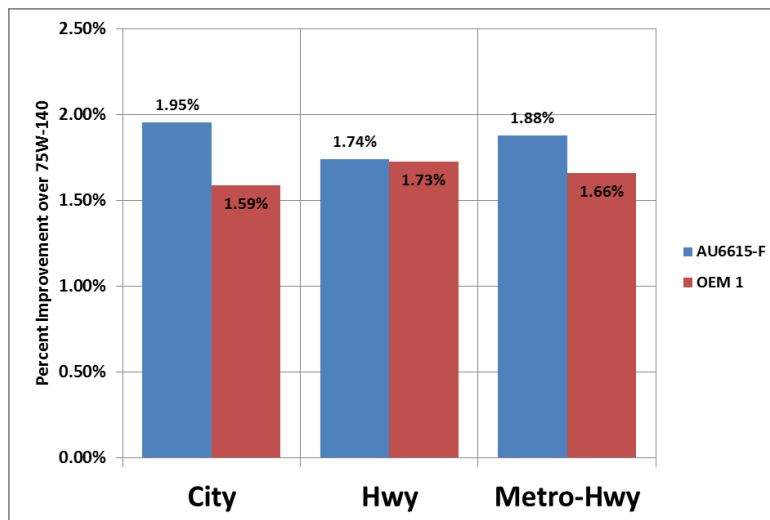


Figure 2. Percent fuel economy improvement over 75W-140 for co-basestock formulation AU6615-F and other reference fluid OEM 1 (75W-85). Percent improvement presented for City driving, Highway (Hwy) driving, and Metro-Highway (Metro-Hwy) categories.

Remainder of Page Intentionally Blank

AVPTA Technology Focus Area 4: Alternative Fuels & Lubricants

A Novel Lubricant Formulation Scheme for 2% Fuel Efficiency Improvement

**DOE-VTO TFA Lead: Dr. Michael Weismiller
TARDEC TFA Lead: Dr. Jay Dusenbury**

**Principal Investigator(s):
Dr. Q. J. Wang**

**Affiliation:
Northwestern University
2145 Sheridan Road
Tech A219
Evanston, IL 60208-3109**

**Project Start: Q2FY13
Estimated Completion: Q4FY18**

Objectives:

- Develop novel lubricant formulation that reduces boundary friction and promotes temporary shear-thinning when viscous losses are the dominate mechanism for energy dissipation.
- Improve vehicle fuel efficiency by at least 2% without adverse impacts on vehicle performance or durability.

Strategic Context:

- Demonstrate a battlefield fuel reduction and reduce the logistics burden.
- Increase power density and energy efficiency resulting in increased vehicle range, endurance and operational tempo, while reducing the number of logistics convoys on the battlefield.
- Increasing fuel efficiency of ground vehicles to reduce life cycle costs.

Accomplishments:

- Successful synthesis of a di-block copolymer viscosity modifier
- Molecular dynamics simulation of friction modifiers (FMs) in the presence of base oil
- Hot-stop friction testing of new cyclen friction modifiers result in reduced friction compared to fully formulated 5W-30 engine oil

- Slide/roll and high temperature reciprocating testing demonstrated the ability of cyclen friction modifiers to reduce boundary friction without affecting hydrodynamic lubrication
- Oil soluble PAO-PiDMA di-block viscosity modifiers (VMs) developed
- Completed testing of di-block viscosity modifiers with varying degrees of coiled structure
- Completed molecular dynamic simulations on the effects of chain length on the performance of the new friction modifiers.

Introduction:

This project aims to (1) reduce friction due to asperity rubbing in start-up and low-speed operations during which boundary friction controls energy dissipation, and (2) temporarily reduce the lubricant viscosity (temporary shear-thinning) in medium- to high-speed cruise operations during which viscous loss is the dominant mechanism for energy dissipation. The proposed research is expected to result not only in a 2% fuel efficiency improvement, but also enhanced performance of the powertrain/drivetrain components.

Achieving more than 2% fuel efficiency improvement of light and medium vehicles requires significant friction reduction in the powertrain and drivetrain systems; if by reducing boundary friction alone, this requires at least a 30% friction reduction. Better friction modifiers (FMs) are needed as a component to achieve this boundary lubrication goal. The frictional loss due to high viscous shear at high speeds cannot be simply tackled by using oil of low viscosity because this will raise the friction at low speeds. We need a chemically and mechanically stable viscosity modifier (VM) that makes the lubricant less viscous only at high shear rates. Many lubricants undergo some shear-thinning in the contact interface, resulting in lower friction than expected from Newtonian flow assumptions. A key problem to solve is to have a modified lubricant that only responds to high shear rate via molecular deformation, not scission. More friction reduction mechanisms should also be included, such as using nanoparticles; hexagonal boron nitride (h-BN or α -BN) and boron oxide (B_2O_3) are two of well-known solid lubricants, which can be excellent material choices for the nanoparticles.

Approach:

The fuel efficiency goal has to be accomplished by reducing friction in the entire operation regime. The S-and-P-free heterocyclic FMs and the shear-thinning VMs should be able to significantly lower friction in boundary (low speed) and hydrodynamic (high speed) lubrication regimes, respectively. The nanoparticle-based additives will facilitate reducing extra friction and wear. The tasks include synthesizing “designer” additives, characterizing their properties at conditions comparable to those in real-world applications, modeling the frictional and viscosity behaviors for design optimization, and testing their friction reduction capability. This project is being conducted collaboratively by Northwestern University (NU) and the Argonne National Lab (ANL), and is supported by collaborative industries. All additives were synthesized or prepared at the NU’s chemistry laboratory, tested at the tribology laboratories at NU and ANL.

Results and Discussion:

Three generations of organic friction modifiers (FMs) – hexahydrotriazines, triazines and cyclens – were synthesized, characterized, and evaluated as sulfur- and phosphorous-free lubricant additives for reducing boundary-lubrication (BL) friction.

Generation I hexahydrotriazine has poor thermal and chemical stability and were not further studied in this project.

Generation II triazine and **Generation III** cyclen have greater thermal and chemical stability. These additives are all stable to above 300 °C, making them viable options as FM additives (see Figure 1). Generation II and III additives were capable of reducing sliding friction dramatically (specifically cyclen achieve more than 70 % friction reduction in the boundary lubrication regime) from 25 °C to 200 °C. The cyclen FMs also produce high levels of friction reduction in speed ramp-up tests and speed ramp-down tests at 25 °C and 200 °C (see Figure 2). Similar results were obtained in the 50 % slide-to-roll ratio tests. C18Cyc added in both PAO4 oil and formulated 5W30 engine oil leads to consistent friction reduction at elevated temperature in reciprocating test. Among the three generations of heterocyclic FMs developed in this research and commercial formulations, cyclen derivatives were found to provide the best performance in the boundary lubrication regime in terms of friction performance and stability. Ultra-thin lubricant film measurements showed that the alkyl-cyclen FM additives in PAO4 oils resulted in a significant enhancement of boundary-lubrication film at elevated temperature over a wide range of speed (see Figure 3). Molecular dynamics simulations demonstrate that, compared to the conventional alkylamine FMs, the heterocyclic FM molecules lead to the increased interaction energy, decreased surface molecular diffusivity, and well-maintained surface coverage at high temperature. The prolonged surface residence time and reduced desorption rate are the critical and fundamental causes for the boundary lubrication film enhancement and the low-friction behavior of the alkyl-cyclen FM additives. The surface adsorption of the new alkyl-cyclen FM can be significantly promoted by preheating the FM-containing lubricants to provide the needed thermal energy for adsorption. A surface treatment method was applied for a DLC coating, and improved wettability was confirmed. Compared to the commercial FM, the heterocyclic C18Cyc FM molecules were proven to be more effective in surface adsorption and friction reduction on the relatively inert DLC surface. In addition to the neat cyclen FM, wear performance was evaluated for a boron oxide (B₂O₃), 30 nm nanoparticle additive with optimized functionalization. The mixture of surface functionalized nanoparticles with a cyclen FM shown to improve the overall tribological performance even further.

Group 10 (Ni, Pd), organolanthanide, and metallocene polymerization catalysts were evaluated in synthesizing the di-block copolymer viscosity modifiers (VMs) with appreciable yields. The shear-thinning performance of the di-block copolymer VMs were evaluated by taking block ratio effect and concentration effect into considerations. Comparing to the significantly larger OCP molecules, the smaller di-block VM molecules demonstrated a comparable or better shear-thinning performance (see Figure 4). A final di-block copolymer VM formulation was prepared and tested. It resulted in improved

hydrodynamic lubrication performance in comparison with representative commercially available oil formulations. A basic understanding of the viscosity modification process was established by measuring the intrinsic viscosity, hydrodynamic diameter, and film thickness. Immiscibility, reduced diffusivity, and the corresponding shearing-induced conformational changes of the polymeric VM molecules appear to dominate viscosity modification for improved hydrodynamic lubrication.

Conclusions:

- Northwestern University has successfully synthesized novel friction modifiers and a novel viscosity modifier. Bench testing and molecular dynamic simulations have been completed to better understand the mechanisms of these additives. A new oil formulation involving the heterocyclic C18Cyc FM and the di-block VM was evaluated in a wide range of loads, speeds, and temperatures, and improved anti-friction property was demonstrated repeatedly for the new formulation.

Figures:

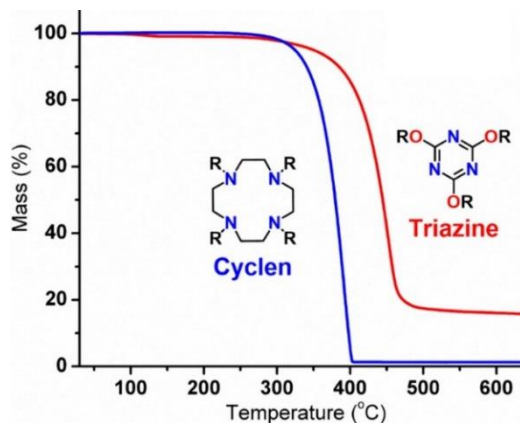


Figure 1. TGA data of thermally stable 4C6PTriaz and C12Cyc; they are respectively selected as representative second generation triazine compounds and third generation cyclen derivatives.

Figures Continue on the Next Page

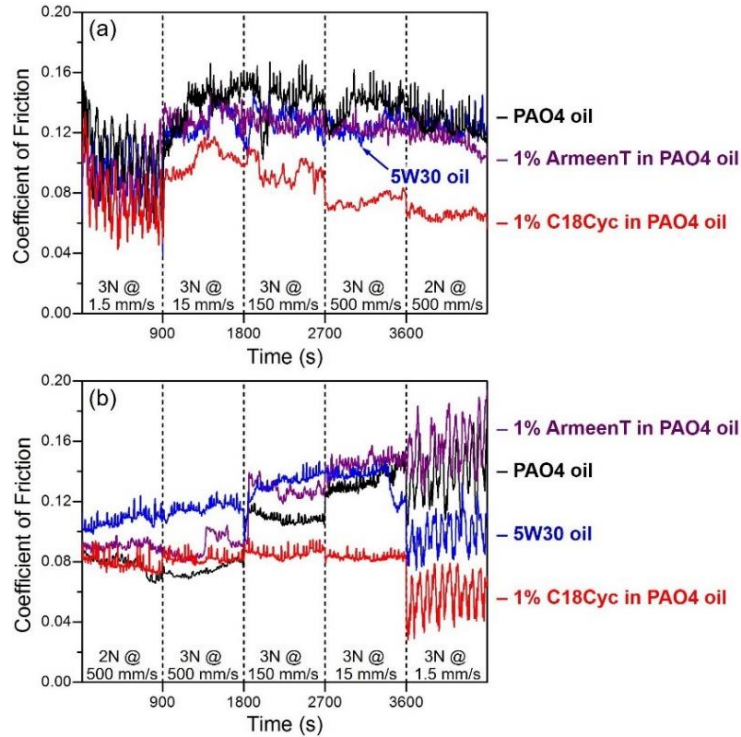


Figure 2. (a) Speed ramp-up and (b) ramp-down pin-on-disk tests using different lubricants at 200° C.

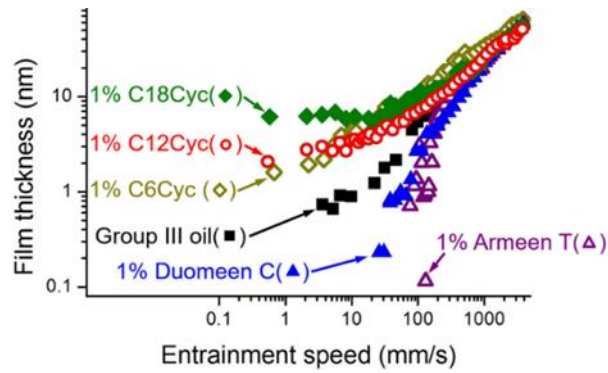


Figure 3. Lubricant film thickness versus entrainment speed for Group III oil with addition of different FMs at 125° C.

Figures Continue on the Next Page

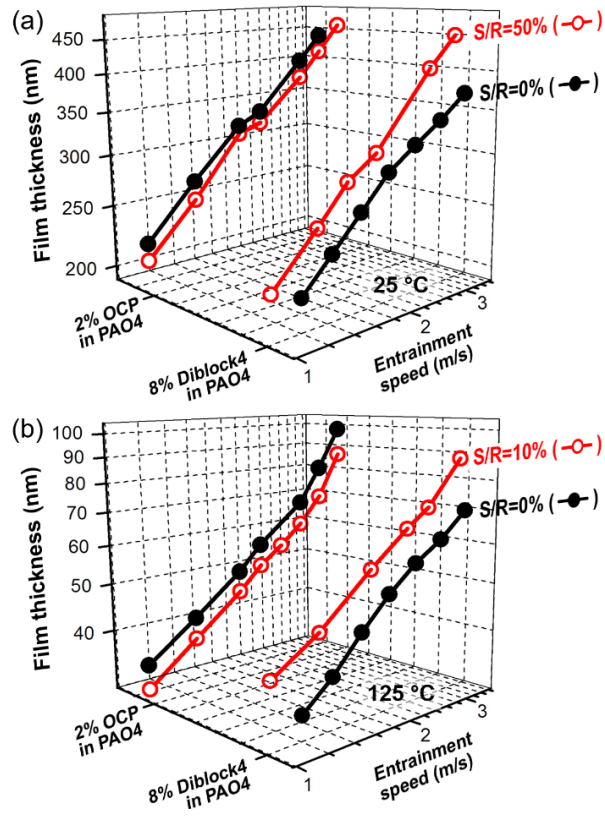


Figure 4. Comparisons of the lubricant film thickness measured at 25 °C (a) and 125 °C (b) under different S/R ratios.

Remainder of Page Intentionally Blank

AVPTA Technology Focus Area 4: Alternative Fuels & Lubricants

Improved Fuel Economy through Formulation Design and Modeling

**DOE-VTO TFA Lead: Dr. Michael Weismiller
TARDEC TFA Lead: Dr. Jay Dusenbury**

**Principal Investigator(s):
Dr. Gefei Wu**

**Affiliation:
Valvoline, a Division of Ashland Inc.
3499 Blazer Parkway
Lexington, KY 40509-1850**

**Project Start: Q2FY13
Estimated Completion: Q2FY18**

Objectives:

- Develop fuel efficient engine, transmission and axle lubricants and verify using SAE J1321 testing
- Improve vehicle fuel efficiency by at least 2% without adverse impacts on vehicle performance or durability.

Strategic Context:

- Demonstrate a battlefield fuel reduction and reduce the logistics burden.
- Increase power density and energy efficiency resulting in increased vehicle range, endurance and operational tempo, while reducing the number of logistics convoys on the battlefield.
- Increasing fuel efficiency of ground vehicles to reduce life cycle costs.

Accomplishments:

- Completed SAE J1321 – Fuel Consumption Test Procedure - Type II testing of three engine oils, three axle oils and two transmission oils

Introduction:

This project focused on developing lubricant formulations that are expected to improve the fuel efficiency of medium-duty, commercial and military vehicles by at least 2% (improvement based on comparative results from engine dynamometer testing, chassis dynamometer testing or test

OPSEC1890

track, e.g., SAE J1321) without adverse impacts on vehicle performance or durability. This was accomplished through engine, transmission and axle lubricant formulation design, modeling and testing.

Approach:

Valvoline applied its extensive experience in the formulation of engine, transmission and axle lubricants to develop improved fuel economy through the optimization of engine, transmission and axle lubricants using advanced base oils and additive technology, including a bio-based base oil, and industry best practices.

Results and Discussion:

In previous years Valvoline used its experience developing heavy-duty diesel engine oils, transmission, and axle lubricants to formulate state-of-the-art candidate lubricants at lower viscosity and using advanced friction modifiers. They conducted bench scale and physical and chemical testing and input these results into computer models developed to predict fuel economy benefits. In this final year of their project they focused on validating their candidate fluids in industry standardized testing, including fuel economy testing in accordance with SAE J1321. Valvoline developed a 5W-30 and 5W-20 heavy-duty diesel engine oil which, in engine dynamometer testing, resulted in a fuel economy improvement over a 15W-40 baseline of 1.6% and 1.8%, respectively. For axle lubricants, Valvoline developed two candidate 75W-90 grade oils and conducted axle efficiency testing with resulting efficiency improvements between 0.63 and 1.36% under demanding conditions. For the transmission Valvoline developed two candidate formulations meant to improve upon a baseline TES-295 fluid. J1321 fuel consumption testing was conducted by the Transportation Research Center (East Liberty, OH) using four class-6 trucks and seven test segments. Four different candidate oil combinations led to fuel economy benefits greater than 2% with the greatest benefit being 2.58%. Candidate engine and gear oils resulted in the greatest improvement above baseline fluids.

Due to the limited acceptance of low viscosity lubricants in heavy duty diesel engines, Valvoline encountered difficulty in locating a fleet which was willing to perform the field test proposed by the project in the Budget Period 3. Hence Valvoline requested the project's Budget Period 3 to be terminated, forfeiting the remaining DOE funds.

Conclusions:

By judiciously selecting base oil and additives Valvoline developed candidate engine, transmission, and axle oils which resulted in significant improvements in fuel economy that were validated in both dynamometer tests and full vehicle testing. The best combination of engine, transmission and axle candidate lubricants improved fuel economy when tested in accordance with SAE J1321 test standard by 2.38% (see Figure 1).

Figure is on the Next Page

OPSEC1890

Figure:

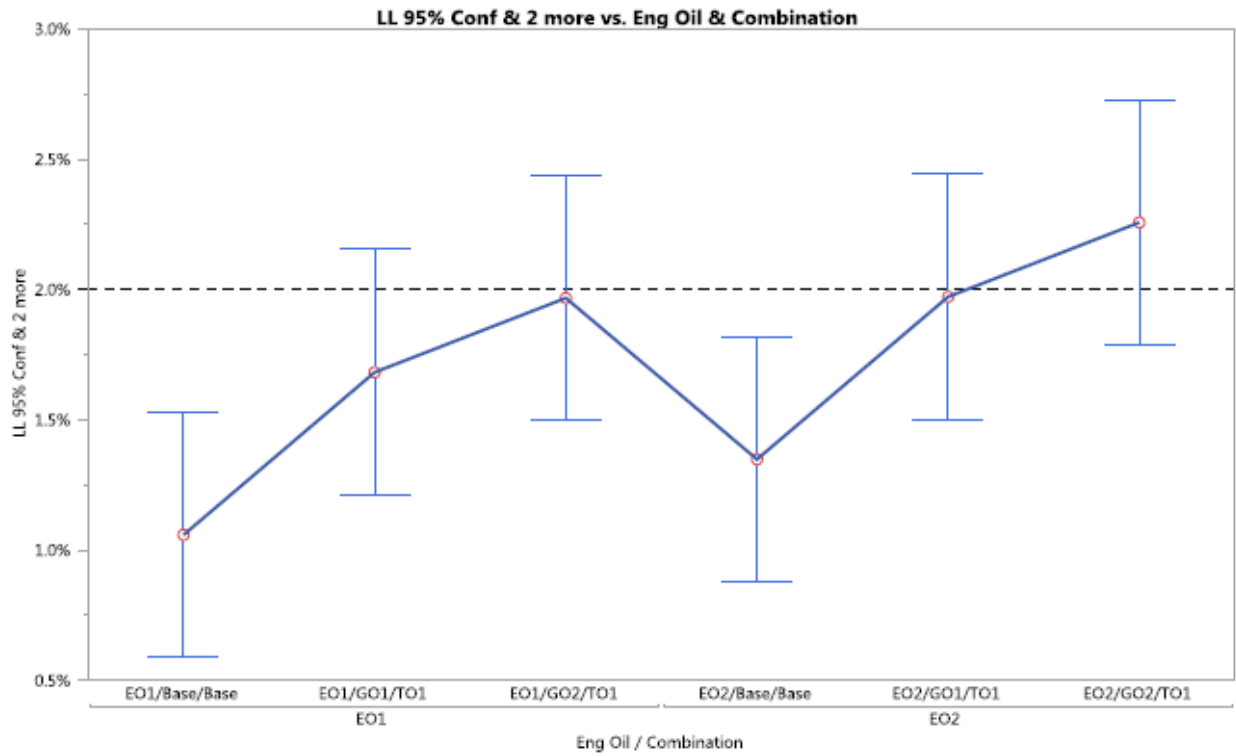


**Figure 1. Fuel economy improvements for various candidate oil combinations.
Note that EO1 = Candidate engine oil 1, EO2 = Candidate engine oil 2,
GO1 = Candidate gear oil 1, GO2 = Candidate gear oil 2,
TO1 = Candidate transmission oil 1, and Base = Baseline engine/gear/transmission oil.**

Remainder of Page Intentionally Blank

This Page is Intentionally Blank

AVPTA Technology Focus Area 4 Adjunct: Tire Efficiency

Improved Tire Efficiency through Elastomeric Polymers Enhanced with Carbon-based Nanostructured Materials

DOE-VTO TFA Lead: Gurpreet Singh
TARDEC TFA Lead: Dr. James Dusenbury

Principal Investigator:
Dr. Georgios Polyzos
Oak Ridge National Laboratory (ORNL)
Oak Ridge TN 37831-6054

Project Start: Q1FY15
Estimated Completion: Q1FY19

Objectives:

- Reduce hysteretic losses for reduction of rolling resistance
- Sharply enhance the wear resistance of the tire without compromising its viscoelastic properties.
- To uniformly disperse well-defined structures of self-assembled graphene layers in the rubber matrix
- 4% improvement in fuel efficiency

Strategic Context:

- Demonstrate a battlefield fuel reduction and reduce the logistics burden
- Increase Power Density and Energy Efficiency resulting in increased vehicle range, endurance and operational tempo.
- Increase fuel efficiency of ground vehicles to Reduce Life Cycle Costs
- Incorporate into Tactical Vehicles currently using Commercial Tires
- Leverage technology to develop for military specific tires

Accomplishments:

- Mixing techniques were developed to synthesize composite elastomers.
- A 10-fold increase in Modulus values were achieved for certain graphene composite elements.
- The graphene filler improved the wear resistance of the composite elastomer.
- Sulfur (S) groups were chemically bonded on the surface of graphene oxide (GO) filler material.

OPSEC1890

- Nano-Indentation measurements were performed on composite elastomers.

Introduction:

In materials science of elastomers the influence of manufactured nanomaterial filler particles is of utmost significance for the performance of innovative rubber products, i.e., passenger and commercial tires with ultralow rolling resistance but high traction. Advances in both performance areas are imperative for the development of improved tire efficiency to meet Department of Energy's (DOE) fuel consumption reduction target of 4%, all while maintaining or improving wear characteristics of the tire. The unique geometrical configuration of the graphene fillers makes them the most promising carbon based fillers for breakthrough reduction of the rolling resistance.

Approach:

Graphene oxide (GO) nanoplatelets were functionalized with organic coupling agents. The chemical composition of the fillers were investigated. The nanoplatelets were exfoliated in styrene-butadiene-rubber (SBR) and styrene-butadiene-styrene (SBS) elastomers. Mixing procedures were developed in order to achieve good dispersion of the filler material in the elastomers. Collaboration was conducted with a major tire manufacturer. The mechanical and abrasion resistance properties of the synthesized elastomers were investigated.

Results and Discussion:

To achieve improvement of the vulcanization of the tire elastomers, sulfur (S) groups on the graphene oxide nanoplatelets were introduced by chemically attaching organic coupling agents based on sulfur. The filler material was reduced with hydrazine to decrease the oxygen content of the surface of the fillers and enhance mechanical performance. X-ray photoelectron spectroscopy (XPS) and X-ray Diffraction (XRD) techniques were used to characterize the surface chemistry of the fillers. XPS was used to study the covalent bond formation between the organic coupling agents and the graphene oxide. See Figures 1 and 2. The coupling agent was successfully covalently bonded to the graphene oxide surface.

The graphene oxide fillers were dispersed in the styrene-butadiene- styrene (SBS) elastomer. The mixing was performed in solvent with ultrasonic agitation to achieve good dispersion. The maximum Modulus improvement was approximately one order of magnitude. Abrasion wear experiments were performed on the SBS polymer with and without the graphene oxide filler. Scanning electron microscopy and atomic force microscopy techniques were used to characterize the differences. The unfilled SBS surface was abraded significantly, whereas the SBS with graphene oxide abrasion was minimal.

Remainder of Page Intentionally Blank

Conclusions:

The optimum dispersion of the filler material in the elastomer was achieved using liquid mixing in solvent followed by ultrasonic agitation. The maximum Modulus improvement was approximately one order of magnitude according to nano-indentation and tensile measurements. The graphene fillers improved the wear resistance of the polymer.

References:

- [1] J.A. Carpenter Jr., J. Gibbs, A.A. Pesaran, L.D. Marlina, K. Kelly, "Road transportation vehicles" MRS Bulletin 33, 439-444, 2008.
- [2] B.E. Lindemuth, "An overview of tire technology", Chapter 1 in "The pneumatic tire", U.S. Department of Transportation, National Highway Traffic Safety Administration, February 2006.
- [3] T. Markel, A. Brooker, V. Johnson, K. Kelly, M. O'Keefe, S. Sprik, K. Wipke, "ADVISOR: a systems analysis tool for advanced vehicle modeling" J. Power Sources 110, 255-266, 2002.
- [4] California Energy Commission, Fuel-Efficient Tires and CEC Proceeding Documents Page, www.energy.ca.gov/transportation/tire_efficiency/documents/index.html (accessed January 2008).

Figures:

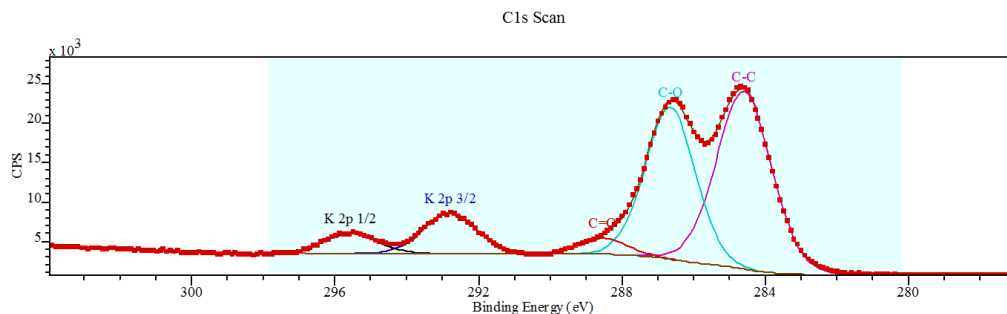


Figure 1: High Resolution C1s XPS analysis of the functionalized Graphene Oxide fillers before reduction

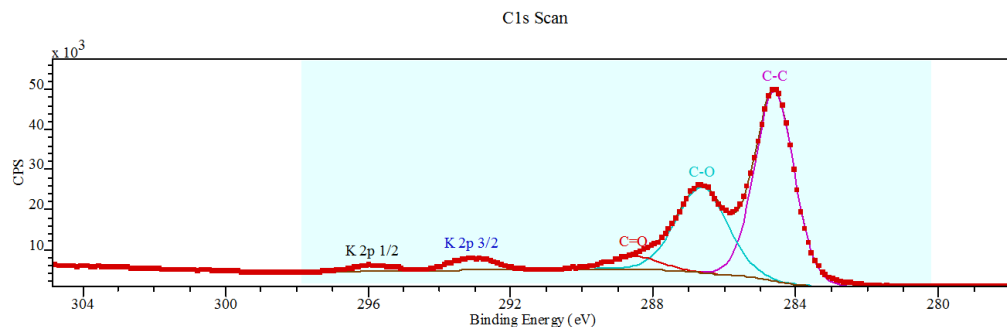


Figure 2: High Resolution C1s XPS analysis of the functionalized Graphene Oxide fillers after the reduction

This Page is Intentionally Blank

AVPTA Technology Focus Area 5: Electrified Propulsion Systems

Non-Rare-Earth Integrated Starter Generator

DOE-VTO TFA Lead: Susan Rogers
TARDEC TFA Lead: Dean McGrew

Principal Investigators:

**Joshua Tylenda,
Joe Heuvers and
Dean McGrew**
U.S. Army TARDEC
Ground Vehicle Power & Mobility

Project Start: Q1FY13

Estimated Completion: Q4FY18

Objectives:

- The TARDEC Advanced Propulsion Team, in collaboration with the DOE Vehicle Technologies Office, is working to develop and demonstrate two Integrated Starter Generators (ISG) without rare-earth permanent magnet materials suitable for onboard vehicle power generation.
- Most high-performance electric machines in hybrid electric applications use rare-earth magnets (NdFeB & SmCo) to achieve the required power and torque densities.
- This effort will additionally explore alternate electric machine topologies to achieve its goals.

Strategic Context:

Through the Non-Rare Earth ISG project, TARDEC's strategy is to develop the following:

- Ability of the motors to meet the specified performance without the use of rare-earth magnetic materials.
- Ability to perform according to schedule given issues and delays that have emerged.
- Ability to minimize audible noise signature of the Switched Reluctance (SR) generator topology.

To help manage risks, weekly status meetings are held to allow issues to be surfaced in a timely manner and mitigations put in place to resolve them in order to maintain schedule. Additional contract actions are planned to address audible noise of the SR topology.

Accomplishments:

- The University of Akron completed the design, build and testing of the **Task 4** SR ISG optimized design with skewing.
- The **Task 5** SR ISG approach for a novel design was finalized. The approach of optimizing around a distributed airgap strategy was found to not be effective across a wide range of operating points, and an approach utilizing stator bridges was decided upon. The Task 5 SR ISG stator bridge design and build was completed in Q4FY18.
- The contractor presented paper at GVSETs in August 2018 titled 'A Demonstration of Noise and Vibration Reduction Techniques for Zero Rare-Earth Magnet Integrated Starter-Generators used in Military Vehicle Applications.' The paper explored the lessons learned and test results from SR ISG optimization for acoustic noise reduction, comparing modeling and simulation with test results for the windowed and skewed SR ISG builds.
- The Non-Rare Earth effort is being augmented with an Army Small Business Innovation Research (SBIR) Phase II contract with Continuous Solutions to develop a 100kW inverter with active torque ripple mitigation to pair with a 100kW SR ISG. Threshold/objective goals include a decrease in 25%/50% of acoustic noise and torque ripple. Modeling and simulation, militarized build for shock and performance for 100kW operation at temperature have been demonstrated in FY18.

Introduction:

The Non-Rare-Earth ISG project has the opportunity to reduce the cost of high-performance power generation hardware. This project seeks alternatives to rare earth designs in case of a supply disruption of rare-earth permanent magnet materials similar to events in 2010-2011. In July 2010, China cut its exports rare earth minerals by 72%. In September 2010, China temporarily cut rare earth exports to Japan due to a maritime dispute. In 2011, China had cut exports further and raised export tariffs for rare earths. The world remains almost completely dependent on China for rare earths.

In 2010, The Department of Energy had published a Critical Materials Strategy, ranking Neodymium and Dysprosium among the most critical from an importance and supply risk perspective. Both materials are used in the highest performance Neodymium Iron Boron (NdFeB) permanent magnets available today, Figures 1 and 2.

Approach:

The project commenced with trade studies to identify the two most promising ISG architectures without rare-earth permanent magnets and to identify permanent magnet materials which could be leveraged for this effort. The two ISG architectures which were down-selected include the SR and Spoke Interior Permanent Magnet (Spoke IPM), Figure 3. The SR architecture does not include permanent magnets. The Spoke IPM is leveraging ferrite magnets which have approximately 1/10 the energy product of high performance rare earth magnets.

A study on permanent magnets revealed that ferrite and Alnico permanent magnets are the only non-rare-earth permanent magnets available in sufficient quantities to achieve the program goals, Figure 4. Due to the low coercivity of Alnico magnets, ferrite was determined to be the most promising choice for the design.

The SR ISG has emerged as the more promising of the two designs evaluated and now being built under the effort. The SR topology is more cost effective than any other known generator architecture - approximately 1/3 the cost of comparable rare earth permanent magnet based designs.

Results and Discussion:

Performance projections for the two ISGs based on Finite Element Analysis are shown in Figures 5 and 6.

Tasks 1 & 2 were closed out, with SR ISG and Spoke IPM builds, optimizations and testing completed.

The SR ISG resulted in better performance, and was chosen for **Tasks 3-5** for building additional ISGs with optimization for reducing audible noise as identified in the trade study.

The **Task 3** design used through windowing in the stator and rotor, as shown in Figure 7.

The **Task 4** design used skewing in the stator and rotor, and optimized at the skew angle of 13.75 degrees to maximize torque production while minimizing torque ripple. Models of this design are shown in Figure 8, as well as the machine's performance, Figure 9.

The **Task 5** design used stator bridges using MAGNOVAL 2067 steel with a 1.4mm thickness to maximize torque production while minimizing torque ripple. Models of this design are in Figure 10. final results for the ISG's performance will be available during Q1FY19.

Build has been completed for all 3 SR ISG optimizations, and test and analysis has been completed for the windowing and skewing optimizations, while test and analysis will complete for the stator bridge design in Q1FY2019. The experimental noise result for the baseline, window and skew ISGs are contained within Figure 11. at the rated condition of 800rpm, 1000Nm, which is the worst-case point for acoustic noise during operation.

The plot contained within Figure 12 shows the 800rpm, 600Nm point comparison, which shows more of a difference between machines, with a maximum 6-7dB decrease between the baseline SR ISG and the windowed SR ISG, and then again between the windowed SR ISG and the skewed SR ISG.

During test, it was discovered that tests results were not correlating as well as expected when compared to the simulations; upon further investigation, it was determined that adding radial force factor to the models significantly increased the fidelity of those models. If the windowed and skewed SR ISGs were to be redesigned, acoustic noise would likely be further reduced by using radial force in optimizing the design.

Conclusions:

Further analysis of wide-range acoustic noise reduction occurred in FY2018 after determining radial force factors were not fully accounted for in analysis. Using this additional knowledge, third and final optimization method of implementing stator bridges was used for the **Task 5** SR ISG. Preliminary results show an improvement on the previous design iterations in acoustic noise.

Future Direction:

Test and evaluation of the **Task 5** stator bridge SR ISG will be completed in Q1FY19 to close out the effort with comparative results amongst each of the SR ISG builds.

Tables and Figures Start on the Next Page

Tables and Figures:

Table 1. Technical Targets

	<i>Objective</i>	<i>Threshold</i>
<i>Machine Dimensions</i>		
Housing Outside Diameter	< 558 mm (22 inches)	
Overall Active Length	100 mm	120 mm
<i>Power Supply</i>		
Nominal Voltage:	600 V ± 35 V	
<i>Thermal Requirements</i>		
Liquid cooling	WEG / PWG	
Inlet Temperature	110°C	105°C
Cold Start Initial Condition	-50°C	
Maximum Flow Rate	< 30 LPM (8 GPM)	
Maximum Pressure Drop	16 PSI	
Operating Air Temperature	-50°C to 125°C	

Tables Continue on the Next Page

Table 2. Performance Targets

	<i>Objective</i>	<i>Threshold</i>
Target performance		
Continuous Power	100 kW	
Max Operating Speed	4250 RPM	3200 RPM
Base (corner) Speed	800 RPM	1100 RPM
Continuous Torque (0-800 RPM)	1200 Nm	
Peak Torque (0-800 RPM)	1800 Nm	
Duration of Peak Torque	30 sec	
Torque Density		
Volumetric Torque Density	80 Nm/L	50 Nm/L
Gravimetric Torque Density	11 Nm/kg	7 Nm/kg
Power Density		
Volumetric Power Density	8 kW/L	5 kW/L
Gravimetric Power Density	1.2 kW/kg	0.8 kW/kg

Table 3. Other Specifications

Other
Compatible with SAE#1 Bell-housing. Designed for integration between Caterpillar C9 engine and Allison 3200SP transmission.
Waterproof (per 3.5.1.2 from MIL-S-3785E(AT))
Conform to MIL-STD-461F (EMC)
Resolver control hall-effect redundancy

Figures Start on the Next Page

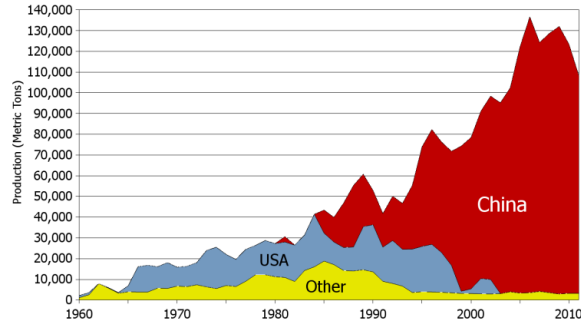


Figure 1. World-Wide Production of Rare-Earth Materials

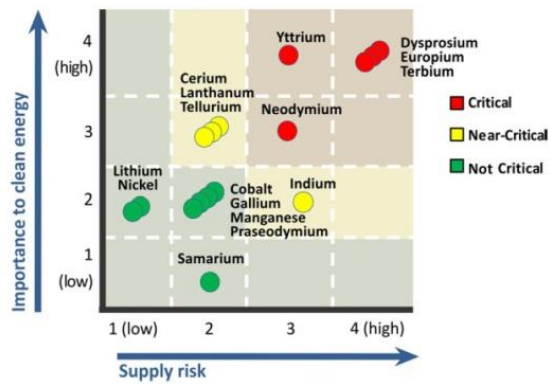


Figure 2. Department of Energy Critical Materials Strategy

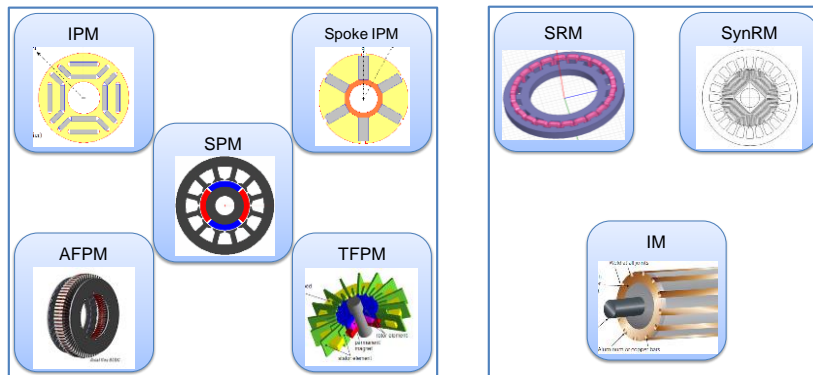


Figure 3. ISG Architectures

Figures Continue on the Next Page

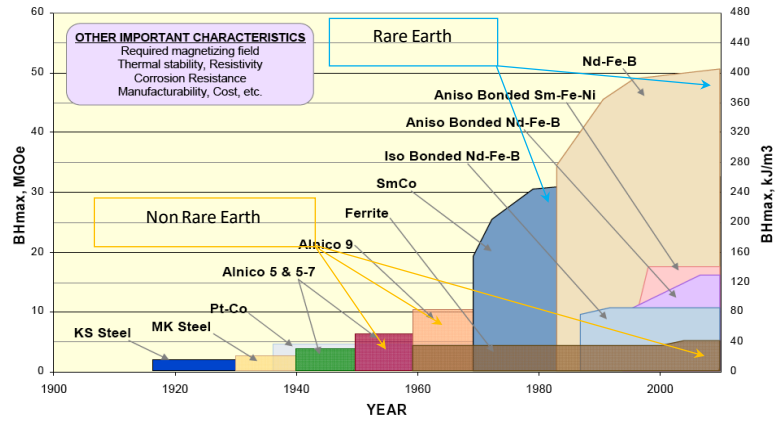


Figure 4. Non-Rare-Earth Permanent Magnet Quantities

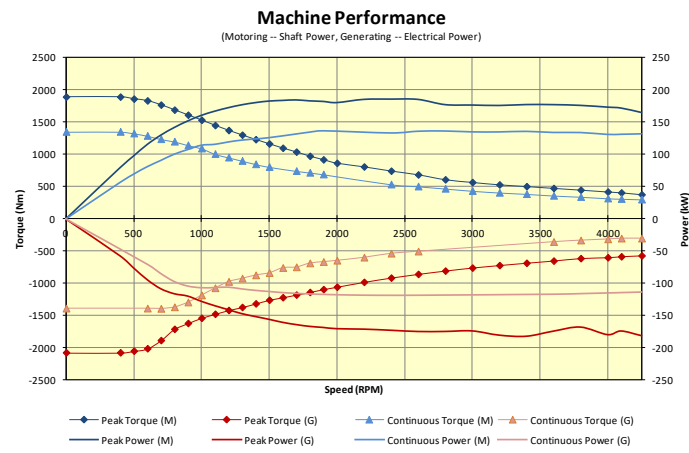


Figure 5. Characteristic Machine Performance

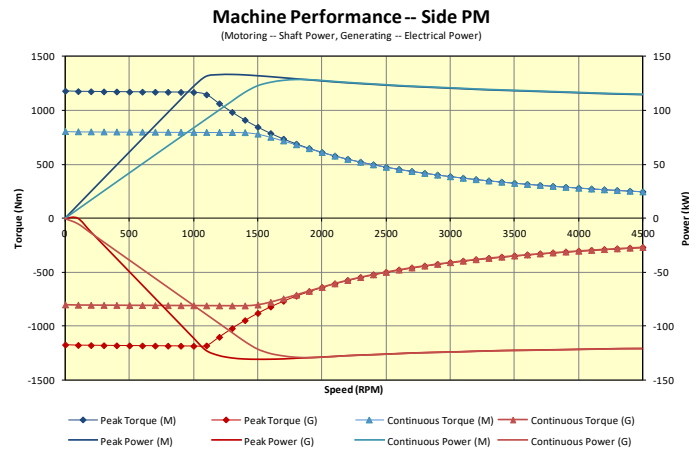


Figure 6. Side PM Machine Performance

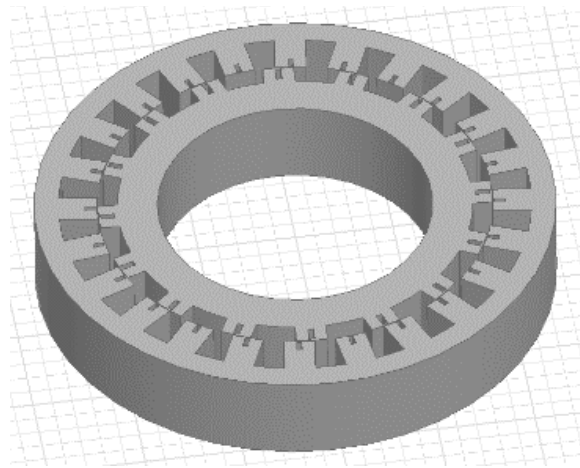


Figure 7. Windowed Stator and Rotor Design

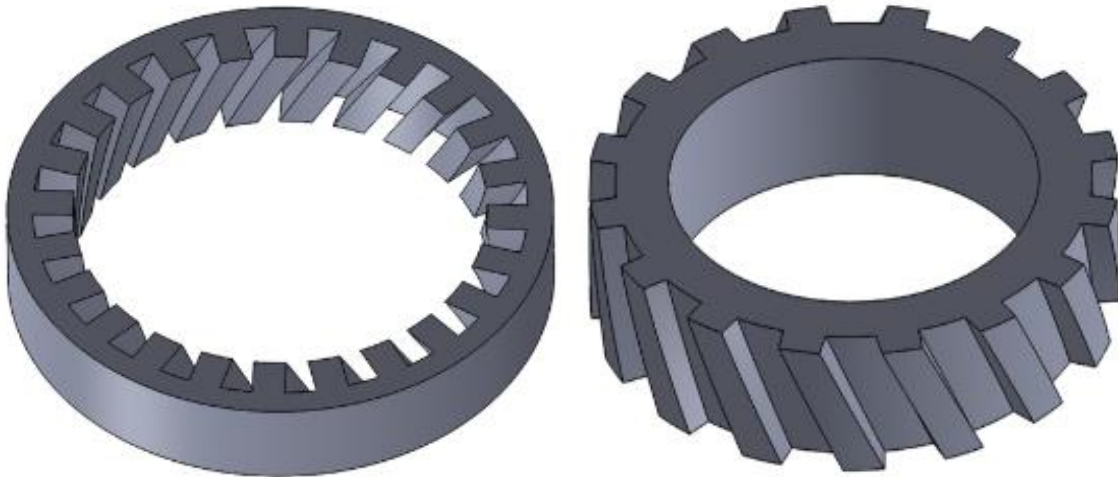


Figure 8. Skewed Stator and Rotor Designs

Figures Continue on the Next Page

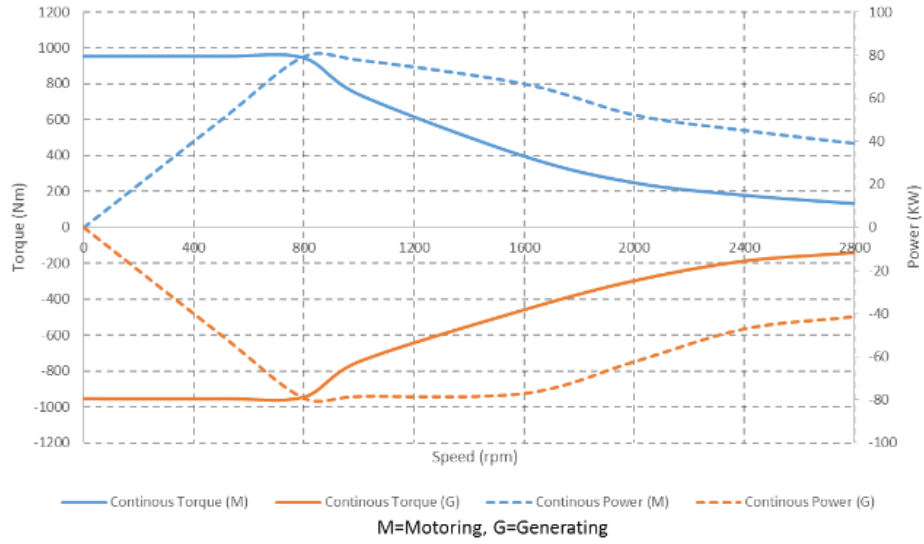


Figure 9. Performance of Skewed Stator and Rotor Design

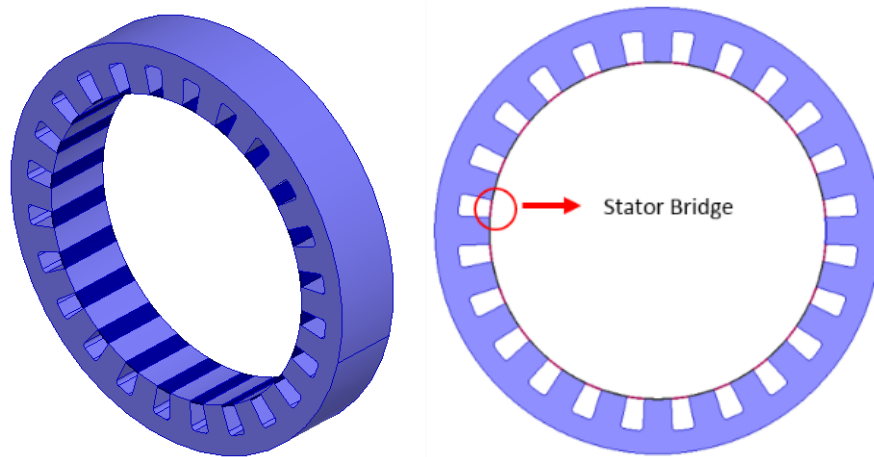


Figure 10. 1.4 mm Thick MAGNOVAL 2067 Steel Task 5 Stator Bridges

Figures Continue on the Next Page

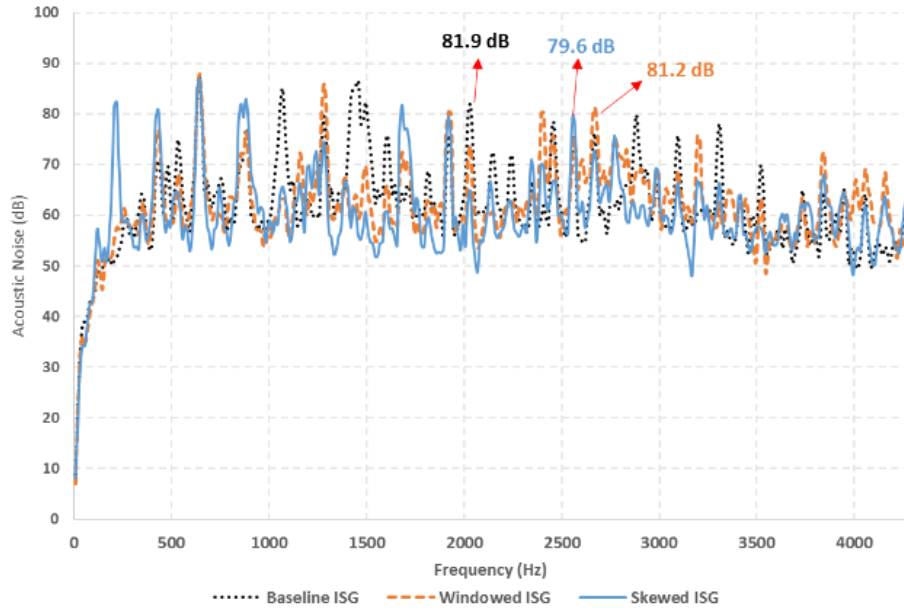


Figure 11. Experimental Noise Result for Three ISGs at 800 rpm and 1000Nm.

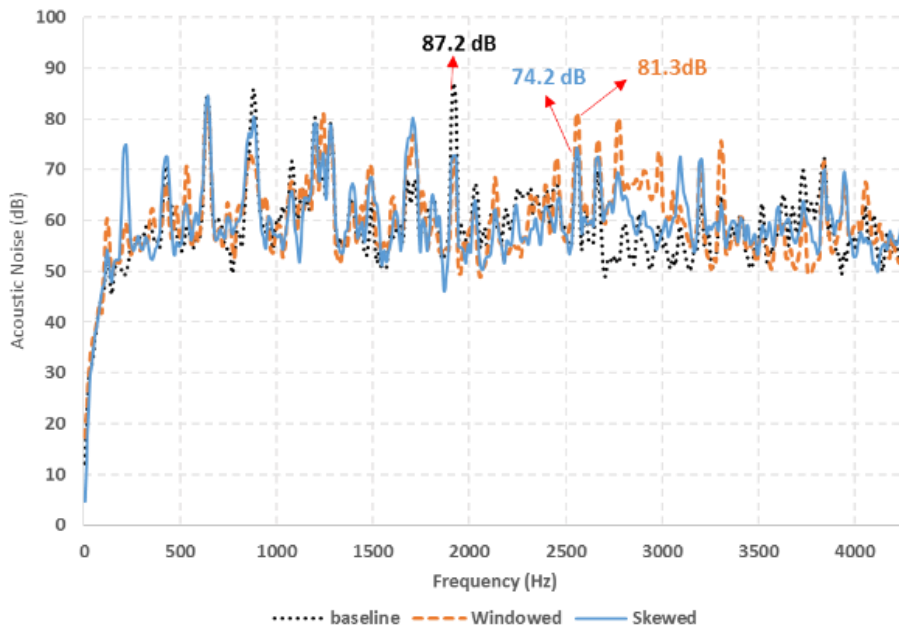


Figure 12. 800 rpm and 600 Nm Comparison Point Showing 6-to-7 dB Decrease between Baseline and Windowed SR ISGs.

This Page is Intentionally Blank

AVPTA Technology Focus Area 6: Energy Storage & Batteries

Multiphysics Computational Tools for Battery Performance, Life, and Safety

**DOE-VTO TFA Lead: Brian Cunningham
TARDEC TFA Lead: Laurence Toomey**

**Principal Investigator(s):
Dr. Kandler Smith**

**National Renewable Energy Laboratory
15013 Denver West Parkway, Golden, CO
80401**

**Project Start: Q4FY16
Estimated Completion: Q4FY19**

Objectives:

- Construct an integrated multi-physics simulation environment/tool for analysis of performance, safety and life of Li-ion battery module used in military vehicles
- Mathematically describe battery safety response in a ballistic environment. Implement mechanical models for Li-ion battery components that capture the response of individual cell components to high-velocity impact.

Strategic Context:

- The energy efficiency and functionality of military vehicles through electrification can be improved through the adoption of Li-ion battery technology. Without significant testing, the cold temperature performance, safety and lifetime of Li-ion technology can be difficult to quantify, however. Computer-Aided Engineering (CAE) tools are capable of accelerating the development of safe, high-performance, and long-lasting Li-ion battery systems for military vehicle applications and reducing the need for time-consuming and expensive tests. NREL is developing a robust and efficient analysis tool for TARDEC by customizing NREL's in-house modeling tools and leveraging new functionalities being produced in ongoing Computer-Aided Engineering of Batteries (CAEBAT) projects. The model has the flexibility to adapt to new chemistries and designs including safety features.

Accomplishments:

- Developed 3D model of 6T battery geometry and defined material thermal and mechanical properties
- Characterized battery electrochemical and aging sub-models from existing TARDEC data
- Carried out additional module-level calorimetry and used data to validate 3D model at 30°C
- Carried out cell-level abuse tests to characterize abuse reaction kinetics model
- Developed a scalable methodology to couple electrochemical-thermal models to explicit mechanical deformation simulations. Models provide a comprehensive understanding of failure thresholds and propagation mechanisms for each component within the battery.
- Delivered preliminary ANSYS 3D thermal/electrochemical and LS-Dyna 3D ballistic safety simulation software to TARDEC for evaluation

Introduction:

Energy storage systems based on lithium-ion battery technology show great promise to improve the energy efficiency and functionality of military vehicles through electrification. CAE tools are able to accelerate development of safe, high-performance, and long-lasting lithium ion battery modules for military vehicle applications. Physics-based models are adaptable as design changes occur over the life cycle of a military program.

As a CAEBAT program [1] performer, NREL supports DOE to develop numerical design tools to shorten design cycles and optimize batteries for improved performance, safety, long life, and low cost. NREL has played a leading role in numerical analysis of multiphysics behaviors of lithium-ion batteries. NREL's multi-scale multi-domain (MSMD) model overcomes the modeling challenges posed by the highly nonlinear multi-scale response of battery systems. The expandable, modular, and flexible architecture connects the physics of battery charge/discharge processes, thermal control, safety, and reliability in a computationally efficient manner.

The MSMD acts as the framework for the suite of tools being developed in this project. Performance-, life- and safety-component models are being customized and integrated as a user defined library in ANSYS Fluent, a computational fluid dynamics code in which MSMD model framework has been standardized. Ballistic simulations are performed using LS-Dyna, providing mechanical response of the battery to intrusion by bullet (or alternately crash or crush) and providing the resulting internal short magnitude to ANSYS Fluent simulations for thermal runaway likelihood analysis. The user will further leverage enhanced capabilities being implemented in the ANSYS Fluent Battery Module as outcomes of other continued CAEBAT projects.

Approach:

A CAE software tool of the 6T module is being developed by customizing NREL's in-house modeling tools and leveraging new functionalities produced by continuing CAEBAT projects. NREL's existing performance, life and safety model is being refined and integrated as a user defined library in ANSYS Fluent Battery Module [2], in which NREL's MSMD battery modeling

OPSEC1890

framework [3] has already become standard as a result of previous CAEBAT projects. The tool is being enhanced to integrate with NREL's life model, so that battery lifetime tradeoffs can be assessed based on 3D thermal/electrical drive cycle response. Ballistic simulations are being built leveraging explicit mechanics and failure models in LS-Dyna and linked to ANSYS for safety evaluation. The simulations include failure criteria for each component (e.g. failure strength for the foils, separator, etc.) as well as for different physics (e.g. decomposition voltage for the electrolyte). To validate the functionality of the CAE toolset, NREL is conducting calorimeter testing of the 6T module as well as cell-level thermal runaway abuse tests.

Results and Discussion:

Battery performance, life and safety component models are being integrated as a user defined library in ANSYS Fluent. LS-Dyna software predicts magnitude and location of damaged regions under mechanical abuse/ballistic response and damaged regions are mapped to ANSYS Fluent for thermal runaway simulation. The tool is aimed to support high performance parallel computing and simulation.

NREL held an on-site training workshop for TARDEC at project kick-off to discuss existing capabilities and new capabilities to be developed under the project. During FY17, NREL developed 3D thermal and mechanical models of the 6T battery geometry and defined material properties. NREL also characterized battery electrochemical and life sub-models from existing cell-level data. During FY17, NREL and TARDEC determined that additional data were needed to characterize cell-level abuse kinetics models and validate module-level models. In FY18, NREL conducted these additional tests, scaled the cell-level models to module-level and began the process to validate the 3D models versus module-level data. The FY18 efforts are further described below.

Module-level Electrochemical/Thermal Simulation

Figure 1 shows 3D geometry of the Navitas 6T battery used for validation studies under this project. The battery module contains 24 Li-ion pouch cells in a 3-parallel, 8-series arrangement. The pouch cells are 20-Ah, 3.3V nominal graphite/iron-phosphate (LFP) chemistry, produced by A123. Figure 2 compares the 3D ANSYS Fluent electrochemical/thermal model of the 6T module to NREL test data. Voltage during C/5, 1C, 2C and 4C discharge is predicted within 0.5V, or 98% accuracy. Capacity at each of these discharge rates is predicted with 96% accuracy. The electrochemical sub-model, parameterized with cell-level data, required no further tuning to match this module-level data.

Figure 3 compares the temperature response during constant current discharge of the side cell (marked as thermocouple location #2 in the left-inset of the figure) for model versus data. The model reasonably captures temperature rise for this cell as well as other cell locations throughout the module. No model parameter tuning was required to match cell temperature rise as thermal and heat transfer elements of the model were built almost entirely from component-level geometry and material properties. A small adjustment was made to match circuit board and terminal temperatures by adding convective heat transfer in the air gap between the top of the cells and the battery management circuit board. The

OPSEC1890

accuracy of the module-level model current/voltage and temperature predictions – built bottom-up from cell-level sub-models, module materials and geometry – underscores the powerful predictive capability provided by the 3D electrochemical/thermal physics battery model.

Cell-level Ballistic Simulation

Ballistic simulations were carried out at both the cell and module levels. At the cell level, Figure 4 shows a numerical study carried out with LS-Dyna for bullet impact with a single 20-Ah pouch cell with various penetration angles. For a bullet entering the cell at 835 m/s, the bullet would depart the cell with velocities ranging from 760 to 790 m/s depending on penetration angle. For a bullet with 0 penetration angle (impact normal to cell face), Figure 4 shows deformed geometries predicted by the model to be comparable with geometries experimentally imaged by CT-scan after bullet penetration.

Figure 5 shows results of single-cell bullet threat simulations for varying initial velocity of the bullet. For initial velocities greater than 280 m/s, the bullet penetrates through the cell. For initial velocities less than 280 m/s, the bullet is lodged within the cell.

Module-level Ballistic Simulation

To capture the mechanical-coupled failure modes of the 6T module under ballistic threat, we developed a finite element model procedure to simulate bullet penetration in LS-Dyna. Our approach is motivated by the observation that the 6T battery has multiscale features ranging from micrometers to centimeters. The traditional approach of solving the problem as the inversion of one big matrix imposes numerical challenges. The traditional approach requires long simulation times due to a large number of degrees of freedom and numerical stiffness stemming from the large in-plane element sizes (of the order of centimeters) versus the micron-sized through-plane dimensions. The proposed approach uses a mathematical formulation that allows us to solve the high strain-rate problem across a section of the battery thickness in an initial step (e.g. the 6T battery case), then uses the velocity of the bullet at the exit point of the first section as the boundary condition for solving a similar high strain-rate problem across a second section of the thickness (e.g. the first cell), and so on, stepping through the battery layer-by-layer until the deformation problem has been solved across the complete geometry.

The 6T form factor was used to simulate the response of multi-cell test articles (Figure 6) under different assumptions. Rather than separately resolving each individual anode/separator/cathode layer within the cells, the lumped model – combining all anode layers, all separator layers, and all cathode layers into three separate layers per cell – greatly improves computational stability and simulation time, enabling us to incorporate realistic module geometries and component failure limits in our simulations. The homogenized model uses equivalent properties across the entire cell instead of resolving the separate anode/separator/cathode components. The homogenized model, while reasonable, cannot resolve individual component failure limits and the lumped model is therefore preferred. The effect of isolation between the cells, angle of incidence and proximity of the impact zone to the tabs are some factors we are currently investigating.

OPSEC1890

Cell-level Accelerating Rate Calorimetry (ARC) and External Short Tests

Cell-level ARC and external short tests were carried out for NREL by an external vendor. Several replicate cells underwent thermal runaway in the ARC at 100% SOC. The cell without external constraint plates experienced the lowest thermal runaway onset temperature of 98°C due to gas generated inside the cell that caused the cell pouch casing to balloon, distorting the electrode layers. All subsequent cells thereafter were run with compression plates to better mimic the mechanical constraint placed on cells within a module. The two replicate cells with constraint plates at 100% SOC exhibited thermal runaway onset temperatures of 117°C and 127°C. Tests were also run at 20% and 50% SOC to characterize SOC dependence. Heat of reaction and heating rate data are being used to parameterize an abuse reaction kinetics model that is integrated within the 3D ANSYS simulations for simultaneous performance/safety evaluation.

Conclusions:

NREL and TARDEC are developing an integrated multi-physics simulation tool for analysis of performance, safety and life of military Li-ion battery systems, with application and validation for the 6T battery. The tool leverages previous electrochemical/thermal model developments under the CAEBAT program, applies them to the 6T battery system and also extends those models to capture 3D aging effects and ballistic response of the 6T battery system. The team has delivered preliminary ANSYS 3D thermal/electrochemical and LS-Dyna 3D ballistic safety simulation software to TARDEC for evaluation and continues to do so during the project.

In FY18, the team conducted additional module-level performance tests and used the data to validate the 3D electrochemical/thermal performance model. A modeling framework to simulate high-strain rate deformation of lithium-ion batteries was expanded to module-level simulations in LS-Dyna. The models accurately predict experimental data and can be used for virtual prototyping of battery modules. Module design should consider propensity for thermal and reaction propagation in addition to purely mechanical response of batteries. High strain-rate deformation results in mechanical damage patterns very different from conventional quasi-static response of battery cell components.

In FY19, the team will complete validation studies of low temperature performance and simulate ballistic-induced mechanical failure propensity to induce thermal runaway by mapping damage zones from LS-Dyna to ANSYS Fluent. Models will be delivered to TARDEC and users will be trained in a workshop at the project conclusion.

References:

- [1] Computer-Aided Engineering for Electric-Drive Vehicle Batteries (CAEBAT). (2016). Retrieved from <http://www.nrel.gov/transportation/energystorage/caebat.html>
- [2] ANSYS Fluent Battery Module, Release 17.0, ANSYS Fluent Advanced Add-On Modules, ANSYS, Inc.

- [3] G-H. Kim, K. Smith, K-J. Lee, S.Santhanagopalan, A. Pesaran, "Multi-Domain Modeling of Lithium-Ion Batteries Encompassing Multi-Physics in Varied Length Scales," J. Electrochem Soc, Volume 158, Issue 8, pp. A955-A969 (2011)
- [4] Chao Zhang, Shriram Santhanagopalan, Michael A. Sprague, Ahmad A. Pesaran, "A representative-sandwich model for simultaneously coupled mechanical-electrical-thermal simulation of a lithium-ion cell under quasi-static indentation tests", Journal of Power Sources, Volume 298, Pages 309-321, 2015.
- [5] Chao Zhang, Shriram Santhanagopalan, Michael A. Sprague, Ahmad A. Pesaran, "Coupled mechanical-electrical-thermal modeling for short-circuit prediction in a lithium-ion cell under mechanical abuse", Journal of Power Sources, Volume 290, Pages 102-113, 2015
- [6] Z. Wu, C. Zhang, L. Cao, and S. Santhanagopalan, "Effect of Aging on Safety of Lithium-Ion Battery Components," Invited Paper, ECS Trans. 2017-77(11): 199-208; doi: 10.1149/07711.0199ecst (2017).
- [7] Y. Chen, S. Santhanagopalan, V. Babu, Y. Ding, "Dynamic Mechanical Behavior of Lithium-ion Pouch Cells Subjected to High-Velocity Impact", To be submitted.
- [8] S. Santhanagopalan, Y. Chen, Q. Li, C. Yang, V. Babu, Y. Ding, "Dynamic response of lithium-ion batteries subjected to mechanical failure under high-velocity impact," NDIA Army Science & Technology Symposium & Showcase, Washington, DC, August 21-23, 2018.

Figures:

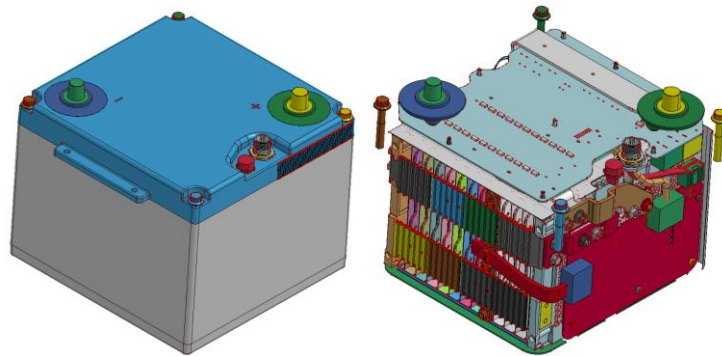


Figure 1. 3D CAD geometry of Navitas 6T module.

Figures Continue on the Next Page

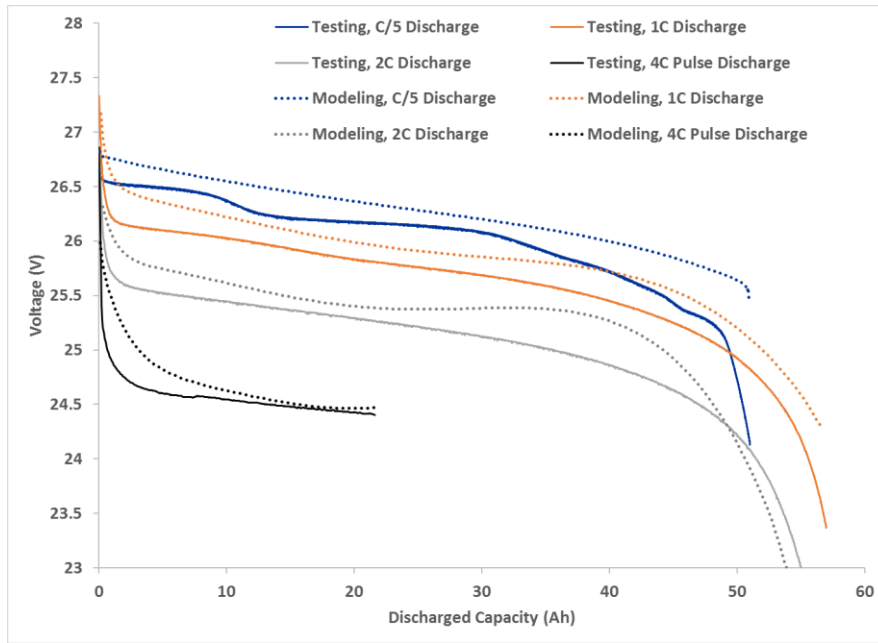


Figure 2. 3D electrochemical/thermal simulation in ANSYS Fluent of 6T module constant current discharge compared to test data.

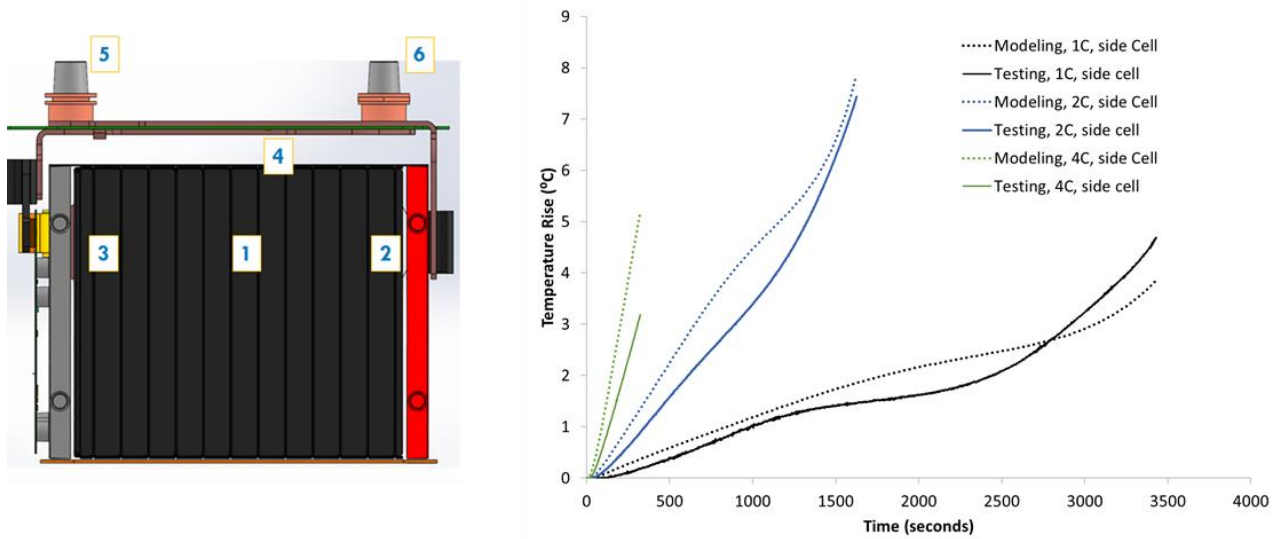


Figure 3. Comparison of 3D electrochemical thermal model with test data for side cell (labeled as thermocouple #2 in schematic at left) for 1C, 2C, and 4C discharge rates.

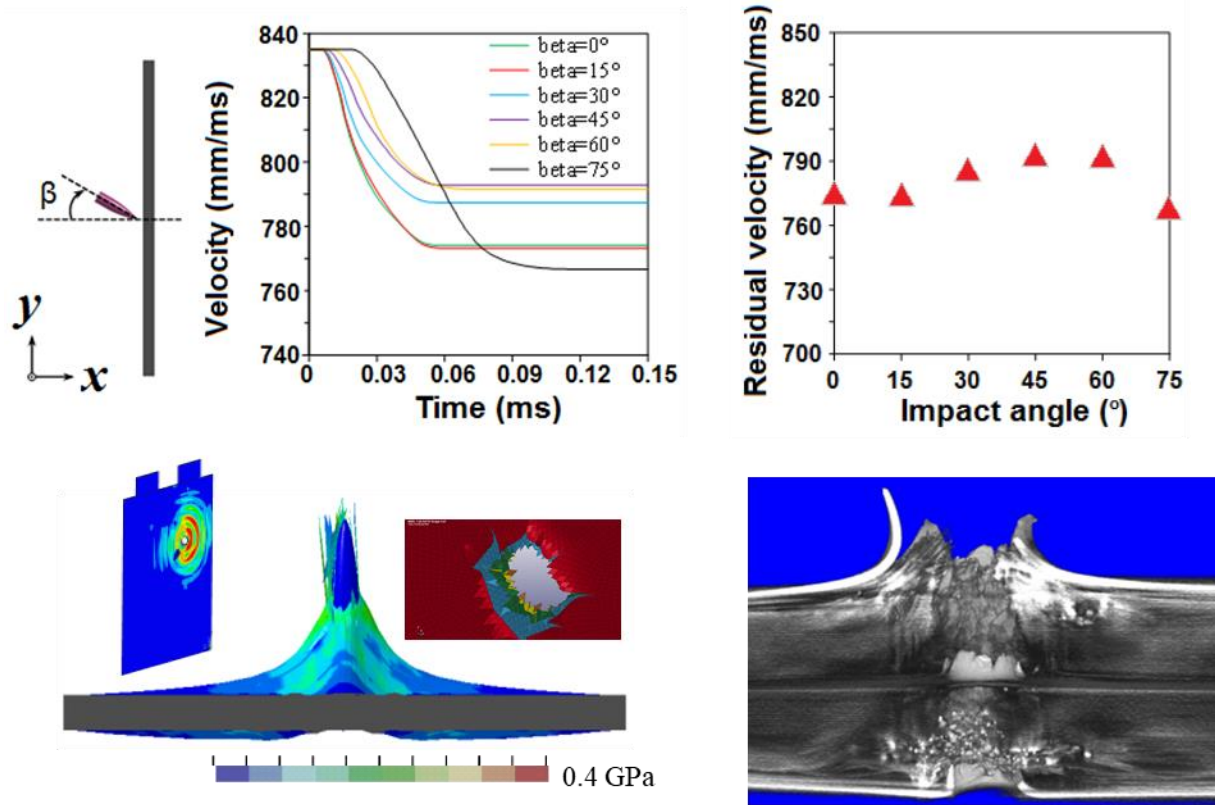


Figure 4. Simulations of bullet penetration through single pouch cell, investigating effects of penetration angle on (a) bullet velocity versus time and (b) residual velocity after passing through cell. Built from component-level constituent models, the (c) model matches deformed geometry of (d) cell-level bullet threat tests.

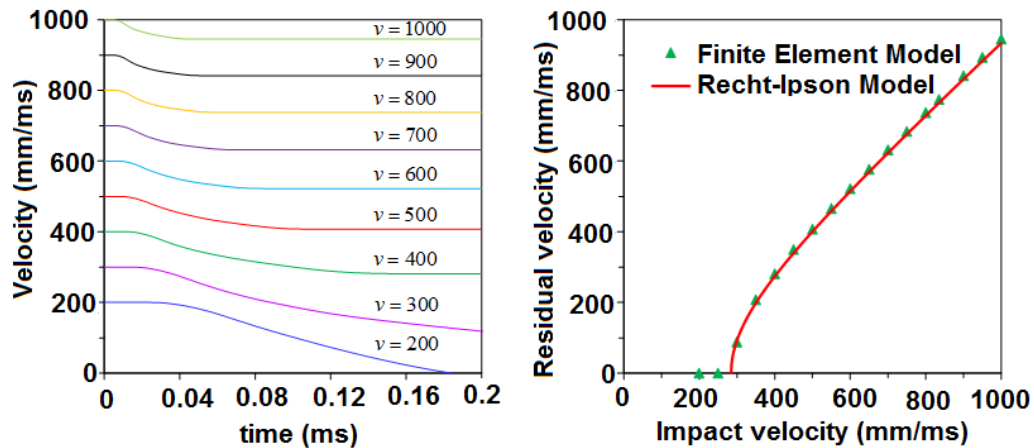


Figure 5. Ballistic simulation of bullet penetrating single cell. For initial velocities greater than 280 m/s, the bullet penetrates and passes through the cell.

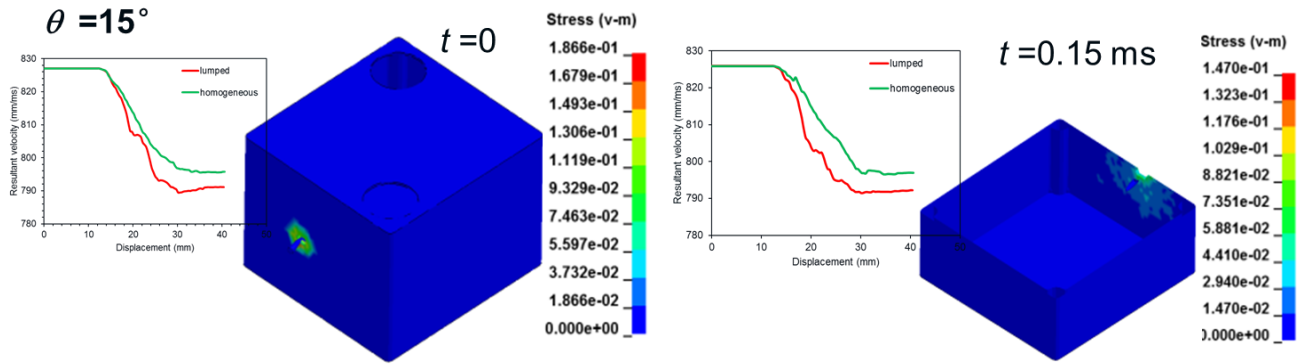


Figure 6. To extend ballistic simulations to module-level with reasonable computational efficiency, individual cell anode/separator/cathode layers are homogenized, yielding a module-level bullet-threat assessment model with reasonable efficiency and accuracy.

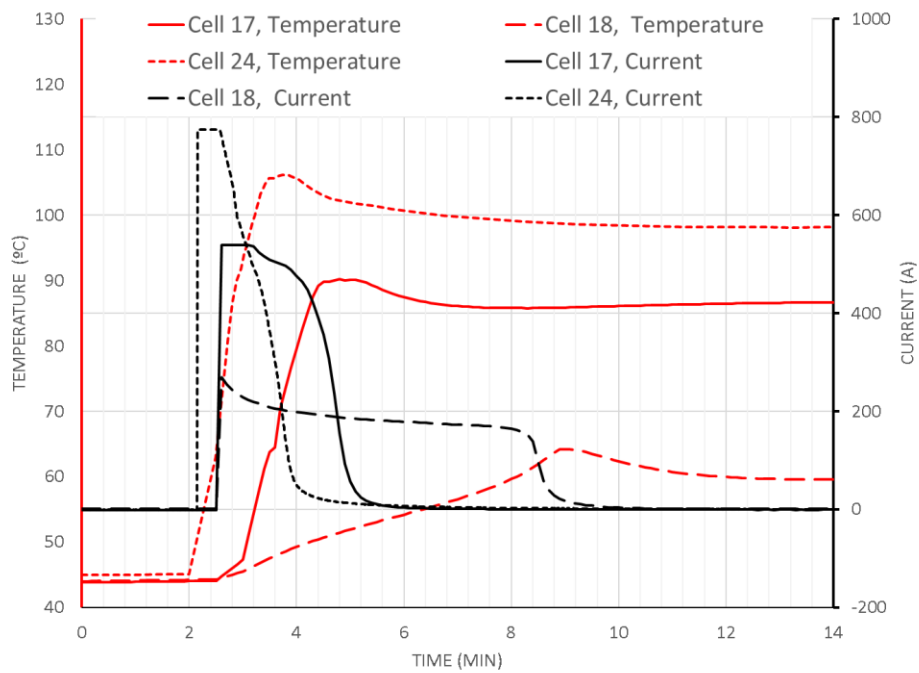


Figure 7. External short circuit test of 20Ah A123 cell at 100mΩ, 6mΩ and 5mΩ, performed at external vendor.

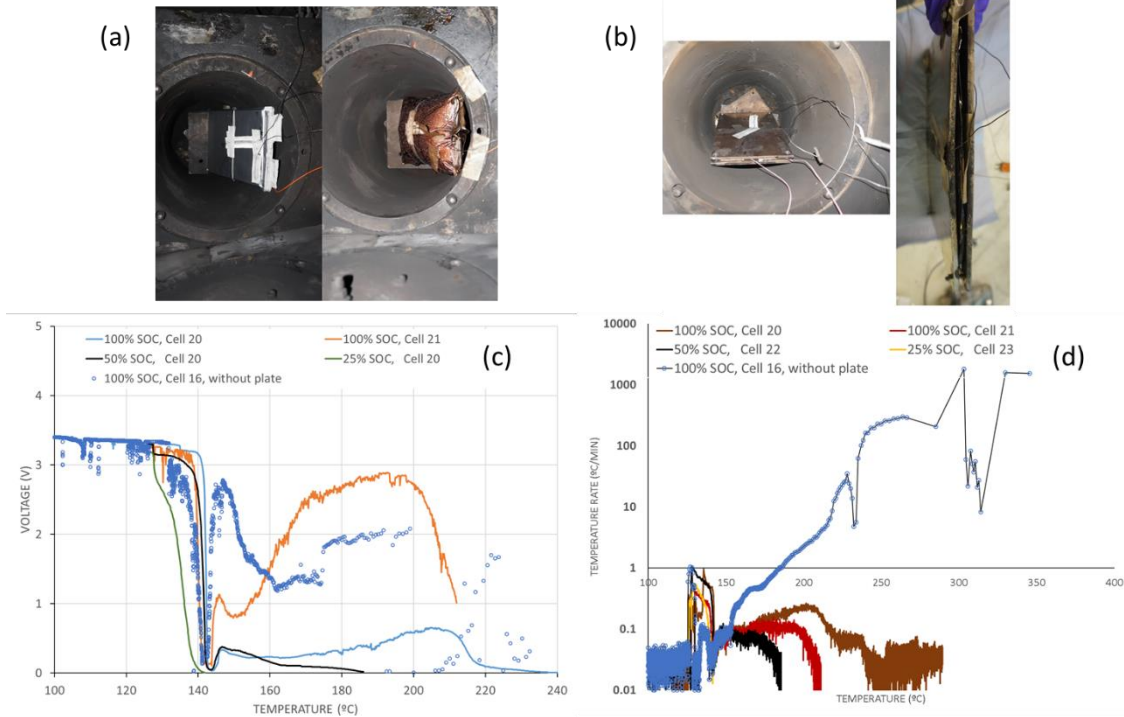


Figure 8: Accelerating rate calorimetry test of A123 20Ah cell run at external vendor.

Remainder of Page Intentionally Blank

AVPTA Technology Focus Area 6: Energy Storage & Batteries

Development and Validation of a Simulation Tool to Predict the Combined Structural, Electrical, Electrochemical and Thermal Responses of Automotive Batteries

**DOE-VTO TFA Lead: Brian Cunningham
TARDEC TFA Lead: Laurence Toomey**

**Principal Investigator:
Dr. Chulheung Bae**

**Ford Motor Company
Energy Storage Research
2101 Village Road
Dearborn, MI 48152**

**Project Start: Q2FY16
Estimated Completion: Q1FY20**

Objective(s):

- To develop and validate a simulation tool with unprecedented fidelity to predict the combined structural, electrical, electrochemical and thermal (SEET) response of automotive batteries to crash-induced crush and short circuit.

Strategic Context:

- Lithium-ion batteries are promising for both military and commercial vehicle applications by improving energy efficiency and functionality of vehicles through electrification. Computer aided tools will help to accelerate development and fielding of safe, high-performance, and long-lasting lithium ion battery modules for both applications. The simulation tool should have unprecedented fidelity to predict SEET response of automotive batteries to crash-induced crush and short circuit.

Accomplishments:

- Enhanced the capabilities of composite t-shell elements in mechanical, electromagnetic (EM) and thermal solvers.

OPSEC1890

- Developed models with composite t-shell elements under different abuse scenarios and demonstrated its advantages compared with solid element models.
- Initiated the development of the macro model that aims to improve computational efficiency of the EM and thermal solvers.
- X-ray tomography has been used to investigate damage in individual cell layers under shear and compression.
- New material models were developed treating active materials as granular materials with parameters chosen to yield good results compared to experiments.
- Developed a microstructure characterization-reconstruction- finite element analysis (FEA) modeling method that facilitates numerical prediction of the mechanical behavior of anisotropic battery separators.
- Quasi-static cell validation testing was performed at Intertek, but problems arose and all cell and module testing will now be performed at Southwest Research Institute, where all fixtures and instrumentation are now in place.

Introduction:

This is the third year of a three-year project to develop a practical simulation tool to predict the combined structural, electrical, electrochemical, and thermal responses of automotive batteries to crash induced crush and short circuit, and validate it for conditions relevant to automotive crash. However, due to unexpected problems in cell testing, model validation fell behind schedule, and a one-year no-cost extension was approved. The project will now conclude by the end of 2019.

The expected benefits of the simulation tool are to reduce development time and cost by reducing the number of physical prototypes required, as well as improve the abuse response of battery systems for vehicle electrification. The project plan including major constituents and progression based on case studies is shown in Figure 1.

Approach:

Develop material constitutive models and finite element method (FEM) element formulations that capture the mechanical response of cell components, including the case material, electrodes, separator, and their interactions with electrolyte.

Clearly identify the required input parameters for the constitutive models, FEM element formulations, and exothermic, electrochemical reaction state equations governing multi-physics phenomena during crush-induced electrical short, thermal ramp, and overcharge conditions.

Design and execute a test matrix encompassing automotive crash strain rates, at a number of kinetic energy levels and physical orientations likely to occur in vehicle impacts.

Develop integrated modeling tools which demonstrate high-fidelity predictions of the onset of thermal runaway from the experimental test matrix using commercially available cells, modules, and packs, spanning multiple chemistries relevant to automotive applications.

Maintain high-fidelity predictions while exploring methods to reduce the computational complexity of the model, and deliver a practical tool that is integrated with the laboratory's Open Architecture Software (OAS), for a broad customer base within automotive product development.

Results and Discussion:

Development of LS-DYNA Solvers

Work continued in refining the mechanical, EM and thermal solvers with composite t-shell elements. Models with composite t-shell elements under different abuse scenarios were developed to demonstrate the performance of composite t-shell elements and their advantages compared with solid elements in battery safety simulations. One example of an abuse event is that of a pouch cell impacted by a semi-sphere indenter, see Figure 2. Models with either solid elements or composite t-shell elements are built with the same in-plane mesh size and boundary conditions. Results show that using composite t-shell elements can achieve comparable results in all three solvers (see Figures 3 and 4) and reduce computational time by orders of magnitude in the mechanical solver. Since the mechanical solver take the majority of time in impact simulations, improving efficiency in the mechanical solver significantly reduces the computational time for the entire simulation that involves three solvers. Moreover, it is found that using composite t-shell elements is more numerically stable at large deformation than solid elements due to their better aspect ratio. Numerical stability is critical to battery safety simulations that involve large deformation such as impact simulations. Similar features are also found in other scenarios where a cell is impacted by a semi-cylinder indenter. These advantages of the composite t-shell element allow us to build reliable and efficient models for battery safety.

The development of the macro model was initiated. The aim of the macro model is to improve the computational efficiency of EM and thermal solvers, and its difference from the composite t-shell element model is illustrated in Figure 5. Early benchmark simulations show that the macro model can capture essential features of battery behaviors and save computational time by more than one order of magnitude compared with composite t-shell element model in an impact simulation that involves three solvers. Currently, the development of the macro model is still in its early stage. For instance, it only works for solid elements and has limited short-circuit conditions. It is expected that after improving the capabilities of the macro model, it will be very attractive to large-scale simulations such as module and pack level simulations.

Development of Layered Solid Elements for Battery Cells

Layered solid finite element formulation has been under development for battery cells. The element accounts for cell component layers within its integration points and integrate their response into the finite element. An accurate model of the cell assembly would be to use separate solid finite elements for each component layer of the cell, although such models are computationally extremely expensive. In fact, multiple elements may be needed across each layer but such models are even more impractical. We use these solid element assemblies as benchmarks against the layered solid element formulation. In

Figure 6, we show an example stress distribution under a rigid sphere that is indenting a battery cell. The repeated unit is shown in Figure 6c. In the layered solid element formulation, each integration point through the thickness of the element contains different material model. However, the element only has eight nodes and 24 degrees of freedom. In the solid element model, two discretization schemes were used. In one, only four top cell repeated units (Figure 6c) were resolved with solid elements, and the remaining layers were modeled with a homogenized material model. In the other solid element model, all 17 repeated cell units through cell thickness were discretized by solid elements.

The layered solid model shows good correlation with the solid assembly counterparts but it requires orders of magnitude less computational time. It can also be seen that the model with solid element discretization of all layers has strong oscillations that are not expected in the actual mechanical response and lead to computational instabilities with increased indentation.

X-Ray Tomography of Deformed Battery Cells

X-Ray tomography was used to investigate characteristics of internal deformation and failure in battery cells. The pouch cells were tested in shear up to different depths and the X-ray tomography was conducted in the regions where the shear deformation was concentrated. The cells' regions of interest were cut (Figure 7a) and placed in the X-ray tomography instrument (Figure 7b).

Figure 8 shows characteristic views in the region of cell tearing. The mode and extent of the breaks as a function of deformation type and extent are used to determine constitutive model types and failure models.

Analysis of the three-dimensional tomography scans indicates significant compression in the active materials and the formation of slanted failures that are similar to the soil or concrete-type materials. The active materials are usually particulate aggregates of active substance with bonding additives, so that it is reasonable that they exhibit large compressibility and sensitivity to shear. Based on the observations from the X-ray scans, we are investigating constitutive models in LS-DYNA that are used for modeling of soils and concrete and using them in the cell deformation and crush models. The limit surfaces in these models are being investigated for modeling the onset of failure in cells.

Constitutive Material Model Development for Active Materials

Material properties and models of the other cell components (foils, separators) are relatively well established. Isotropic and anisotropic elastoplastic material models for these cell components have shown good agreement with the experimental data. The properties and models for current collectors (metal foils) are well established in the literature [Merchant, 2004]. The models for tearing and failure of thin metal foils also exist [Atkins, 2003, Andreasson, 2014], and they are implemented in commercial codes through various failure criteria. Anisotropic elasto-plastic material models for separators have developed [Kalnaus 2017, 2018 a & b] in related battery safety projects and applied in the analysis of cell deformation. However, the material models for active materials have

not yet been established. The experiments on battery cells have shown that active materials have mechanical response similar to cohesive granular materials [Wang, 2016], such as soil, rocks and concrete. The experience with such material models is not prevalent in automotive engineering. LS-DYNA has several constitutive models that are used for soils and concrete, and we are analyzing the feasibility of that class of material models for modeling active materials in battery cells. Because the material parameters for granular material models are measured on length scales orders of magnitude larger than the scale of active materials in the battery cells, new tests need to be developed for characterizing active materials, as well.

Material models MAT 25, 145, 173 and 193 in LS-DYNA are relevant to modeling cohesive granular materials. Out of the group, MAT 145, *MAT_SCHWER_MURRAY_CAP_MODEL, has ability to model material after onset of failure. However, the material has a large number of parameters that have to be determined and require extensive experimental program and numerical calibration. On the other hand, MAT 193, *MAT_DRUCKER_PRAGER, has limited number of parameters and requires much simpler experiments. A recent paper [Zhu, 2018] has reported material parameters measurements for MAT 193, and our experiments shown in Figures 9 and 10, have also been used to derive properties of anode active materials.

Given that the MAT 145 provides the most flexibility for modeling active material deformation, onset of failure, and post failure behavior, we have used MAT 193 model and measured properties to calibrate corresponding parameters for MAT 145. The two materials use similar formulations, however, the yield functions and material parameters had to be mapped from MAT 193 to MAT 145 to produce similar response.

The result of this formulation and parameter mapping for the two material is shown in Figure 11. The graph shows the effective uniaxial stress versus time for uniaxial compression for the two materials. The response of the two material is essentially the same.

We are currently developing a fixture for material testing that will allow us to get more material parameters that can be used for MAT 145 and allow us to model progressive deformation and failure in active materials. The material parameters will also be calibrated through combination of testing and computational simulation of battery cells under various loadings.

Development of a 3D Microstructure Model for Battery Separators

The 3D microstructure modeling approach consists of three major steps: (1) image-based statistical characterization, (2) stochastic reconstruction, and (3) FEA with a solid-beam hybrid model. In the first step, microstructure characteristics are characterized from the processed microscopic images (Figure 12). In the processed image, the lamellae phase is represented by black pixels and the “porous phase” (thin fibrils and voids) are represented by white pixel clusters. The size of the “porous phase” is characterized using t-copula model, as the height and width of the white clusters are correlated random

quantities. The profile of the “porous phase” boundaries, which can be considered of a curve with randomness, is characterized using Gaussian copula random process model.

In the second step, 3D microstructure reconstructions are generated based on the statistical models of microstructure characteristics. The size and geometry of each “porous phase” cluster is determined by sampling the statistical models obtained in the previous step. The “porous phase” and the lamellae phase are modelled by voxels of different values.

In the third step, the reconstructed 3D microstructure is converted into a Finite Element mesh in LS-DYNA and a solid-beam hybrid model is developed. The voxels representing the lamellae phase are converted into solid elements, and the thin fibrils are modeled by beam elements. Orthotropic elastic-plastic material model is used for the solid elements, and elastic model is used for the beam elements. Compared to the pure solid element models, the solid-beam hybrid model has significantly less number of elements, so it enables the modeling of a larger physical domain ($1.04^3 \mu\text{m}^3$). We have tested the model in two simulations: uniaxial tension along the machine direction (Figure 14), and uniaxial tension along the transverse direction (Figure 15).

The simulated material properties are compared to the experimental testing data reported in literature (Figure 16). It is demonstrated that the 3D microstructure model can successfully capture the anisotropic behavior of the microstructure model. However, the prediction accuracy needs to be improved by calibrating the constitutive models.

Conclusions:

With the one-year extension and new schedule, the project is progressing well and should be completed successfully before the end of the next year. The use of composite t-shell elements in mechanical, electromagnetic and thermal solvers has been demonstrated to greatly reduce computation while maintaining accuracy. Material input parameters for the new models and solvers have been obtained through experimental tests and modeling, including the newly developed modelling of the 3D microstructure of commercial separators.

References:

- [1] Atkins AG. Thin Sheet Fracture. In: Milne I, Ritchie R, Karihaloo B, editors. Comprehensive Structural Integrity: Elsevier; 2003.
- [2] Andreasson E, Kao-Walter S, Stahle P. Micro-mechanisms of a laminated packaging material during fracture. *Engineering Fracture Mechanics*. 2014;127:313-26.
- [3] Sarah Bateau-Meyer, Pierre L’Eplattenier, Jie Deng, Min Zhu, Chulheung Bae, Theodore Miller, “Randles circuit parameters set up for battery simulations in LS-DYNA”, Proceedings of 15th International LS-DYNA Users Conference, 2018.
- [4] Jie Deng, Chulheung Bae, James Marcicki, Alvaro Masias, Theodore Miller, “Safety modelling and testing of lithium-ion batteries in electrified vehicles”, *Nature Energy*, 3, 261-266, 2018

- [5] Jie Deng, Chulheung Bae, Theodore Miller, Pierre L'Eplattenier, Sarah Bateau-Meyer, "Accelerate battery safety simulations using composite tshell elements", Journal of The Electrochemical Society, 165, A3067-A3076, 2018.
- [6] Jie Deng, Min Zhu, Chulheung Bae, Theodore Miller, Pierre L'Eplattenier, Sarah Bateau-Meyer, "Safety modeling of lithium-ion batteries under mechanical abuse", Proceedings of 15th International LS-DYNA Users Conference, 2018.
- [7] Kalnaus S, Wang YL, Turner JA. Mechanical behavior and failure mechanisms of Li-ion battery separators. Journal of Power Sources. 2017;348:255-63.
- [8] Kalnaus S, Kumar A, Wang YL, Li JL, Simunovic S, Turner JA, et al. Strain distribution and failure mode of polymer separators for Li-ion batteries under biaxial loading. Journal of Power Sources. 2018;378:139-45.
- [9] Kalnaus S, Wang YL, Li JL, Kumar A, Turner JA. Temperature and strain rate dependent behavior of polymer separator for Li-ion batteries. Extreme Mechanics Letters. 2018;20:73-80.
- [10] Merchant HD, Khatibi G, Weiss B. Elastic and elastoplastic response of thin copper foil. Journal of Materials Science. 2004;39:4157-70.
- [11] Wang H, Simunovic S, Maleki H, Howard JN, Hallmark JA. Internal configuration of prismatic lithium-ion cells at the onset of mechanically induced short circuit. Journal of Power Sources. 2016;306:424-30.
- [12] Zhu JE, Li W, Xia Y, Sahraei E. Testing and Modeling the Mechanical Properties of the Granular Materials of Graphite Anode. Journal of the Electrochemical Society. 2018;165:A1160-A8.
- [13] Jie Deng gave a presentation at the 15th International LS-DYNA Users Conference in Dearborn, MI on June 12, 2018.

Figures Begin on the Next Page

Figures:

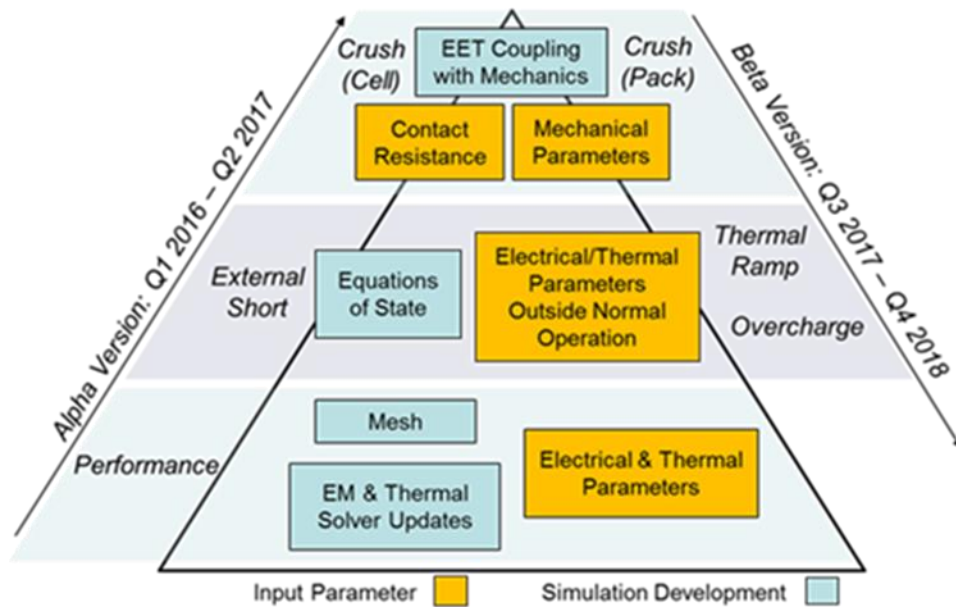


Figure 1. Project schematic showing major constituents and progression of Alpha and Beta versions.

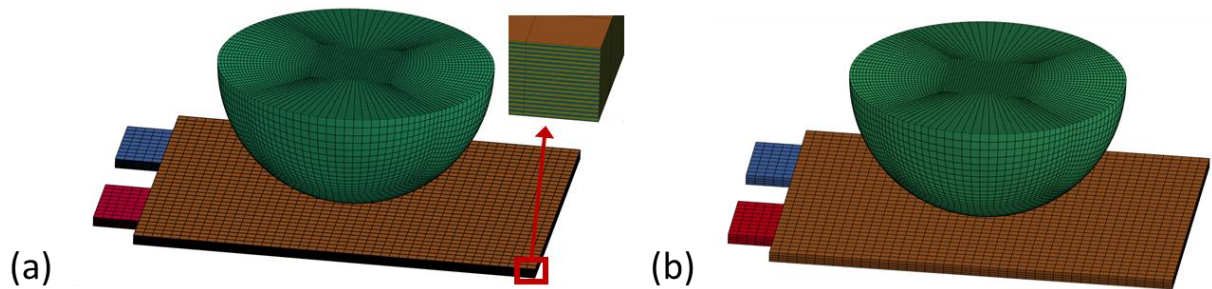


Figure 2: Two models for the battery impact simulation. These models have the same settings except that different elements, (a) solid elements and (b) composite t-shell elements, are used in the cell bulk.

Figures Continue on the Next Page

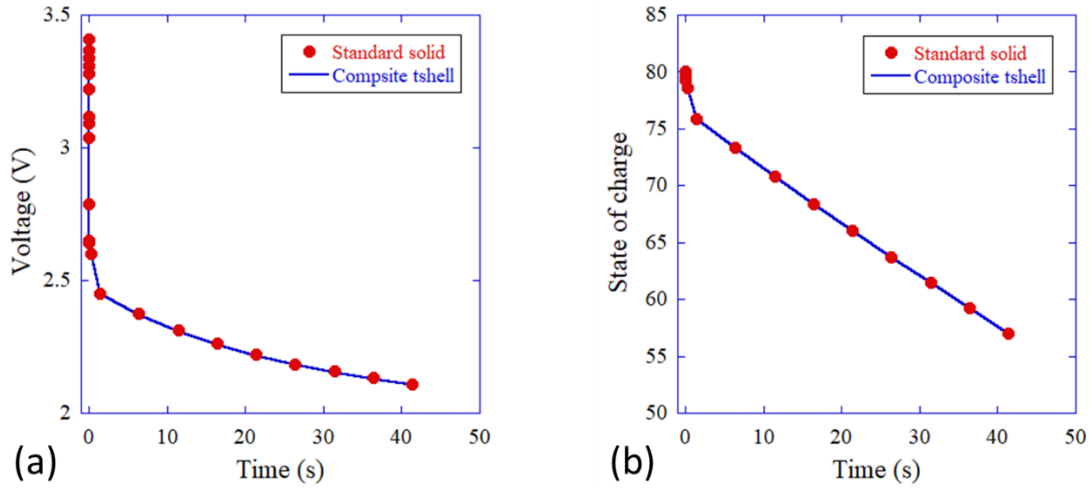


Figure 3: Comparison of (a) voltage and (b) state of charge evolution in two types of models.

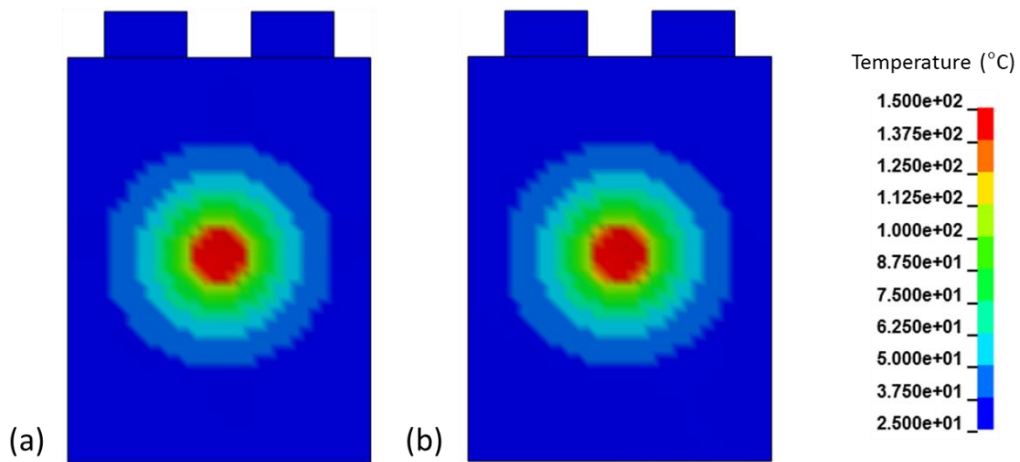


Figure 4: Comparison of temperature distribution at 41 seconds in (a) the composite t-shell element model and (b) macro model.

Figures Continue on the Next Page

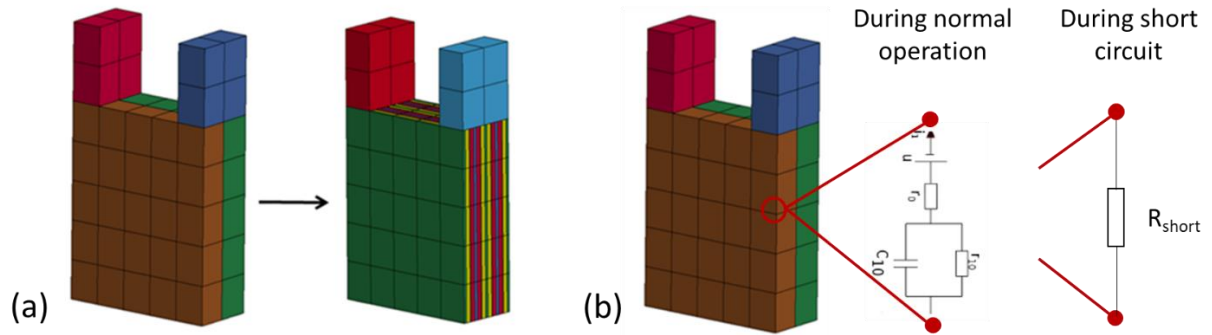


Figure 5: Both (a) composite tshell models and (b) macro models can use a small number of elements in the cell thickness direction. The difference is that in the former, the EM and thermal solvers rebuild a mesh internally to resolve each individual layers. In the latter, no internal mesh is needed, and each node contains two potential fields connected by either Randle circuit or short-circuit resistance depending on local parameters such as stress, strain or temperature.

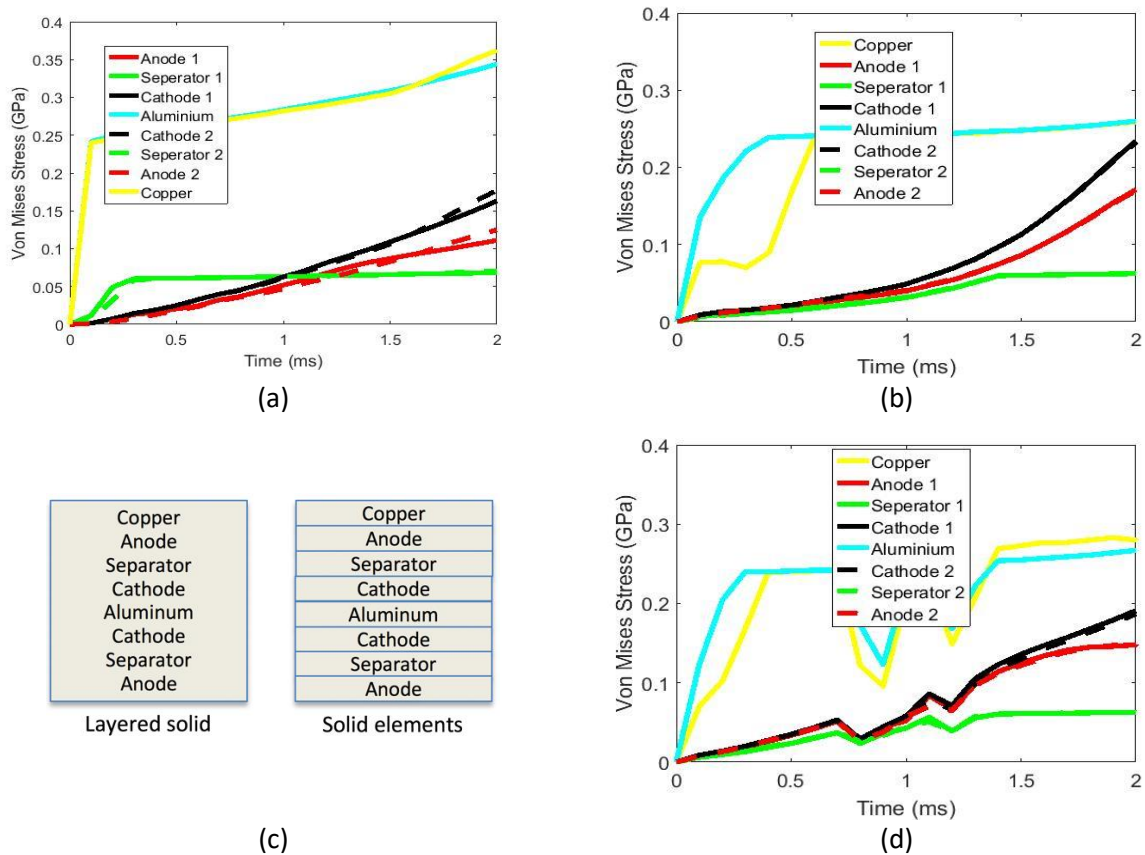


Figure 6: Comparison of the cell stresses in the (a) layered solid and (b, d) solid element assembly. In (b), the four top unit cells are resolved, and in (d) all unit cells are resolved. The layers in one unit cell is shown in (c).

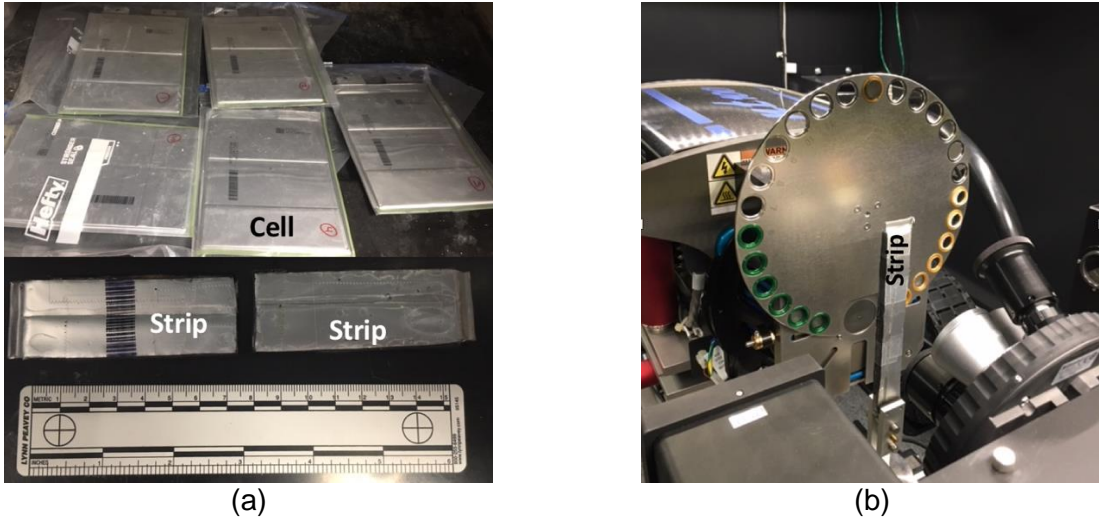


Figure 7: X-ray tomography of deformed cells (a) cell sectioning, and (b) scanning.

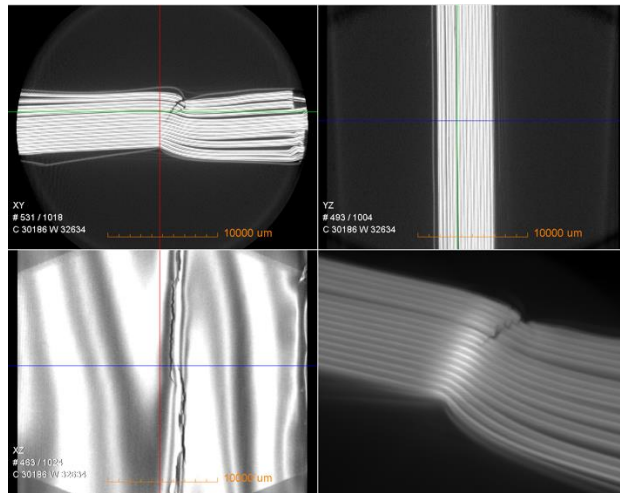


Figure 8: X-ray tomography of the internal damage in a sheared cell.

Figures Continue on the Next Page

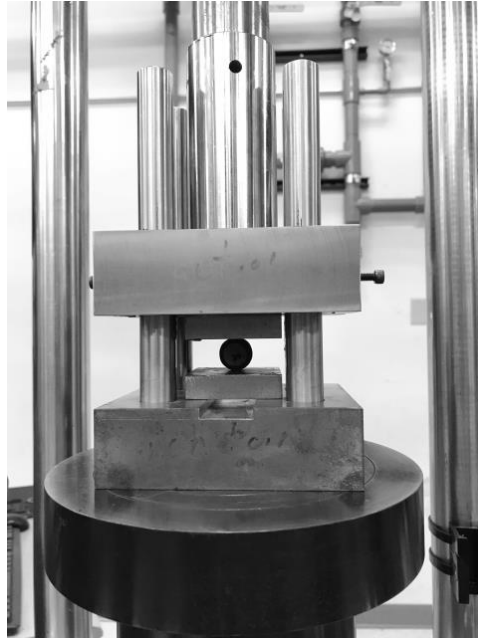


Figure 9. Experimental test for lateral compression of active material specimen.

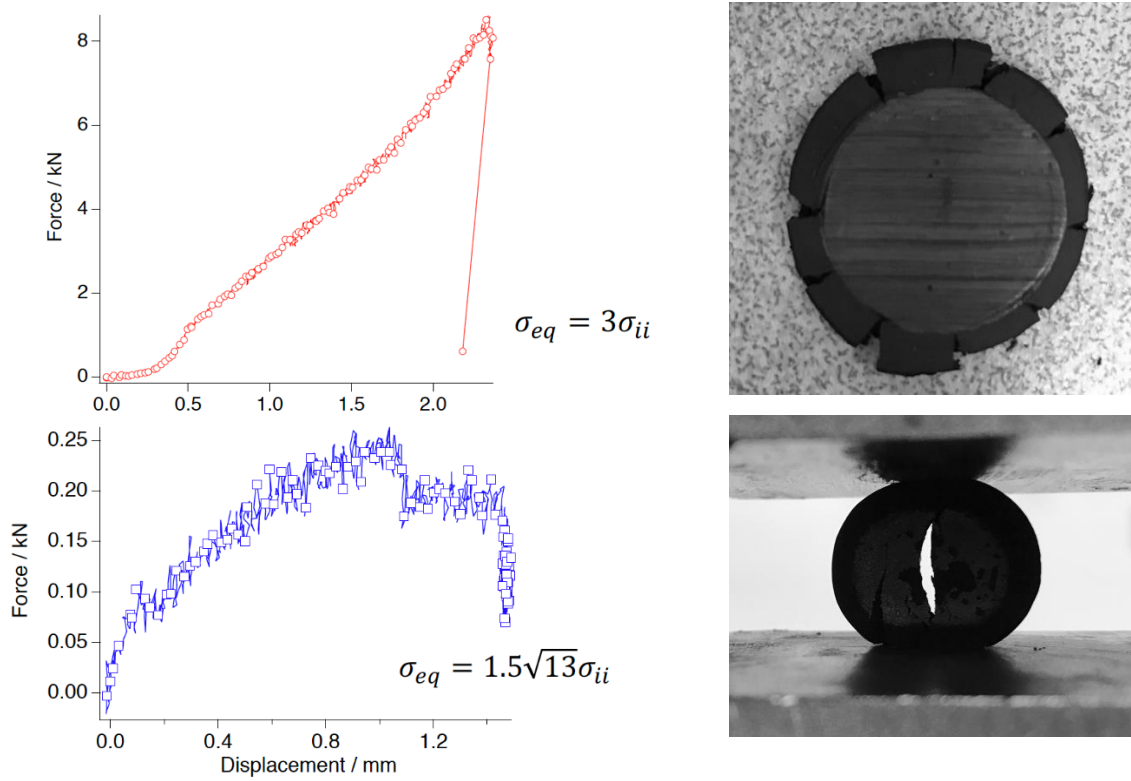


Figure 10. Experimental results for uniaxial and lateral compression test of active material specimens.

OPSEC1890

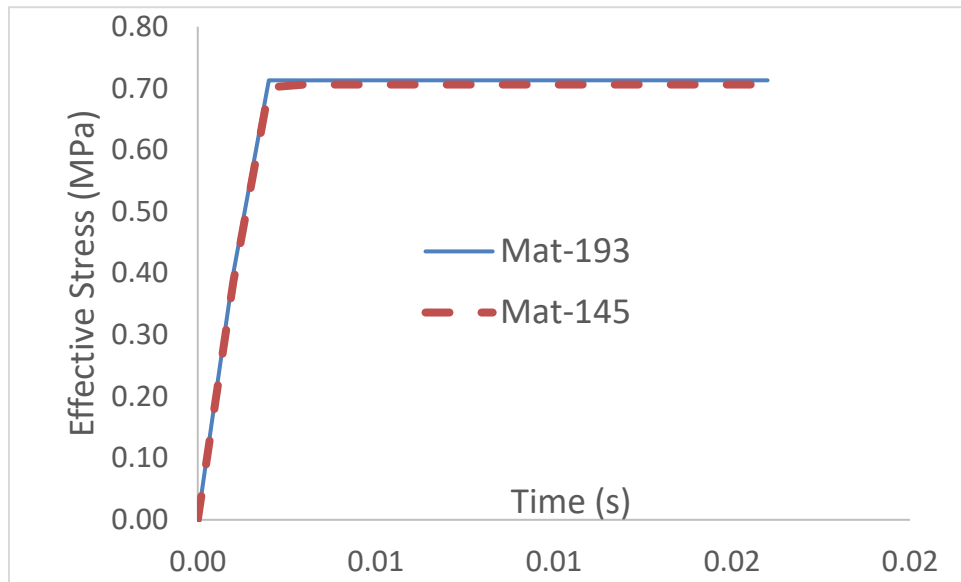


Figure 11. The uniaxial compression test response for LS-DYNA materials 145 and 193.

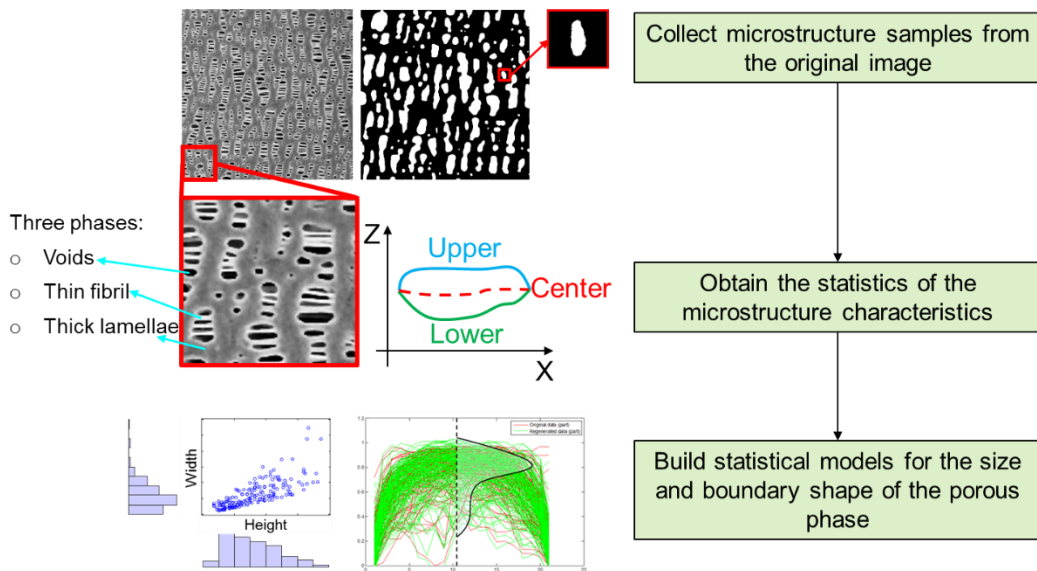


Figure 12: Characterization of microstructure characteristics based on image analysis.

Figures Continue on the Next Page

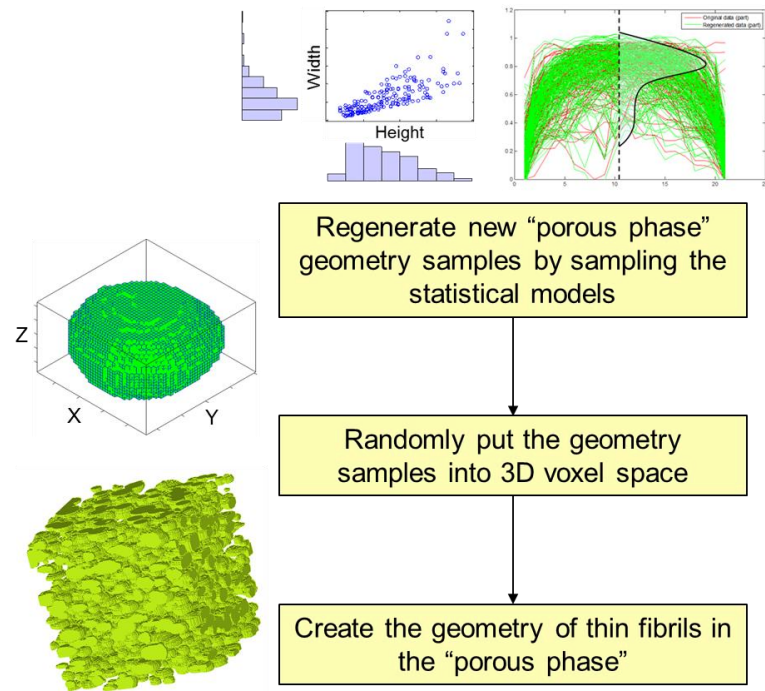


Figure 13: Stochastic reconstruction of 3D microstructures. The reconstructed "porous phase" is shown in green pixel. The lamellae phase is not shown.

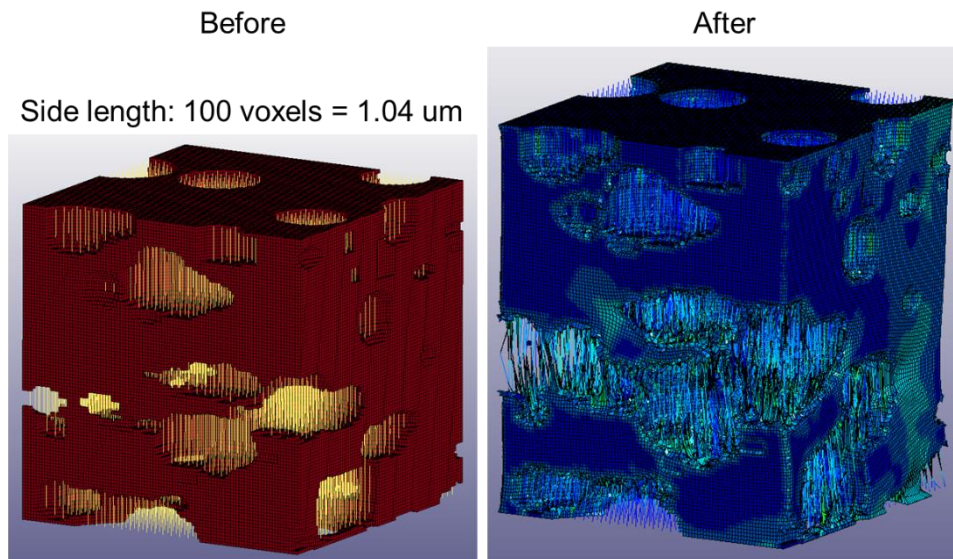


Figure 14: Solid-beam hybrid model. Tension along the machine direction.

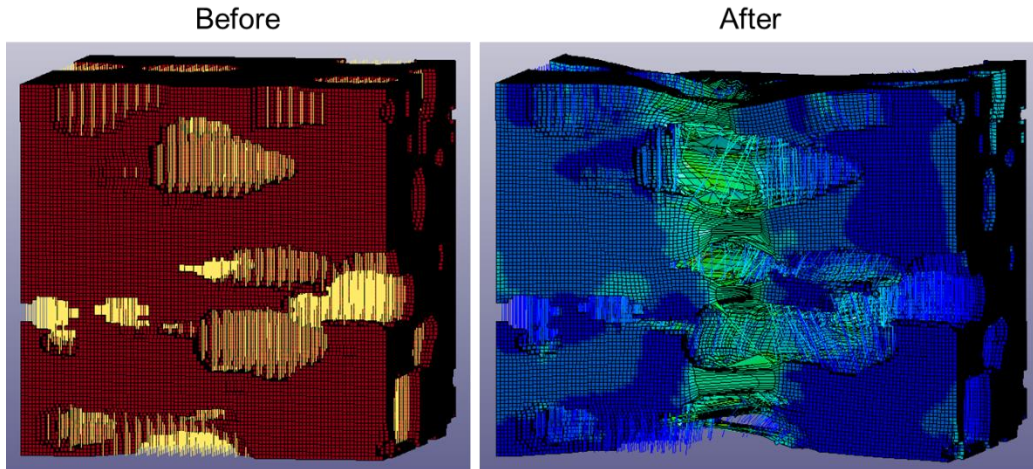


Figure 15: Solid-beam hybrid model. Tension along the transverse direction.

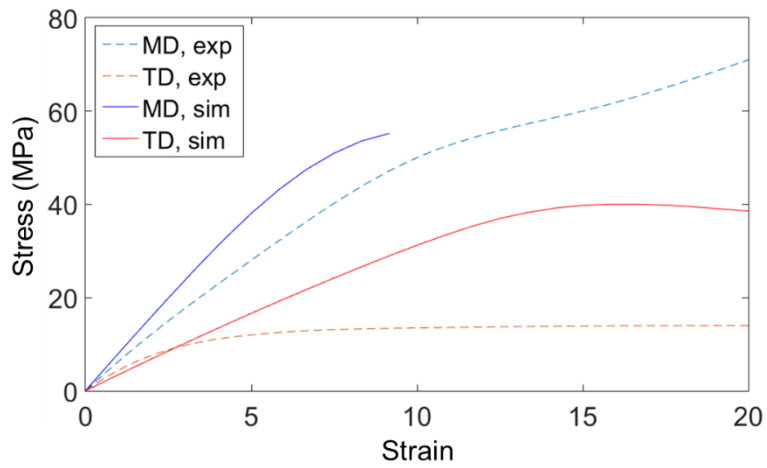


Figure 16: Simulation results: stress-strain curves on machine direction (MD) and transverse direction (TD).

Remainder of Page Intentionally Blank

This Page is Intentionally Blank

AVPTA Technology Focus Area 6: Energy Storage & Batteries

Self-Forming Thin Interphases and Electrodes Enabling 3-D Structures High Energy Density Batteries

**DOE-VTO TFA Lead: Tien Duong
TARDEC TFA Lead: Laurence Toomey**

**Principal Investigator(s):
Dr. Glenn G. Amatucci**

**Affiliation:
Rutgers, The State University of New Jersey
Energy Storage Research Group
671 US Highway 1
North Brunswick, NJ 08902**

**Project Start: Q2FY16
Estimated Completion: Q4FY19**

Objectives:

- Develop and implement a novel *in-situ* formed lithium-metal-based metal fluoride battery that will enable packaged 10mAh batteries of energy density > 1000 Wh/L and specific energy > 400 Wh/kg at 12 V, by the end of the program
- Establish negative reactive current collector compositions that enable high efficiency of lithium plating and stripping in excess of 90% during the *in situ* formation step and > 95% during subsequent cycles
- Establish optimal type and composition of bi-ion conductors that achieve ionic conductivities in excess of 1×10^{-4} S/cm after *in situ* formation
- Establish cell-stack designs with 75% utilization of the positive reactive current collector and 12 V
- Achieve self-formed cell stacks with energy densities of at least 750 Wh/L and 200 Wh/kg, and >80% capacity retention after 20 cycles at a rate of C/10
- Achieve 12 V output within one planar design

Remainder of Page Intentionally Blank

OPSEC1890

Strategic Context:

- Reduce battery weight and volume burden by developing: 1) electrochemical systems with the highest practical energy density, and 2) unique pathway to high voltage systems enabling high energy density packaged cells
- Develop safe energy storage systems with non-flammable solid state electrolytes that would reduce abuse tolerance during shipping and operation
- Develop safe and cost effective energy storage systems with the elimination of lithium metal during fabrication, handling and shipping
- Develop cost effective fabrication processes with the maskless scalable patterning technique providing potential for high throughput and low material cost that would reduce cost of complex architecture fabrication
- Utilize low cost materials to further decrease overall costs.

Accomplishments:

- Achieved bi-ion conductors of $> 1 \times 10^{-4}$ S/cm ionic conductivities after *in situ* formation
- Achieved $> 90\%$ Li utilization at the negative electrode during formation, $> 95\%$ thereafter
- Identified limiting transport pathways within the positive electrode
- Demonstrated nanolayered multicomponent structured architectures improved utilization and areal capacity by a factor 2
- Demonstrated mixed conductor nanolayered multicomponent structured architectures improved electrochemical performance
- Achieved positive electrode utilization of $> 75\%$ at 2.5 V
- Identified formation/priming protocols beneficial to electrochemical performance
- Identified chemistry encapsulation favorable to electrochemical performance
- Transitioned from a single 2.5 V cell technology configuration to 12 V baseline configuration and demonstrated parity
- Achieved reproducible self-formed baseline cells with 12 V output voltage.

Introduction:

This project remains extremely relevant with the potential to bring a step change in energy density, cost, safety and high voltage scalability of battery technology compared to the current state of the art secondary battery technologies. The technology is based on an *in-situ* formed solid-electrolyte battery leading to high energy metal fluoride vs. lithium metal chemistry in a planar battery electrode format and provides the following advantages: 1) enabling the use of lithium metal electrodes via solid-state electrolytes, 2) eliminating Li metal in fabrication and handling of cells, 3) providing the highest practical energy density electrochemical system, and 4) enabling a unique pathway to high voltage systems.

In FY17, the team showed consistent progress in energy density and achieved high energy density with solid state cells > 570 Wh/L in our single cell technology at 2.5 V. All cell fabrication was performed using a low cost maskless scalable patterning technique we implemented in mid FY17. Solid state cells comprise bi-ion conductors whose compositions were demonstrated to

achieve ionic conductivities in excess of 1×10^{-4} S/cm after *in situ* formation (FY18 Milestone), one year ahead of schedule. Lithium utilization at the negative electrode above > 90 % during formation and > 95 % thereafter (FY18 Milestone) was also demonstrated ahead of schedule. As such, much effort this year focused on the in depth analysis of the positive electrode and particularly the impact of transport and mechanical stability on electrochemical performance. In addition, we implemented our technology to higher voltage with a 12 V electrochemical cell.

Approach:

We chose to fabricate our solid state *in-situ* batteries with a maskless scalable patterning technique. The rationale is that such maskless scalable patterning technique offers a pathway to high throughput, low material loss and fabrication of complex architectures. The resulting solid state *in-situ* cells have shown transport barriers in positive electrode that need to be addressed in order to optimize utilization and discharge rate and achieve our milestones. The team has shown in FY17 that hybridization of transport pathways successfully improved discharge rates up to the desired C/10. This year we isolated the positive electrode in order to evaluate and optimize its properties in a more traditional stacking arrangement that we developed. In parallel, we also optimized the formation/priming protocols of the single planar architecture for long cycle life. Finally, the single solid state *in-situ* self-formed baseline technology was translated into a 12 V baseline technology.

Results and Discussion:

Bulk transport: Multicomponent nano-layered structured architectures.

The early half of FY18 was directed at identifying and understanding the limitations of transport within the positive electrode. We isolated the positive electrode formation reaction and evaluated the cell components in a more traditional stacked arrangement. Such study determined transport properties were mainly limited by diffusion. In order to promote F^- ion transport, shorter pathways needed to be created. In response, the team developed a unique vapor deposition technique that enabled the rapid fabrication of new multicomponent structured architectures with features in the nanoscale. These nanostructured composite of enhanced F^- ion transport resulted in the improvement of the positive reactive electrode utilization/capacity by a factor 2 leading to 78% and > 1000 mAh/cc, with areal capacity approaching 0.4 mAh/cm². Nanostructured architectures have also enabled improved cycling stability as shown in Figure 1. In short, multicomponent nano-layered structured architectures demonstrated drastic improvement of cell electrochemical performance: positive electrode utilization / capacity / cycling stability.

Bulk transport: Mixed conductor electrodes

Utilizing our unique nano-layering process enabled control of the chemistry of the multicomponent structure via additives to modify the type of conductivity, ionic (Li^+ and F^-) and/or electronic, and the amount of transport pathways within the bulk of the solid state electrode structure. Figure 2 shows the three types of nano-layered additives investigated

for the positive electrode. Layer additive “A” enhanced the ionic transport which resulted in a slight increase in capacity retention. Layer additive “B” enhanced electronic conductivity but resulted in a detrimental effect on capacity. Layer additive “C” was a hybrid composition that enhanced both electronic and ionic transport. This mixed conductor provided the best performance as it resulted in an increase in capacity by 40% and improved capacity retention. As such, transport limitations were identified as both ionic and electronic. In conclusion, mixed conductor multicomponent nano-layered structured architectures demonstrated enhanced electrochemical performance: positive electrode utilization / capacity / cycling stability.

Mechanical stability.

In the third quarter we focused on the mitigation of stress/strain energy to produce more uniform transformations during reactions for longer cycle life. One particular area of focus was on optimization of cycling protocols. As previously reported, we included studies on pulsed charging steps and addition of intermediate slow discharge formation steps prior to our standard discharge protocols. Our investigations concluded the most beneficial impact came from the additional slow intermediate discharge step. It was determined that this “priming” step allowed for a more uniform distribution in nucleation so that transformations during reactions are less likely to create highly concentrated areas of active components leading to mechanical failure. Finally, cells were encapsulated to apply light pressure and protect the chemistry from environment exposure. Encapsulation of chemistry seemed to improve reaction uniformity in the formation step as demonstrated by good capacity retention followed by increased capacity output at a higher rate. In short, “priming” with slow intermediate step and encapsulation were beneficial to electrochemical cycling.

12 V cell architecture development.

In the late third and fourth quarter, the focus of our research shifted from addressing transport limitations and mechanics to enabling another one of our goals, the development of a 12 V architecture. Our first high voltage design showed limited voltage output with 8 V revealing transport issues related to the structure. Optimization of the cell reorientation to simplify transport pathways enabled the successful achievement of an electrolytically formed cell with a 12 V output voltage. These new 12 V architectures have been fabricated reproducibly, charged to an excess of 12 V and subsequently successfully discharged. However, positive electrode utilization was poor since these initial cells were fabricated as baseline designs without any of the chemical and nano-structural improvements we developed at low voltage. As we previously reported, diffusion limitations prevent full access to the cell’s electrochemically active materials inducing inactive pockets thereby leading to low utilization. The first phase of improvement we conducted on the 12 V cell architecture focused on the design optimization at the electrode level and layout. This was executed with variations in the electrode design, aspect ratio, thickness and electrode width. Figure 3 depicts some of the results for modifications of electrode thickness and width studies. From this investigation, it was determined that decreasing the aspect ratio of the electrodes and

OPSEC1890

thereby increasing the surface area enhanced diffusion properties thereby enabling access to previously electrochemically inactive pockets within the cell. This increased utilization by 18%. Within the electrode design optimization, other limiting factors to the positive electrode utilization include discontinuity in electrolyte coverage. The presence of a physical break in the continuity of the reactive electrolyte was discovered only later during finer analysis. Increasing the reactive electrolyte thickness to ensure proper coverage significantly improved the positive electrode utilization to approximately 40%. Figure 4 shows the voltage profile for the first cycle of a 12 V cell with both increased electrolyte thickness and electrode cell modifications charged to 14 V and subsequently discharged to 7.5 V in a stepped discharge protocol. Moving forward, we plan to aggregate the chemical and nano-structural advances we made on the 2.5 V format to the 12 V format and achieve > 75 % utilization within the 12 V architecture.

Conclusions:

Continued progress has been made toward the development of a high energy solid state battery technology and 12 V output platform. Characterizing the transport properties of the positive electrode enabled the identification of pathways to advance electrochemical performance including capacity, cycle life, and utilization. To date, we have achieved a positive electrode utilization of > 75 % by moving towards multicomponent nanostructured architectures. Mixed conductive additives in these positive nano-layered electrodes have showed an increase in capacity by 40%. In addition, formation/priming protocols and chemistry encapsulation have demonstrated improvements in cycling stability. Finally, our 2.5 V single cell technology (baseline) was successfully translated into a 12 V planar cell (baseline) demonstrating parity in performance. In FY19, we plan to apply our positive electrode modifications to the 12 V cells in order to achieve next years' milestone of > 90 % utilization and deliver 10 mAh cells that achieve energy densities of 1400 Wh/L and 600 Wh/kg per cell stack.

References:

N/A

Figures Begin on the Next Page

Figures:

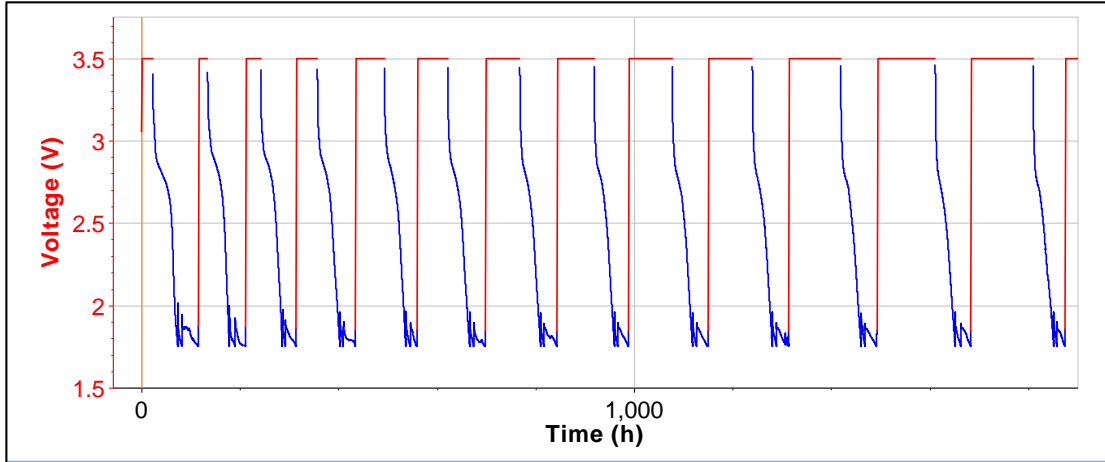


Figure 1. Constant voltage charge (red) /constant current discharge (blue) profile representative of multicomponent structured architecture cells cycled between 1.75 and 3.5 V.

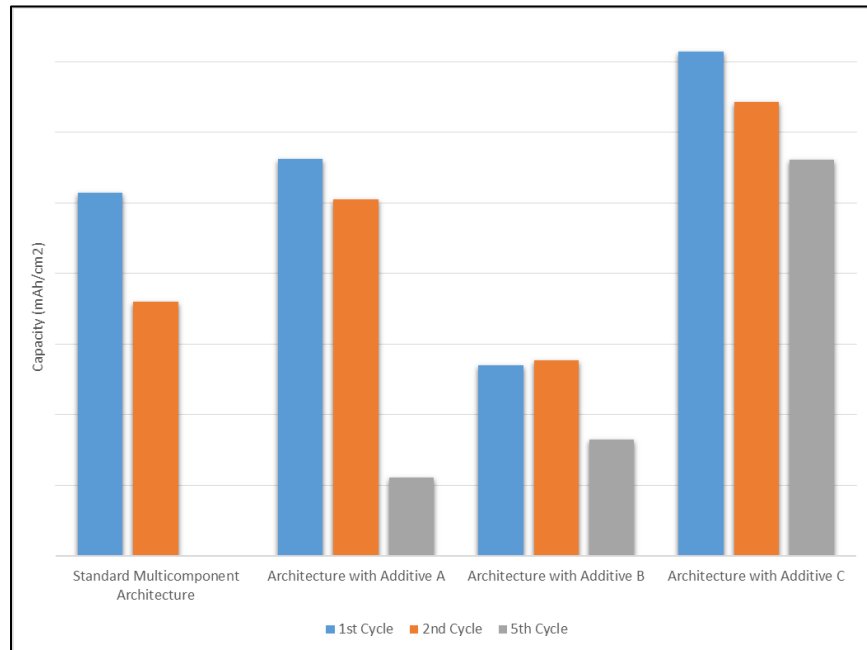


Figure 2. Impact of transport additive composition on discharge capacities of solid state multicomponent nanolayered structured architecture cells in the 1st, 2nd and 5th cycles. Additives A, B and C enhance ionic, electronic and mixed conductivity, respectively. Cells cycled between 1.75 and 3.5V.

Figures Continue on the Next Page

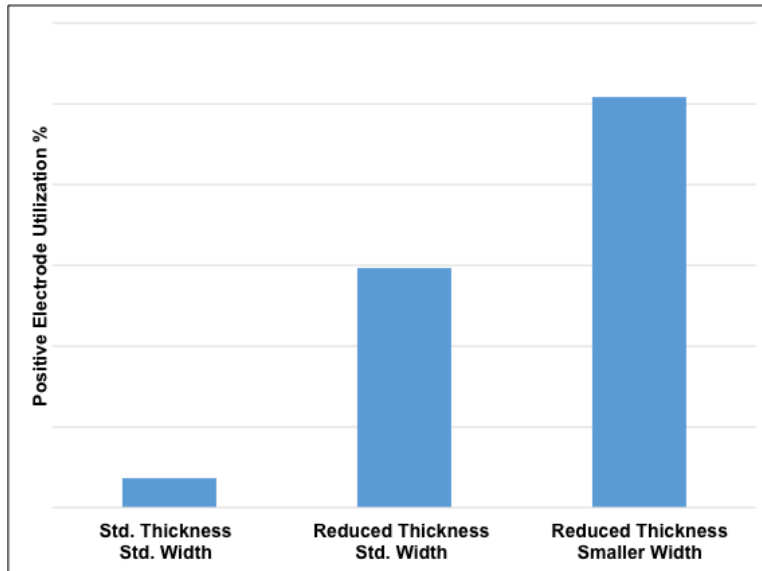


Figure 3. Impact of electrode design, including electrode thickness and width, on the positive electrode utilization of 12 V *in-situ* cells. Cells were cycled between 7.5 and 13.5 V. By decreasing the aspect ratio of the electrodes and thereby increasing surface area, enhanced diffusion properties enabled access to previously electrochemically inactive areas leading to higher utilization.

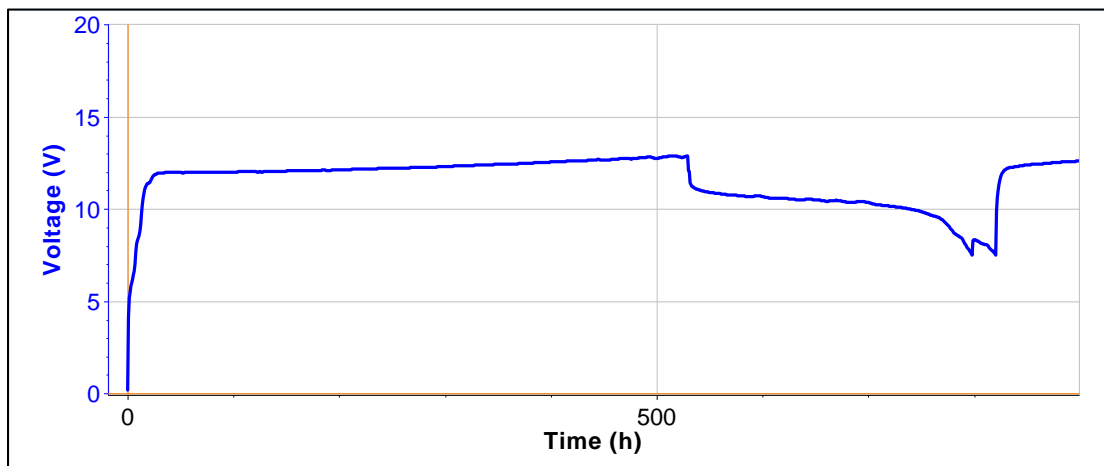


Figure 4. First cycle voltage profile for self-formed 12 V cell with improved transport pathways due to cell design modifications and increased reactive electrolyte thickness. The cell was charged up to 14 V before undergoing a stepped discharge protocol down to 7.5 V.

Remainder of Page Intentionally Blank

This Page is Intentionally Blank

AVPTA Technology Focus Area 6: Energy Storage & Batteries

Advanced Lithium Ion Battery Technology – High Voltage Electrolyte

DOE-VTO TFA Lead: Tien Duong
TARDEC TFA Lead: Laurence Toomey

Principal Investigator(s):
Dr. Ron Hendershot, Dr. Joseph Sunstrom, Dr. Alec Falzone

Affiliation: Daikin America, Inc.

Non-TARDEC Address:
2749 Highway 20 West Suite A
Decatur, AL 35601

Project Start: Q2FY18
Estimated Completion: Q4FY19

Objectives:

- Understand lithium ion battery gassing mechanisms and kinetics as a result of electrolyte decomposition.
- Examine both physical and chemical aspects of film formation on the anode and cathode in lithium ion batteries
- Observe any chemical and structural changes at the electrode surfaces under various operating conditions.

Strategic Context:

- Developing an electrolyte for lithium ion batteries capable of long-term operation at high voltage (> 4.5 V) will increase power density and improve energy efficiency to both new and retrofitted ground systems.
- Minimizing cell decomposition as a result of gas generation will enable safer operation of high-powered vehicles and devices in addition to extending cycle life.

Accomplishments:

- Installation of new scientific equipment and training to enable examining film characteristics of the anode and cathode (XPS and AES).
- Developed various methods for determining the thickness SEI layers on cathode materials.

OPSEC1890

- Established elemental and chemical compositional differences of the SEI layer as a function of various parameters: electrolyte formulation, voltage, etc.
- Increased the capacity retention at high voltage with the addition of fluoroethylene carbonate (FEC) to the electrolyte. Optimization of electrolyte-cathode chemistry conditions after reviewing obtained data from FY2017 and FY2018.

Introduction:

The use of electrolytes containing small fluorinated molecules to enable stable high voltage (> 4.3 V) battery operation is the focus of this project. Previously, Daikin has shown that it is possible to operate lithium ion batteries utilizing several different cathode chemistries up to 4.5 V. This is accomplished by reducing the gas generation originating from electrolyte decomposition at high voltage. The primary mechanism for this is not completely understood, but the hypothesis is that the fluorinated molecules form a film on the highly oxidizing cathode. It is known that battery cycle performance above 4.5 V drops significantly, however the source of the observed performance loss is not yet understood. The target for this project is to achieve 300 cycles above 80% capacity retention at 4.6 V. A better understanding of gas evolution, which happens above 4.3 V and the failure mode above 4.5 V, is sought in order to propose mitigation strategies which will facilitate better high voltage performance in lithium ion batteries.

The battery industry trend for cathode materials is toward reducing the overall cobalt content (i.e. higher nickel) for a variety of reasons. Some of which include: increasing cost, loss of supply, and human rights issues. The experiments proposed for this project will encompass a range of cathode materials with successively higher nickel content. This will be performed in order to comprehend how fluorinated electrolyte interacts with various cathode surfaces. This is with the anticipation that the lithium ion battery industry will move towards nickel-rich cathodes, which can operate at higher voltage in order to achieve more energy-dense batteries.

Approach:

The baseline of current best-practice fluorinated electrolyte was determined by reviewing already obtained data from high-voltage lithium ion batteries from a previously funded project (DOE EE0006437). In parallel, an up-to date literature and patent review has also been performed to explore other cutting edge developments in 2017. Three electrolytes were selected as standards for this project: 1.2 M LiPF₆ ethylene carbonate (EC)/ethyl methyl carbonate (EMC) 80:20 (v/v %), 1.2 M LiPF₆ EC/EMC/fluoroether (FE) 20:60:20 (v/v %) and 1.2 M LiPF₆ FEC/EMC/FE 20:60:20 (v/v %). These represent electrolytes with zero, one and two fluorinated solvents added, respectively. All electrolytes also contain propane sultone (PS) (1% w/w) as an additional anti-gassing additive. 200 mAh dry wound cells have been purchased as test vehicles. The cathode chemistries studied (with increasing mole fractions of nickel are: LiCoO₂ (LCO), LiNi_xMn_yCo_zO₂ (NMC xyz = 111, 532, 622) and LiNi_{0.8}Co_{0.15}Al_{0.05}O₂ (NCA) all paired with artificial graphite anodes. Analysis of the gases produced at high voltage (> 4.3 V) will be completed and compared to cells cycled at a baseline voltage of 4.2 V, which is the current battery industry standard. A post mortem analysis of the gas sampled cells will be conducted for qualitative and quantitative gas analysis. In addition, the cathodes and anodes will be removed for surface analysis to observe SEI film formation and changes in material properties. A mass balance

approach to the cells will be used in order to propose performance limiting factors and strategies to overcome them.

Results and Discussion:

Film Composition (Elemental) vs. Time/Voltage

During FY2017, efforts were focused on investigating gassing mechanisms observed during high voltage operation of lithium ion batteries. Throughout these studies varying compositions of electrolyte were tested and compared to the baseline, hydrocarbon (HC) electrolyte (1.2M LiPF₆, 80% EMC, 20% EC, 1% w/w PS). Analysis of the electrochemical data supports the hypothesis that a more fluorinated electrolyte results in better performance above 4.5 V compared to the hydrocarbon electrolyte. One contributing factor in the high-voltage performance of lithium ion batteries utilizing a highly fluorinated electrolyte is the formation of a protective film, or SEI layer, on the cathode surface.

Determination of the SEI layer's elemental composition uses Auger Electron Spectroscopy (AES) as the first method of analysis. Figure 1 depicts the elemental survey scans of a dried, uncycled NMC622 cathode (left) and a NMC622 cathode cycled at 4.6 V with a highly fluorinated electrolyte (right) both before and after a depth-profile experiment. In addition to AES identifying the elemental components of the SEI layer, it also serves as a technique to determine the film's thickness. AES depth profile experiments study changes in the surface composition as a function of depth of the material.

As seen in survey scans pre-depth profiling (Figure 1), the surface elemental composition is almost identical, even after cycling at 4.6 V. The strongest signal comes from Carbon, and is present in many forms (adventitious, carbon black, PVDF binder, SEI layer, etc.). Oxygen also has a strong Auger signal, largely from the bulk NMC622 cathode material. Lithium (cathode, SEI layer, and electrolyte), Fluorine (PVDF, SEI layer, and electrolyte), Cobalt (cathode), and Nickel (cathode) also contribute to the surface Auger signal.

Following the depth profile, the Auger signal from the transition metals (Mn, Co, and Ni) and oxygen are stronger as the SEI layer is sputtered away, exposing more of the bulk metal oxide material. Carbon's intensity is diminished, in both the cycled and uncycled cathode. Due to the presence of PVDF binder and conductive carbon black throughout the material, its signal is measureable after sputtering. Although the elemental composition of the SEI layer is identical to that of an uncycled cathode, the differences lie in the chemical composition and overall thickness of the amorphous film on the surface. Time-of-Flight Secondary Ion Mass Spectrometry (TOF-SIMS) imaging was performed in collaboration with Physical Electronics, USA (PHI). Investigating the surface composition of NMC622 cathodes through TOF-SIMS provides high-resolution mass spectra in all areas of interest.

Positive mode depth-profile data from an NMC622 cathode cycled at 4.6 V with the hydrocarbon electrolyte is depicted in Figure 2. The metal oxide particles are represented by the transition metals (Ni, Mn, and Co) in addition to Al from the current collector.

OPSEC1890

Aluminum was not detected in any of the cycled cathodes with fluorinated electrolyte, suggesting the protective SEI layer in these cells is thicker and more uniform, and prevents exposure of the current collector after electrochemical testing.

Figure 3 displays the negative mode ions detected using TOF-SIMS in the identical spatial region depicted in Figure 2. Various lithium salts (LiF and LiF_2 for example) are evident both on the surface of the particles, and also in the depressed areas between them. Like that of the transition metal signals, oxygen is largely present on the particles. Residual PF_6^- is the result of salt deposition following the evaporation of organic components in the electrolyte. F^- is heavily prevalent in Figure 3E, originating from both the PF_6^- salt and PVDF binder. No organic fragments with measurable intensity were detected on the NMC622 cathode with the hydrocarbon electrolyte. This suggests that if there is an SEI layer on the surface, it is either disordered or too fragile to be analyzed under identical TOF-SIMS conditions.

In the depth-profile depicted in Figure 4, organic fragments ionized with lithium were observed with significant intensity. These fragments are of similar composition ($\text{C}_x\text{H}_y\text{O}_z\text{-Li}^+$), with a varying amount of carbon and hydrogen ($m/z = 78, 81, 83$). These fragments are located spatially on the surface of the cathode particles, which suggests they are a component of the SEI layer. Lithium ions complexed with water and hydronium are evident in the valleys between particles in Figure 4D.

Figure 5 represents the spatial distribution of negative ions on a cycled NMC622 cathode with a fluorinated electrolyte at 4.6 V. The total negative ion count (TIC) depicted in Figure 5A is of similar intensity to that in Figure 3A (hydrocarbon electrolyte), however the chemical composition of the SEI layer is dissimilar. Evident in Figure 5B are organic fragments comprised of: carbon, hydrogen, oxygen, and fluorine ($m/z = 79, 80, 81$) whereas these are absent from the SEI layer on the cathode with a hydrocarbon electrolyte. Additional organic film fragments in Figure 5C ($m/z = 26, 45, 82$) and D ($m/z = 103, 105, 108$) are only present in the cathode with fluorinated electrolyte, further suggesting the surface composition is electrolyte-dependent. Data analysis of NMC622 cathodes cycled at 4.2 V and with additional electrolyte formulations is ongoing and will provide additional insight into operating condition effects on cathode SEI layer formation.

Film Thickness vs. Time/Voltage

Argon ion sputtering, traditionally calibrated to 1000 Å of O in SiO_2 , coupled with AES is a widely used method to determine material thicknesses. This method serves as the initial approach to measuring the SEI layer in cathode materials. AES survey scans coupled with TOF-SIMS profiling suggest the SEI layer more closely resembles that of a carbon-like material than an oxide layer. Amorphous carbon films were grown on a silicon wafers (UHV Sputtering Inc.), and serve as the sputter rate determinant material. AES depth profiles of the carbonaceous films will then be compared to that of various cathode materials.

Three carbon film thicknesses were fabricated (500, 1000, and 5000 Å) in order to provide a comprehensive understanding of different conditions. Low resolution SEM images are

OPSEC1890

depicted in Figure 6 of the 1000 (A) and 5000 (B) Å films. The underlying silicon substrate is visible on the left, and the bright layer on the right is a sputtered gold layer which serves as an imaging contrast. The black area between the two bright layers is the carbon film. Current efforts are focused on confirming the thickness of these samples using FIB-SEM in collaboration with the Missouri University of Science and Technology.

Figure 7 depicts the average signal from depth profile experiments of cycled (fluorinated electrolyte, 4.6 V) and uncycled NMC622 cathodes using AES. Carbon, Oxygen, and Nickel were the analytes of interest for Auger analysis.

The AES depth profile displays the elemental signal as a function of Argon ion sputtering through the material. Initial AES survey scans suggest the surface composition of both cycled and uncycled cathode materials is carbonaceous, and the bulk cathode material a metal-oxide. Independent depth profile experiments were carried out on each cathode in order to develop a statistically meaningful understanding of the surface chemistry of each condition. The difference in the average Argon ion current to reach the C-O intercept is proportional to the SEI layer thickness on the surface of a cycled cathode. This difference of 4.1×10^{14} Argon ions will be compared to the depth profiles of the amorphous carbon film standards in order to calculate the thickness of the SEI layer.

We are also currently collaborating with Dr. Yi Cui at Stanford University to measure the SEI layer thickness using additional analytical techniques.

Electrochemical Testing of NCA Cells

In addition to investigating the LCO, NMC111, 532, and 622 cathode materials as previously reported we also aim to probe the NCA cathode. NCA is a common cathode for electric vehicle applications, which to date is not capable of long-term operation at high voltage. Preliminary experiments on NCA batteries with a few different electrolytes show promising results we aim to optimize this throughout the project (Figure 8).

As seen with our previously reported work (NMC111, 532, and 622 cells cathodes) cycling above 4.2V requires an electrolyte with a minimum of 10% FEC, with an optimal concentration between 10 and 15%. We are able to retain >85% capacity at high voltage (4.5 V and 4.6 V) after 200 cycles; however, these cells do exhibit significant gassing. Efforts to identify and quantify this gas are ongoing. Figure 9 shows OCV drop and gas volume change results in a 55 °C calendar life test at 4.2 and 4.6 V.

Conclusions:

Significant work at Daikin in the second year involved setup and validation and training for equipment needed to complete this project. This included the commissioning of several new pieces of equipment supporting analysis of the SEI layer, AES and XPS. In addition, several collaborations have been initiated to utilize their expertise and capabilities for film thickness and chemical analysis measurements. In FY2018 we also experienced significant personnel changes, which included the onboarding and continuous training of four team members.

Gas composition and electrochemical testing have been completed for additional cathode materials (NMC111, 532, and NCA). All contain significant amounts of CO, CO₂, CH₄ and O₂ along with select fluorinated hydrocarbons attributed to the decomposition of FEC in the electrolyte at high voltage. Efforts to submit optimized electrolyte/cathode material to the DOE to fulfill FY2018 milestone requirements are ongoing.

The surface elemental composition is identical in both a cycled and uncycled battery. The strongest signal comes from Carbon, and is present in many forms (adventitious, carbon black, PVDF binder, SEI layer, etc.). Oxygen also has a strong Auger signal, largely from the bulk cathode material. Lithium (cathode, SEI layer, and electrolyte), Fluorine (PVDF, SEI layer, and electrolyte), Cobalt (cathode), and Nickel (cathode) are also present. However, the chemical composition varies greatly, and is a function of the electrolyte formulation. There is a protective, fluorinated film that is present on the surface in cathodes using a highly fluorinated electrolyte. This film is not present when the baseline, hydrocarbon electrolyte is used.

Multiple methods for film thickness determination have been identified and implemented. The AES depth profile calibrations to known carbon thickness standards have been successful, and have aided in our deconvolution of the SEI layer's properties on the cathode. Preliminary analysis of the data set suggest the film's thickness in a fluorinated electrolyte after cycling at 4.6 V is < 100 nm, with additional quantification work ongoing.

Following our observation of electrochemical testing in NMC622 and LCO cells, the addition of FEC to electrolyte results in increased cycle life and capacity retention in NMC111, 532, and NCA cells. The full cycling performance benefit of FEC in the electrolyte is realized at a 10% (v/v %), and can be marginally increased with additional FEC. The data obtained thus far for NCA cells (OCV loss, gas evolution, etc.) suggests that the significant amount of gassing observed is an inherent property of the cathode material.

References:

N/A

Figures Begin on the Next Page

Figures:

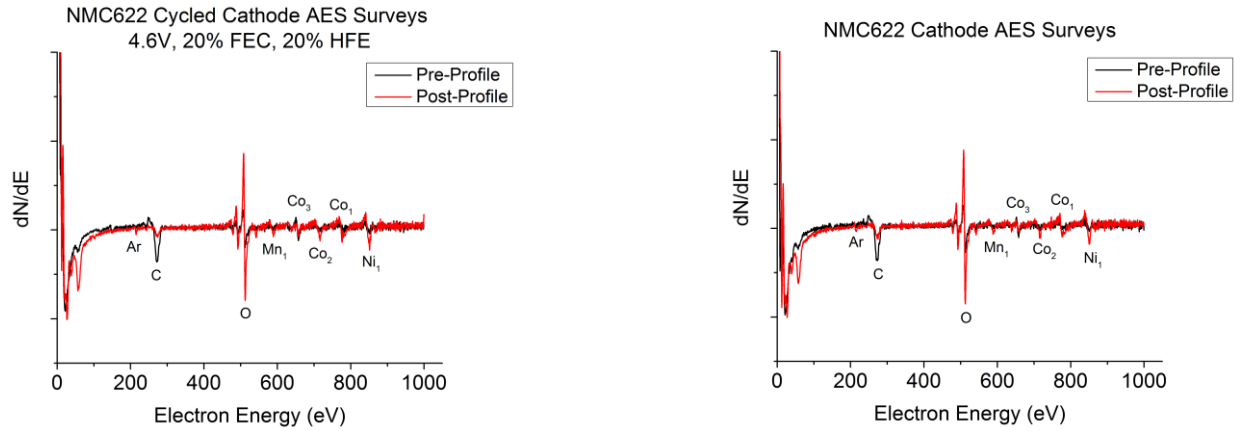


Figure 1. AES survey scan of an uncycled (left) and cycled (right) NMC622 cathode before (black) and after (red) a depth profile experiment

Figures Continue on the Next Page

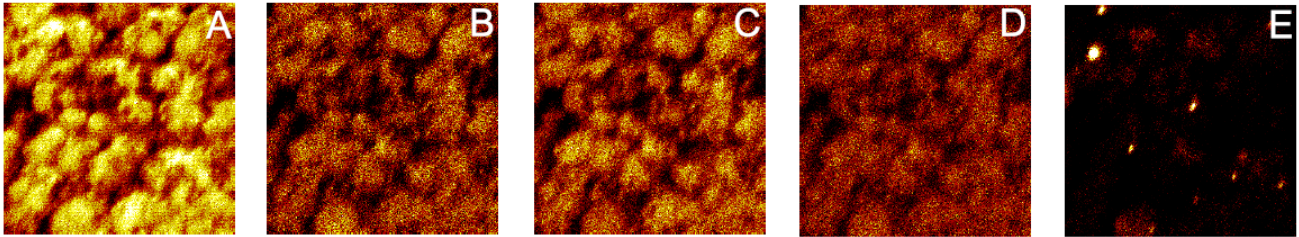


Figure 2: TOF-SIMS maps of positive ions in a cycled NMC622 cathode at 4.6 V with the hydrocarbon electrolyte. A) TIC B) Ni⁺ C) Mn⁺ D) Co⁺ E) Al⁺

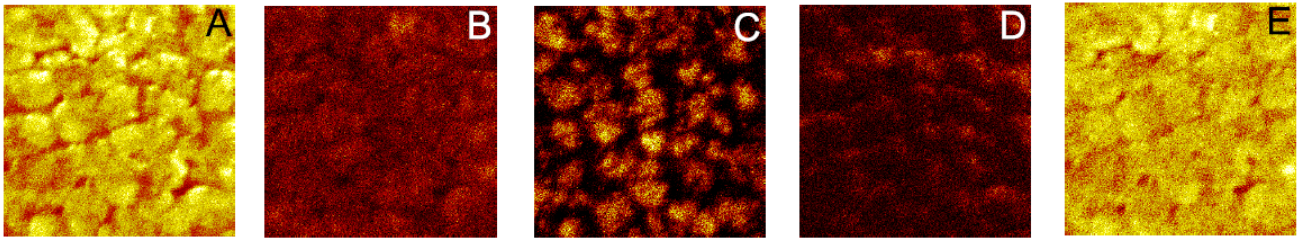


Figure 3: TOF-SIMS maps of negative ions in a cycled NMC622 cathode with the hydrocarbon electrolyte. A) TIC B) LiF⁻ and LiF₂⁻ C) O⁻ D) PF₆⁻ E) F⁻

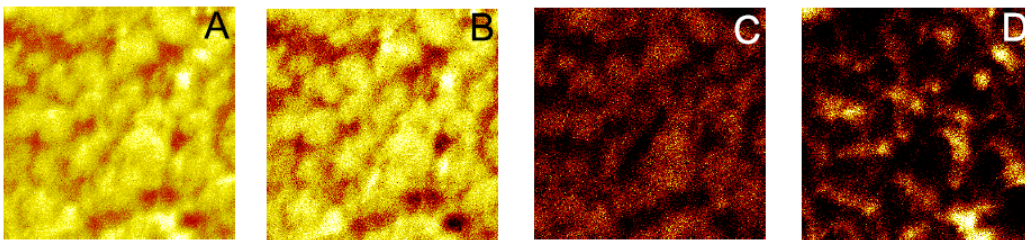


Figure 4: TOF-SIMS maps of positive ions in a cycled NMC622 cathode at 4.6 V with a highly fluorinated electrolyte (1.2M LiPF₆, 60% EMC, 20% HFE, 20% FEC, 1% w/w PS). A) TIC B) Combined Li⁺ C) C_xH_yO_z-Li⁺ D) LiOH₂/LiOH₃⁺

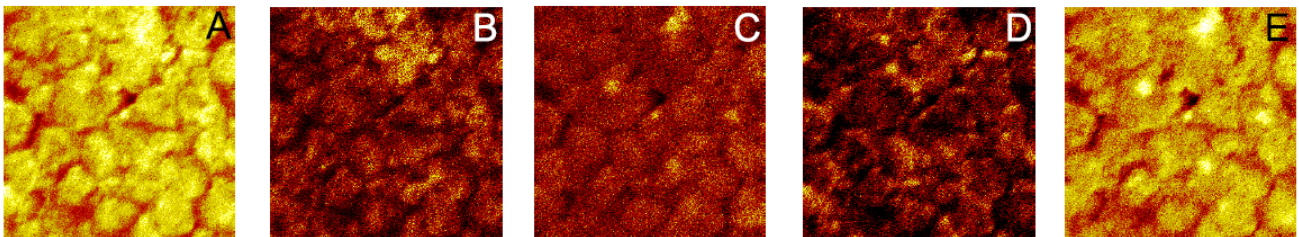


Figure 5: TOF-SIMS maps of negative ions in a cycled NMC622 cathode with the fluorinated electrolyte. A) TIC B) C_xH_yO_zF_w C) C_xH_yO_z D) C_xH_yF_zP_w E) F⁻

Figures Continue on the Next Page

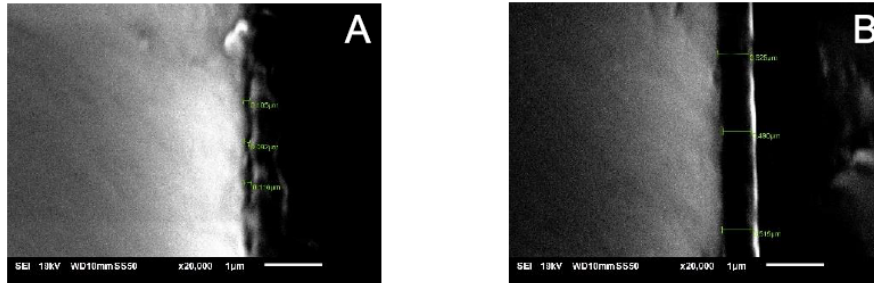


Figure 6: SEM images of amorphous carbon films A) 1000 Å B)

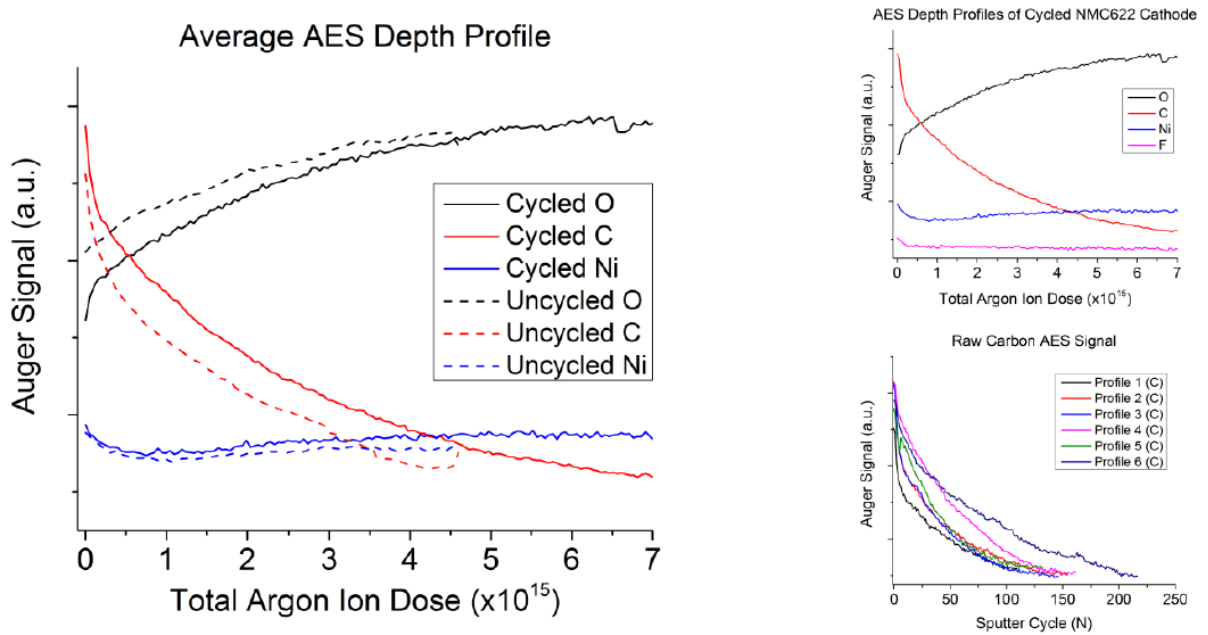


Figure 7: Average depth profile data of different spots on an NMC622 cathode (left). Solid lines represent that from a cycled cathode (4.6 V, fluorinated electrolyte), dashed lines from an uncycled cathode. Average AES signal of cycled NMC622 cathode (top right). Raw carbon AES signal from each depth profile (bottom right).

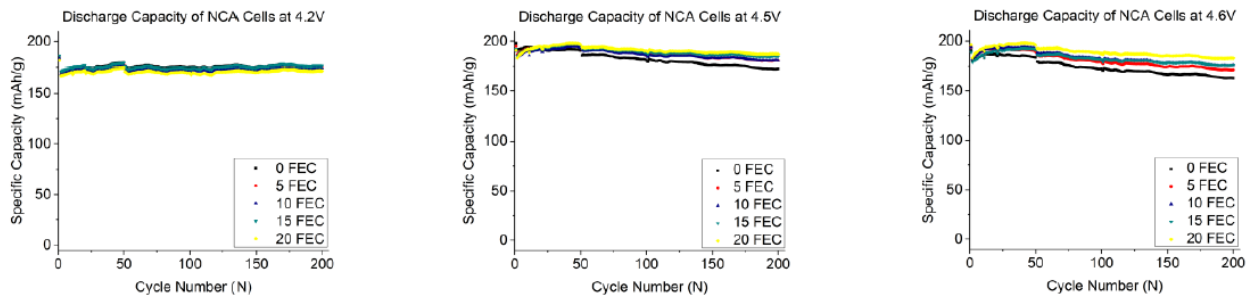


Figure 8: 200 mAh NCA cells cycled at .7C at r.t. as a function of FEC concentration (0-20% v/v) and voltage (4.2, 4.5, and 4.6)

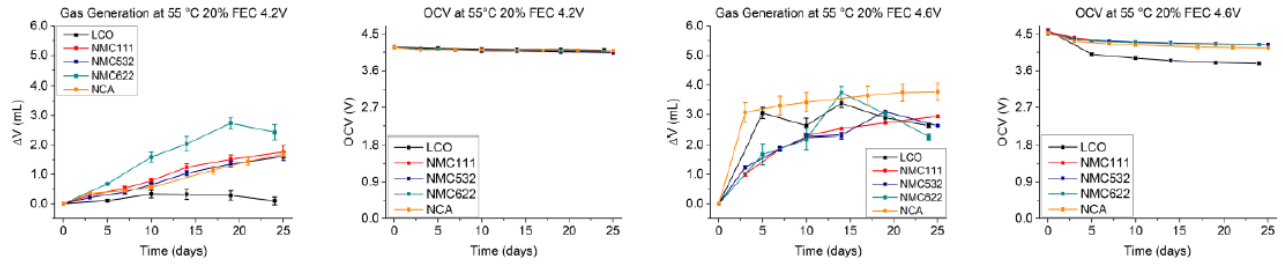


Figure 9: Calendar life test (□OCV and □ gas volume) at 55 °C with 20% FEC at an OCV of 4.2 (left) and 4.6 V (right)

Remainder of Page Intentionally Blank

AVPTA Technology Focus Area 7: Analytical Tools (Modeling & Simulation)

Physics-Based Computational Fluid Dynamics (CFD) Sub-model Development

**DOE-VTO TFA Lead: Dr. Michael Weismiller
TARDEC TFA Lead: Dr. Vamshi M. Korivi**

Principal Investigators:

**Dr. Ajay K. Aggarwal,
Dr. Emily Ryan,
Dr. Caroline L. Genzale,
Dr. Sage Kokjohn,
Dr. Seong-Young Lee,
Dr. Seung Hyun Kim,
Dr. Daniel C. Haworth,
Dr. Chia-Fon Lee**

Respective Affiliations:

**University of Alabama,
Boston University,
Georgia Institute of Technology,
University of Wisconsin-Madison,
Michigan Technological University,
Ohio State University,
Penn State University,
University of Illinois at Urbana-Champaign**

**Project Start: Q2FY16
Estimated Completion: Q4FY19**

Objectives:

Development and validation of more accurate, physics-based mathematical sub-models (fuel injection spray, cavitation within fuel injectors, flash boiling, spray/wall interaction, super critical fuel injection, in-cylinder radiation and heat transfer, engine knock and soot emissions) for use in Computational Fluid Dynamics (CFD) software.

Strategic Context:

The impact of transient mixing and charge formation during the initial stages of the fuel injection event for high pressure JP-8 injection is a research gap identified by office of Chief Scientist.

Improvement of these sub-models will help develop the fire protection competency of advanced modeling and simulation tools to address emerging threats and technologies due to fuel fires inside the ground combat vehicles.

Accomplishments:

Development and validation of more accurate, physics-based mathematical sub-models for use in Computational Fluid Dynamics (CFD) software have been initiated with different universities and a national lab partner for developing following eight sub-models. Computational and experimental studies have been initiated for development of these sub-models.

- Super critical fuel injection (University of Alabama & Argonne National Labs [ANL])
- Cavitation within fuel injectors (Boston University & Oak Ridge National Labs [ORNL])
- Fuel injection spray (Georgia Tech & ANL)
- Soot emissions (University of Wisconsin-Madison & Sandia National Labs)
- Spray/wall interaction (Michigan Technological University [MTU] & ANL)
- Engine knock (Ohio State University & ORNL)
- In-cylinder radiation and heat transfer (Penn State University & ORNL)
- Flash boiling (University of Illinois at Urbana-Champaign & ANL)

Introduction:

Computational Fluid Dynamics (CFD) Software has led to improved engine designs but not yet realized full potential for attaining the goals of shortened engine development time, reducing fuel consumption, and minimizing exhaust emissions due to predictive accuracies of the sub-models used in commercial and government sponsored software.

Also, it is a general consensus among academic, national labs and industry community that there is a lack of experimental data for validation of the new or improved sub-models. Developing accurate sub-models that are physics-based, predictive in nature, and validated with experimental data, will require less calibration and tuning than currently available sub-models.

Approach:

Experimental protocols and apparatuses to identify the inaccuracies and formulate a technical approach to overcome.

Publication and Dissemination of information regarding improved sub models for inclusion in all commercial and government sponsored CFD codes.

Results and Discussion:

Summary for each sub model development updates from year II is summarized in following sections I-VIII separately.

Development and Validation of Physics-Based Sub-Models of High Pressure Supercritical Fuel Injection at Diesel Conditions:

The Eulerian-Eulerian (EE) framework is a viable numerical approach for simulating fuel injection at high-pressure diesel engine conditions. The uncertainty is reduced compared to the Lagrangian-Eulerian approach because of the fewer empirical models used. However, the accuracy in calculating thermo-physical properties of pure fluids and their mixture plays a vital role in high- fidelity simulations using the EE approach. Traditional diesel spray CFD models include droplet effects as the fuel exits the injector. Operation above the critical conditions requires different modeling approach because of the absence of surface tension. Proposed research will enable robust experimental validation of developed models and CFD codes to reduce modeling uncertainty, and increase operational flexibility.

In budget period III, principal investigators (PI) introduced the goal of completing initial validation data sets using propane as the injected fuel, and several images were acquired both at high and low spatial resolutions. A new challenge was also identified. The mixing model that was previously used for relating measured mixture refractive index to local mixture properties (density, temperature, fuel fraction) is not valid for fluids near the critical point. Thus, a new mixing model was developed.

The relationship between the fuel mixture fraction and temperature can be used to develop the relationship with the refractive index of the mixture. In past applications of Rainbow Schlieren Deflectometry (RSD), PI utilized the Dale-Gladstone formulation which is valid for ideal-gas mixtures with refractive indices near unity. However, for real-fluid mixtures of components with refractive index much greater than unity, the original formulation given by Lorenz-Lorentz is more accurate. The important variables in this equation are mixture molecular polarizability and density. The mixture density can be determined from the real-fluid mixing models using real-fluid properties and adiabatic mixing assumption. The mixture molecular polarizability is determined by applying a mixing law that has been validated against measurements published in literature.

Previously developed real-fluid property models must be combined with real-fluid mixing models to account of real gas effects at diesel conditions. It was found that it is not appropriate to use volume or mass weighted combinations of pure component real-gas properties when considering a real-gas mixture. Thus, PIs have undertaken the development of a user defined function (UDF) that reads in three-dimensional property tables based on real-gas mixing models and interpolates as needed to return the desired thermal or transport properties at specified values of pressure, temperature, and mixture fraction.

A previously presented experimental test condition - *n*-heptane injected at 1000 bar, 363 K into air at 28 bar, 825 K – was simulated by Argonne National Laboratory collaborators using Converge CFD software. The simulation data were post-processed to generate synthetic

RSD images for direct comparison with experimental RSD images. This approach is not limited by the requirement of the axisymmetric, and thus, instantaneous realizations can be compared with each other. Figure 1(a) shows a few comparisons between experimental RSD images and synthetic RSD images generated from the CFD density fields. The synthetic RSD images show good agreement of the 1st stage reaction behavior both spatially and temporally. Figure 1(b) shows the comparison of spray penetration for the simulation and experiment. Simulation slightly over predicts the onset of second stage ignition.

Development & Multiscale Validation of Euler-Lagrange based Computational Methods for Modeling Cavitation within Fuel Injectors:

This project is developing methods for simulating cavitation dynamics in a fuel injector that can be used in preliminary design and for final design analysis, and performing experiments for validation of the models. Research focuses on three specific thrusts: computational model development, small-scale cavitation experiments and high flux isotope reactor (HFIR) imaging of a real fuel injector.

Traditional Eulerian methods for cavitation make assumptions and simplifications:

- Vapor fraction as a function of the radius of the bubbles, which is assumed to be the same for all the bubbles.
- Ignores bubble interactions, non-spherical bubble geometries, and local mass-momentum transfer around the interface.
- Requires estimation for the initial value of cavitation nuclei, bubble radius, and empirical constants for the condensation, and vaporization.

Computational development included in this study mainly consisted of high fidelity model of bubble dynamics and coupling to Reynolds averaged Navier-Stokes CFD. Experimental characterization and validation included in this study mainly consisted of small scale experiments in idealized fuel injector and HFIR imaging of cavitation in real fuel injector at Oakridge national laboratory. Main goals of the study are to develop more physically based sub-models of cavitation for large scale CFD models with focus on the following:

- High fidelity modeling of bubble dynamics using smoothed particle hydrodynamics (SPH) which is a Lagrangian particle based method for multiphase flows. This method has a challenges with density ratios. Another approach using open FOAM CFD software using a traditional Eulerian CFD with volume of fluid (VOF) approach. Recent improvement in the code have allowed more accurate modeling of bubble dynamics.
- Filtered modeling approach is to use simulation campaign to develop physics based constitutive model for cavitation.

In budget period III, the CFD simulations have been verified against the analytical solution of the Gilmore equation for this case. Figure 2(a) shows the comparison of radius in time curves between the solution of the Gilmore equation and results of the CFD simulation. Figure 2(b) shows the time-averaged velocity field results from the CFD simulations. The simulations show that the maximum velocity occurs in the upper section of the nozzle outlet. These higher

velocities would not be recorded by a flow meter placed downstream. As such, the determined velocities from experiment differ with the expected velocities from theory. It can be seen from the results in that the max velocities as predicted by the CFD are indeed higher than the onset velocities calculated by theory. This confirms the hypothesis that localized velocities are inducing cavitation in the system and not velocities recorded by the outlet flow meter.

Development and Validation of Turbulent Liquid Spray Atomization Sub-model for Diesel Engine Simulations:

This research aims to develop a new spray atomization sub-model that will appropriately capture the role of liquid turbulence on diesel jet breakup and enable accurate predictions for multicomponent fuels. A novel joint-facility experimental plan will quantify spatially-resolved liquid volume fraction distribution, Sauter mean diameter, and optical thickness under controlled scenarios to quantify the role of liquid turbulence and aerodynamic forces on spray atomization.

In budget period III, the experimental project teams from Georgia Tech and Argonne completed the last remaining test campaigns from the Year II test matrix and further processed these data sets to complete an improved set of drop size measurements for spray model validation. Georgia Tech researchers completed Phase II visible light extinction experiments by performing diffuse back illumination (DBI) measurements of diesel spray optical thickness within a continuous flow spray chamber. Multiple viewing angles were taken to better assess spray asymmetries observed in previous experimental campaigns. During this data campaign, optical setup was further optimized to maximize measurement bandwidth, signal-to-noise, and reduce measurement uncertainties. This included a detailed study of pixel ghosting effects that can occur with commercial high-speed cameras, where residual pixel charge can affect the pixel intensities in subsequent frames of the imaging sequence, leading to measurement errors. To assess this issue, the light emitting diode (LED) was both pulsed and skip-pulsed to illuminate every other frame in the sequence, allowing a dark image between measurement frames to “reset” the noise floor. In the upcoming quarter, researchers will analyze these results to assess which configuration produced the least measurement error. At Argonne national labs, measurement results from Ultra Small Angle X-ray Scattering (USAXS) were analyzed. These measurements quantify the near-nozzle surface area of the spray, and are a metric for spray atomization. The USAXS measurement conditions were chosen to match the DBI measurements in order to provide validation data for this new diagnostic. In addition, the measurements provide validation data for the spray model development that is part of the task.

Figure 3(a) shows an example of the acquired data from this quarter, illustrating the measured optical thickness of Spray D at an ambient density of 1.2 kg/m³ and an injection pressure of 50 MPa, with the injector at a 90° orientation. This measurement was conducted using a pulsed LED setting (illumination during every imaging frame). The steady portion of the spray was time averaged and 20 injection events were ensemble averaged. Meanwhile, the KH-Faeth primary breakup model developed thus far was further validated as shown in Figure 3(b). As of budget period III, PIs have been able to quantitatively validate and compare

OPSEC1890

the new spray atomization model to existing models for diesel sprays at a range of low and high ambient density conditions.

Development and Validation of a Lagrangian Soot Model Considering Detailed Gas Phase Kinetics and Surface Chemistry:

The objective of this project is to develop and validate a new, Lagrangian based soot model. This model will include a detailed reaction mechanism including polycyclic aromatic hydrocarbon (PAH) chemistry up to benzo pyrene. Particle modeling will be separated from gas-phase modeling through the use of Lagrangian soot parcels that contain a soot population. Particle nucleation will be modeled considering PAH dimerization. Once primary particles are formed, they will be transferred out of the gas phase and tracked using statistical soot "parcels". The soot parcels will include a full soot population and description of the soot aggregates. The soot population in each soot parcel will evolve according to Smoluchowski's population balance equation using a Monte-Carlo particle technique. The population balance solver will consider surface chemistry, collision, condensation, and wall interactions. The model will be rigorously validated through comparisons with existing constant volume vessel experiments and engine experiments.

In budget period III, the University of Wisconsin completed the metal engine validation experiments and completed validation of the improved soot model. PI compared the model predictions to existing soot models and package the model for inclusion in all government sponsored, open source, and commercial codes. Figure 4 shows particle size distributions (PSDs) for the injection pressure sweeps, highlighting the effects of the sweep. Measured and simulated PSDs are in parallel plots for trend comparison. The quantity of accumulation mode particles increases as the start of injection timing (SOI) timing is retarded from -8.5° to -3° After Top Dead Center, but in general, the PSD shape is rather insensitive to SOI timing. As injection pressure is increased, the number of nucleation mode particles increases and the number of accumulation mode particles decreases. In general, the simulations show very good agreement with both the trends and magnitudes of the measured particle size distributions. Namely, the simulations show that changes in start of injection timing result in similar shapes of the PSD, while changes in injection pressure cause changes in the shape of the distributions and the balance between nucleation mode and accumulation mode particles. The simulations accurately capture the increase in the nucleation mode particles (and decrease in accumulation mode) as injection pressure is increased. Note that no model constants were adjusted.

In an effort to make the developed methodology as accessible as possible, a completely new post processing method has been created. This allows the model to be used with any combustion CFD code with detailed chemistry. To demonstrate this technique, soot parcels that were generated in KIVA software used by PI are replaced by parcels generated through the post processing and visualization software, Enight that is used widely in the industry.

Evaporation Sub-Model Development for Volume of Fluid (VOF) Method Applicable to Spray-Wall Interaction Including Film Characteristics with Validation at High Pressure Temperature Conditions:

The goals of this research project are to develop, implement and validate a volume-of-fluid (VOF) approach for modeling evaporation, which is integrated into computational fluid dynamics (CFD) codes to provide accurate and predictive simulation of spray-wall interactions without extensive need of parameter tunings. This is accomplished by development and inclusion of an evaporation sub-model in existing VOF modeling framework. This sub-model will be validated through extensive experimentation of the spray-wall interaction and film formation, spreading and vaporization dynamics.

In budget period III, direct numerical simulation (DNS) calculations are performed at UMass Dartmouth highlighted the dynamic characteristics of droplet impingement and the importance of impact frequency. Figure 5(a) shows the impact of the droplet impingement and its impact on film formation. This resulted in the necessity to define a suitable impact frequency for Lagrangian parcels. The following is a list of the quantities that were computed by Argonne in support of the project.

- Probability Density function vs time of liquid Weber and Reynolds numbers w/r to liquid mass;
- Sauter Mean Diameter (SMD), weighted average of velocity components, and weighted velocity standard deviation of liquid parcels;
- Average temperature of parcels used to estimate viscosity, density, and surface tension of the liquid.

A series of DNS calculations (48 in total), performed on Argonne's supercomputer Mira, will be used to determine if and how splash occurs under operating conditions typical of high-pressure sprays in internal combustion engine applications. The information obtained from DNS will be synthesized and fed back to the Lagrangian Spray Wall Interaction model to improve the prediction of impinged spray quantities.

At Michigan Tech, new test set as a part of the feedback test proposed in the budget period III was developed for the elevated wall and droplet temperature test. The objective is to vary the droplet temperature and wall temperature independently and explore the temperature effect on droplet-wall interaction dynamics. The first design of the test setup was using the heating tape to increase the temperature of the stainless-steel syringe outlet tubing. The heating tape method didn't really work due to the poor contact between the stainless steel tubing and heating tape. Based on the IR image, the heating tape core temperature was reached 190°C, but the fuel temperature never reached the desired temperature due to the poor contact. A new test design was adopted with the acrylic tubing. The acrylic material's melting temperature is tabulated above 300°C and holds up the 150°C very well without softening. Acrylic tubing, thermocouple, and a cartridge heater were wrapped with aluminum foil and set up with syringe pump. Cartridge heater was individually controlled by a heater controller. The snap-shot images taken from a high-speed images are shown in Figure 5(b) to illustrate the effect of the temperatures on droplet impinging dynamics. The non-isothermal

case undergoes expansion (advance) process and receding process. However, isothermal case showed only expansion, no retraction. The high temperature of the fuel in the isothermal case leads to less receding behavior probably due to the low viscosity.

Development of a Physics-Based Combustion Model for Engine Knock Prediction:

The objective of the research is to develop a new, physics-based large eddy simulation (LES) combustion model for engine knock prediction, which 1) accurately describes turbulence-chemistry interactions during end-gas ignition and spark-ignited flame propagation and 2) enables the use of a detailed (reduced) chemical mechanism in engine large eddy simulations. 3) Validation of simulation results with high-fidelity knock experiments.

Effects of turbulence on end-gas ignition: In typical engine conditions, in-cylinder flows are highly turbulent. Complex turbulent motions substantially affect heat release rates and end-gas ignition. The physics-based and accurate modeling of such turbulence-chemistry interactions is necessary, in particular to predict processes in high scalar dissipation layers.

Detailed chemistry description: Accurate description of end gas ignition requires the use of a detailed chemical mechanism. This project aims to enable engine knock LES where ignition chemistry is described by a reduced mechanism that contains about 100 species, while employing a physics-based model for turbulence-chemistry interactions.

Validation with high-fidelity knock experiments: For thorough validation, engine knock and knock-free experiments coupled with direct measurements and chemical characterization of in-cylinder gas species temporal evolutions will be performed to provide high-fidelity data sets. The laboratory experimental data will be complemented by direct numerical simulations (DNS), which serve as numerical experiments to provide detailed statistics necessary to assess the specific aspects of the developed model.

In budget period III, PIs worked on improving premixed combustion model to reproduce the degree of cycle-to-cycle variations (CCV) in an Oakridge national labs (ORNL) engine case. The improvements include a new numerical scheme for the discretization of the regularized delta function in the combustion model and the further development of the laminar-to-turbulent flame transition model. The new numerical scheme is developed to reduce the unnecessary numerical diffusion, which can affect the simulation accuracy. The laminar-to-turbulent flame transition model is further improved to consider variations in the laminar-to-turbulent flame transition time, which affect the initial flame kernel growth and CCV. The multi-cycle LES of an ORNL engine case confirms the importance of variations in the laminar turbulent flame transition in predicting CCV. The simulation results are analyzed in details and compared with the experimental data.

Figure 6(a) shows the pressure and specific internal energy (sie) fields before and at the time of knocking. It can be seen that, before knocking, the pressure field is almost uniform. After an end gas ignites, strong pressure waves propagate and pressure oscillates in the end-gas region. This leads to oscillations in the specific internal energy field through the pressure-dilatation work. For the essentially same reason, pressure oscillations lead to fluctuations of

enthalpy. The pressure wave-induced fluctuations in enthalpy then introduces unphysical oscillations in filtered species mass fractions since the filtered species mass fractions are determined by the probability density function or front propagation formulation (FDF) of enthalpy. To remedy this problem, the low Mach number assumption is to be applied to the equation for enthalpy used as a conditioning variable in condition moment closure model. Figure 6(b) shows the flame front evolution in the fast cycle, defined as the cycle with the highest peak pressure, and in the slow cycle, defined as the cycle with the lowest peak pressure.

Development and Validation of Predictive Models for In-Cylinder Radiation and Wall Heat Transfer:

Objective of the proposed research is to develop predictive CFD models for radiation and wall heat transfer, and made openly available. The models will explicitly account for couplings between different modes of heat transfer. New experimental data and high-fidelity simulation-based data for model development and validation will be generated and made available.

In budget period III, baseline boundary-layer wall heat transfer and radiative heat transfer models are implemented in the CFD software. The modeling and simulation effort has shifted toward specific real engine configurations. Work continued on refining the quantitative comparisons between measured and computed infrared spectral radiative intensities in the engine. Recent effort has focused on a 40 kPa manifold absolute pressure (MAP), 1300 r/min operating condition. This is an operating condition that has been used in previous experimental and simulation studies for this engine. Because of the strong and irregular absorptance by the quartz engine liner in the infrared, the comparisons are currently limited to a wavenumber range of $\sim 2.1\text{-}2.5\ \mu\text{m}$. This captures some of the key CO₂ and H₂O bands, but misses an important CO₂ band that peaks at approximately $4.3\ \mu\text{m}$.

At 1300 r/min, time-resolved spectra can be obtained at intervals of two crank-angle degrees of rotation. An example of measured time-resolved spectra is shown in Figure 7(a). The improved spectral resolution in the most recent measurements shows more detail in the band structure, which will aid in future validation of simulations. These measurements also provide information about the relative weights of different emission features throughout the engine cycle, which might eventually be used to extract temperature and/or composition information.

Figure 7(b) is a comparison between the most recent simulated and experimental spectra for the engine operating at 1300 revolutions/min. This plot compares spectra at 30° after top-dead-center (aTDC) combustion. Both spectra have been normalized to the spectral feature from $1.7\text{-}2.2\ \mu\text{m}$. There is large discrepancy for wavelengths longer than $\sim 2.5\ \mu\text{m}$, because of the strong attenuation of the measured signal at those wavelengths by the quartz cylinder liner. A sapphire piston window has been procured, which will allow measurements to be made at wavelengths as long as $5.5\ \mu\text{m}$, corresponding to the upper wavelength limit of the infrared camera.

Progress continued on the implementation and testing of non-equilibrium models for turbulent boundary-layer wall heat transfer, and exploration into couplings between boundary-layer heat transfer and radiative heat transfer. In both cases, the test configuration has been fully-developed turbulent planar channel flow between two parallel plates held at different constant temperatures, and with a radiatively participating medium flowing between the two-plates. This is a configuration for which direct numerical simulation (DNS) data are available in the literature for model validation.

Model Development for Multi-Component Fuel Vaporization and Flash Boiling:

Main objectives of the proposed research are to develop multi-component fuel droplet and wall film vaporization sub-models using both discrete and continuous thermodynamics methods; develop a sub-model for multi-component flash boiling; integrate sub-models into multi-dimensional engine models; validate numerical models with measurements acquired from a droplet chamber and a spray chamber under a wide range of ambient temperature and pressure conditions.

To achieve objectives of the research, PI worked on - design and develop a multi-component fuel droplet and wall film vaporization model using both discrete and continuous thermodynamics methods; design and develop an analytical model for multi-component flash boiling; integrate the multi-component droplet and film model into multi-dimensional engine calculations to predict the fuel vaporization process under engine operation condition; conduct multi-component droplet and fuel film vaporization experiments in a noncombusting chamber to verify the proposed vaporization models; characterize flash boiling phenomena of multi-component fuel sprays by optical and laser diagnostic techniques.

In budget period III, Lagrangian simulations of the spray according to the discrete droplet model (DDM), coupled with 3D Eulerian solution of the gas transport equations have been run in CONVERGE software. Most of the preliminary simulations have been carried out exploiting the symmetry of the nozzle geometry, taking into account just one nozzle in a sector mesh. Later, the full eight-hole injector has been simulated with lessons learned from the sector mesh numerical set-up with iso-octane fuel. The results reported in figure 8(a) refer to the implementation of the evaporation model, which allows a partial interaction between the jets and a fuel vapor profile consistent with the flash boiling behavior. Flash boiling spray characterization through Phase Doppler Anemometry (PDA) measurements were done as well, which will be used for further model assessments.

Figure 8(b) shows the droplet diameter distribution at different ambient pressures for pure isooctane spray. Decreasing the ambient pressure from 100 kpa to 50 kpa, the distribution curve shifted to the smaller side and profile got narrower. At 50 kpa, the occurrence of spray flash boiling significantly reduced the overall droplet size, where large droplets were nearly eliminated. Enhanced spray atomization caused by the flash boiling was the main reason for such behavior. Figure 8(c) shows the droplet distribution curves for sprays with different fuel blends under each ambient pressure. At ambient pressure of 100 kpa, both E30 and ethanol reached flash boiling conditions.

Conclusions:

Both Computational and experimental efforts are underway for developing eight different sub-models. Four project leads are using open source software for development and four universities are working with a commercial software vendor to implement these sub models. In Q4FY18 all Principle Investigators (PIs) submitted for a no cost extension with final completion date scheduled for end of FY19.

References:

None

Figures:

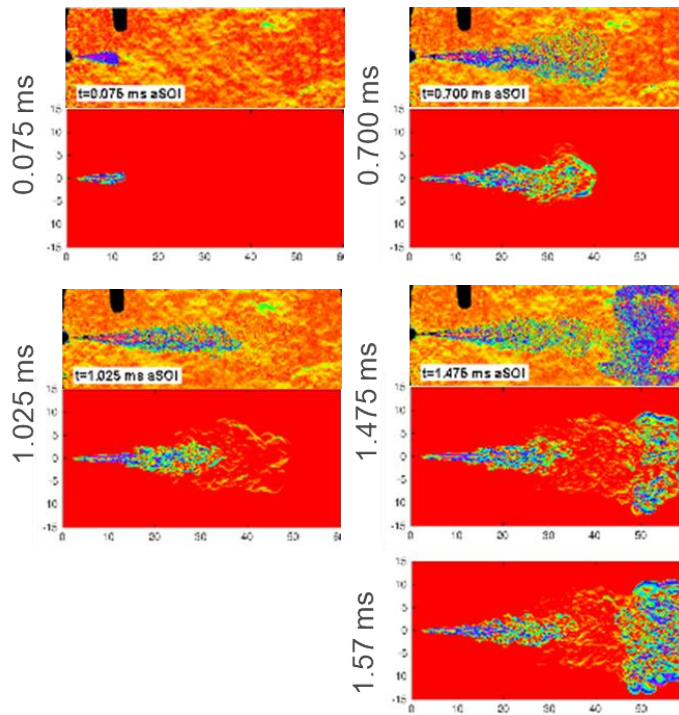


Figure 1 (a). Comparison of experimental RSD images (top in each pair) and synthetic RSD images (bottom in each pair) processed from CFD results for n-heptane injected at 1000 bar, 363 K into air at 28 bar, 825 K.

Figures Continue on the Next Page

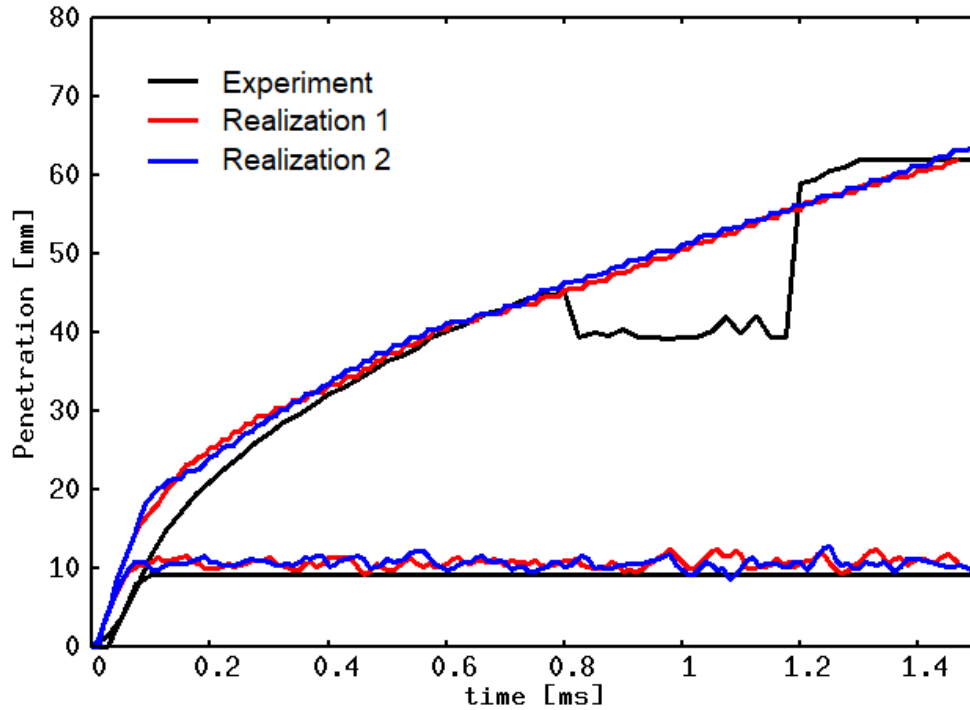


Figure 1 (b). Spray penetration for two Large Eddy Simulation realizations.

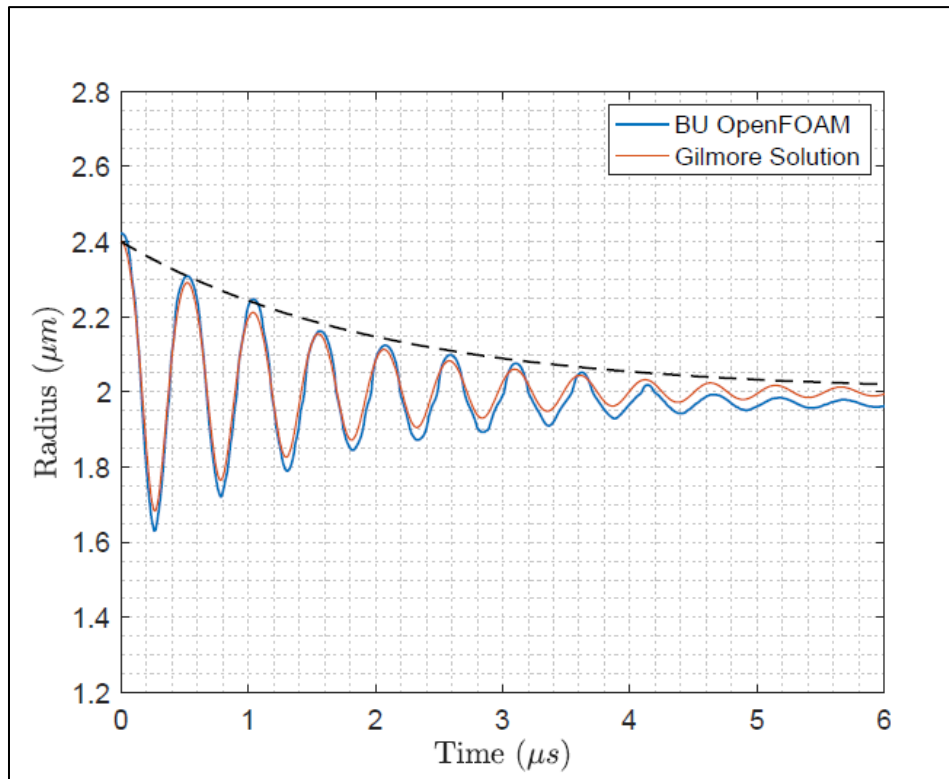


Figure 2(a). Comparison of OpenFoam simulations to analytical solution.

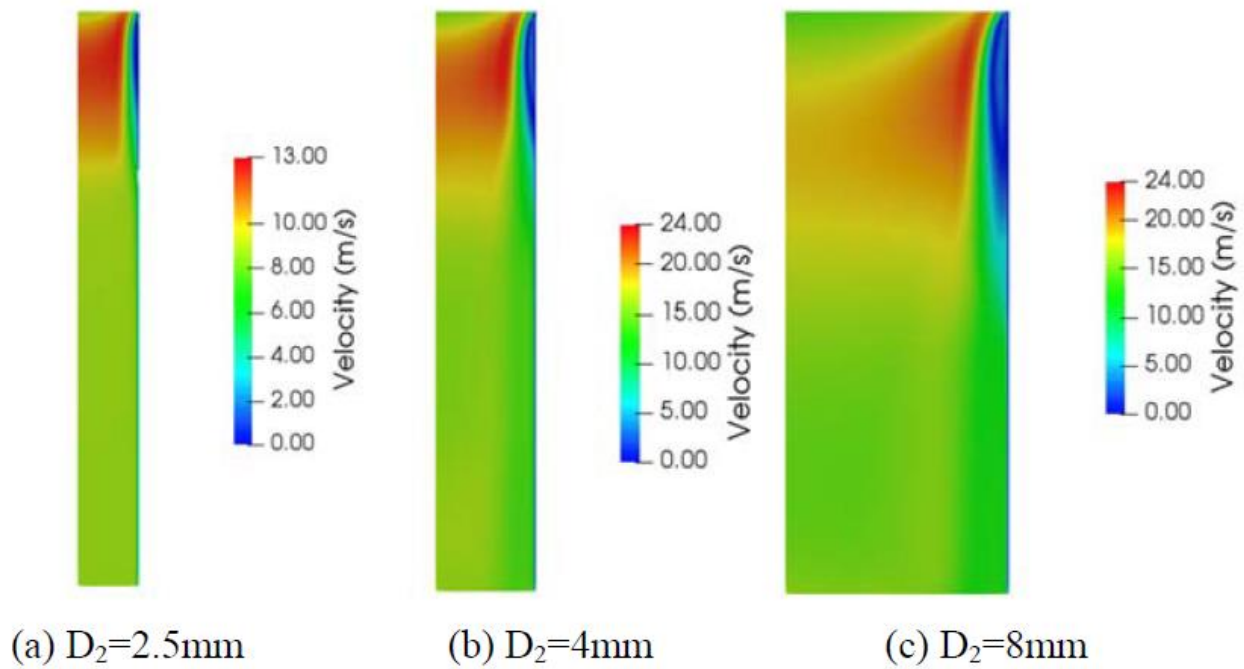


Figure 2(b). Time averaged velocity field from numerical simulations of nozzle flow varying cylindrical outlet diameters.

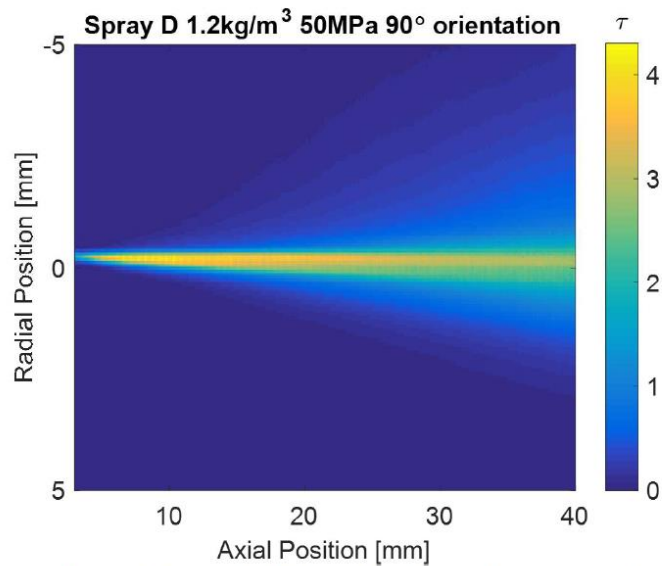


Figure 3(a). Two-dimensional map of optical thickness for spray D ($\rho_{\text{ambient}} = 1.2 \text{ kg/m}^3$, $P_{\text{injection}} = 50 \text{ MPa}$), for the pulsed Light Emitting Diode (LED) setup.

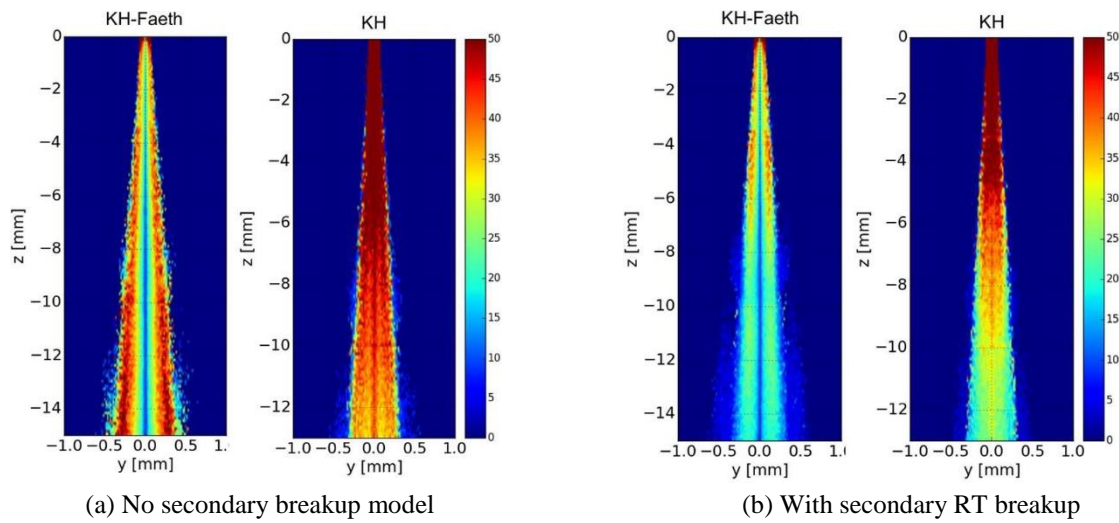


Figure 3(b). Predicted Sauter Mean Diameter (SMD) distribution in space with and without secondary breakup model.

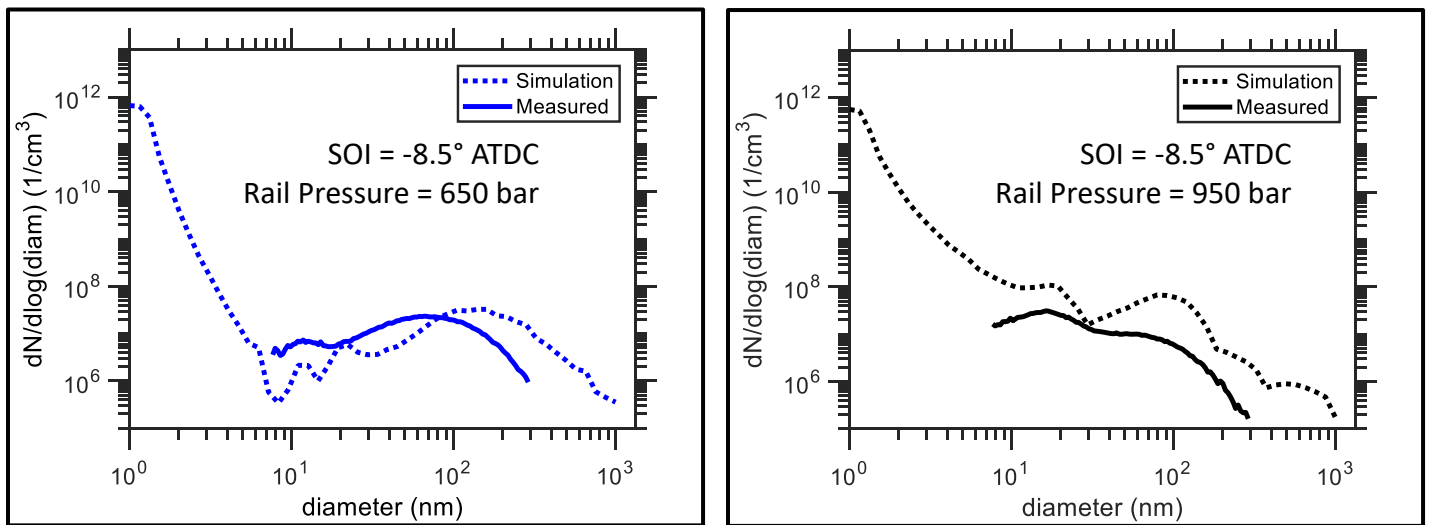


Figure 4. Comparison of measured and predicted soot concentration

Figures Continue on the Next Page

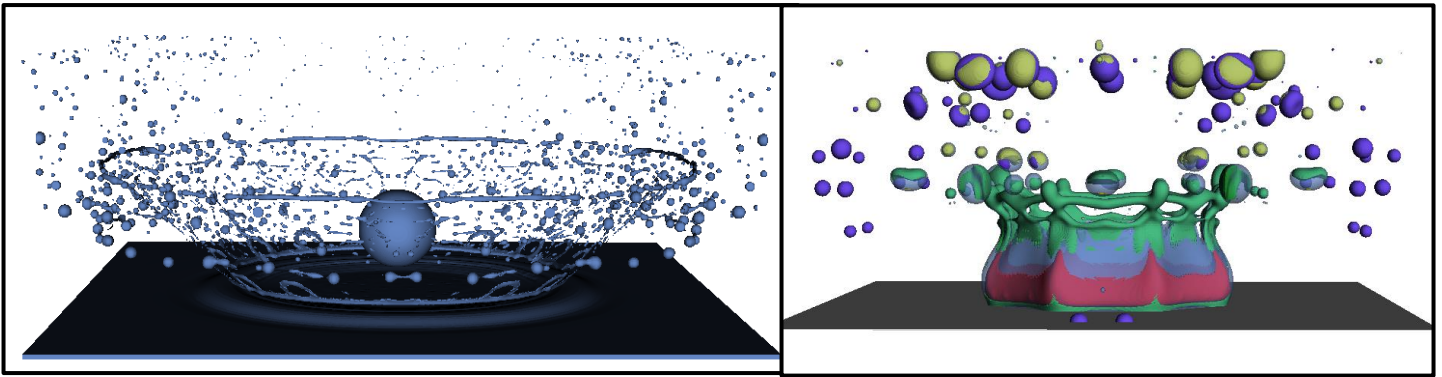


Figure 5(a). A detailed analysis of pre-impingement under several operating conditions (including evaporating and non-evaporating cases, at several injection pressures and ambient densities, 12 cases in total)

Non-isothermal case

$T_{\text{wall}}=127^{\circ}\text{C}$

$T_{\text{Drop}}= 25^{\circ}\text{C}$



Isothermal case

$T_{\text{wall}}=127^{\circ}\text{C}$

$T_{\text{Drop}}= 127^{\circ}\text{C}$



Figure 5(b). High-speed imaging at 30 ms after impinging for both isothermal and non-isothermal conditions

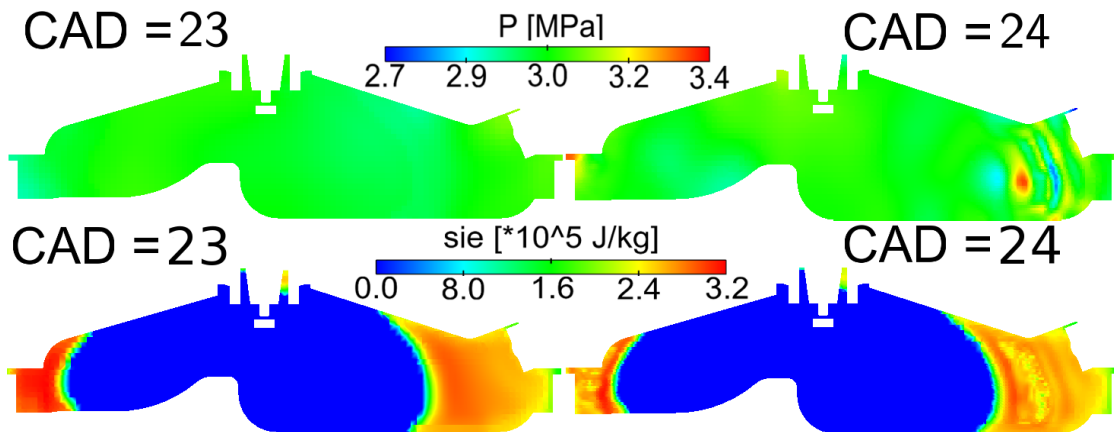


Figure 6(a). Pressure and specific internal energy fields at the time of knocking.

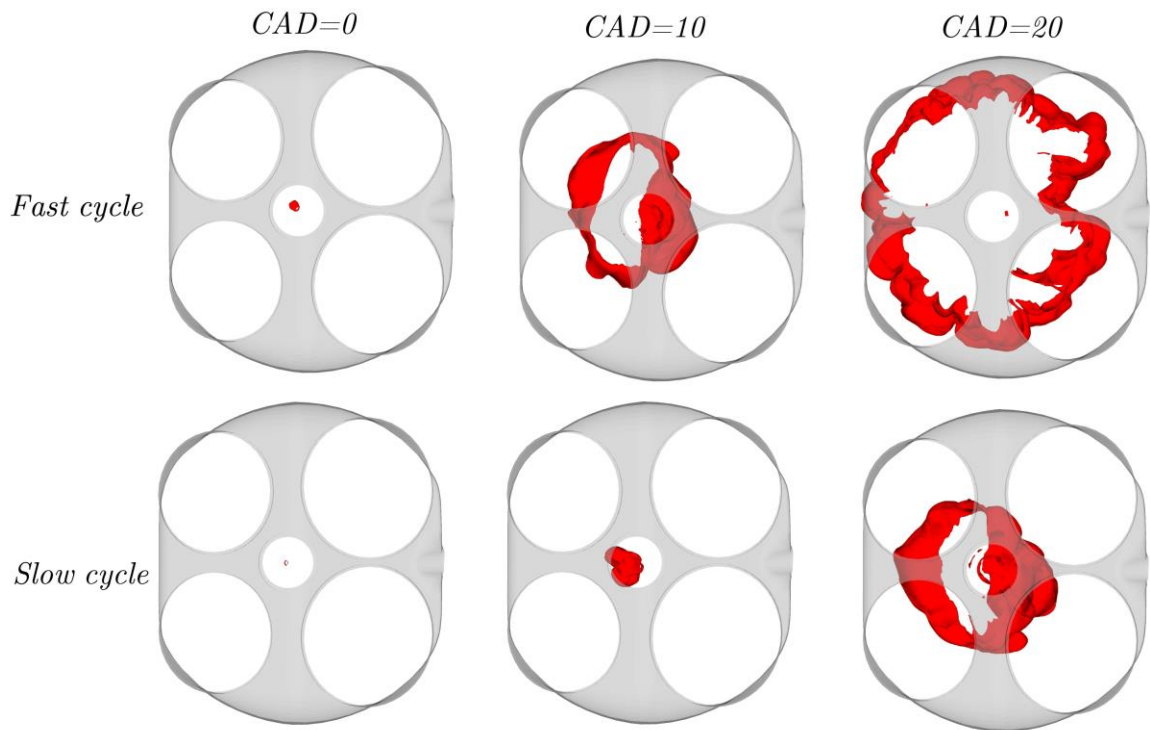


Figure 6(b). Comparison of flame front evolution between the fast cycle and the slow cycle

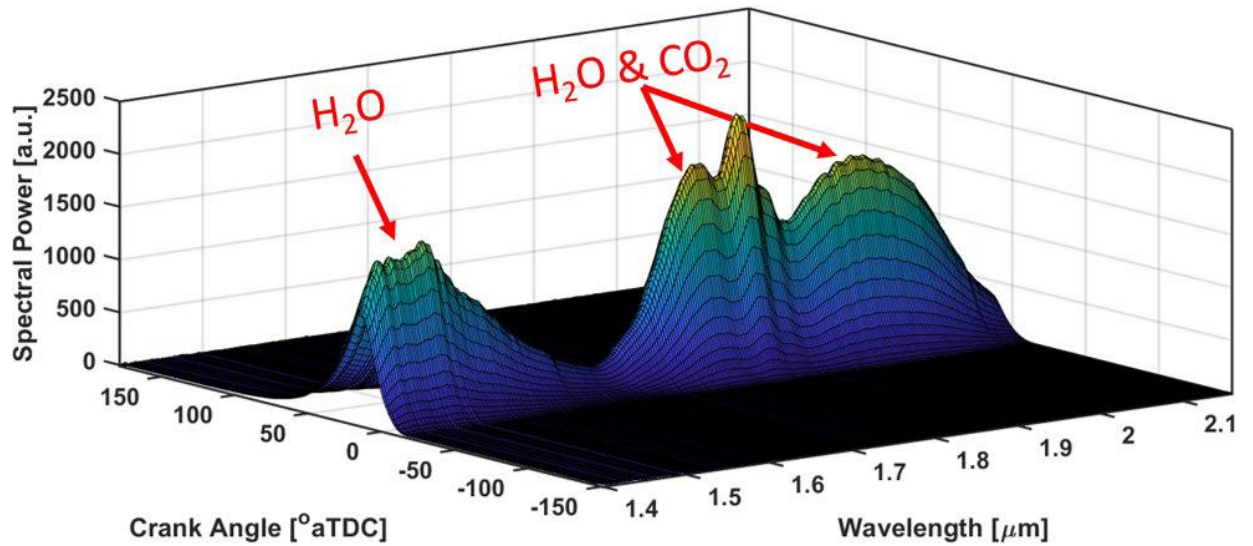


Figure 7(a). Time-resolved (at intervals of two crank-angle degrees of rotation) measured spectral radiative intensities in the engine at 1300 r/min

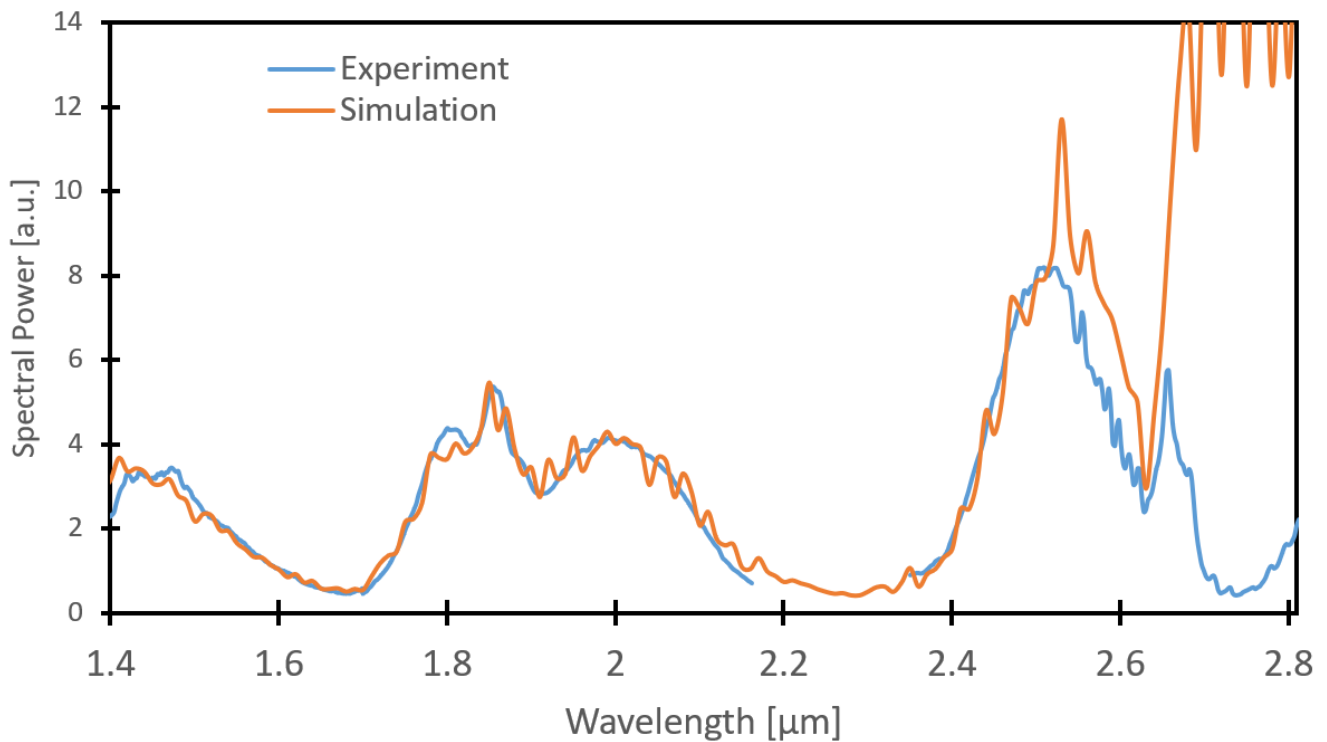


Figure 7(b). Comparison of measured and simulated spectral intensities for the engine operating at 1300 r/min. The comparisons are made at 30° after Top dead center

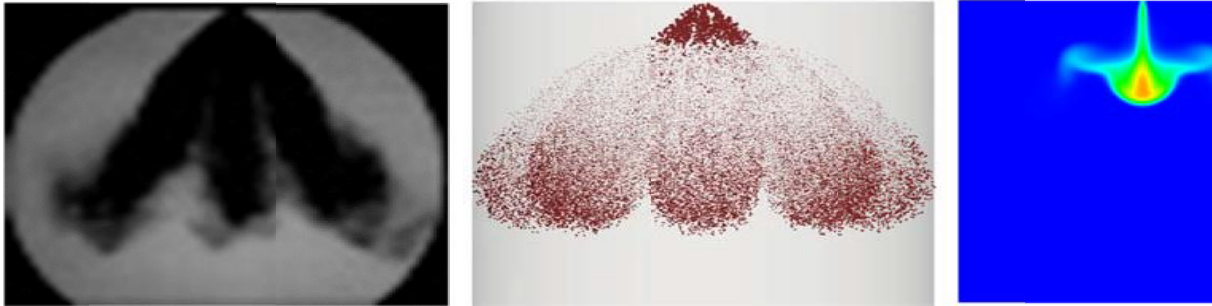


Figure 8(a). Diffused back –illumination imaging (DBI) spray image (left), simulated spray at 1 milli-second after start of injection (center) and fuel vapor mass fraction profile at 1 milli-second after start of injection (right).

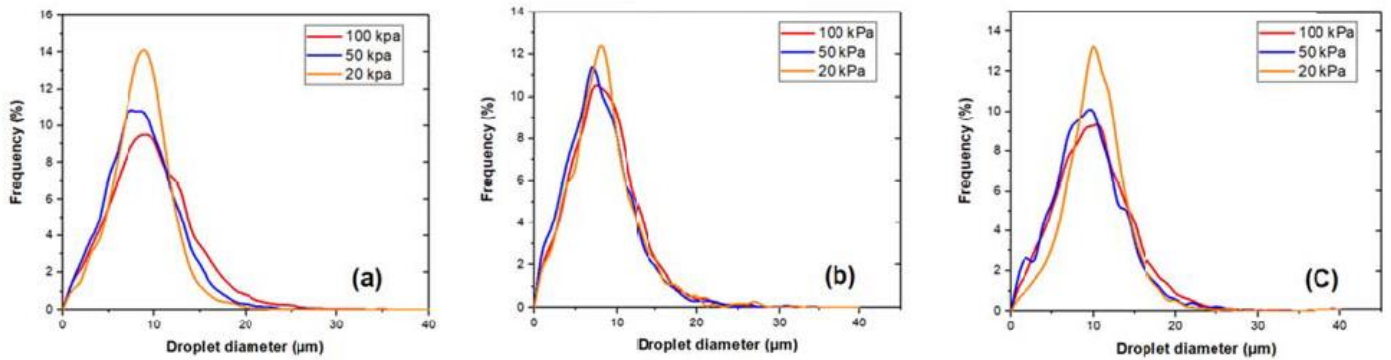


Figure 8(b). Droplet distribution for sprays with all testing fuels under different ambient pressures.

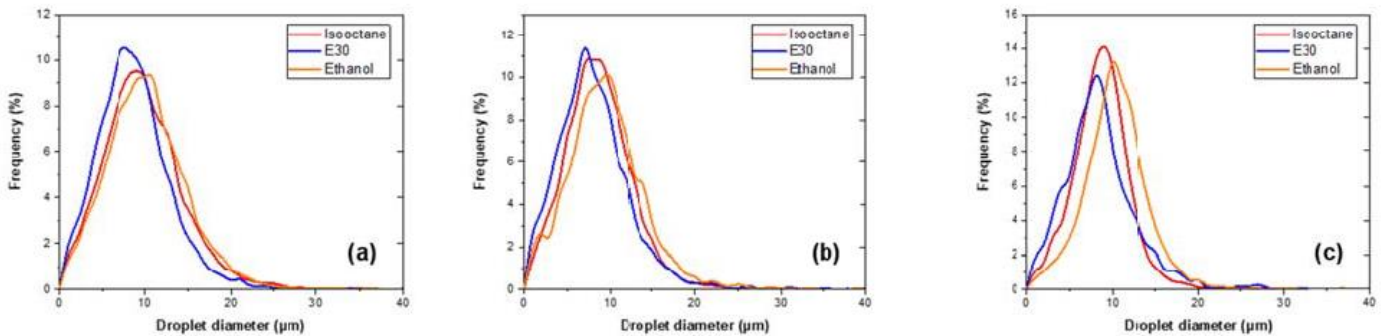


Figure 8(c). Droplet distribution curves for sprays with different fuel blends under same ambient pressure

Remainder of Page Intentionally Blank

AVPTA Technology Focus Area 9: Autonomy-enabled Technologies



**DOE-VTO TFA Lead: David Anderson
TARDEC TFA Lead: TBD**

**There was no project activity under this
TFA during FY18.**

Remainder of Page Intentionally Blank

This Page is Intentionally Blank

AVPTA “Extended Enterprise” Activities

Optimization of Scalable Military Fuel Cell Hybrid Vehicles

DOE-FCTO TFA Lead: Peter Devlin
TARDEC TFA Lead: Kevin Centeck

Principal Investigators:

Dr. Denise Rizzo
U.S. Army TARDEC
Systems Integration & Engineering
Analytics - Vehicle Performance &
Tradespace

Dr. Jason Siegel
University of Michigan
Mechanical Engineering Department
Ann Arbor, MI

Project Start: Q1FY17
Estimated Completion: Q1FY19

Objectives:

- Develop scalable tools to address optimization electrified Proton Exchange Membrane Fuel Cell (PEMFC) powertrains ranging from 300W robots to 250kW vehicles
- Optimize sizing of battery and fuel cell systems, coupled with the control strategy for power split for military load profiles and understand the impact of different mission profiles
- Address PEMFC challenges unique to military application, such as heat rejection in armored vehicles with low surface area, startup from sub-zero temperatures, and operation at dry ambient conditions.

Strategic Context:

- This research seeks to address PEMFC challenges unique to military applications, such as heat rejection in armored vehicles with low surface area, startup from sub-zero temperatures, and operation at dry ambient conditions.
- Military vehicles have power requirements ranging from 300W robots to 250kW vehicles, requiring scalable and flexible simulation models for assessing the design and operation tradeoff for hybrid electric drive systems. The vehicle sizes targeted in this research range in size, including the Pack Bot, Squad Maneuver Equipment Transport (SMET), SCARAB, Next Generation Combat Vehicle (NGCV), and an Electric Tank.

OPSEC1890

Accomplishments:

- Integrated existing validated battery thermal models into the optimal power split problem formulation.
- Developed scalable liquid-cooled fuel cell model for high power stacks, by including a compressor and radiator models to account for parasitic loads.
- Parameterized the liquid-cooled fuel cell model to match the Hydrogenics 15kW PEMFC stack presently used in TARDEC demonstration vehicles.
- Studied the impact of system architecture (balance of plant components and sizing, including stack sizing battery and DC/DC converter) on efficiency for a given load profile.
- Translated MATLAB/Simulink Fuel Cell models into Gamma Technology (GT) Suite code in support of technology transfer to TARDEC.
- Evaluated the impact of regenerative braking for military cycles. The results were presented in the 2018 IEEE Conference on Control Technology and Applications in Copenhagen, Denmark in August 2018. Corresponding publication is titled: "Role of Regenerative Braking in Velocity Trajectory Optimization of Electrified Powertrains over varying Road Grades."
- Formulated and solved the optimal control problem for joint sizing, power split and velocity trajectory (assuming autonomous vehicles) using Pontryagin's minimum principle and Dynamic Programming. The results were presented at the American Society of Mechanical Engineers (ASME) Dynamic System and Controls Conference (DSCC) in Atlanta, October 2018. The paper is titled "OPTIMIZATION OF ENERGY-EFFICIENT SPEED PROFILE FOR ELECTRIFIED VEHICLES."

Introduction:

Given the high-power demand requirements of military drive cycles and extreme environmental conditions in temperature and humidity, modeling and simulation tools are needed to perform Right sizing and power control for Proton Exchange Membrane (PEM) Fuel Cells (FC) running on hydrogen and hybridized with a lithium ion battery pack. This research aims to address the optimal sizing of Lithium ion battery and PEM FC stack for:

- A1) Various Military Cycles (with high power demand)
- A2) Powertrains ranging from 300W robots to 250kW vehicle
- A3) Startup from freezing temperatures
- A4) Operating at dry ambient conditions

When hybridizing a power train, it is challenging to size the energy buffer (EB) or lithium ion battery because the drive cycle, the control policy, and the hardware architecture all affect the optimal size. The type and characteristics of the energy buffer used also affect the EB sizing, for example reduced performance of the lithium ion batteries at cold temperatures limits their power capability. When increasing the EB size in hybrid electric vehicles, the total vehicle weight increases, which affects the fuel consumption [1] and maneuverability. In order to prepare the PEMFC stack for startup from harsh environmental conditions such as subfreezing temperatures [1], [2], [3], energy intensive purging strategies are required as part of the shutdown process to ensure excess water is removed from the stack. Therefore, the startup and shutdown energy

requirements should also be considered as part of the sizing study. These requirements have not been previously addressed in the sizing literature or how to handle the warm-up from cold temperatures when considering the temperature dependent performance of both the battery and PEMFC system.

The problem outlined above involves design of the power split for the fuel cell and battery and joint systematic sizing of both FC and battery for various vehicle sizes and drive cycles. The objective of the research is to develop scalable physics-based models of the PEMFC system and balance of plant components, including Hydrogen storage, that capture the relevant tradeoffs in designing hybrid systems. This includes performance (power output), fuel consumption, startup time, volume and weight.

Figure 1 shows the Balance of Plant (BOP) components required to support operation of the PEMFC stack. The major parasitic losses are associated with the pumps and air compressor. The advantage to using physics-based models is that they can be upgraded to include degradation (lifetime) concerns under dry ambient conditions, limited cooling scenarios or during fast startup.

Approach:

There are 3 main technical challenges that we plan to address during this research

- 1) Coupling of electrical, thermal, and water management systems of the PEM Fuel Cell during warmup from low temperatures and potential to exchange thermal energy with the battery to enhance battery warmup.
- 2) Complexity of combined sizing, optimal power split and trajectory optimization problem.
- 3) Unknown impact of power-split and sizing on the degradation rates of the Battery and Fuel Cell (Stretch Goal).

Our goal is to develop a scalable reduced-order model for the hybrid system that can predict dynamic battery and fuel cells temperatures and terminal voltages within 5% error during a military drive cycle. We aim to demonstrate via simulation that > 5% Increase in vehicle range can be achieved through hybridization and right sizing of components.

We will apply scalable physics-based models of the fuel cell integrated with existing scalable electro-thermal models of the lithium ion battery including phenomenological models of the degradation rate parameterized from experimental data. Based on these physical models we can develop reduced-order models which capture the dominant trends relevant to component sizing and system performance. For scaling of the battery in the hybrid system we can use a modular approach, adding cells in parallel and series, and changing the chemistry and electrode thickness to yield cells with different power/energy ratio.

The team at UofM is working work with TARDEC Engineers to collect baseline performance data on the available 15kW PEMFC stacks needed to parameterize the fuel cell stack and Balance of plant models. Once this data has been collected and used to parameterize the physics based PEMFC model, we will validate the model performance on additional data sets. The

parametrized PEMFC model will then form the base for studying sizing of fuel cell /energy of storage, cooling/heating requirements and parasitic loads (e.g. air compressor). These results will be shared with our industry partners to get feedback and additional validation where possible.

Dynamic Programming [6],[7] and pseudo-spectral co-location (using GPOPS II [5],[9]) will be used to establish the baseline optimal system performance and perform the joint sizing and velocity optimization studies. Using these results an on-line implementable controller based on an Equivalent Consumption Minimization Strategy (ECMS) will be applied to determine performance under various drive cycles with different battery sizes and initial temperatures. The equivalence factor converts battery power to an equivalent fuel power that must be added to the actual fuel power to attain a charge-sustaining control strategy [11]. We will investigate opportunity to leverage excess heat from the PEMFC system during warmup [4] to aid/speed battery warmup and study the impact on overall system efficiency.

Results and Discussion:

The role of regenerative braking for autonomous and electrified military vehicles:

The work presented in this section of the report is also published in [34]. The adoption of electric and autonomous vehicles provides an exciting opportunity to reduce energy consumption by optimizing the velocity trajectory, while considering constraints on trip time and speed limits. This reduced battery energy consumption increases vehicle range for both Hybrid Electric (HEV) and Electric Vehicles (EV). Another method of increasing range is by using the regenerative braking systems which can recover some of the kinetic energy that would otherwise be wasted in friction brakes. It was shown in [27] that regenerative braking can have a significant impact on range extension for EVs for urban driving cycles. However, by the second law of thermodynamics, braking and recuperating energy for later use is less efficient than not braking and utilizing the kinetic or potential energy for propulsion. In this research we investigated the Impact of regenerative braking for military cycles on autonomous vehicles of various sizes.

Prior optimal energy management solutions for electric vehicles have been found for flat roads in both online and offline implementations [28], [29]. However, changing road grades adds an additional gradient force acting for and against the vehicle. [30], the authors used Pontryagin's Minimum Principle to solve the optimal velocity trajectory of a vehicle traversing a hill. They concluded that the optimal velocity was to “increase speed while approaching the base of the hill, and then allow the speed to drop off while climbing the hill ... and the reverse while descending.” Similar results have been proposed for the traversing of road grades by trucks [31] and conventional vehicles [32].

The regenerative braking system is not 100% efficient and there are losses during energy conversion. If we consider optimal velocity trajectory implementation for autonomous vehicles, then the highest possible efficiency is sought. Hence, braking will be avoided as far the constraints allow, even in hill descent. Here we find the optimal velocity trajectory while traversing road grades for electric vehicles, through offline globally optimal solutions using dynamic programming. The cost function to be minimized in the optimization is the power demanded by the motor. In this way, the negative power from regeneration reduces

OPSEC1890

the cost. Utilizing the vehicle model defined before, a 2-D map of the regenerative braking efficiency can be generated as shown in [34]. The efficiency is of converting mechanical power at the wheels to electric power in the generator. The generator capacity is limited and is shown by the thick black solid line in Figure 2, beyond which additional power is dissipated as heat.

Three different vehicle cases are considered in this paper with varying power to weight ratios as shown in Figure 3. The first two cases are run for EPA's GEM drive cycle while Case III is run over steeper military grades. For each case, three different constraints are applied all of which force the optimal velocity to traverse the given distance in the same time as constant speed lead. While traversing varying road grades, the optimal solutions were shown to avoid braking as far as the constraints allowed and not use the regenerative braking system. These results were replicated for lighter robots on much steeper road grades. While regenerative braking and eco-driving are both methods for range extension of EVs, the former was only utilized to meet vehicle limitations or traffic constraints. For example, the heavier vehicle (twice the mass of a Tesla S) had a greater gravitational pull and had to brake in Constraint II to meet the distance limitations. But when the limitations were relaxed in Constraint III, the optimal trajectory avoided regenerative braking. Utilizing the motor energy minimization strategy, significant energy reductions up to 24% were shown for changing road grade, which translates into a corresponding increase in range. In other words, a significant increase in driving range can be achieved without increasing battery size.

Selected distance segments of the results are shown in Figure 4, where the optimal velocity deviates significantly from the constant velocity case by following the optimal principles of hill climbing. These deviations reduced electric energy demand for the motor by 24.2%. In the left plots from 3-3.5 km, the optimized cycle does not use the motor, but the robot velocity does not violate the limit. On the other hand, in the right plots, with a much steeper drop, the robot must apply regenerative braking to maintain the velocity within the constraints.

Velocity Trajectory Optimization for Autonomous Vehicles to minimize energy consumption:

The work presented in this section is also published in [43] and [44]. In this section, the minimum energy consumption problem is presented and analytically solved by applying Pontryagin's Maximum Principle (PMP). PMP is a powerful computational and analytical tool used to solve optimal control problems. PMP provides a set of necessary conditions that an optimal control must satisfy while maximizing (or minimizing) the Hamiltonian function. For a certain class of optimal control problems, such as power management of hybrid electric vehicles, the solutions obtained from PMP and DP are almost identical, which makes PMP widely used in automotive applications [18], [20], [21]. For simplicity, the following assumptions are made: (1) the efficiency of the system is invariant, that is, motoring and generating efficiency of the electric motor is fixed; (2) the vehicle moves forward only; (3) road grade and velocity limit are distance-dependent and known a priori. It is noted that although the efficiency of an electric motor is generally nonlinear [19], the

efficiency is relatively constant above certain force or torque levels covering nominal operating range, which makes the first assumption reasonable. Preliminary analysis using nonlinear efficiency motor map are underway and show similar results.

Model Description:

The motion of a ground vehicle considered in this study is described by the following equations:

$$\frac{ds}{dt} = v, \quad (1a)$$

$$M \frac{dv}{dt} = F_p + F_b - A - Bv - Cv^2 - Mg \sin \theta, \quad (1b)$$

Where s and v represent distance and velocity respectively while M is vehicle mass and t is time. The variables A , B , and C are coefficients used to determine resistance forces by rolling and aerodynamic drag, and the grade angle θ is a function of distance, i.e. $\theta = \theta(s)$. The variables F_p and F_b denote control inputs regarding propulsion and braking, respectively. Hereafter, $\bar{*}$ and $\underline{*}$ are used to refer to the maximum and minimum values of parameter $*$.

For the purpose of analysis, Eq. (1b) is rewritten as:

$$M \frac{dv}{dt} = F_m + F_g + F_{fb} - A - Bx_2 - Cx_2^2 - Mg \sin \theta, \quad (2)$$

Where F_m , F_g , and F_{fb} represent motoring, generating, and friction braking forces, respectively. This choice is deliberate to clearly distinguish operational modes of the vehicle. By defining states and controls such that:

$$x = [s, v]^T,$$

$$u = [u_1, u_2, u_3]^T = \left[\frac{F_m}{M}, \frac{F_g}{M}, \frac{F_{fb}}{M} \right]^T,$$

the equations of motion (1) and (2) can be expressed as following:

$$\dot{x}_1 = x_2 \quad (3a)$$

$$\dot{x}_2 = u_1 + u_2 + u_3 - \alpha \cos \theta(x_1) - \beta x_2 - \gamma x_2^2 - g \sin \theta(x_1) \quad (3b)$$

Where $\alpha = \frac{A}{M}$, $\beta = \frac{B}{M}$, $\gamma = \frac{C}{M}$. The coefficients A , B , and C are used to compute the resisting forces; rolling and aerodynamics forces, with the resisting forces being speed-dependent, whilst the grade force depends on the angle, θ , such that:

$$f_r = A + Bx_2 + Cx_2^2$$

$$f_g = Mg \sin \theta$$

Control inputs are bounded by their limits such that $0 \leq u_1 \leq u_1(x_2)$, $u_2(x_2) \leq u_2 \leq 0$, and $u_3(x_2) \leq u_3 \leq 0$. It is noted that the force limits of an electric machine and a friction brake are typically functions of speed. Initial and terminal conditions of the states are:

$$x_1(0) = 0, \quad x_2(0) = 0, \quad (4a)$$

$$x_1(t_f) = S_f, \quad x_2(t_f) = 0 \quad (4b)$$

Where t_f and S_f are operational time and distance traveled, and these are bounded, meaning that the vehicle stops at time t_f after traveling a given distance, S_f . The vehicle is assumed to move forward only, i.e., $x_2(t) > 0$, $t \in (t_0, t_f)$.

Optimal Control Modes:

The primary focus of this study is to optimize a speed profile which minimizes the energy consumption while traversing a given distance. Therefore, the cost function to be minimized is the normalized total energy consumption for a given mission and defined by:

$$J = \int_0^{t_f} \frac{P_e^{elec}}{M} dt = \int_0^{t_f} (x_2 u_1 \eta_1 + x_2 u_2 \eta_2) dt \quad (5)$$

Where P_e^{elec} is the electrical power by the motor; and η_1 and η_2 denote motoring and generating efficiency of the electrical machine, respectively.

As a result of the Hamiltonian analysis, we find that the number of feasible control modes is five (Table 1) and that two different braking modes are used in an electrified vehicle unlike a conventional vehicle without regenerative braking capability.

Constraints on Propulsion and Braking:

Propulsion and regenerative-braking of the electrified vehicle are limited by the maximum power from electric components such as electric motor(s), a fuel-cell and a battery. As a result, the influence of these limits or constraints on vehicle operation need to be clearly understood to properly formulate the control problem. In general, electric motors used in transportation system are characterized by the maximum torque curve, a function of their operating velocity as shown in Figure .

Dynamic Programming Implementation:

The formulation of an optimal control problem is complicated and has implications for the obtained solution. By solving the same problem in different ways, we can determine more straightforward and less computationally intensive methods. Specific factors impact the

optimization of energy consumption in an electric vehicle. These factors include the constraints on the speed, acceleration, time, distance, and braking force.

In practice, speed restrictions or limits are set throughout roads, or based on the vehicle characteristics. To simplify implementation, the equations of motion are rewritten in the distance domain. This reformulation is beneficial in handling road data such as grade and speed restrictions as also mentioned in [19]. Thus, the optimal control problem (OCP) can be reformulated as:

$$\begin{aligned}
 \min J &= \int_0^{s_f} (\eta^q f_e(x_2, u)) ds \\
 \text{s.t. } x'_1 &= \frac{1}{x_2}, \\
 x'_2 &= \frac{(f_e(x_2, u) + f_f(u) - f_r - f_g)}{Mx_2}, \\
 x_1(0) &= 0, \quad x_1(s_f) = t_f, \\
 x_2(0) &= 0, \quad x_2(s_f) = 0, \\
 u &\in \{1, 2, 3, 4, 5\},
 \end{aligned} \tag{18}$$

Where η is the motor efficiency and the mode-dependent variable q is defined such that $q = 1$ for regenerative-braking and $q = -1$ for propulsion. Note that the equations of motion are expressed in terms of s and hence x' is used instead of \dot{x} to represent a derivative with respect to distance rather than time. i.e., $x = [x_1, x_2]^T = [t, v]^T$.

To solve the optimal control problem, Dynamic Programming (DP) is used in this study. DP is a powerful numerical technique to determine optimal trajectories explicitly using the Bellman's optimality principle while searching from the final state backward in time. It is well known that DP suffers from computational burden when the number of state and control variables increase, i.e., curse of dimensionality. Nonetheless, DP is still useful to find a global optimum even for nonlinear systems with constraints when the number of variables is small enough [23]. To perform optimization using DP, the equation of motion needs to be expressed in a discrete domain. Discretization inherently introduces numeric errors, which degrades the accuracy of the found solution. To avoid these numerical errors, a careful implementation is important [24]; in this study, discretization steps for time, velocity, and distance are chosen as provided in Table 2.

In mode 4, Full braking mode, friction braking is used in addition to regenerative braking. It is important to clarify that the benefit of this mode is reflected in its use when braking in excess of the regenerative braking motor torque limit is needed. This mode would allow the vehicle to respect the speed and time constraints; that is, the vehicle would be allowed to operate at higher speed because rapid deceleration is possible. Additionally, this mode

enables the system designer to choose an energy storage device with a smaller capacity that might otherwise limit regenerative braking capability.

Case Study:

A light-weight military ground robot, such as the PackBot [25], is considered as a target vehicle. As the needs of military vehicles rapidly increase, energy-efficient maneuvering becomes one of the most important requirements among robust performance, mobility and ability to support a variety of electrical loads. Because of the last requirement, electrified powertrains have been receiving attention in all branches of the military for their potential strategic benefits [12]. It should be noted that, although the application considered in this work is to a military ground vehicle, the presented work and approach can be applied to any electrified vehicles.

The Army Ground Vehicle Programs use various drive cycles including time, speed, and grade, for testing and validation of new vehicle systems and models. These cycles have traditionally been characterized by run speed, number of stops, and terrain profile. For the sake of powertrain analysis, there have been a number of additional metrics proposed for characterization of such drive cycles in the context of fuel economy evaluation. The drive cycles for ground vehicles focus on running at a constant speed over varied terrain for practical reasons [26]. Thus, two different drive conditions are studied: relatively flat (Convoy) and hilly roads (Churchville B). Specifically, these two drive cycles are considered as the baseline operations when comparing the performance of the optimized speed profile obtained from DP; that is, the total energy consumption and trip time traversing these two cycles are computed from a given set of time, speed, and grade information. Table 3 displays the parameters used in the case study. Note that due to the motor's speed limit, the original Convoy and Churchville B cycles are scaled by a factor of 0.67 when applied to the small robot.

Non-hilly environment - Convoy cycle:

The Convoy Cycle, shown in Figure 6, has some deviation in speed and a small variation in grade. From the cycle and parameters in Table , the resisting force, f_r , the grade force, f_g , and the acceleration required to operate the robot can be computed.

The total electrical energy consumed from the Convoy cycle was calculated to be 1.06 MJ, which represents the baseline value for a non-hilly operation. Figure displays the results of total energy consumption for different trip durations, which clearly shows a trade-off between energy consumption and trip time. Particularly, when the trip time is the same as the baseline, the total electrical energy consumed to traverse the optimal speed profile obtained by DP is 21% less, i.e., 0.84 MJ. For the same energy consumed as the base cycle, a 14% reduction in trip time is achieved as highlighted in Figure .

Figure shows the speed profiles over two different trip times in addition to the baseline Convoy cycle. With the speed limit set at 23 m/s and with a non-hilly road, the vehicle does not show frequent mode changes, but a stable cruising operation that allows the vehicle to stop within the set trip time. Additionally, for the same distance but with a longer

trip time, the vehicle tends to decrease its speed, which obviously reduces the energy consumption. The propulsion and cruising that the vehicle executes are due to the little deviation in grade that allows the vehicle to increase its speed at downhill without enduring additional energy loss. The regenerative braking is used at the end of the trip to stop in accordance with the final velocity constraint.

Rugged hilly environment - Churchville B Cycle:

Unlike the Convoy cycle, the Churchville B cycle provides constant velocity throughout the trip however, this cycle has a more discernible grade change that highlights the performance benefits of velocity optimization over a more irregular course or terrain that has steeper grades.

The total electrical energy consumed from the Churchville B cycle was calculated to be 0.41 MJ, which represents the baseline value for the rugged-hilly operation. Using trip time similar to the baseline, the solution to the OCP shows a 24% reduction in energy consumption, i.e., 0.31 MJ. Moreover, it is observed from Figure 8 that a 24% reduction in total trip time can be achieved when consuming the same amount of electrical energy as the baseline.

The results in Figure 8 display the speed profile for Churchville B cycle over two different trip times compared to the baseline. The vehicle exhibits several mode changes as it drives over an uphill and downhill distinctively; in particular, coasting and cruising modes are effectively utilized to minimize energy consumption. As the trip time decreases, the vehicle tends to make better use of increased speed at downhill and uses the propulsion mode more often. In contrast, for a longer trip time, the vehicle tends to use regenerative braking to store energy while sticking to the final distance/speed constraints.

Battery and PEM Fuel Cell stack sizing under armor: balance of plant energy consumption and sizing.

Military vehicles currently have high power demands for external components such as weapons, communications devices, and active armor. These vehicles must provide silent mobility for some established missions which may not be achieved under the current use of internal combustion engines. Due to these requirements, the military has currently started transitioning to electric powertrains. One type of energy system that might be suitable for the military vehicles is the proton exchange or polymer electrolyte membrane fuel cell (PEMFC). This is due to their silent and low temperature operation (no heat signature or noise, and around 80°C of operating temperature) and higher efficiency (around 50% efficiency).

Liquid cooled PEMFCs are mainly used for high power density fuel cells (>5 kW) due to the heat transfer coefficients being higher than the ones used by air cooling [33]. In this study, a liquid cooled PEMFC will be used since the military vehicles under this study are high power systems. A battery that takes all the transient loads of the system will be combined with the fuel cell. The optimal power split between these two systems needs to be determined.

Another limitation in military vehicles that needs to be addressed is the limited space for the cooling system. Therefore, a compressor, motor and radiator will be included in this study with the fuel cell and battery. The sizing effect of the battery and the fuel cell will be investigated. Three different military vehicles (small, medium, and large) will be used with a speed and road grade vehicle model to obtain the required load profile from different drive cycles [34]. A compressor model that consists of a dimensionless pressure head [35] will be used to calculate the oxygen pressure and required airflow for the fuel cell polarization curve. A scalable radiator model that considers the air and coolant velocity will be used to determine the cooling temperature [36]. A fuel cell model consisting of dynamic membrane water content, stack temperature and channel humidity will be used [37], [38], with an electro-thermal battery model to determine the optimal power split between the systems. The effect of different fuel cell and battery sizes will be studied for the three military vehicles.

System Model:

A small (infantry unmanned ground vehicle), medium (wheeled tactical), and large (tracked combat) military vehicle will be taken into consideration for the power split. Details and information of these three types of vehicles are given in Table 4. The model of the vehicle drivetrain will consist of a compressor, radiator, electric drive motor, fuel cell and battery that will be explained in the following sections. A block diagram of the components and the connections between them is shown in Figure 1. The vehicle model used considers the speed and road grade to obtain the required load profile for the electric motor and is the same as the one explained on the previous section.

Compressor Model:

The fuel cells performance depends on the airflow supplied to it. Therefore, the compressor needs to supply the required airflow for the fuel cell. We use a compressor map to determine the electric power demand for maintaining a given air flow. The efficiencies are experimentally determined for different pressure ratios and air flow rates by the manufacturer. We use these points to construct the compressor map as shown in Figure 9. The thick black lines indicate the limits of operation of the compressor.

Radiator Model:

The fuel cell performance is affected by its temperature and maintaining temperature below 80°C extends membrane lifetime. However, it also decreases fuel cell performance and adds requirements to the radiator size. A radiator is used to cool the system to an appropriate temperature and avoid performance losses and failure due to high temperatures on the fuel cell. A scalable radiator model that consists of sub-model equations for the heat transfer coefficient of the air and the coolant to obtain the overall heat transfer of the system is used [36]. Figure 10 shows the different airflows and the corresponding power required to produce the given coolant flowrate for a constant temperature. In this project we are considering this parasitic loss (power required to operate the radiator) as part of the fuel cell load or power.

OPSEC1890

Fuel Cell Model:

For this project, the main component that will be used to produce the required power for the vehicle to operate will be the fuel cell. The fuel cell used for optimal power split analysis of the vehicle is a 15 kW hydrogenics liquid cooled fuel cell is used. Experiments were scheduled and the data from operation with a constant stack current corresponding to fixed stack power (1, 3, 5, 7, 9, 11, 13 kW) was used to anchor the model parameters. The corresponding stack voltage, airflow, fuel cell and coolant temperature were obtained from the onboard data acquisition system. A temperature and membrane water content (λ_{mb}) dependent fuel cell model was adopted [39] and fit to this data. As can be appreciated in Figure 11 and Figure 12, the polarization curve and peak power varies depending on the temperature of the fuel cell. Figure 13 shows the resistance dependence on λ_{mb} for a fixed temperature of 30°C. As λ_{mb} increases, the resistance decreases. This affects the polarization curve and peak power. Therefore, with this developed model we should be able to capture the physical phenomena from the fuel cell more accurately and obtain an efficient power split.

Battery Model:

For this project, we are using a Sanyo cell of 4.5 Ah. This battery has a power range of 225.5 and -225.5 kW and a 24.7 MJ energy from 0.9-0.1 SOC range. After running some experiments of constant current at low C-rates and pulsed current, a simple thermal OCV-R battery model [40] is used and later fitted to the data. The reason for developing a thermal OCV-R model is shown in Figure 14. As the temperature decreases the resistance increases. This affects the open circuit voltage (OCV) of the battery and consequently the power produced and efficiency of the battery. Therefore, with this developed model we should be able to capture the physical phenomena from the battery more accurately and obtain an efficient power split.

Optimal Control Strategy:

The battery and fuel cell performance depend on their respective temperatures. For example, at high temperatures the internal resistance in the battery (R_b) and the membrane resistance in the fuel cell (R_{mb}) both decrease. The membrane resistance in the fuel cell also depends on the concentration of water (λ_{mb}). If the membrane is dry ($\lambda_{mb} < 2$) the membrane resistance increases, which is more likely to occur at elevated operating temperature due to the increased saturation pressure, which promotes water removal from the stack. Therefore, in order to obtain the optimal power split we need to determine the appropriate inputs and states of the system and use an efficient method. The inputs of the system are: the current of the fuel cell (I_{fc}), the input mass flow rate (W_{in}), the fan mass flow rate (W_{fan}), and the coolant power ($P_{coolant}$). The states of the system are the state of charge of the battery (SOC), the fuel cell temperature (T_{fc}), and the coolant temperature ($T_{coolant}$).

The problem with having 4 inputs and 3 states is that methods such as Dynamic Programming (DP) will take a lot of computational time to obtain an optimal power split solution (around hours or even days). Pseudo spectral methods that use a direct collocation method to approximate a state using a global polynomial could be used for our optimization problem [41]. We currently use GPOPS software that consists of Legendre-Gauss-Radau (LGR) points for approximation. Its layout and solutions are similar to DP [42] and it's able to reduce computation time significantly.

Conclusions:

This work highlights the importance of combined sizing and power split for PEMFC hybrid systems where the battery supplies less than 50% of the total trip energy, and thus the fuel cell serves as a range extender. The effects of battery temperature and battery thermal limits have been incorporated into the modeling framework, using previously validated models of high-power batteries of nickel manganese cobalt chemistry from a ford fusion hybrid. A physics-based model of membrane hydration and GDL flooding has also been incorporated to guide the optimal power split when operating in extreme environmental conditions. Including the dynamics of battery and FC temperature resulted in an improvement in system efficiency, due to the reduced cooling requirement during stack warmup as compared to the rule-based strategy. The final project deliverable which includes tools to evaluate and optimize the combined battery and fuel cells sizing and power split design are in progress and expected to be completed next year along with the finalized on-line implementable controllers.

An extension of the power-split optimization has also been investigated for the case of autonomous or semi-autonomous vehicles to include optimization of the vehicle velocity over a driving cycle. Thus, enabling us to leverage the kinetic and potential energy storage of the vehicle itself, and avoiding un-necessary energy conversion. This optimization of the vehicle velocity over the cycle has the potential to save up to 24% energy on the tested military driving cycles and could hence further increase an electric vehicle range. The framework for studying the impact of velocity optimization on the best power split has been outlined and will be further investigated in the following quarter.

References:

- [1] R. K. Ahluwalia, X. Wang, J-K Peng, and C. F. Cetinbas "Fuel Cells Systems Analysis" DOE Hydrogen and Fuel Cells Program 2016 Annual Merit Review and Evaluation Meeting. Washington, D.C. June 6-10, 2016.
- [2] Ahluwalia, R.K., and Wang, X. (2006) Rapid self-start of polymer electrolyte fuel cell stacks from subfreezing temperatures, *J. Power Sources*, 162, 502–512.
- [3] Fangming Jiang, Chao-Yang Wang, and Ken S. Chen "Current Ramping: A Strategy for Rapid Start-up of PEMFCs from Subfreezing Environment" *J. Electrochem. Soc.* 2010 157(3): B342-B347;
- [4] E. A. Muller, A. G. Stefanopoulou, and L. Guzzella. Optimal power control of hybrid fuel cell systems for an accelerated system warm-up. *IEEE Transactions on Control Systems Technology*, 15(2):290-305, March 2007.

- [5] Patterson, M. A. and Rao, A. V. 2012. GPOPS-II: A MATLAB software for solving multiple-phase optimal control problems using hp-adaptive Gaussian quadrature collocation methods and sparse nonlinear programming. *ACM Trans. Math. Softw.* 41, 1, Article 1 (October 2014), 37 pages.
- [6] Sundstrom, O.; Guzzella, L., "A generic dynamic programming Matlab function," *Control Applications, (CCA) & Intelligent Control, (ISIC), 2009 IEEE* , vol., no., pp.1625,1630, 8-10 July 2009
- [7] Sundström, O., D. Ambühl, and L. Guzzella. "On implementation of dynamic programming for optimal control problems with final state constraints." *Oil & Gas Science and Technology–Revue de l'Institut Français du Pétrole* 65.1 (2010): 91-102.
- [8] Patterson, Michael A., and Anil V. Rao. "Exploiting sparsity in direct collocation pseudospectral methods for solving optimal control problems." *Journal of Spacecraft and Rockets* 49.2 (2012): 364-377.
- [9] Patterson, Michael A., and Anil V. Rao. "GPOPS-II: A MATLAB software for solving multiple-phase optimal control problems using hp-adaptive Gaussian quadrature collocation methods and sparse nonlinear programming." *ACM Transactions on Mathematical Software (TOMS)* 41.1 (2014): 1.
- [10] W. Zhou, C. Zhang, J. Li and H. K. Fathy, "A Pseudospectral Strategy for Optimal Power Management in Series Hybrid Electric Powertrains," in *IEEE Transactions on Vehicular Technology*, vol. 65, no. 6, pp. 4813-4825, June 2016.
- [11] S. Onori, L. Serrao, G. Rizzoni. "Hybrid Electric Vehicles Energy Management Strategies" Springer-Verlag London 2016.
- [12] B. Lu, B. Natarajan, and N. Schulz. "Optimal control based power management in hybrid military vehicle". In *2012 IEEE International Electric Vehicle Conference*, pages 1-7, March 2012.
- [13] R.D. Geertsma, R.R. Negenborn, K. Visser, and J.J. Hopman. "Design and control of hybrid power and propulsion systems for smart ships: A review of developments". *Applied Energy*, 194:30 – 54, 2017.
- [14] Lu, S., Hillmansen, S., Ho, T. K., and Roberts, C., 2013. "Single-train trajectory optimization". *IEEE Transactions on Intelligent Transportation Systems*, 14(2), June, pp. 743–750.
- [15] Xu, J., Nikovski, D., and Kimura, S., 2015. "A frame-work for real-time near-optimal train run-curve computation with dynamic travel time and speed limits". In *2015 American Control Conference (ACC)*, pp. 533–540.
- [16] Petit, N., and Sciarretta, A., 2011. "Optimal drive of electric vehicles using an inversion-based trajectory generation approach". *IFAC Proceedings Volumes*, 44(1), pp. 14519 – 14526. 18th IFAC World Congress.
- [17] Mensing, F., Trigui, R., and Bideaux, E., 2011. "Vehicle trajectory optimization for application in eco-driving". In *2011 IEEE Vehicle Power and Propulsion Conference*, pp. 1–6.
- [18] Chen, D., Kim, Y., and Stefanopoulou, A. G., 2018. "Soc node planning for PHEVs with segmented traffic information". In *2018 American Control Conference*.
- [19] Chen, Y., Li, X., Wiet, C., and Wang, J., 2014. "Energy management and driving strategy for in-wheel motor electric ground vehicles with terrain profile preview". *IEEE Transactions on Industrial Informatics*, 10(3), Aug, pp. 1938–1947.

- [20] Kim, N., Cha, S., and Peng, H., 2011. "Optimal control of hybrid electric vehicles based on Pontryagin's Minimum Principle". IEEE Transactions on Control Systems Technology, 19(5), Sept, pp. 1279–1287.
- [21] Ahmadizadeh, P., Mashadi, B., and Lodaya, D., 2017. "Energy management of a dual-mode power-split powertrain based on the pontryagin's minimum principle". IET Intelligent Transport Systems, 11(9), pp. 561–571.
- [22] Kelley, H. J., 1964. "A second variation test for singular extremals". AIAA Journal, 2, Aug., pp. 1380–1382.
- [23] Bellman, Richard (1954), "The theory of dynamic programming", Bulletin of the American Mathematical Society 60: 503–516, doi:10.1090/S0002-9904-1954-09848-8, MR0067459.
- [24] Kirk, D. E (1970). Optimal Control Theory: An Introduction. Englewood Cliffs, NJ: Prentice-Hall. p. 86–90. ISBN 0-13-638098-0.
- [25] "Military and Veteran Benefits, News, Military.com. [Online]. Available: <https://www.military.com/defensetech/2018/02/01/army-test-first-robotic-combat-vehicle-2021.html>.
- [26] Sebeck, K., Mange, J., MacLennan, J., and Rizzo, D., 2017. "Characterization of army ground vehicle drive cycles". In NDIA Ground Vehicle Systems Engineering and Technology Symposium.
- [27] Gao, Yimin, Liping Chen, and Mehrdad Ehsani. *Investigation of the Effectiveness of Regenerative Braking for EV and HEV*. No. 1999-01-2910. SAE Technical Paper, 1999.
- [28] Dib, Wissam, Lorenzo Serrao, and Antonio Sciarretta. "Optimal control to minimize trip time and energy consumption in electric vehicles." In *Vehicle Power and Propulsion Conference (VPPC), 2011 IEEE*, pp. 1-8. IEEE, 2011.
- [29] Dib, Wissam, Alexandre Chasse, Philippe Moulin, Antonio Sciarretta, and Gilles Corde. "Optimal energy management for an electric vehicle in eco-driving applications." *Control Engineering Practice* 29 (2014): 299-307.
- [30] Schwarzkopf, A. B., and R. B. Leipnik. "Control of highway vehicles for minimum fuel consumption over varying terrain." *Transportation Research* 11, no. 4 (1977): 279-286.
- [31] Hellström, Erik, Maria Ivarsson, Jan Åslund, and Lars Nielsen. "Look-ahead control for heavy trucks to minimize trip time and fuel consumption." *Control Engineering Practice* 17, no. 2 (2009): 245-254.
- [32] Ozatay, Engin, Umit Ozguner, John Michelini, and Dimitar Filev. "Analytical solution to the minimum energy consumption based velocity profile optimization problem with variable road grade." *IFAC Proceedings Volumes* 47, no. 3 (2014): 7541-7546.
- [33] Zhang, Guangsheng, and Satish G. Kandlikar. "A Critical Review of Cooling Techniques in Proton Exchange Membrane Fuel Cell Stacks." *International Journal of Hydrogen Energy*, vol. 37, no. 3, 2012, pp. 2412–2429.
- [34] N. Prakash, Y. Kim, D. Rizzo, M. Brusstar, J. B. Siegel, "Role of Regenerative Braking in Velocity Trajectory Optimization of Electrified Powertrains Over Varying Road Grades," 2018 IEEE Conference on Control Technology and Applications (CCTA), August 21-24 at Copenhagen, Denmark.
- [35] Moraal, Paul, and Ilya Kolmanovsky. "Turbocharger Modeling for Automotive Control Applications." SAE Technical Paper Series, 1999.

- [36] Jung, Dohoy, and Dennis N. Assanis. "Numerical Modeling of Cross Flow Compact Heat Exchanger with Louvered Fins Using Thermal Resistance Concept." SAE Technical Paper Series, 2006.
- [37] Nandjou, F., Poirot-Crouvezier, J.-P. et al., "Impact of Heat and Water Management on Proton Exchange Membrane Fuel Cells Degradation in Automotive Application," Journal of Power Sources 326, 2016.
- [38] Siegel, J.B., Yesilyurt, S., and Stefanopoulou, A.G., "Modeling and Experiments of Voltage Transients of Polymer Electrolyte Membrane Fuel Cells with the Dead-Ended Anode," Journal of Fuel Cell Science and Technology 9, 2012.
- [39] Siegel, J.B., "Experiments of Voltage Transients of PEM Fuel Cells for Dead-Ended Anode Operation," PhD diss., University of Michigan, 2010.
- [40] Perez, Hector E., et al. "Parameterization and Validation of an Integrated Electro-Thermal Cylindrical LFP Battery Model." Volume 3: Renewable Energy Systems; Robotics; Robust Control; Single Track Vehicle Dynamics and Control; Stochastic Models, Control and Algorithms in Robotics; Structure Dynamics and Smart Structures; 2012.
- [41] Patterson, Michael A., and Anil V. Rao. "Exploiting Sparsity in Direct Collocation Pseudospectral Methods for Solving Optimal Control Problems." Journal of Spacecraft and Rockets 49.2 (2012): 364-377.
- [42] W. Zhou, C. Zhang, J. Li and H. K. Fathy, "A Pseudospectral Strategy for Optimal Power Management in Series Hybrid Electric Powertrains," in IEEE Transactions on Vehicular Technology, vol. 65, no. 6, pp. 4813-4825, June 2016.doi: 10.1109/TVT.2015.2466671.
- [43] H. Abbas, Y. Kim, J.B. Siegel, D.M. Rizzo, "Optimization of Energy-Efficient Speed Profile for Electrified Vehicles", Dynamic Systems and Control Conference, Atlanta, 2018.
- [44] H. Abbas, Y. Kim, J.B. Siegel, D.M. Rizzo. 2018. Synthesis of Pontryagin's Maximum Principle Analysis for Speed Profile Optimization of Electrified Vehicles, Journal of Dynamic Systems, Measurement, and Control, to appear.

Figures and Tables Begin on the Next Page

Figures and Tables:

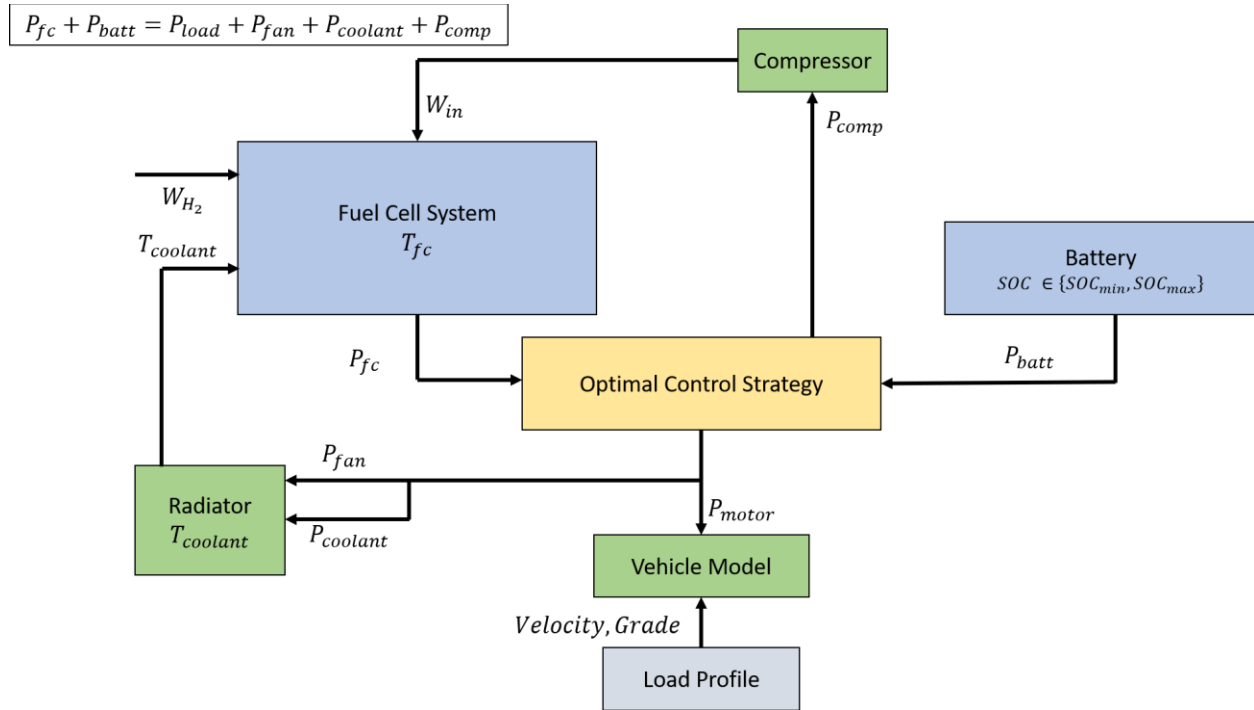


Figure 1. Block Diagram of the components used in the vehicle model and the relationship between the variables obtained from each component. The green boxes denote components that are energy sinks, the blue boxes denote the component that are energy sources, the yellow boxes denote the optimal control strategy and the gray box denotes the load input. The white box denotes the power rule used in the system.

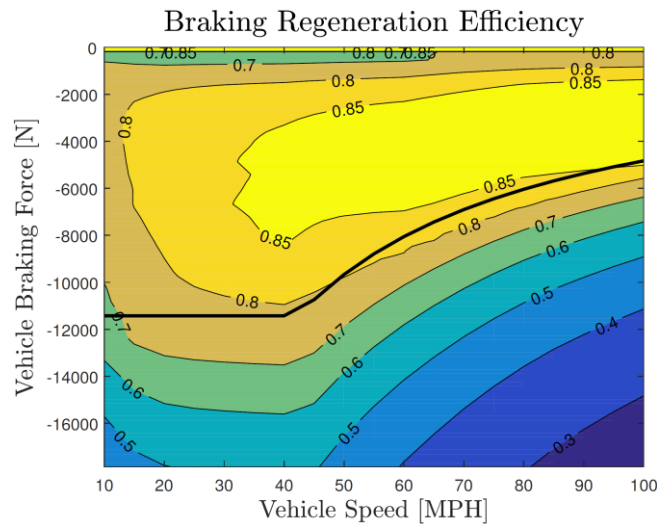


Figure 2: Motor Efficiency and peak torque (black line) used to calculate the regenerative braking efficiency for the vehicle model.

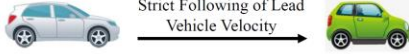
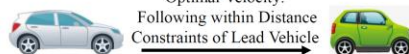
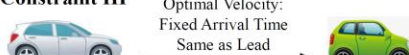
Simulation Case Vehicle/ Grade	Case I Tesla/ GEM grade	Case II Twice Mass Tesla/ GEM grade	Case III Military Robot/ Military grade
Constraint I Baseline: Strict Following of Lead Vehicle Velocity 	Regen Braking during - Hill Descent to maintain given velocity - Baseline	Regen Braking during - Hill Descent to maintain given velocity - Baseline	Regen Braking during - Hill Descent to maintain given velocity - Baseline
Constraint II Optimal Velocity: Following within Distance Constraints of Lead Vehicle 	No Regen Braking during - Hill Descent as all constraints satisfied without braking (+3.2%)	Regen Braking during - Hill Descent to satisfy given position constraints (+5.3%)	Not Considered
Constraint III Optimal Velocity: Fixed Arrival Time Same as Lead 	No Regen Braking during - Hill Descent as all constraints satisfied without braking (+8.0%)	No Regen Braking during - Hill Descent as all constraints satisfied without braking (+14.6%)	Regen Braking during - Hill Descent to satisfy maximum velocity constraints (+24.2%)

Figure 3. Summary of three vehicle and three constraint cases. Regen braking occurs only in cases where constraint violation might occur and not to minimize electric motor power demand. Motor power reduction over the baseline is shown in bold.

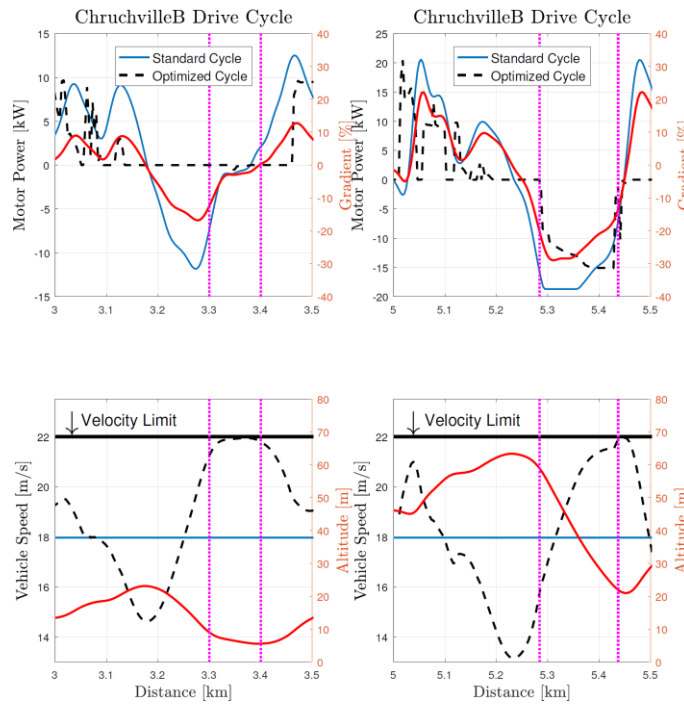


Figure 4. In the left plots, the velocity limit is not violated and the electric motor is shut off, while in the right plots since the descent is much steeper, conventional friction brakes must be applied to stay within the constraints.

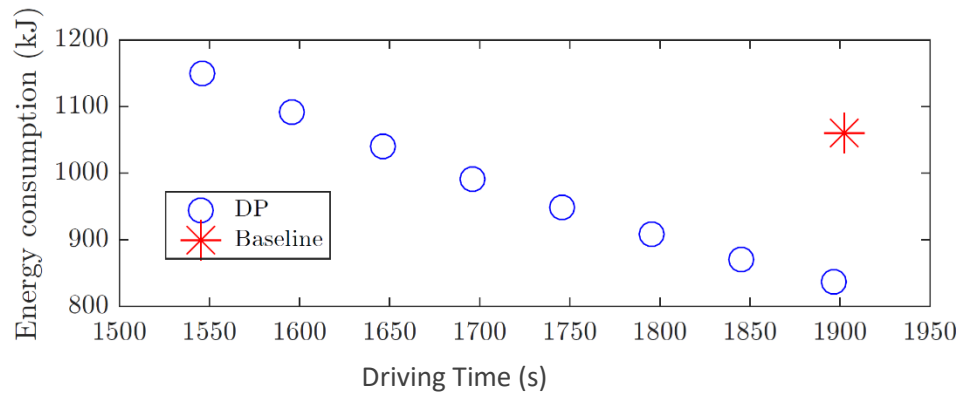


Figure 5. Tradeoffs Between Energy Consumption and Trip Time for Convoy Cycle

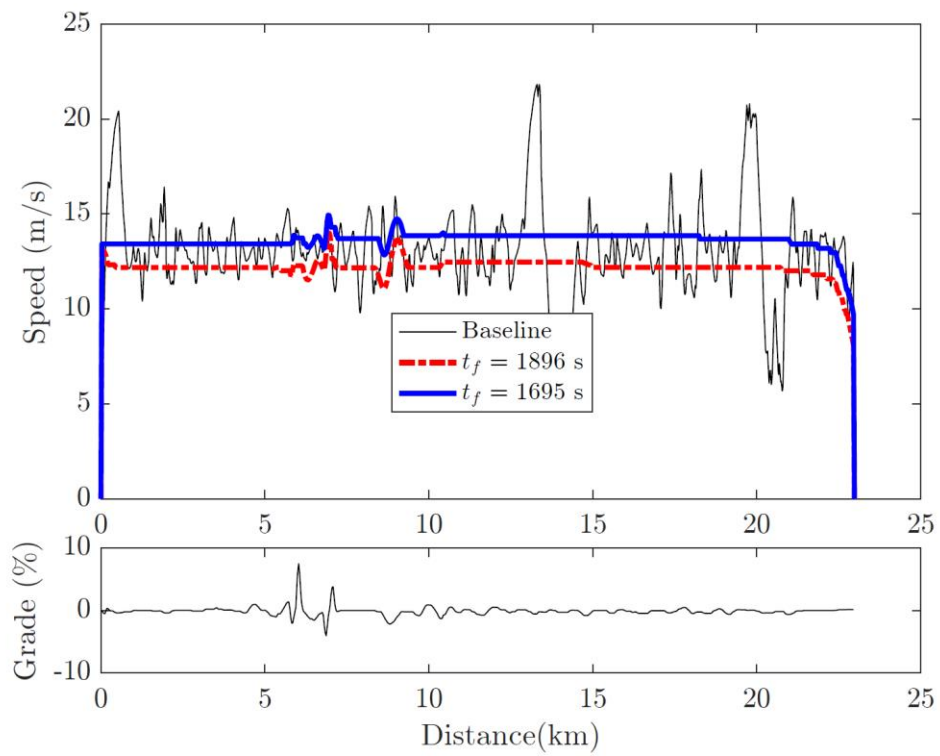


Figure 6. Comparison of Speed Profiles Over Convoy Cycle

Figures Continue on the Next Page

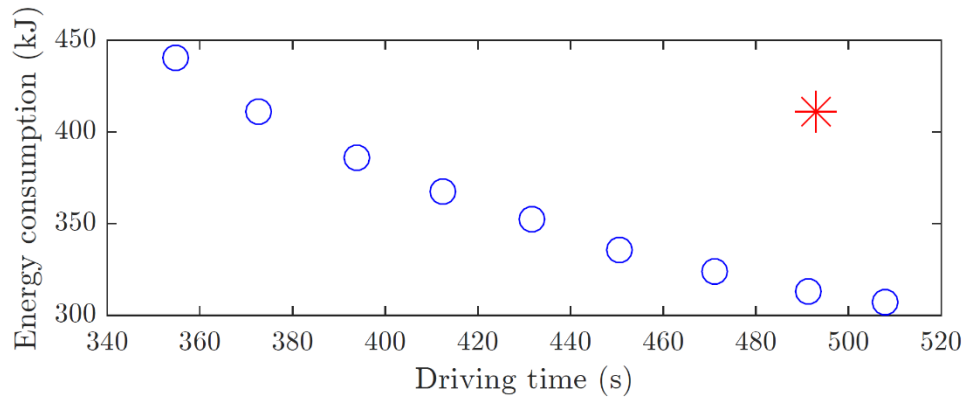


Figure 7. Tradeoffs Between Energy Consumption and Trip Time for Churchville B Cycle.

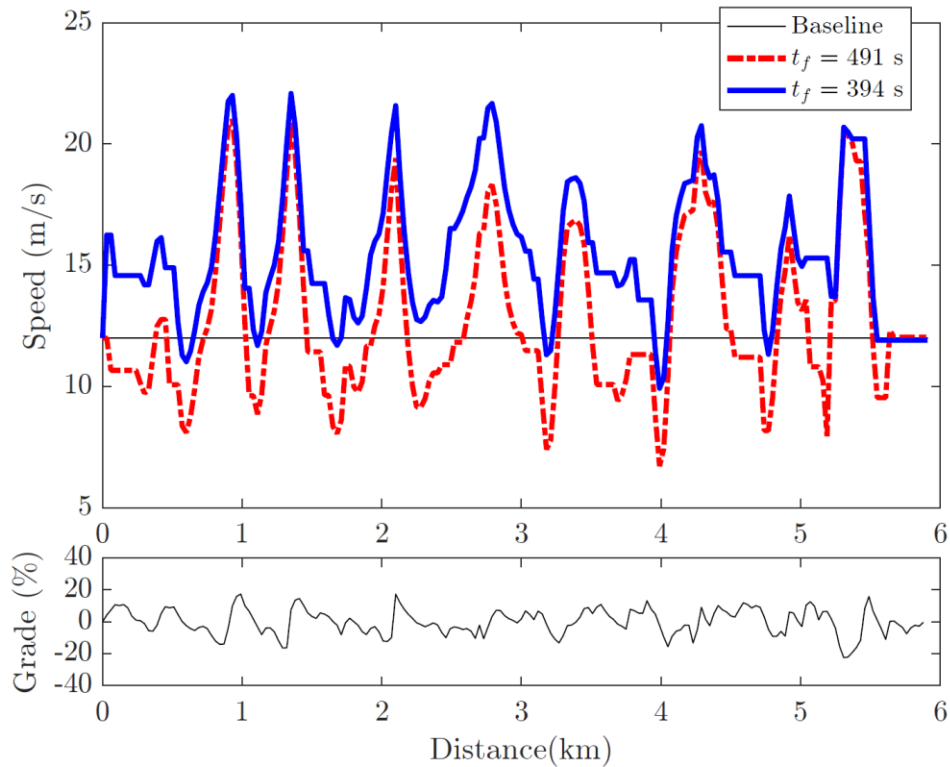


Figure 8. Comparison of Speed Profiles Over Churchville B Cycle.

Figures Continue on the Next Page

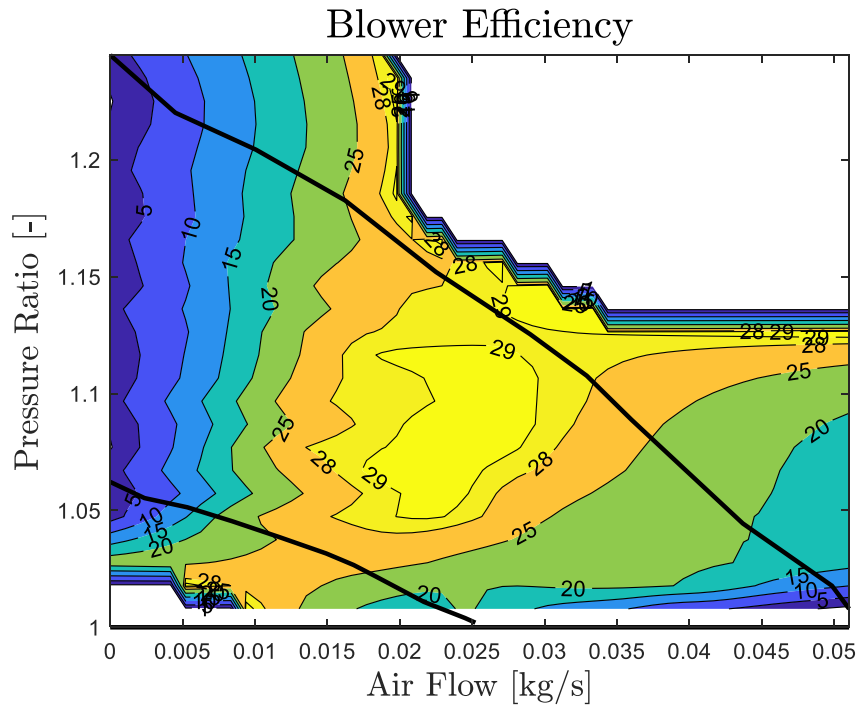


Figure 9. Compressor Map that consists of Blower Efficiency, Airflow and Pressure ratio

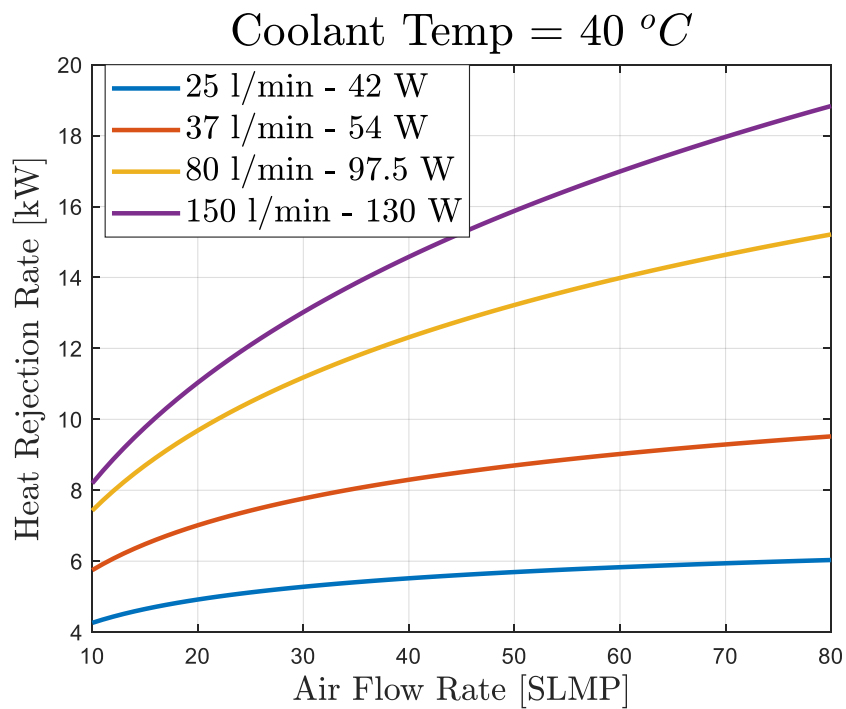


Figure 10. Heat rejection rate for the radiator given the coolant flow rate as a function of the airflow rate blown across it.

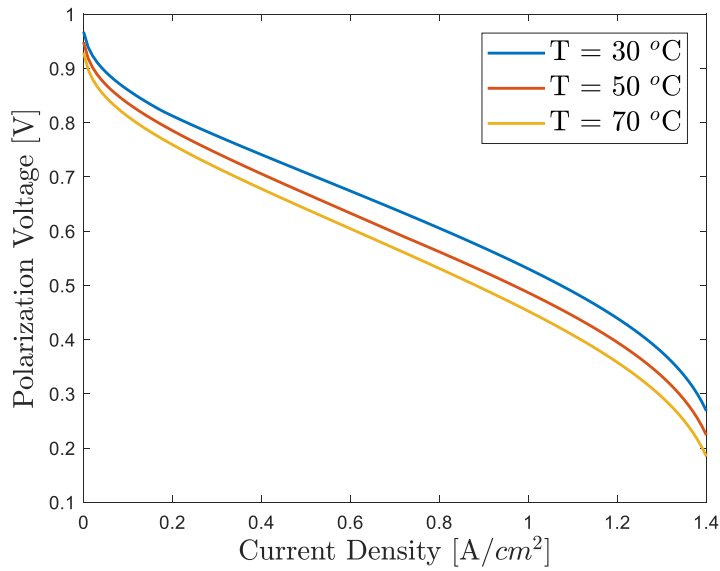


Figure 11. Fuel cell voltage (per cell) as function of current, at three baseline operating temperatures assuming a fully humidified membrane.

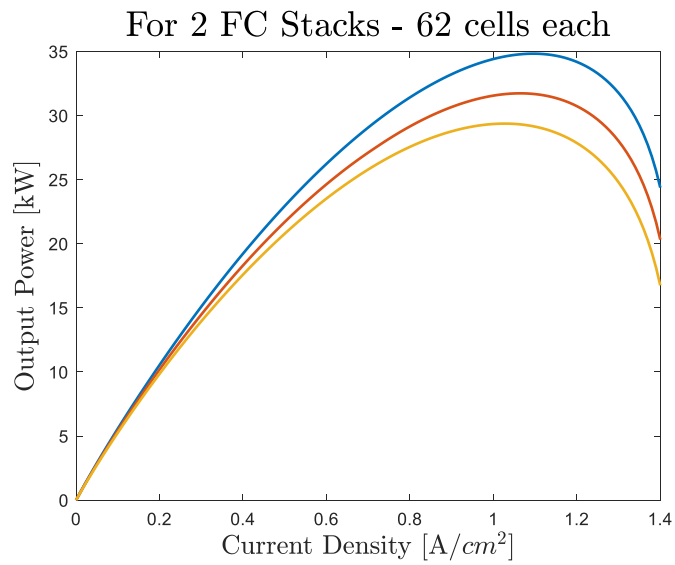


Figure 12. Fuel cell stack power as a function of operating current density (normalized to active area).

Figures Continue on the Next Page

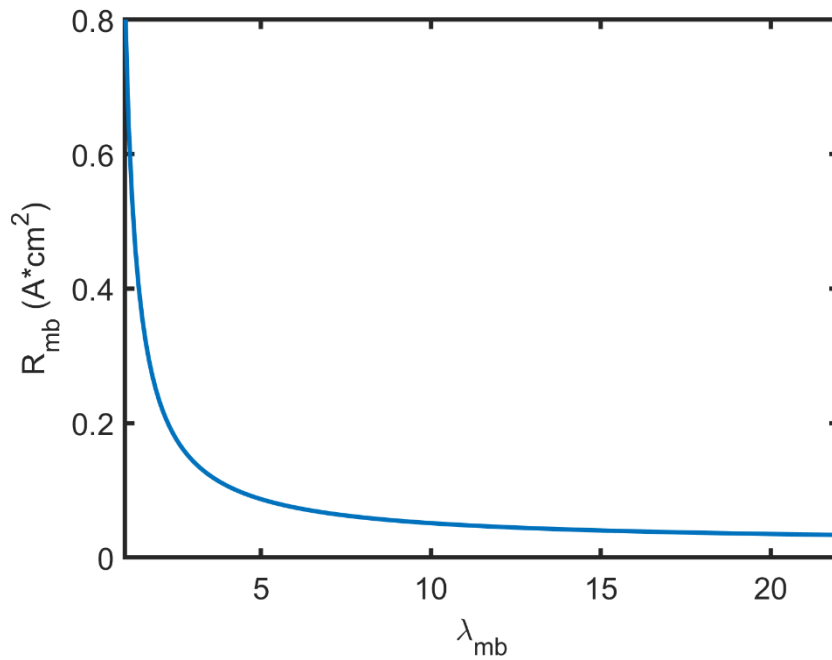


Figure 13. Dependence of membrane effective resistance (ohmic losses) as a function of membrane water content (moles of water per mole of sulfonic acid group) at 30 degrees Celsius. The resistance increases sharply as the membrane dries out, leading to further ohmic heating of the device.

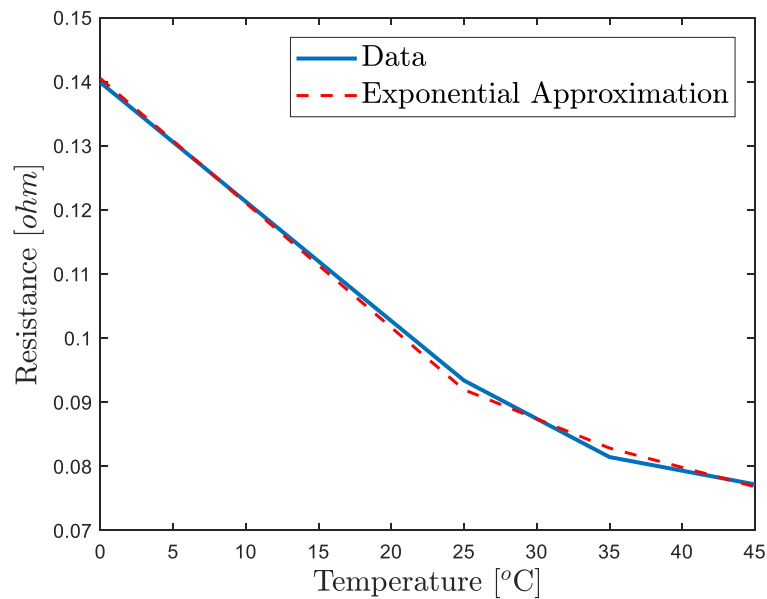


Figure 14. Ohmic resistance of the battery as a function of Temperature, the battery temperature increases sharply for low temperature operation leading to inefficient hybrid system operation during warmup.

Table 1 - Possible Control Modes

Control $u = [u_1, u_2, u_3]$	Description
$[\bar{u}_1, 0, 0]$	1) Full Propulsion
$[0, 0, 0]$	2) Coasting
$[0, \underline{u}_2, 0]$	3) Full Regenerative Braking
$[0, \underline{u}_2, \underline{u}_3]$	4) Full Braking
$[\alpha \cos\theta(x_1) + \beta x_2 + \gamma x_2^2 + g \sin\theta(x_1), 0, 0]$	5) Cruising
$[0, \alpha \cos\theta(x_1) + \beta x_2 + \gamma x_2^2 + g \sin\theta(x_1), 0]$	Cruising

Table 2 - Discretization in DP Implementation

State	Symbol	Value	Unit
Velocity	Δv	0.2	m/s
Time	Δt	2	s
Distance	Δs	30	m

Tables Continue on the Next Page

Table 3 - Vehicle Parameters and Constraints

Parameter	Symbol	Value	Unit
Mass	M	453.6	kg
A	A	0.17	N
B	B	0.06804	Ns/m
C	C	13.608	Ns^2/m^2
Tire radius	r	0.2794	m
Final drive ratio	i_a	7.54	-
Speed limit	v_{lim}	23	m/s
Max. Acceleration	\bar{a}	3	m/s^2
Min. Acceleration	\underline{a}	-3	m/s^2
Motor Efficiency	η_1	0.95	-
Generator Efficiency	η_2	0.88	-

Table 4. Small, Medium, and Large Vehicle Specifications

Vehicle	Small	Medium	Large
Weight (<i>lbs</i>)	3500	24500	100000
Frontal Area (<i>ft</i> ²)	25	58.7	96
Wheel/Sprocket Radius (<i>in</i>)	12	20	12
Engine Displacement	0.2	7	30
Engine, motor power limits	15 <i>kW</i> generation,	270	1000

Remainder of Page Intentionally Blank

This Page is Intentionally Blank

AVPTA “Extended Enterprise” Activities

Wrought FeMnAl Study

DOE-VTO TFA Lead: Sarah Kleinbaum
TARDEC TFA Lead: Ravi Thyagarajan

Principal Investigator(s):
Dr. Katherine Sebeck

Affiliation:
TARDEC Product Lifecycle Engineering
Materials Application & Integration

Project Start: Q1FY18
Estimated Completion: Q4FY20

Objectives:

- Evaluate new class of lightweight steel alloys for use in armor.
- Support effort to transition production of material from lab scale to commercial production.
- Identify thermomechanical processing to optimize hardness, high-strain performance
- Identify suitable welding and machining processes for wrought FeMnAl
- Characterization of material properties to support modeling and simulation efforts
- FY18: evaluate a new lightweight steel alloy for use in armor and the weldability in the as-cast condition.

Strategic Context:

- 10-15% weight reduction over current wrought armor steel with no change in thickness
- Interest from Program Management Main Battle Tank Systems (PM MBTS) Product Manager (PdM) Abrams to reduce weight of turret, hull
- Coupled to other efforts to transition production of materials from lab scale to commercial production.

Accomplishments:

- Initial results from weldability study with Oak Ridge National Lab
- Results from the Wrought FeMnAl study were presented at Materials Science and Technology in Pittsburgh, PA in October 2017, Defense Manufacturing Conference in Tampa, FL in December 2017 and at The Minerals, Metals and Materials Society Meeting in Phoenix, AZ in March 2018.
- Edison Weld Institute (EWI) project to develop weld wire parameters started

OPSEC1890

- High temperature XRD stage and software ordered
- Gleeble evaluation of hot rolling behavior

Introduction:

Increasing weight to protect against changing threats is a challenge across all Army ground vehicle platforms, with major consequences for platforms such as the Abrams Main Battle Tank. (Gerth & Howell, What is a Ton of Weight Worth?, 15-17 Nov., 2016) [2] As additional capabilities are developed without weight as an explicit requirement, this weight creep continues. For legacy vehicle systems, the available light-weighting solutions are limited by current form, fit and function requirement.

FeMnAl is a high-Mn, high-Al steel alloy that has a 10% lower density with similar mechanical performance to existing armor steels. Prior to integration onto existing vehicles, it is necessary to mature the manufacturing process of this material, as well as conduct studies to better understand best practices for joining, machining, corrosion prevention and design implementation. The base material has previously been evaluated in the Ph.D thesis of LTC Ryan Howell [3]. This work is leveraging funding from PdM Abrams and Army ManTech to increase the production scale pursued. General Dynamics Land Systems has identified this material as one of the largest potential ways to reduce weight on the Abrams platform. [4]

Integration of this new lightweight steel into a vehicle platform requires development of joining and machining methods, as well as evaluation of base material properties.

Approach:

Plate procurement is funded through alternate routes.

Using leveraged funding, two 45T heats of materials were cast and hot-rolled to plate by Ellwood Quality Steels (EQS) and ArcelorMittal (AM) respectively. The material produced in these heats fed manufacturability, weldability, and machinability studies along with providing data for modeling and simulation efforts.

The planning strategy centered on defining 8 major areas of development, and identification of associated data points and activities necessary to support development and integration of this material. The eight major areas are:

- Manufacturability
- Blast Data (see AVPTA Lightweight Blast Applique)
- Ballistic Penetration
- Machinability
- Weldability
- Modeling and Simulation
- Corrosion
- Stiffness/Mobility

The AVPTA effort will address work primarily in weldability, machinability, manufacturability, and modeling & simulation. For each development area, internal capabilities were evaluated. If TARDEC facilities were unavailable or at capacity, TARDEC Materials Application and Integration (MAI) reached out to other DoD facilities or DoE labs. Manufacturability is largely to be pursued with industrial partners, but will also be supported by small-scale lab work. Critical path analysis of the schedule indicates that the longest timeline is with corrosion testing. Efforts are underway to pull forward the start of corrosion and coating testing and development.

MAI worked with Oakridge National Lab (ORNL) to conduct a Gleeble evaluation on hot rolling behavior of FeMnAl. Both ORNL and Edison Welding Institute (EWI) have been working to develop weld wire parameters. ORNL has been executing a high strength martensitic weld wire study on as-cast FeMnAl plate while EWI has been focused on high strength austenitic weld wires along with providing machining feedback for the rolled FeMnAl plates. Internal to TARDEC, Center for Systems Integration (CSI) has been working on machining and tapping efforts using as-cast FeMnAl. Efforts with TARDEC Small Arms Ballistics Lab (SABL) are in the planning stage until material becomes available and H-plates are created. Pacific Northwest National Lab (PNNL) received plate material from large ingot heats. Samples for fatigue analysis were machined in Q4FY18. Quasi-static mechanical tests were performed to baseline anticipated range of fatigue performance.

Results and Discussion:

Manufacturability

Hot rolling physical simulations were performed by ORNL using material from a cross section taken from an ingot that failed to roll in industrial trials. After work to minimize the thermal gradient across the copper jaws, deformation simulations were performed at 1050°C, 1100°C, 1150°C, 1175°C and 1200°C. Samples were held a 925°C for 2 minutes to solutionize and austenitize, elevated to test temperature, held for an additional 2 minutes, and then deformed in compression and tension at varying strain rates. The results for 12mm/s deformation are shown below in Figure 1. Flow stress drops off rapidly between 1175°C to 1200°C. Tests were also run at a stroke speed of 1.2 mm/s and 95 mm/s.

The fracture surfaces show increasing cleavage fracture regions after the drop off of flow stress, as well as an increase at higher strain rates. Compressive tests were run to higher maximum temperatures, but challenges were encountered with thermocouple adherence. SEM micrographs of the outer surface also show large ruptures not present at lower temperatures. Analysis of post-test microstructures showed evidence of dynamic recrystallization at austenitic grain boundaries. More complete results are being prepared for joint publication.

Remainder of Page Intentionally Blank

Weldability

ORNL used three different weld wires; ER308L, LTTW1764, and LTTW1766. ER308L is a commercially available austenitic stainless steel welding consumable, while the two low temperature transformation wires (LTTW) were previously jointly developed by ORNL and TARDEC for use with armor steels. Out of the three wires studied, porosity was found in the ER308L weld, shown in Figure 2. The LTTW wires exhibited no cracking or weld defects during examinations, as shown in Figure 3.

ORNL is currently preparing samples for mechanical evaluation of joints welded on the cast material, with results anticipated in Q1FY19.

Results from EWI and CSI are actively being collected, and reports have not been completed. The reports are anticipated in FY19. EWI has completed some bead on plate welding trials, and is machining plates for groove joints. CSI has completed drilling trials, and tapping trials are ongoing.

Durability

Fatigue testing is underway at PNNL: material was received in Q3FY18 from industrial plate production and sent out for machining. Samples were received in late Q4FY18, and initial quasi-static tensile tests (Figure 4) were performed to verify material strength. Initial tests are focusing on outlining the expected fatigue behavior, and verifying the existence of a fatigue limit.

Material Characterization

As different processing routes have been pursued, material has been metallographically and mechanically characterized. One key question for industrial scale up was segregation and defects within the larger ingots. Sections were taken from ingots that failed early in rolling due to low rolling temperature and compositionally evaluated. The general distribution of chemistry is presented in Figure 5 for Mn, Al, C and Si, which are the key alloying elements in this system.

In both ingots, manganese was lowest at the top center, with some variation throughout the ingot. The aluminum was surprisingly homogenous within each ingot, though there is a difference between the two ingots. Carbon, like manganese, is lowest in the top center piece. The silicon varied substantially throughout both ingots, segregating to the centerline in Ingot 3, but showing no trend in Ingot 2.

Conclusions:

FY18 focused on characterization of ingots produced through large scale industrial practice, as well as development of integration techniques such as welding. Thus far, efforts indicate that large scale production of wrought FeMnAl is feasible, but additional work is required to fully characterize and optimize the material for Army ground vehicle performance requirements.

References:

- [1] R. J. Gerth and R. A. Howell, "What is a Ton of Weight Worth?," in *Ground Vehicle Survivability Training Symposium*, Ft. Benning, GA, 15-17 Nov., 2016.
- [2] US Army PM Abrams, *Abrams Special Topic: Transportability IPT Briefing*, 2015.
- [3] R. A. Howell, *Microstructural Influence on Dynamic Properties of Age Hardenable FeMnAl Alloys*, Rolla: Missouri S&T, 2009.
- [4] General Dynamics Land Systems, *Lightweighting IPR - Value Engineering for Abrams Briefing*, Sterling Heights: TARDEC, 2016.

Figures:

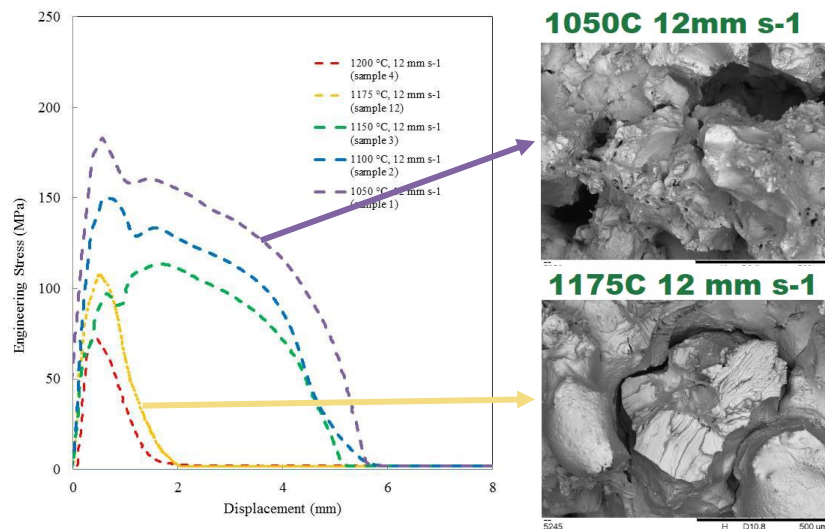


Figure 1. Tensile testing via Gleeble thermomechanical simulation.

Figures Continue on the Next Page

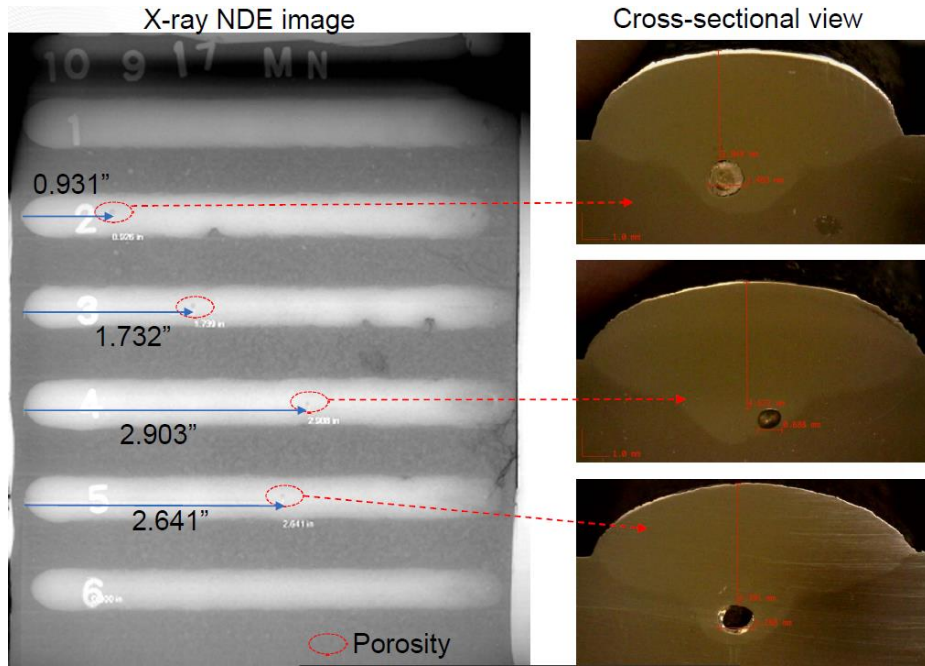


Figure 2. Porosity in ER308L wire

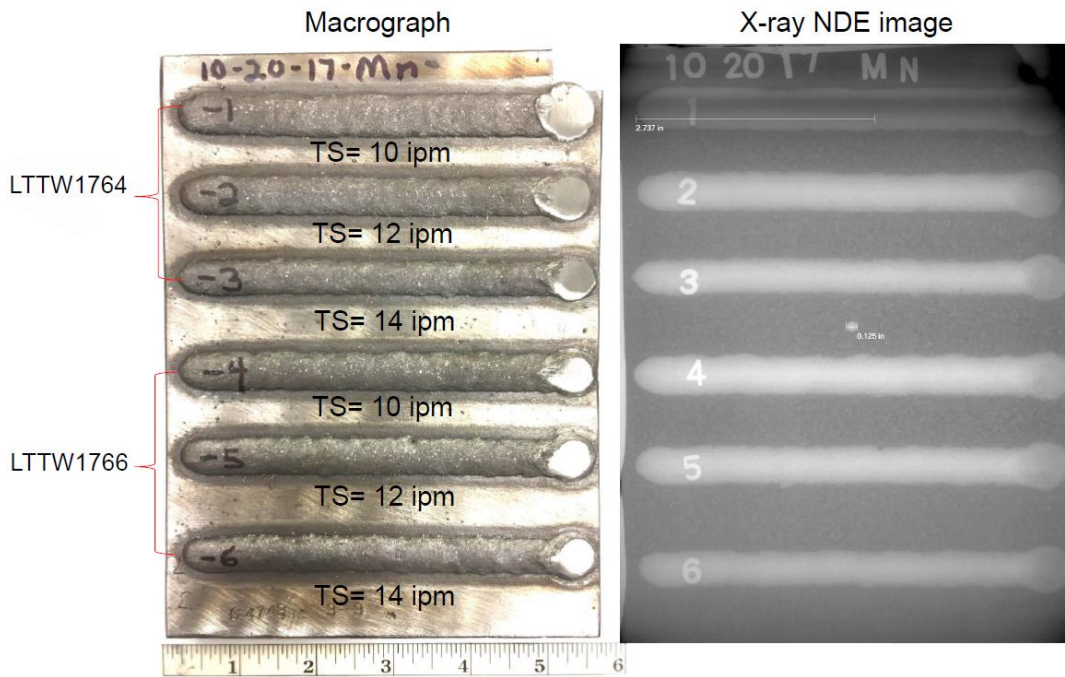


Figure 3. ORNL LTTW weld wire NDE results

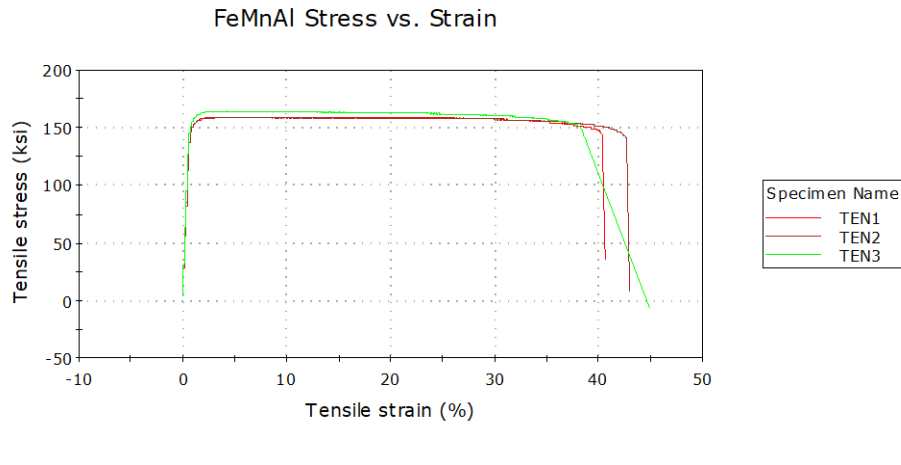


Figure 4. Quasi-static stress-strain results for industrial heat material tested at PNNL

	Ingot 2			Ingot 3		
Mn	31.37	29.81	32.35	31.58	30.51	31.24
	30.14	30.65	32	31.44	31.4	31.55
	32.97	32.65	32.06	31.27	31.72	31.21
Al	8.94	8.88	8.71	8.46	8.64	8.19
	8.96	8.84	8.61	8.47	8.39	8.25
	9.07	8.82	8.7	8.46	8.41	8.09
C	1	0.82	0.99	0.99	0.78	0.98
	1	1.01	0.99	1.01	1	0.99
	0.99	1	0.99	0.99	0.99	0.99
Si	0.31	0.16	0.23	0.44	0.46	0.2
	0.17	0.17	0.51	0.31	0.42	0.25
	0.26	0.29	0.23	0.34	0.45	0.24

Figure 5. Weight percent composition distributed across ingots produced in the same industrial heat

Remainder of Page Intentionally Blank

This Page is Intentionally Blank

AVPTA “Extended Enterprise” Activities

Cast FeMnAl Study

DOE-VTO TFA Lead: Sarah Kleinbaum
TARDEC TFA Lead: Ravi Thyagarajan

Principal Investigator(s):
Dr. Katherine Sebeck

Affiliation:
TARDEC Product Lifecycle Engineering
Materials Application & Integration

Project Start: Q1FY18
Estimated Completion: Q1FY19

Objectives:

- Determine weld materials and process for joining cast FeMnAl steel
- Support development and adoption of a 3rd generation Advanced High Strength Steel (AHSS)

Strategic Context:

- 10-15% weight reduction over current wrought armor steel with no change in thickness
- Interest from Program Management Main Battle Tank Systems (PM MBTS) Product Manager (PdM) Abrams to reduce weight of turret, hull
- Coupled to other efforts to transition production of materials from lab scale to commercial production.

Accomplishments:

- Initial results from weldability study with Oak Ridge National Lab
- Results from the Cast FeMnAl study were presented at Materials Science and Technology Meeting in Pittsburgh, PA in October 2017 and Defense Manufacturing Conference in Tampa, FL in December 2017

Introduction:

Increasing weight to protect against changing threats is a challenge across all Army ground vehicle platforms, with major consequences for platforms such as the Abrams Main Battle Tank. (Gerth & Howell, What is a Ton of Weight Worth?, 15-17 Nov., 2016) [2] As additional capabilities are developed without weight as an explicit requirement, this weight creep continues. For legacy

OPSEC1890

vehicle systems, the available light-weighting solutions are limited by current form, fit and function requirements.

FeMnAl is a high-Mn, high-Al steel alloy that has a 10% lower density with similar mechanical performance to existing armor steels. Prior to integration onto existing vehicles, it is necessary to mature the manufacturing process of this material, as well as conduct studies to better understand best practices for joining, machining, corrosion prevention and design implementation. The base material has previously been evaluated in the Ph.D thesis of LTC Ryan Howell [3]. This work is leveraging funding from PdM Abrams and Army ManTech to increase the production scale pursued. General Dynamics Land Systems has identified this material as one of the largest potential ways to reduce weight on the Abrams platform. [4]

Integration of this new lightweight steel into a vehicle platform requires development of joining and machining methods, as well as evaluation of base material properties.

Approach:

Cast plates of 0.5" and 1" thickness were procured from Waukesha Foundry. These plates were heat-treated by a subcontractor to meet the hardness properties laid out in MIL-STD-12560. Base material hardness, tensile and impact properties were evaluated following appropriate ASTM standard practices. Electron dispersed spectroscopy (EDS) was used to evaluate the local compositional variations of the material. Samples were also prepared for metallographic analysis.

Results and Discussion:

The following is a high level summary of work completed in FY18 under this effort.

Weldability

Oak Ridge National Lab (ORNL) evaluated three weld wires for compatibility with the cast plates. Weldability of cast material is critical for both fabrication and for weld repair of castings during production. Three weld fillers were evaluated, with varying heat inputs and feed speeds. Figure 1 shows a typical metallographic cross section of the bead on plate samples. At the boundary between the weld bead and the base plate, there is a boundary region which was determined to be an unmixed zone.

There are also several micro-cracks emanating from this unmixed zone following the grain boundaries. These are believed to be related to defects in the base material. A large number of small pores are visible in the base material. These were discussed in greater detail in the FY17 report on the base material. A Vicker's hardness trace was taken to see if there was a significant heat affected zone. The hardness values and corresponding cross section are shown in Figure 2.

Remainder of Page Intentionally Blank

No significant heat affected zone is observed. As expected, the weld metal is softer than the base metal. The unmixed zone was slightly harder than the base metal or weld metal. This zone was examined in more detail by scanning electron microscopy (SEM) and energy dispersive spectroscopy (EDS), shown in Figure 3.

The unmixed zone (UMZ) shows interesting dendritic features. Elemental analysis shows some diffusion of chrome into the base metal, and some manganese and aluminum into the weld metal. Nickel does not show significant diffusion. To better understand the dendritic features, a phase map was generated, shown in Figure 4.

While the majority of the unmixed zone is austenitic, like the base material, some ferrite formation is observed. This is attributed to elemental segregation at the boundary, particularly due to the migration of carbon.

In addition to the bead on plate evaluation, two wires were evaluated in a 4 pass single groove butt weld configuration. Mechanical properties of the plates were evaluated, including tensile testing and Charpy V-notch impact testing. Both wires showed good transverse tensile strength, though there was significant scatter in the elongation to failure (11%-39%). Charpy V-notch testing showed highest impact strength in the heat affected zone, with generally good performance (~100 ft-lbs at room temperature) in all cases.

Drill and Tap Tests

TARDEC Center for Systems Integration (CSI) conducted a series of drilling and tapping trials to evaluate alternate fabrication issues for the high Mn, work hardenable alloy system. A number of different drill bits and taps were attempted, with different coatings and feed rates. A coating of Titanium Aluminum Nitride (TiAlN) was found to be more effective than carbide coatings. Small diameter holes were not successfully tapped, and would require a threadmill. Larger holes were successfully tapped with a Titanium CarboNitride (TiCN) coated tap. Cutting fluid was used throughout.

Conclusions:

FeMnAl steels were successfully cast and evaluated through this AVPTA effort. A number of production challenges, such as residual stresses, were identified. Lessons learned from the rapidly produced cast version of this alloy in welding and machining will be extended to the wrought form of the alloy through another AVPTA Extended Enterprise project which is already ongoing.

References:

- [1] R. J. Gerth and R. A. Howell, "What is a Ton of Weight Worth?," in *Ground Vehicle Survivability Training Symposium*, Ft. Benning, GA, 15-17 Nov., 2016.
- [2] US Army PM Abrams, *Abrams Special Topic: Transportability IPT Briefing*, 2015.
- [3] R. A. Howell, *Microstructural Influence on Dynamic Properties of Age Hardenable FeMnAl Alloys*, Rolla: Missouri S&T, 2009.

[4] General Dynamics Land Systems, *Lightweighting IPR - Value Engineering for Abrams Briefing*, Sterling Heights: TARDEC, 2016.

Figures:



Figure 1. (Left) Metallographic cross section of 308L weld bead on cast FeMnAl steel plate showing a number of casting defects as well as (right) micro cracks forming at the grain boundary at the unmixed zone

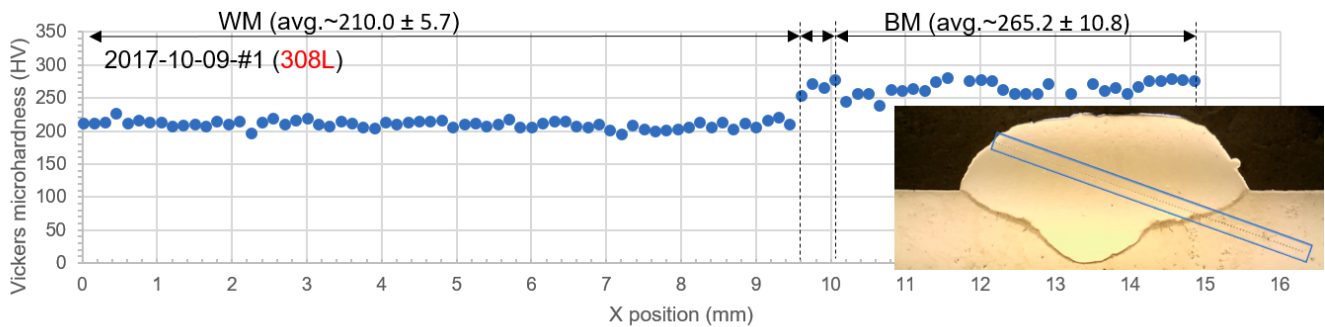


Figure 2. Vicker's hardness traverse of weld and base metal

Figures Continue on the Next Page

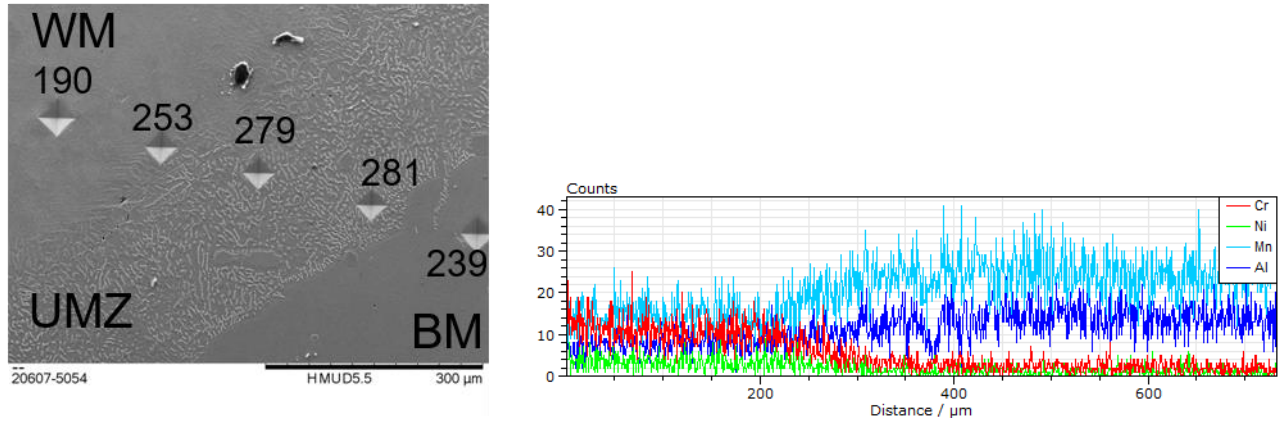


Figure 3. (Left) Scanning electron microscope image of the boundary (UMZ) between the weld metal (WM) and base metal (BM) and (right) energy dispersive spectroscopy trace of this region, showing major elements of interest

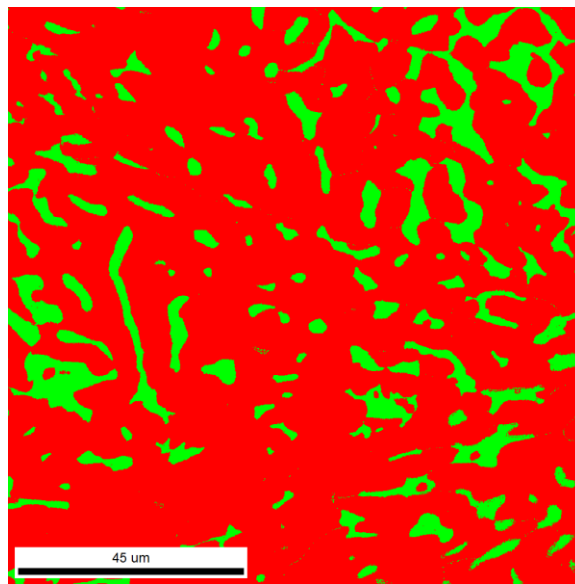


Figure 4. Phase map of the unmixed zone showing FCC austenite (red) and BCC ferrite (green)

Remainder of Page Intentionally Blank

This Page is Intentionally Blank

AVPTA “Extended Enterprise” Activities

Cryo-compressed Hydrogen Storage for Heavy-Duty Vehicles

**DOE-FCTO TFA Lead: Peter Devlin
TARDEC TFA Lead: Kevin Centeck**

**Principal Investigator:
Mr. Rajesh Ahluwalia**

**Affiliation:
Argonne National Lab
9700 South Cass Avenue
Argonne, IL, 60439, USA**

**Project Start: Q4FY18
Estimated Completion: Q4FY19**

Objectives:

- Evaluate the merits of deploying cryo-compressed hydrogen (C₂H₂) storage in heavy-duty fuel cell vehicles that require on-board H₂ storage capacities in excess of 100 kg
- Explore optimization space around C₂H₂ storage to guide future funding opportunities for hydrogen storage on Army vehicles

Strategic Context:

- Electrification of military vehicles will allow improved tactical capabilities but will demand high energy storage density due to the high power and energy requirements of military vehicles. Hydrogen fuel cells and hydrogen storage are one way to enable electrification while minimizing energy consumption and maintaining electrification tactical advantages.

Accomplishments:

- Collaborated with Department of Energy, Fuel Cell Technology Office, Hydrogen Storage Subject matter experts and refined the scope to best align with commercial heavy duty vehicle needs.
- Reviewed literature on vacuum based insulation systems for insulation materials
- Conducted baseline analysis on heat transfer for a hydrogen storage module with parameters of 10 kg H₂ usable capacity, 7 day dormancy at 95% fill. This will serve as the reference point for upcoming design configurations.

Introduction:

This project will evaluate the merits of deploying cryo-compressed hydrogen (C_cH₂) storage in heavy-duty fuel cell vehicles that require on-board H₂ storage capacities in excess of 100 kg and have well-defined duty cycles with favorable dormancy conditions. The project will focus on military needs with intentional alignment to commercial heavy-duty vehicles expected hydrogen storage needs.

Cryo-compressed hydrogen (C_cH₂) storage is a practical method to achieve 2-3 times more hydrogen storage density onboard a vehicle than commercial gaseous hydrogen (G_{H2}) storage technologies [1]. It involves storing supercritical hydrogen in a metallic liner, composite overwrap pressure vessel isolated in a medium-to-high vacuum container surrounded by radiation shielding. Supercritical H₂ is a cryogenic liquid that easily evaporates, but by being stored at high pressure can achieve a supercritical thermodynamic condition. This allows the hydrogen to be stored without evaporative loss for many days while maintaining a very high storage density [2]. Evaporative loss is the main reason not to use a liquid hydrogen (LH₂) storage system. Furthermore, C_cH₂ systems can take advantage of the quantum mechanics phenomena where hydrogen cools as it expands at very low temperatures, known as para-ortho hydrogen conversion, further reducing or eliminating evaporative loss.

The necessity for hydrogen storage research is centered on vehicle electrification. In a military ground vehicle context, electrification offers opportunities for tactical benefits such as reduced signatures, improved automotive performance, reduced fuel logistics burden, and enabling high energy weapon systems. The challenge of electrification is that military vehicles consume significantly more energy than commercial vehicles due to their high operational tempo, high weight and high auxiliary power needs. This means that current and near-future battery technologies will not be sufficient to eliminate the need for onboard power generation. Hydrogen fuel cells are currently the most mature power generation solution available that preserves all of the electrification benefits for military vehicles. C_cH₂ storage is one of the more promising current technologies to meet the on-board storage needs for military vehicles.

In this project the design space for C_cH₂ systems will be explored for optimized performance and cost.

Approach:

A suite of tools will be used by Argonne to conduct preliminary design and analysis over a range of possible C_cH₂ architectures that will all utilize multi-layer vacuum insulation and Type III composite overwrap pressure vessels. The parameter variation includes:

- Cycle life of 5500 and 11000 cycles
- Length/Diameter ratios of 4 and 8
- Operating Pressure Limits of 350 and 700 bar
- Insulation vacuum of 3 and 0.1 milliTorr absolute
- Performance at 52°C
- Total hydrogen capacity of 10 and 20 kg per pressure vessel

OPSEC1890

After exploring the variation in these designs' performances, a single configuration will be selected and practical military vehicle conditions will be explored. These include fill rates, performance degradation due to time, performance loss due to damage, and configuration optimization. The final deliverable will be a preliminary system design relevant to military vehicles, including a computer aided design model, balance-of-plant requirements, and projected performance metrics.

Results and Discussion:

NA – Project kicked-off in late Q4FY18.

Conclusions:

NA – Project kicked-off in late Q4FY18.

References:

- [1] Salvador M. Aceves, Guillaume Petitpas, Francisco Espinosa-Loza, Manyalibo J. Matthews, Elias Ledesma-Orozco *Safe, long range, inexpensive and rapidly refuelable hydrogen vehicles with cryogenic pressure vessels*. United States. <https://doi.org/10.1016/j.ijhydene.2012.11.123>
- [2] Ahluwalia, R. K., Peng, J. K., Roh, H. S., Hua, T. Q., Houchins, C., & James, B. D. *Supercritical cryo-compressed hydrogen storage for fuel cell electric buses*. United States. <https://doi.org/10.1016/j.ijhydene.2018.04.113>

Figures and Tables:

NA

Remainder of Page Intentionally Blank

This Page is Intentionally Blank

APPENDIX A

Memorandum of Understanding

Between

U. S. Department of Energy

And

U. S. Department of Defense

Concerning Cooperation in a Strategic Partnership to Enhance Energy Security

I. Purpose

The purpose of this Memorandum of Understanding (MOU) is to identify a framework for cooperation and partnership between the Department of Energy (DOE) and the Department of Defense (DOD), hereafter referred to as the Parties, to strengthen coordination of efforts to enhance national energy security, and demonstrate Federal Government leadership in transitioning America to a low carbon economy. This MOU covers, but is not limited to, efforts in the areas of energy efficiency, renewable energy, water efficiency, fossil fuels, alternative fuels, efficient transportation technologies and fueling infrastructure, grid security, smart grid, storage, waste-to-energy, basic science research, mobile/deployable power, small modular reactor nuclear energy, and related areas.

II. Legal Authority

DOE enters into this MOU under the authority of section 646 of the Department of Energy Organization Act (Pub. L. 95-91, as amended; 42 U.S.C. § 7256). DOD enters into this MOU under the authority of DOD Instruction 4000.19 "Inter-Service and Intra-Governmental Support" August 9, 1995.

III. Background

In the 2010 Quadrennial Defense Review, the DOD expressed an intent to partner with other U.S. agencies to research, develop, test, and evaluate new sustainable energy technologies. The DOD aims to speed innovative energy and conservation technologies from laboratories to military end users, and it uses military installations as a test bed to demonstrate and create a market for innovative energy efficiency and renewable energy technologies coming out of DOE laboratories, among other sources. The DOE is currently supporting a range of projects aimed at improving energy efficiency and renewable energy efforts across the military services.

Energy security for the DOD means having assured access to reliable supplies of energy and the ability to protect and deliver sufficient energy to meet operational and Installation energy needs. Energy efficiency can serve as a force multiplier, increasing the range and endurance of forces in the field while reducing the number of combat forces diverted to protect energy supply lines, as well as reducing long-term energy costs. DOD is also increasing its use of renewable energy supplies and reducing energy demand to improve energy security and operational effectiveness, reduce greenhouse gas (GHG) emissions in support of U.S. climate change initiatives, and protect the DOD from energy price fluctuations. Solving military challenges through innovation has the potential to yield spin-off technologies that benefit the civilian community as well.

The DOE is the lead Federal agency responsible for the development and deployment of advanced energy technologies, yet DOD will need to invest in many of these same energy technologies as well as other energy technologies which may be unique to DOD's operational requirements. Partnering with DOD provides DOE the opportunity to accelerate the deployment of its technologies and expertise toward the critical economic and energy security needs of the United States and to promote scientific and technological innovation.

The Parties acknowledge the significant positive collaboration that already exists between DOE and DOD and intend through this MOU to strengthen and broaden that cooperation.

IV. Activities

Specific activities covered under this MOU include, but are not limited to:

- A. Evaluate energy systems and technology management solutions that meet DOD objectives including developing energy technologies that meet DOD energy requirements. Work collaboratively to identify a strategy for their development and deployment.
- B. Maximize DOD access to DOE technical expertise and assistance through cooperation in the deployment and pilot testing of emerging energy technologies. Technology areas may include, but are not limited to, energy efficiency, renewable energy, water efficiency, fossil fuels, alternative fuels, efficient transportation technologies and fueling infrastructure, grid security (e.g., superconductivity, power, electronics, microgrids, cyber, EMP), smart grid, storage, waste-to-energy, basic science research, mobile/deployable power, small modular reactor nuclear energy, and related areas.

- C. Expand cooperation related to energy management practices and knowledge exchange, working to ensure that Federal leadership is in compliance with all statutory and Executive Order goals and objectives, particularly in the area of GHG reductions. Encourage the sharing of data, including, but not limited to, data on internal energy management projects and technical assistance projects.
- D. Collaborate on science and technology (S&T) projects at research institutions sponsored by either agency. Synchronize research and development (R&D) of new knowledge and technologies to expand complementary efforts.
- E. Develop joint initiatives for major energy technology research, development and demonstration programs of mutual interest to DOD and DOE, such as pilot or demonstration facilities which address military needs and also may address national security needs that transcend military requirements. DOD installations may serve as test beds for such technical demonstrations.
- F. Develop human capital within DOE and DOD through teaching and education. Work to integrate respective agency energy training and knowledge exchange practices.
- G. Encourage professional exchanges and formal liaison relationships between all DOE and DOD components including, but not limited to, laboratory, headquarters, military installations, combatant command headquarters, and forward operating bases.
- H. Collaborate on issues regarding nuclear power, except naval nuclear propulsion, including developing a business, licensing and regulatory strategy as appropriate, and evaluating the integration of energy technologies with other industrial applications that support DOD objectives for energy security and GHG reduction. Collaboration will include NRC review and licensing of nuclear power plants that are deployed for DOD purposes, and are located on or adjacent to DOD U.S. installations.

V. Implementation

DOE and DOD intend to develop and conduct cooperative activities relating to identified high priority energy strategic needs, where such cooperation contributes to the efficiency, productivity, and overall success of the activity. The Parties intend for the activities to be executed under the MOU to be established by a joint DOE/DOD senior-level Executive Committee. This Executive Committee will be co-chaired by a designee of the Under Secretary of Defense (Acquisition,

Logistics and Technology) and a designee of the Deputy Secretary from DOE. The Executive Committee will be responsible for the operations and governance of this MOU. Under the direction of the Co-Chairs, the Committee will include representatives from each of the principal DOE offices, specifically, the Office of the Under Secretary for Science, the National Nuclear Security Administration, and the Office of the Under Secretary for Energy. From the Department of Defense representatives will include the Deputy Under Secretary of Defense (Installations and Environment) and the Director of Operational Energy Plans and Programs. Additional members from both Agencies that may be involved in issues or functions of this MOU may be added. Upon agreement of both Departments, the Co-Chairs will appoint a team to develop, within 60 days, a charter and operating structure, membership, products, and decision processes.

The Executive Committee may establish working groups of Federal employees to perform and execute necessary activities contemplated by this MOU at their discretion. The Executive Committee and its working groups may make consensus recommendations based on their collaboration.

The Executive Committee will determine an appropriate regular meeting schedule, not to be less than four times annually. The Co-Chairs will be responsible for the development and distribution of agendas, presentations, and minutes of each meeting. Action items will be clearly identified and tracked in the minutes.

The Co-Chairs will be responsible for any reporting to the appropriate Departmental Secretarial Officers and will outline accomplishments, issues, redirections, and change assessments. The reporting will be coordinated by the Co-Chairs as appropriate.

The Co-Chairs will be responsible for any reports or presentations that are requested by other organizations, subject to the necessary review of each Party.

VI. Funding

Each party intends to coordinate their individual funding and resource decisions in order to maximize the benefits of cooperation under this MOU. Any transfer of funds or sharing of resources between the parties will be pursuant to a separate or pre-existing agreement.

VII. General

Work under this MOU will be jointly planned and monitored by the DOD and DOE.

In the event any activity undertaken by the agencies to implement the purposes of this MOU involves access to and sharing or transfer of technology subject to patents or other intellectual property rights, such access and sharing or transfer will be provided on terms which recognize and are consistent with the adequate and effective protection of intellectual property rights.

This MOU is strictly for internal management purposes for each of the Parties. It is not legally enforceable and shall not be construed to create any legal obligation on the part of either Party. This MOU shall not be construed to provide a private right or cause of action for or by any person or entity.

This MOU in no way restricts either of the Parties from participating in any activity with other public or private agencies, organizations, or individuals.

This MOU is intended to complement, and not to duplicate, cooperation by the Parties under the Memorandum of Understanding between the Department of Energy (National Nuclear Security Administration)/(Office of Science)/(Office of the Under Secretary) and the Department of Defense (Acquisition, Technology and Logistics) concerning Cooperation in a Strategic Partnership to Enhance National Security of January 26, 2009.

All agreements herein are subject to, and will be carried out in compliance with, all Federal applicable laws, regulations and other legal requirements.

This MOU is neither a fiscal nor a funds obligation document. Nothing in this MOU authorizes or is intended to obligate the Parties to expend, exchange, or reimburse funds, services, or supplies, or transfer or receive anything of value.

VIII. Contacts/Designated Representatives

Under Secretary for Science
U.S. Department of Energy
Washington, DC 20585

Under Secretary for Energy
U.S. Department of Energy
Washington, DC 20585

Under Secretary for Nuclear Security
U.S. Department of Energy
Washington, DC 20585

Deputy Under Secretary of Defense
Installations and Environment
U.S. Department of Defense
Washington, DC 20301

Director of Operational Energy Plans and Programs
U.S. Department of Defense
Washington, DC 20301

Deputy Assistant to the Secretary of Defense for Nuclear Matters
U.S. Department of Defense
Washington, D.C. 20301-3050

IX. Duration of Agreement

This MOU is effective on the date of the final signature and will remain in effect until it is terminated by mutual agreement of the Parties or by either Party providing ninety days written notice to the other. This MOU may be modified at any time by written agreement of the Parties. Nothing in this MOU shall be interpreted to limit or otherwise affect any authorities, powers, rights, or privileges accorded to DOD or DOE or any of the officers, employees, or organizational units under any statute, rule, regulation, contract, or agreement.



Daniel B. Poneman
Deputy Secretary of Energy

JUL 22 2010
Date



William J. Lynn III
Deputy Secretary of Defense

JUL 22 2010
Date

APPENDIX B



The Deputy Secretary of Energy
and
The Under Secretary of the Army



CHARTER

Advanced Vehicle Power Technology Alliance

I. DESIGNATION

By authority of this charter, effective on July 18, 2011, the Advanced Vehicle Power Technology Alliance (AVPTA) was established. AVPTA shall be active until the charter is rescinded, repealed, terminated, or suspended.

II. MISSION

The AVPTA is a partnership between the Department of the Army (DA) and the Department of Energy (DOE) in accordance with Section IV. E of the Department of Defense (DoD) and DOE Memorandum of Understanding (MOU) Concerning Cooperating in a Strategic Partnership to Enhance Energy Security, for the establishment of a joint technology research initiative in the area of ground vehicle power technology research, development, and transition. The seven focus areas of science and technology are: (1) advanced combustion engines and transmissions, (2) lightweight structures and materials, (3) energy recovery and thermal management, (4) alternative fuels and lubricants, (5) electrified propulsions systems, (6) energy storage & batteries, and (7) autonomy-enabled technologies. Where requirements are common, the two Departments will leverage resources to improve transition of technologies into both the commercial and military marketplace. The AVPTA leverages industrial research and development involving commercial automotive and defense ground vehicle manufacturers to transition technologies and increase precompetitive research and development.

III. RESPONSIBILITY

The AVPTA is designated as the DA's and DOE's primary point of contact for automotive power technology in the seven focus areas of science and technology. Consistent with applicable law, regulation, and policy the AVPTA may conduct its activities in accordance with such agreements as are deemed necessary for its efficient operation.

IV. AUTHORITY

The AVPTA is jointly led by the Director, U.S. Army Tank Automotive Research, Development and Engineering Center, and the Department of Energy Director, Vehicle Technologies Office (hereinafter "Directors"). Both Directors maintain authorities over their

OPSEC1890

respective budgets. The AVPTA conducts activities in accordance with the DoD-DOE Energy Security MOU. DOE entered into the MOU under the authority of section 646 of the DOE Organization Act (Pub. L. 95-91, as amended; 42 U.S.C.). The Army entered into the MOU under the authority of DoD Instruction 4000.19, "Inter-Service and Intra-Governmental Support," April 25, 2013. The Directors are the principal and primary points of contact for the prioritization of automotive/ground vehicle power and energy technologies in the seven focus areas of science and technology.

V. COORDINATION

The AVPTA shall, as appropriate, coordinate activities and actions with associated government agencies, industries, and academia with a focus on efficient vehicle power systems. The AVPTA will conduct a yearly meeting to coordinate science and technology (S&T) activities, and will align S&T projects and products where requirements are similar. A yearly meeting will be conducted to assess results, update requirements, and determine new joint efforts. The AVPTA will report results to the Under Secretary of the Army and the Deputy Secretary of Energy.

VI. ADVISORY BOARD

The Directors may establish a Senior Advisory Board with other government agencies to review strategic planning and make recommendations on future activities. All activities associated with the Senior Advisory Board will comply with the Federal Advisory Committee Act (FACA), 5 U.S.C. App. 2 and implementing regulation and policy, as applicable. As authorized by law, regulation, and policy, the Senior Advisory Board may seek the individual advice of non-Government employees (e.g., individual members of industry or academia) to secure facts and other information to assist the Senior Advisory Board's review.

VII. LEGAL AUTHORITY

The Directors will ensure that AVPTA activities are conducted in a manner consistent with all applicable laws, regulations, and policies. In particular, the appropriate agency counsel will review in advance all interaction with industry, academia, or other non-governmental entities to confirm that any necessary enabling authorities exist and to ensure compliance with the FACA and implementing regulations and policies.

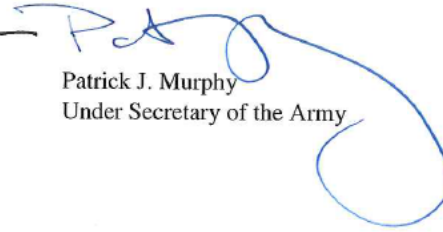
VIII. TERMINATION AND REVIEW

This charter shall terminate automatically on the 5-year anniversary date unless the undersigned expressly approves it for renewal. Directors will review this charter biannually on its anniversary date to ensure currency, completeness, and adequacy. Changes to mission

and/or responsibilities will require the review by, and approval of, the Secretary of the Army and the Secretary of Energy.



Elizabeth Sherwood-Randall
Deputy Secretary of Energy



Patrick J. Murphy
Under Secretary of the Army

Remainder of Page Intentionally Blank

This Page is Intentionally Blank